THE SYNTHESIS AND APPLICATIONS OF TUNGSTEN AND VANADIUM OXIDES/OXYHYDROXIDES IN BOTH BULK AND NANOPARTICULATE FORMS

By
ASMA ABDULLAH ALOTHMAN
Bachelor of Science in Chemistry
King Saud University
Riyadh, Saudi Arabia
2003

Master of Science in Chemistry
King Saud University
Riyadh, Saudi Arabia
2008

Submitted to the Faculty of the
Graduate College of the
Oklahoma State University
in partial fulfillment of
the requirements for
the Degree of
DOCTOR OF PHILOSOPHY
December, 2016

THE SYNTHESIS AND APPLICATIONS OF TUNGSTEN AND VANADIUM OXIDES/OXYHYDROXIDES IN BOTH BULK AND NANOPARTICULATE FORMS

Dissertation Approved:

Dr. Allen W. Apblett

Dissertation Adviser

Dr. Nicholas F. Materer

Dr. Toby L. Nelson

Dr. Yolanda Vasquez

Dr. Clint P. Aichele

ACKNOWLEDGEMENTS

In the Name of Allah, Most Gracious, Most Merciful

Thanks to Almighty God for the innumerable blessings has bestowed upon me to flourish my thoughts and thrive my ambition to have the cherish fruit of my modest efforts in the form of this dissertation. My success can only come from Allah (SWT). In Him I trust, and unto Him I turn.

Thanks to you all people who have helped me along the way and contributed in some way to the work described in this dissertation. First and foremost, my sincere appreciation and gratefulness goes to my work advisor, Dr. Allen Apblett, for his intelligent supervision, constructive guidance, inspiration and friendship over the years of my graduate research work at Oklahoma State University. My appreciation extends to my doctoral committee members, Dr. Nicholas Materer, Dr. Toby Nelson, Dr. Yolanda Vasquez, and Dr. Clint P. Aichele for their input and support.

I greatly appreciate the faculty and staff at the Department of Chemistry at Oklahoma State University for their hard work, expertise, and patients. I would like also to extend my warm thank to Oklahoma State University (OSU) Microscopy Laboratory director Dr. Charlotte L. Ownby, and senior research specialist Ms. Lisa Whitworth for helping with SEM images. I am very grateful to Cory Perkins and Travis Reed for all of their advice and being helpful and supportive. To the Apblett Research Group, past and present, thank you all for your assistance and friendships.

My sincere appreciation to my friends, Paula Hopson, Yen Nguyen, and Vini Singh for listening, offering me advice, and supporting me through this entire process. Particularly Paula Hopson for cheering me up whenever I felt low and being great true friend, the most supportive and caring. I also appreciate her mother Jacquelyn Arscott, for all her prayer and love. My appreciation also

Acknowledgements reflect the views of the author and are not endorsed by committee members or Oklahoma State University.

extended to her family, Jarrett Hopson and their beautiful daughter Raidyn Paige for what they have done being supportive and such amazing wonderful people. O' Allah bless their life with love, joy, and peace.

My deepest gratitude to my loving parents (Abdullah and Basmah) for their unconditional love, faith, wisdom, support, and care. My gratitude to you is beyond words. My appreciation extends to my siblings: Mona, Mohmmad, Shaima, Abdulrahman, Hammad, Sulaiman, Fatimah and Saud who have been my best friends all my life. Thanks to my extended family as well. You all have been a constant source of inspiration and this work is especially dedicated to you. I do love you all. O' Allah please bless and take care of them. Finally, I would like to thank the Kingdom of Saudi Arabia, Ministry of Foreign Affairs, Ministry of education, and Saudi Cultural Mission for the provided opportunity to pursue my PhD degree and their continuous support. My appreciation extended to King Saud University, and foremost to the Deanship of Faculty and Personnel Affairs, College of Science, and Chemistry Department for their support. I would also express my gratitude to those people who taught, support, and encourage me throughout my student life.

To the people who deserve recognition for making my academic life fun, interesting, and even worthwhile, and I forgotten to list their name I would express my gratefulness and my genuine apology.

I would like to conclude my acknowledgement with prayer as narrated by the Almighty Allah in The Holy Qur-ān in Sūrat Al-'Aĥqāf (The Wind-Curved Sandhills), verse 15, "My Lord, enable me to be grateful for Your favor which You have bestowed upon me and upon my parents and to work righteousness of which You will approve and make righteous for me my offspring. Indeed, I have repented to You, and indeed, I am of the Muslims".

ASMA ALOTHMAN, 2016

Acknowledgements reflect the views of the author and are not endorsed by committee members or Oklahoma State University.

Name: ASMA ABDULLAH ALOTHMAN
Date of Degree: DECEMBER, 2016
Title of Study: THE SYNTHESIS AND APPLICATIONS OF TUNGSTEN AND VANADIUM OXIDES/OXYHYDROXIDES IN BOTH BULK AND NANOPARTICULATE FORMS
Major Field: CHEMISTRY

Abstract: The reactions of tungstic acid towards alkenes, alkynes, and nitriles were explored in order to determine the scope of its reactions with unsaturated hydrocarbons. The chemistry was found to be complex with small changes in substrates leading to significant changes in the products produced. Most reactions, but not all, resulted from strong acid catalysis. Dehydrogenation, dimerization, cyclotrimerization, oligomerization, and hydration reactions were observed. Single-step reactions to produce useful triazenes or to convert light petroleum fractions to diesel fuel, the Jacobsen rearrangement of alkyl benzenes, and the first non-enzymatic retro benzoin condensation were discovered. The products have potential applications in organic synthesis, industry, and medicine. The reduction of colloidal suspensions of vanadium bronze were found to produce suspensions of vanadium bronze nanoparticles while reactions with bulk materials produced bulk bronzes. Bimetallic oxides and oxyhydroxides of vanadium combined with aluminum, zirconium, yttrium, and lanthanum were successfully obtained through reaction of the aqueous vanadyl oxalate and the corresponding metal oxide or hydroxide. These materials have important applications in catalysis, pigments, and explosive sensing. In the latter respect, sensing systems for hydrogen peroxide detection utilizing colloidal vanadium bronzes, vanadyl solutions, and thin film of vanadium oxide materials were developed. Thin films of $V_{10}O_{24}\cdot 12H_2O$ were made successfully from a nanometric suspension of the material produced by reduction of peroxovanadic acid by oxalic acid. This film showed electrical conductivity and stability for long periods of time. All of the vanadium-containing systems tested showed rapid dramatic colors change after exposure to hydrogen peroxide exposure. Supporting the materials on porous alumina surfaces resulted in a significant enhancement of the sensitivity towards peroxide. Two of these sensing systems showed exceptional promise for sensor development due to their ability to regenerate their original color after hydrogen peroxide exposure ends. Kinetic analysis of color regeneration found it to be a first order reaction. The resting states of these two catalytic systems are the blue reduced vanadium compound. When exposed to hydrogen peroxide the materials adopt the red coloration of a vanadium hydroperoxide complex but once removed from hydrogen peroxide, the blue color slowly regenerates as the red color fades.

TABLE OF CONTENTS

LIST OF TABLES

CHAPTER V

CHAPTER VI

LIST OF SCHEMES

LIST OF FIGURES

CHAPTER I

CHAPTER II

CHAPTER III

CHAPTER IV

CHAPTER V

CHAPTER VI

CHAPTER VII

CHAPTER I

INTRODUCTION

1. Dissertation Overview:

This current dissertation, entitled '*The Synthesis and Applications of Tungsten and Vanadium Oxides/Oxyhydroxides in both Bulk and Nanoparticulate Forms*', includes the main body in addition to the introductory chapter. The introductory chapter (Chapter I) presents an overview of the purpose and scope of the research along with a brief background discussion of the materials of interest, their structures, and their synthesis. The main body of the dissertation is subdivided into four parts. The first part, Chapters II, discusses the catalytic activity of tungstic acid and tungsten blue with selected alkenes, alkynes, and nitriles. The second part, consisting of Chapters III, IV, V, and VI, describes the development of novel methods for the synthesis of mixed valence vanadium oxides/oxyhydroxides and bimetallic vanadium oxides/oxyhydroxides and the characterization of the novel materials. Chapter III is devoted to an investigation of the reaction of sodium dithionite with bulk vanadium pentoxide in bulk powder form and as a colloidal suspension. Chapter IV discusses the synthesis and characterization of vanadyl oxalate solution and the thermal decomposition of vanadyl oxalate. In addition, this chapter also reports an investigation of the reaction of aqueous vanadyl oxalate solutions with aluminum hydroxide and the formation of mixed aluminum vanadium oxyhydroxides precursor material for aluminum orthovanadate and

alumina-supported yttrium orthovanadate. Chapter V reports the extension of the discovery of newly discovered reactivity of vanadium oxalate towards aluminum hydroxide to three other materials: zirconium hydroxide, yttrium oxide, and lanthanum oxide. Chapter VI explores the reaction of vanadium pentoxide with pyruvic acid oxime via a method that is analogous to the preparation of vanadyl oxalate. The dark blue $VO(PAO)_2$ thus produced was investigated as a precursor for vanadium pentoxide that would be useful for producing supported V_2O_5 catalysts. The possible conversion of vanadyl pyruvic acid oxime to a single-source precursor was explored and is also reported in this chapter. Finally, the reaction of the novel reagent with aluminum hydroxide will be discussed. The third part of the main body of this dissertation (Chapter VII) reports the investigation of the peroxide-based explosive sensing applications of several of the vanadium compounds developed in this research.

2. Background:

Layered transition metal oxides and oxyhydroxides of vanadium, molybdenum and tungsten have rich physicochemical properties that to this day are not completely explored. Their ability to form conducting bronzes through the reversible incorporation of hydrogen or alkali metals into their lattices with partial reduction of the host metal ions is particularly interesting.[1] Molybdenum, vanadium, and tungsten layered oxides and oxyhydroxides play important roles in numerous applications in many fields; such as including catalysis [2-13], sensing devices [14-17], electrodes [18, 19], lithium ion batteries [20-27], and electrochromic or liquid crystal displays [8, 21, 28-35].The physicochemical properties of these materials depend strongly on the structures they adopt which are numerous and cover a broad range of oxidation states.

This review of the literature will focus of the materials most pertinent to this investigation. In the case of vanadium, Peter Y. Zavalij et al. (1999) provided a structural classification and notation system for pure vanadium oxide open framework structures with vanadium in oxidation states greater than 3+. Approximately 60 types of vanadium materials are divided into five classes according to the

type of coordination polyhedra present and into 14 subclasses according to the more complex structure formed. [36]

In the case of nanomaterials, Boris I. Kharisov et al. (2010) offered a discussion of rare nanostructures with animal-like shapes as well as a non-formal classification for nanostructures based on rare nanostructures. [37] It has been stated that different nano-forms of inorganic compounds possess different useful properties. The nano-form adopted by materials are strongly dependent on the templates used, the packing mechanism, and the arrangement of surfactants between the metal layers. For example, hierarchical WO_3 nanoparticle that resemble sea urchins were produced by a hydrothermal method using sodium tungstate, the ammonium salt of EDTA, and Na_2SO_4. In the absence of the EDTA salt, the reaction produced WO_3 nanowire bundles instead. These two different morphologies of WO_3 nanoparticles display different electrochemical responses and possess dissimilar luminescence properties.

The morphologies of vanadium oxide particles were also observed to be strongly dependent on the valency of the vanadium ion in addition to the dependence the organic surfactant template used, the packing mechanism, and the arrangement of the surfactant between the vanadate layers. For example, nanoparticles of VO_x have morphologies that mimic sea urchins vanadium oxides (VO_x) and are composed of a central spherical particle from which project oriented arrays of vanadium oxide nanotubes or nanorods. The variations in the projecting "needles" influence the electrocatalytic and photocatalytic activities of the particles. [37]

Jacques Livage et al. (2010) also reported how the molecular structure of precursors in the solution are somewhat correlated to the nanostructure products phases produced via hydrothermal methods. Numerous vanadium oxides with a variety of nanostructures have been hydrothermally synthesized from an aqueous vanadium (V) solutions. Nanotubes are obtained via a self-rolling process while nanospheres, nanoflowers and nano- sea urchins are formed via the self-assembling of nanoparticles. [38]

Henri van Damme et al. (1990) reported the synthesis of pillared vanadium oxide. [39] Pillaring the layers of a vanadium pentoxide xerogel, which has acidic and weak mixed valence V^{V}-V^{IV} characteristics with Al_{13} Keggin ions, $[Al_{13}O_4(OH)_{24}(OH_2)_{12}]^{7+}$ was accomplished via a double ion exchange method while pillaring with Mo_6 and Nb_6 polynuclear cations was accomplished using a single ion exchange method.

Yoshio Oka et al. (1990) prepared green fibrous vanadium oxyhydroxides $H_2V_3O_8$ hydrothermally from $VOSO_4$ aqueous solutions. [40] The structure of the produced was determined using the XRD data and the Rietveld method. It has a layered structure composed of V_3O_8 layers that are comprised of two VO_6 octahedra and one VO_5 trigonal bipyramid that were assigned to V^{5+} and V^{4+} respectively. The arrangement of the vanadium oxide polyhedra are related to those of the vanadium bronzes β-$Na_{0.33}V_2O_5$.

Chi-Chang Hu et al. (2007) reported the formation of highly pure $H_2V_3O_8$ single crystal nanobelts through hydrothermal treatment of a precursor solution containing V^{5+} and V^{4+} in fixed ratio of two to one. [41] Studying the growth mechanism of $H_2V_3O_8$ nanobelts during the hydrothermal synthesis clarified that the hydrothermal route involved the formation of metastable, whisker-like $V_{10}O_{24}\cdot nH_2O$ particles that react continuously with the dissolved V^{4+} ions to form $H_2V_3O_8$ nanobelts.

Guyomard et al. (2002) reported a study of the lithium insertion/deinsertion properties of $H_2V_3O_8$ precursor and three oxidized derivatives $M_yH_{1-y}V_3O_8$ (M = Li, Na, K; y = 0.6-0.9). [23] The new derivatives were formed through the oxidation of $H_2V_3O_8$ under mild conditions. The electrochemical performance of these materials with respect to lithium insertion differed from that of the precursor $H_2V_3O_8$. Only $Na_{0.9}H_{0.1}V_3O_8$ showed remarkable electrochemical behavior and lithium insertion properties that make it a promising candidate positive electrode material for rechargeable lithium batteries.

Masaharu Nakayama et al. (2005) described the fabrication of molybdenum and vanadium mixed oxyhydroxide films from Keggin-type V-substituted polymolybdophosphate precursors. [42] The

fabrication of molybdenum and vanadium mixed oxyhydroxide films on gold electrodes was accomplished by electrochemical reduction route. The modified electrodes showed stable redox behavior in 0.5 M Na_2SO_4 electrolyte at pH 3. Cyclic voltammetry of the resulting films showed a response to nitrite in the form of a current enhancement. The deposited V ions were found to participate in the electrocatalytic reduction of nitrite ion.

Mingdeng Wei et al. (2009) synthesized single crystal $V_3O_7 \cdot H_2O$ nanobelts and investigated their electrochemical properties. [22] The nanobelts were prepared using a hydrothermal method without any of templates or catalysts. Electrochemical measurements showed that impregnation of these nanoparticles into the working electrode of a lithium ion battery enhanced the performance due to the intrinsic properties of the $V_3O_7 \cdot H_2O$ phase.

Yi Xie et al. (2009) synthesized a smart electrical switch material based on haggite $V_4O_6(OH)_4$ nanobelts. [35] This was produced through the controlled oxidation of $V(OH)_2NH_2$ in a formic acid (HCOOH) buffer solution. The theoretical and experimental analysis demonstrated the uniformity of the vanadium valence state of 4+, and thus the accurate formula of haggite is $V_4O_6(OH)_4$. The haggite phase showed semiconductor-insulator transitions and has potential for the construction of intelligent switching devices.

Sun-Il Mho et al. (2009) reported the synthesis of vanadium oxyhydroxides $H_2V_3O_8$ nanobelts and their application as electrode materials for lithium ion batteries. [24] Vanadium oxyhydroxides $H_2V_3O_8$ and vanadium oxide V_2O_5 were synthesized hydrothermally from a V_2O_5 xerogel with and without a multidentate polymer with many oxygen atoms, polyethylene oxide PEO or polyethylene glycol PEG. PEO and PEG polymers were found to serve as surfactants as well as reducing agent during the hydrothermal reaction to form the $H_2V_3O_8$ nanobelts. These $H_2V_3O_8$ and V_2O_5 nanobelts were examined as cathode materials for lithium ion batteries using a multichannel galvanostat/potentiostat system. Based on the specific discharge capacities, $H_2V_3O_8$ showed better electrochemical performance than V_2O_5 nanobelts.

Flaviano Garcia-Alvarado et al. (2013) synthesized $H_2V_3O_8$ nanobelts through a fast and environmental friendly microwave-hydrothermal method from only commercial V_2O_5 powder, water, and ethanol. [43] The characterization of the resulting material's morphology as well as their intercalation chemistry indicated the formation of $H_2V_3O_8$ nanobelts that were 100 nm wide and several micrometers long.

Yi Xie et al. (2010) described the synthesis of montroseite VOOH hollow nano- sea urchins on a large scale using a simple template free hydrothermal route. [27] These were determined to be formed through the hydrolysis-driven Kirkendall effect coupled with new phase of vanadium oxyhydroxide $V_{10}O_{14}(OH)_2$ that served as a self-produced and self-sacrificed template. The resulting VOOH hollow nanoparticles converted to paramontroseite VO_2 without any alteration of the size or original appearance during the annealing process. In addition, both the montroseite as well as the paramontroseite nanoparticles displayed relatively high discharge capacity and better cycle retention as anode materials in aqueous lithium ion batteries.

J. Muller et al. (1974) reported the synthesis of vanadium oxyhydroxide $V^{3+}OOH$ synthesis from hydrolysis of $NaVO_3$ under reducing hydrothermal conditions. It had been revealed that the structure of VOOH is isotypic with the A1OOH structure. Oxidation of VOOH gave a metastable phase of vanadium dioxide VO_2. Both VOOH and VO_2 phases showed semiconductor behavior. [44]

Markus Niederberger et al. (2008) presented the synthesis of a novel hollandite-type vanadium oxyhydroxide $VO_{1.52}(OH)_{0.77}$ nanorods using a nonaqueous liquid-phase method involving the reaction of vanadium oxychloride ($VOCl_3$) with benzyl alcohol. [45] The physical and structural properties of the resulting $VO_{1.52}(OH)_{0.77}$ phase were elucidated through the combination of experimental data and theoretical modeling. Guicun Li et al. (2009) reported an approach to sea urchin-like VO_2(B) nanostructures composed of radially aligned nanobelts via homogeneous reduction reaction between peroxovanadic acid and oxalic acid. [46] These monoclinic $V_{10}O_{24}\cdot 12H_2O$ nanostructures were observed during the reduction-dehydration process as a phase transition to form the monoclinic VO_2(B).Yan

Xing et al. (2011) synthesized 3D uniform flower like $Cu_3V_2O_7(OH)_2.2H_2O$ microstructures through a simple hydrothermal route using cetyltrimethylammonium bromide (CTAB). [47]

Kyoung-Shin Choi et al. (2012) reported the synthesis of amorphous bismuth vanadate precursor thin films through an electrodeposition route. This amorphous bismuth vanadate precursor was subsequently converted to crystalline n-type $BiVO_4$ electrode via a mild annealing step. The resulting crystalline n-type $BiVO_4$ electrodes were tested in a photoelectrochemical water splitting cell. The photo-oxidation data for water revealed a poor photoelectrochemical performance while that for sulfite exhibited stable and significant photoelectrochemical performance. However, coating the $BiVO_4$ surface with an FeOOH layer created a material with superior photoelectrochemical diode performance compared to other oxide-based photoanode systems. [2]

Xiong Wen (David) Lou et al. (2013) reported preparation of uniform VO_2 hollow microspheres with various interiors including yolk-shelled, multi-shelled, and single-shelled structures, through a one-step template-free solvothermal method. Through an annealing process, VO_2 hollow microspheres have been converted to V_2O_5 microspheres with enhanced electrochemical performance in lithium-ion batteries. [26]

Xie et al. (2006) investigated the hydrothermal synthesis of uniform $V_2O_5 \cdot 0.9H_2O$ nanobelts and ultra-long $V_2O_5 \cdot 0.6H_2O$ nanorolls with novel scroll-like structures on a large scale using NH_4VO_3/sulfuric or acetic acid mixtures.[8] Calcination of $V_2O_5 \cdot 0.9H_2O$ nanobelts or $V_2O_5 \cdot 0.6H_2O$ nanorolls result in the formation of the corresponding anhydrous V_2O_5 nanostructures with better crystallinity. The morphologies and composition of the synthesized products were shown to have an influence on the electrochemical intercalation properties with Li^+ and photocatalytic activities. [8]

Michael Pollet et al. (2013) proposed a rapid hydrothermal synthesis of VO_2 (B) with platelet morphologies for aqueous lithium ion batteries using a novel combination of V_2O_5 and citric acid precursors under low synthesis temperature and duration. VO_2 (M_1) was also obtained through an indirect way by annealing VO_2 (B) under vacuum for 1 h. Both VO_2 (B) and VO_2(M) structures differ

from V_2O_5 since these structures consist of two edge-sharing octahedral units while V_2O_5 consists of one edge-shared octahedron and one corner-shared octahedron. Moreover, the orientation of the 4-fold axis of the oxygen octahedra is the only difference between VO_2 (B) and VO_2 (M_1). That of VO_2 (M_1) is aligned along two perpendicular directions as shown in Figure 1. [34]

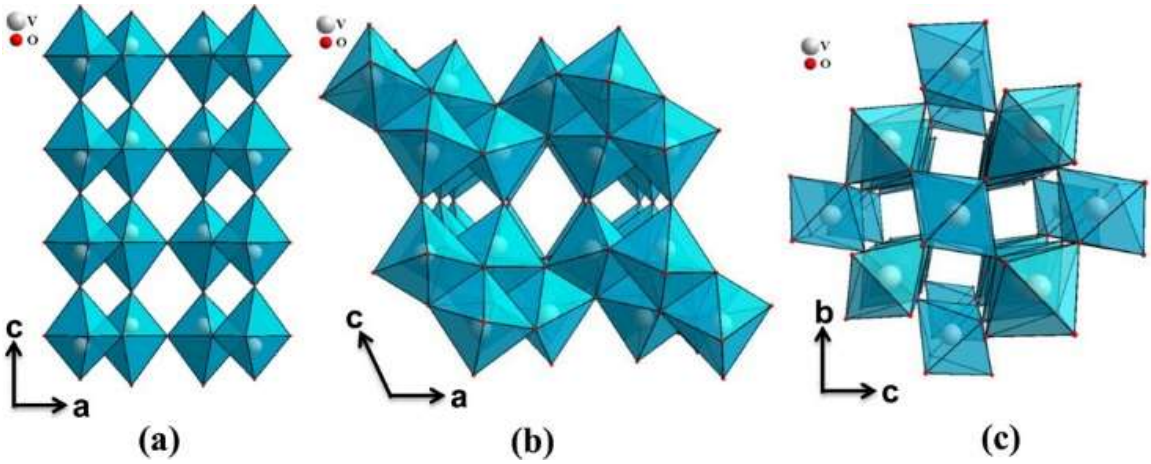

Figure 1- 1. Crystal structures of (a) orthorhombic V_2O_5, (b) monoclinic VO_2 (B), and (c) monoclinic VO_2 (M_1), adapted from Michael Pollet et al. (2013) [34]

The multiple applications of vanadium and tungsten layered transition metal oxides/oxyhydroxides, along with the versatility of their physicochemical properties make these materials very interesting and extremely complex. The variation in the oxidation state and the coordination numbers for tungsten and vanadium give these materials a very diverse chemistry and allow them to form compounds with most inorganic and organic ligands with significant structural, catalytic, magnetic, and electronic properties.

3. Tungstic Acid:

Tungstic acid, H_2WO_4 ($WO_3.H_2O$), is one of the transition metal oxides that have a unique properties and several applications such as catalysis [3, 4, 13], electrochromic devices [1, 29, 31, 48], photochromic devices [28, 30], and gas sensing [15, 16]. It is produced through the reaction of hot alkali

tungstate solution with hydrochloric acid.[49] The crystal structure of $WO_3.H_2O$ is comprised of a four equatorial oxygen corner-sharing layers of [WO_6] octahedra in the ac plane, with the water molecules in the axial positions. The water molecules form hydrogen bonds with the next layer. The layered structure of tungstic acid results in much more open structure offering more opportunities to react with other reactants as compared to the three-dimensional structure of m-WO_3 [50, 51] (see Figure 2) or tungsten hydrogen bronzes.

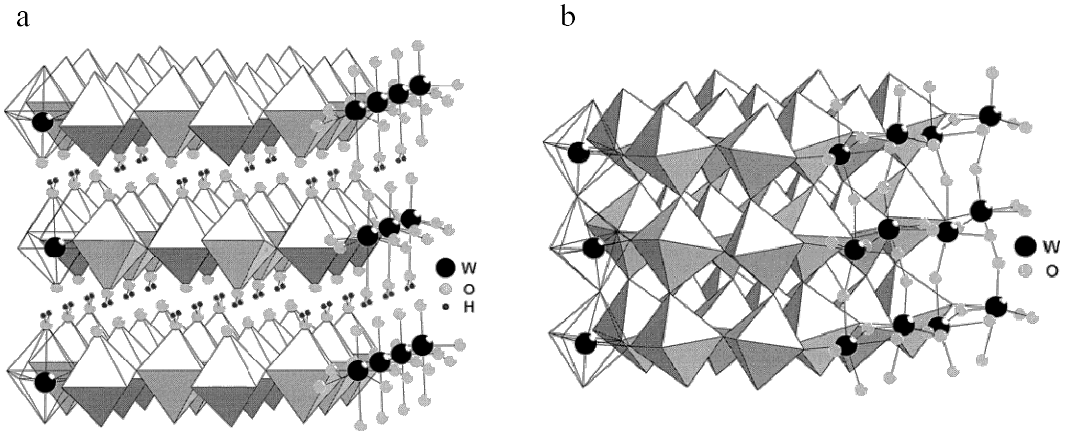

Figure 1- 2. The structures of m-WO_3 (a) and tungstic acid (b) [50, 51]

4. Vanadium Oxides Species; V_2O_5, $H_6V_{10}O_{28}$, and $V_{10}O_{24}{\cdot}12H_2O$:

Vanadium oxides materials have wide usage as catalysts, smart materials, thermal detectors, and metamaterials in industry, energy, environmental protection, and defense and security fields. [52] Vanadium oxide species exist in a numerous geometry and crystallinity forms depending on the vanadium oxidation state, which can vary from 3+ to 5+, and on the ambient acidity (pH) during their formation (see Figure 3). [38, 53] Vanadium is capable of existing in both single and mixed valence states on forming oxides. The most common of the oxides with single valence state are vanadium (II) oxide (VO), vanadium (III) oxide (V_2O_3), vanadium (IV) oxide (VO_2), vanadium (V) oxide (V_2O_5). The latter is considered the most stable one. Others with a mixture of two valence state follow the categories of the so-called Magnéli (V_nO_{2n-1}) and Wadsley ($V_{2n}O_{5n-2}$) homologous series such as: V_3O_5, V_4O_7, V_6O_{13} etc.[54] The possibility of very irregular structures raised since vanadium ions with +5 oxidation state

are considered to be relatively large for tetrahedral coordination to oxygen and relatively small for octahedral coordination. Bulk vanadium pentoxide, V_2O_5, consists of either distorted tetragonal pyramids or distorted octahedra with shared the edges forming zig-zag ribbons. These links to each other by corner sharing to produce sheets. These are tacked one over the other so that the apices of the pyramids of one sheet are placed over vanadium ions located in the centers of basal plane of the pyramid of the adjacent sheet to complete the distorted octahedron and form a three dimensional network (see Figure 4). [55] In the vanadium pentoxide V_2O_5 structure there are three structurally inequivalent oxygen centers, terminal vanadyl oxygen, oxygen bridging two vanadium centers, and bridging oxygens coordinated to three vanadium centers (see Figure 5). [55, 56]

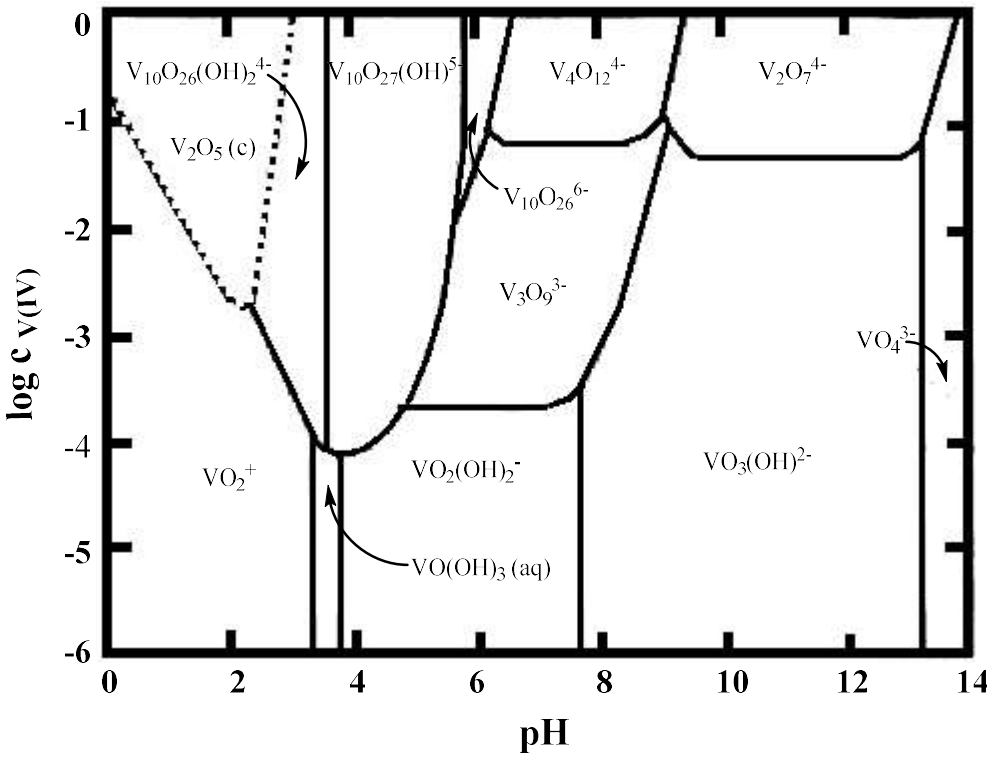

Figure 1- 3. Aqueous phase equilibrium of vanadium oxide as a function of both the concentration of vanadium and pH of the solution [38, 53]

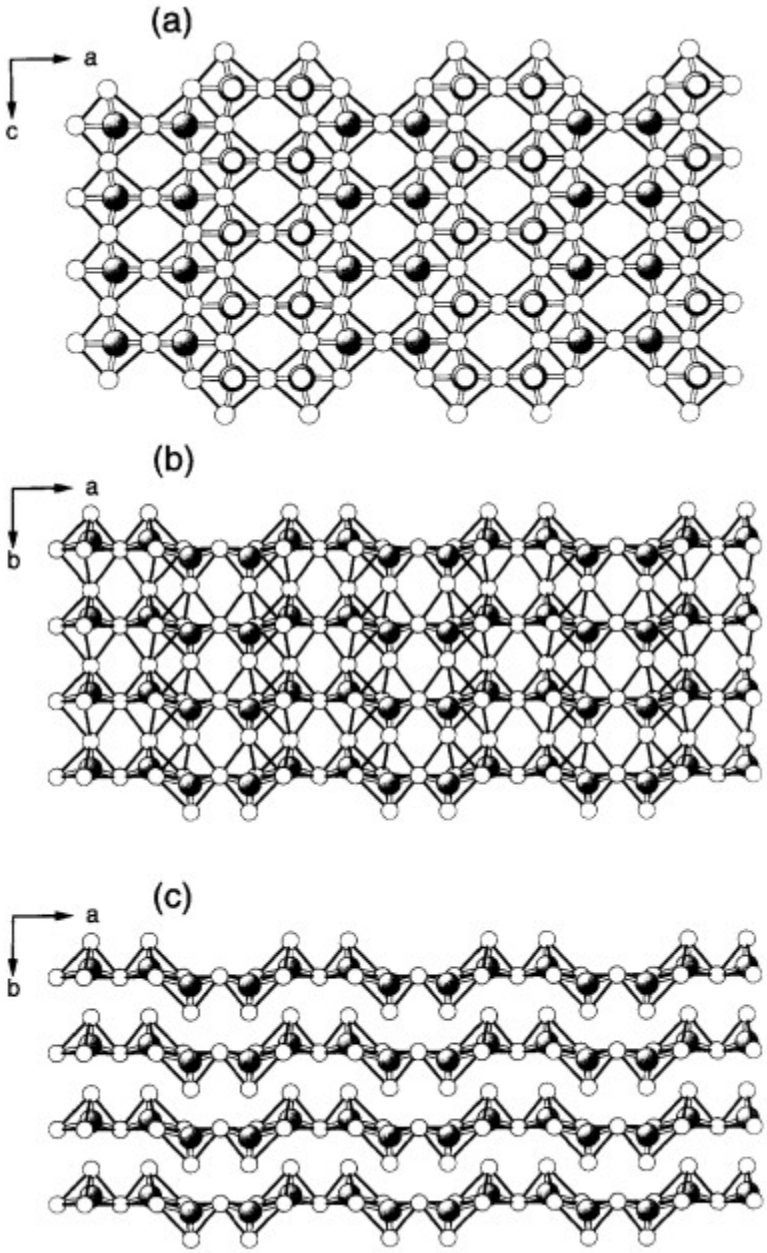

Figure 1- 4. Idealized structure of V_2O_5. Small circles denote V atoms, large circles, O atoms. (a) (0 1 0) plane projection drawn as square pyramids; (b) (0 0 1) plane projection drawn as square bipyramids; (c) (0 0 1) plane projection drawn as trigonal bipyramids [55]

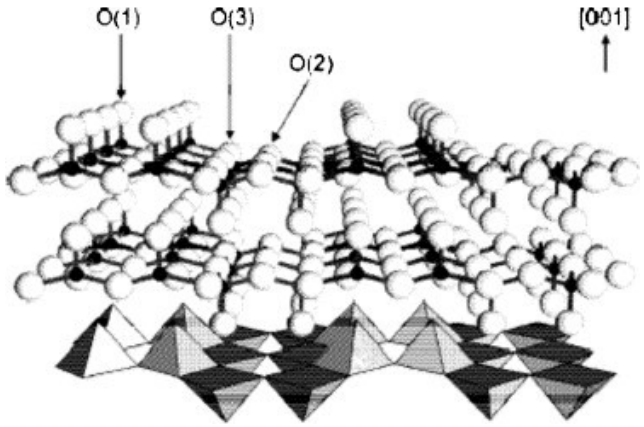

Figure 1- 5.The three structurally inequivalent oxygen centers of V_2O_5, terminal vanadyl oxygen (1), oxygen bridging two vanadium centers (2), and bridging oxygen coordinated to three vanadium centers (3) [56]

As shown in Figure 5, [38, 53] orthovanadates (VO_4^{3-}) contain V(+5), a highly charged cation that is surrounded by four equivalent oxide atoms. Orthovanadates are formed in highly alkaline aqueous solutions. Protonation occurs as the pH decreases, giving rise to hydrolyzed polymeric species; for example, pyrovanadates ($V_2O_7^{4-}$) obtained at intermediate alkalinity, and hydrated meta-vanadates (VO_3^-), containing infinite chains of VO_5 polyhedra that are formed at near neutral pH. Note that the anhydrous metavanadates are made of VO_4 tetrahedra. Vanadic acid ($V_{10}O_{28}^{6-}$) occurs between pH 1.3 and 6.5 and is made of ten VO_6 octahedron.[57] This vanadic acid can be prepared by careful acidification of alkali vanadate by passing through an ion-exchange column or by dissolution of V_2O_5 in hydrogen peroxide and then decomposition of the peroxide formed.[57, 58] Polymerization by aging at room temperature of vanadic acid solution gives a dark red gel.[58] Some reduction occurs during the polymerization process resulting in a greenish mixed-valence oxide.[58, 59] The dark red gel of vanadic acid forms ribbon-like films of vanadium pentoxide xerogel after slow evaporation of water. Thermal treatment of the colloidal vanadic acid above 300 °C results on formation of the crystalline orthorhombic V_2O_5 suggesting the existence of some correlation between vanadium coordination in both species.[60] The negative charge of vanadium species (Figure 3) decreases with the pH down to the point of zero charge for ($V_2O_{5(C)}$) at pH = 2. Below the cationic species of VO_2^+ is observed. [38, 53] Bariandite,

$V_{10}O_{24}\cdot 12H_2O$ ($V_2O_4\cdot 4V_2O_5\cdot 12H_2O$), is one of the mixed valence vanadium oxides having layered structure with dark green color and is found in mineralized sand stones of the uranium and vanadium deposit at Mounana, Gabon, and Minasragra, Peru), associated with other vanadium species. It is monoclinic, pseudo-orthorhombic, with space group: Cc or C2/C. [61, 62] Mixed-valence vanadium oxide $V_{10}O_{24}\cdot nH_2O$ nano-structure is synthesized by simple sol-gel routes through the reaction of V_2O_5 powder with peroxide.[63, 64] Mixed-valence vanadium oxide $V_{10}O_{24}\cdot nH_2O$ nano-structure is also prepared through a hydrothermal method by adding a vanadium compound to the organic acidic solution. [65] The end-product of mixed-valence vanadium oxide $V_{10}O_{24}\cdot nH_2O$ has a nano-porous structure that makes it a promising candidate to be used as a cathode in lithium-based batteries.[63, 64]

CHAPTER II

CATALYTIC REACTIONS OF TUNGSTIC ACID

1. Introduction:

The chemical transformation of alkenes, alkynes, and nitriles to other compound is one of the more useful routes in organic chemistry. Hydration of alkenes, alkynes, and nitriles is of particular interest because it provides easy access to carbonyl compounds for chemical industries.[66] Brønsted and Lewis acids such as noble metals and mercury (II) salts combined with sulfuric acid or boron trifluoride are active and selective catalysts for the hydration reactions, but are still based on expensive late-transition metals and/or toxic salts.[67-98] In efforts to explore potential replacements for liquid acids and halide-containing solids, oxide-based strong acid catalysts have emerged as the key to green chemistry due to the ability to alter their activity and selectivity reaction sites structures.[92-106] Among these, tungsten oxide-based materials have attracted significant attention due to their interesting and useful catalytic activities.[107-115] In 1945, tungstic acid was first described as an effective catalyst for hydroxylation of olefins via the addition of hydrogen peroxide to an ethylenic linkage to yield the corresponding glycol.[12] Young *et al*. proposed a mechanism involved an ionic 1, 2 trans-addition of an intermediate peroxy acid, $HOOWO_3H$ to the double bond. [7] Saegebarth reported evidence for the ionic character of the

tungstic acid catalyzed addition reaction and also determined the extent of oxygen transfer from the oxidizing agent to the olefin.[3] Bilal et al. reported the synthesis of malonic acid ester through the one-step ozonolysis of palm olein using tungsten oxide nanoparticles.[4]

Previously, tungsten blue, HW_3O_9, was used in a variety of catalytic reactions including the conversion of cyclopentene to decalin, hydrolysis of alkynes and nitriles, trans alkylation of aromatics, and trimerization of alkynes.[13, 116, 117] Apblett et al. developed a simple one-pot synthesis procedure for the synthesis of altretamine, a chemotherapeutic agent used to treat advanced ovarian cancer, under mild reaction conditions. [13] The altretamine was synthesized via cyclotrimerization reaction of dimethylcyanamide using tungsten or molybdenum hydrogen bronze as catalyst. The chemistry of tungsten blue is unpredictable since it can act as a superacid, a hydrogenating reagent, and a reducing agent. Herein in this chapter we explore the catalytic reactions of tungstic acid with several alkenes, alkynes, and nitriles.

2. Experimental:

2.1.Materials

The reactions of alkenes, alkynes, and nitriles reagents were studied using tungstic acid as a catalyst. Tungstic acid was purchased from Alfa Aesar. All organic reagents commercially available were used without further purification. Figures 1-3 show the selected regents in this chapter to investigate the catalytic activity for tungstic acid.

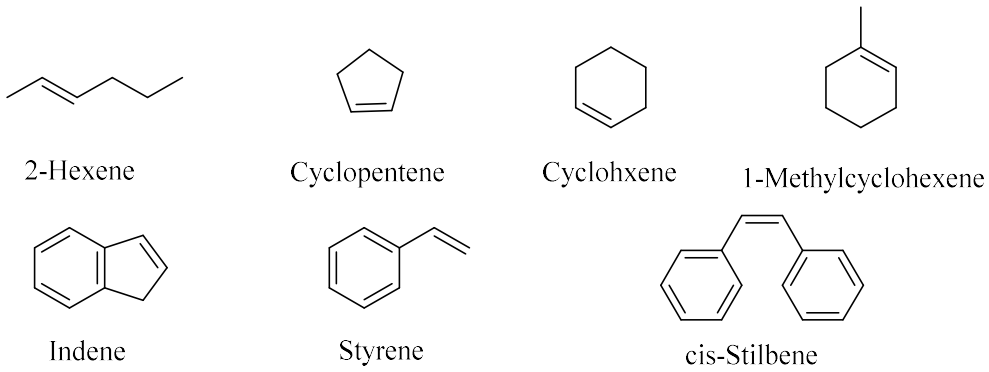

Figure 2- 1. The selected alkenes used to investigate the catalytic activity for tungstic acid

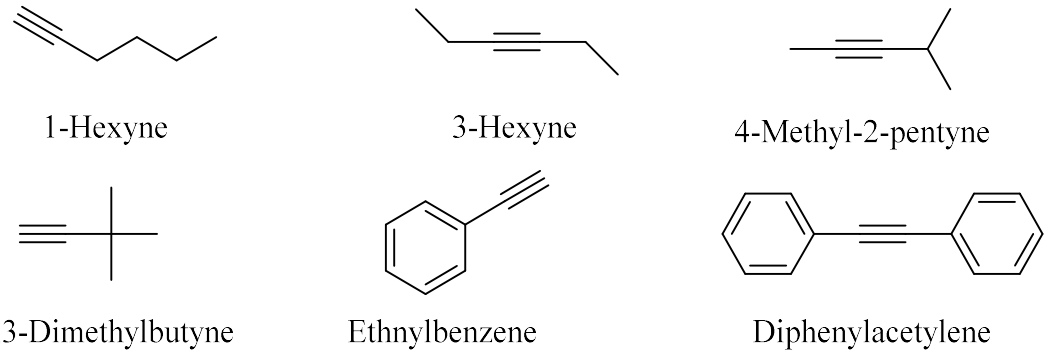

Figure 2- 2. The selected alkynes used to investigate the catalytic activity for tungstic acid

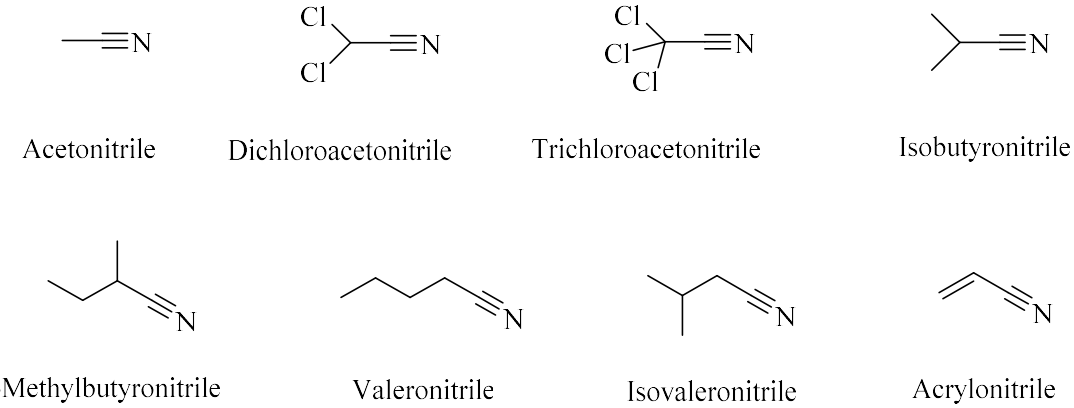

Figure 2- 3. The selected nitriles used to investigate the catalytic activity for tungstic acid

2.2.Characterization techniques

Thermogravimetry (Mettler-Tiledo TGA Instrument) was performed to determine the water content and dehydration temperature of tungstic acid. TGA experiments were run from ambient temperature to 900 ˚C with ramp rate of 5 ˚C/min. Dehydration of bulk samples of tungstic acid was performed in ambient air in a temperature programmable muffle furnace, Vulcan 3–130 NDI using a temperature ramp of 5 ˚C/min, and a hold time of 24 hours. The products were collected after cooling the furnace to 50 ˚C, at a rate of 10 ˚C/min. The surface areas were determined via nitrogen physisorption using the Brunauer, Emmett, and Teller (BET) technique. The products were characterized by vibrational spectroscopy using Nicolet Is50 FT-IR spectrometer with recording range from 4000–500 cm^{-1} and Nicolet 9610 Raman Spectrometer in the range 4000 to 50 cm^{-1}

with 4 cm^{-1} resolution. X-ray powder diffraction (XRD) patterns were recorded on a Bruker AXS D-8 Advance X-ray powder diffractometer using copper Kα radiation.

2.3.Procedure or tungstic acid/organic substrate reaction

The various substrates and tungstic acid (H_2WO_4) were mixed in sealed culture tubes. These were then placed into a heat block (either a HACH Cod reactor or J-KEM Scientific, Inc. Lab reactor) at a variety of temperatures and residence times. The products were extracted with diethyl ether (ACS reagent, anhydrous, ≥99.0%) after the tubes were cooled to room temperature. The extracts were analyzed by gas chromatography-mass spectroscopy, Hewlett Packard HP-G1800A detection. Compounds were identified by comparison of their mass spectra to the NIST database.

3. Results and Discussion:

3.1.Characterization of tungstic acid

Thermal gravimetric analysis was performed in order to characterize the dehydration behavior of the tungstic acid used in this investigation and to determine its water content. The TGA results are plotted in Figure 4. The ceramic yield was 94.1 % by weight, corresponding to 0.79 molar equivalents of water, somewhat lower than the expected amount based on the formula $WO_3 \cdot H_2O$. It can be seen that water loss occurs in two steps. 0.16 molar equivalents of water are readily evolved in the temperature range from ambient to 180˚C. The remaining water evolves reasonably fast above 180 ˚C but water loss tails to high temperature (450 ˚C). The observed dehydration behavior suggests that at first water is lost from non-adjacent positions in the tungstic acid. There are two possibilities for how this occurs: water molecules could be lost evenly from both surfaces of the interlayer region or one surface might be completely dehydrated while the one facing it remains hydrated. The initial dehydration step is reversible indicating that the layered structure has not collapsed as might be expected in the latter case. This conclusion is supported by the slight change increase in the surface area (Table 1). Further dehydration does appear to be

accompanied by the collapse of the layers that leads to trapping of water in the interior, some of which requires exceptionally high temperature to be released. It has been reported that complete dehydration of tungstic acid produces triclinic tungsten trioxide at 210 ˚C. [118] Dehydration of bulk samples of tungstic acid was performed in an oven. The products analyzed by surface area measurements, X-ray powder diffraction, and vibrational spectroscopy. The gravimetric results and the surface areas are reported in Table 1. The bulk dehydration results echo those seen in the thermal gravimetry results. The surface area does not undergo a statistically significant change as shown in Figure 5.

Table 2- 1. The gravimetric results and the surface areas of tungstic acid

Temperature (˚C)	Initial mass of tungsten acid (g)	Final mass of tungsten acid (g)	Mass of water lost (%)	Molar equivalents of water lost	Surface area (m^2/g)
R.T.	NA	NA	NA	NA	20.9 ± 1.3
100	1.005	1.000	99.5	0.07	21.9 ± 0.7
120	1.454	1.444	99.3	0.09	19.9 ± 1.7
150	1.300	1.283	98.7	0.17	19.8 ± 0.5
180	1.407	1.360	96.7	0.45	22.4 ± 1.1

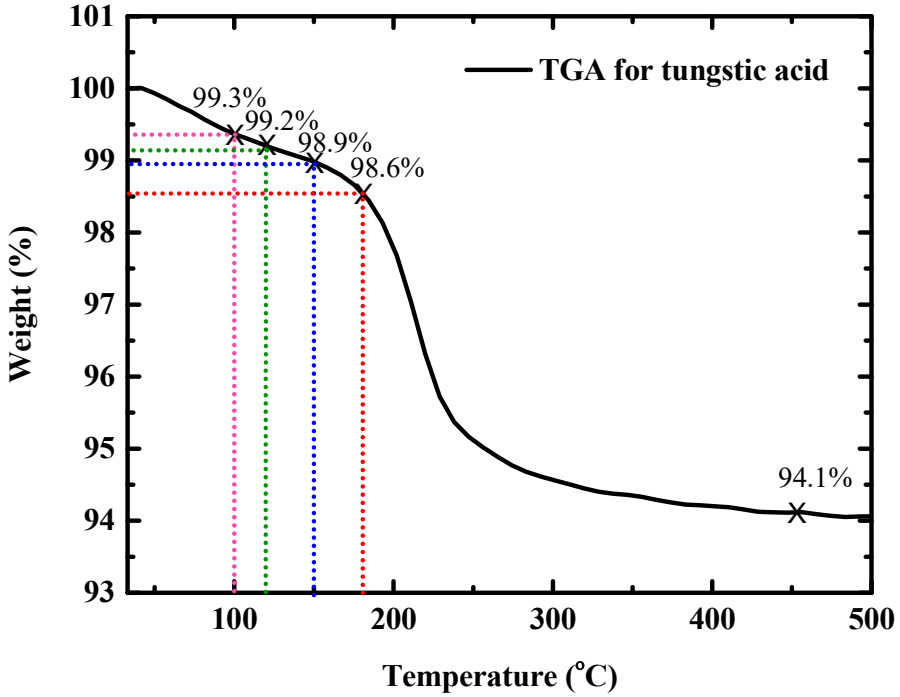

Figure 2- 4. Thermogravimetric analysis of tungstic acid

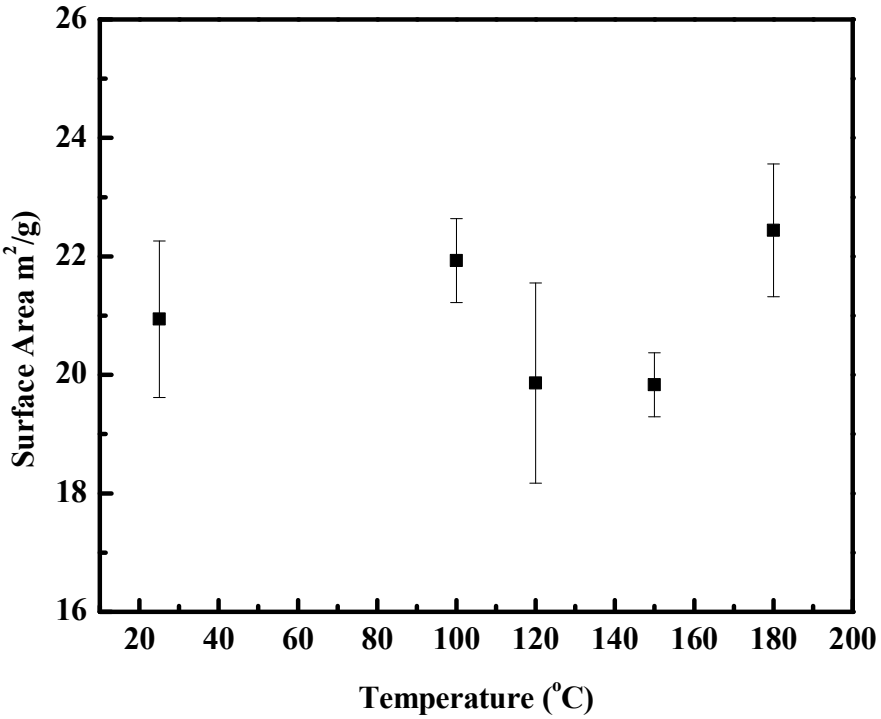

Figure 2- 5. Surface area (m^2/g) for undried and dried tungstic acid as a function of temperature

The XRD pattern of the as-received tungstic acid (Figure 6) has an excellent match with the ICDD database pattern for tungstic acid but there are extra peaks that do not match a known tungsten-containing phase. Since, as discussed above, the tungstic acid is partially dehydrated, it is possible that the unidentified peaks in the XRD is a crystalline partially dehydrated tungstic acid phase. This hypothesis is confirmed by the growth of these X-ray reflections when the tungstic acid is further dehydrated by heating to 180 ˚C (Figure 7) where it is converted to a material with the formula $WO_3 \cdot 0.67H_2O$ [$W_3O_9(OH_2)_2$]. Further dehydration upon heating to higher temperature produces tungsten trioxide.

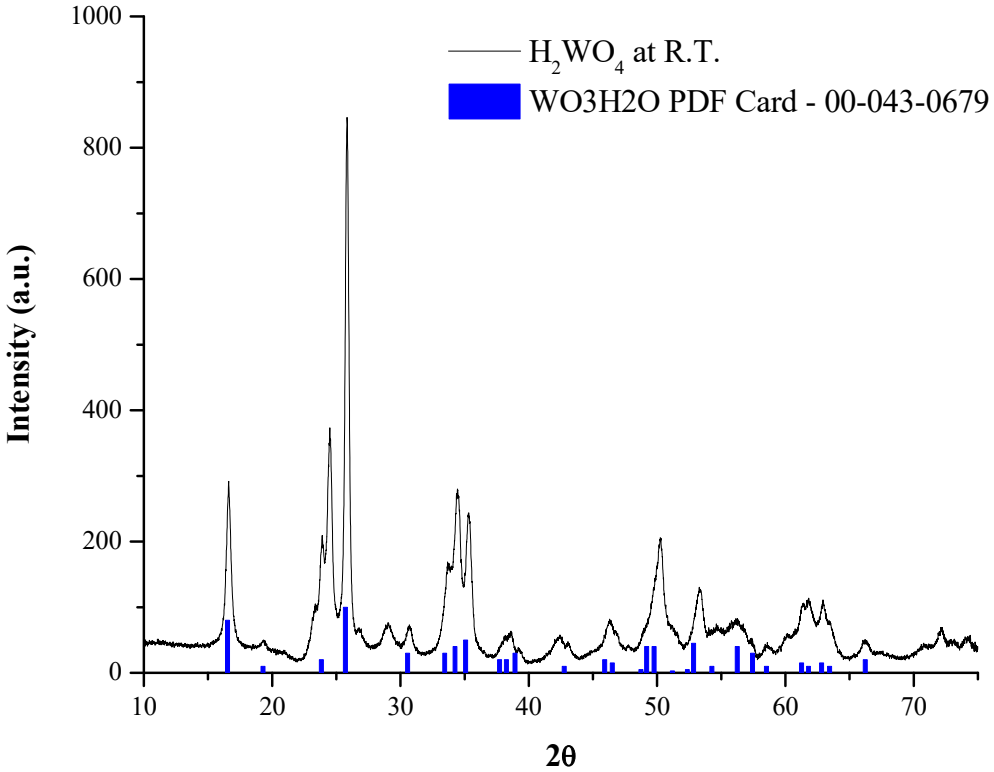

Figure 2- 6. The XRD pattern of the as-received tungstic acid

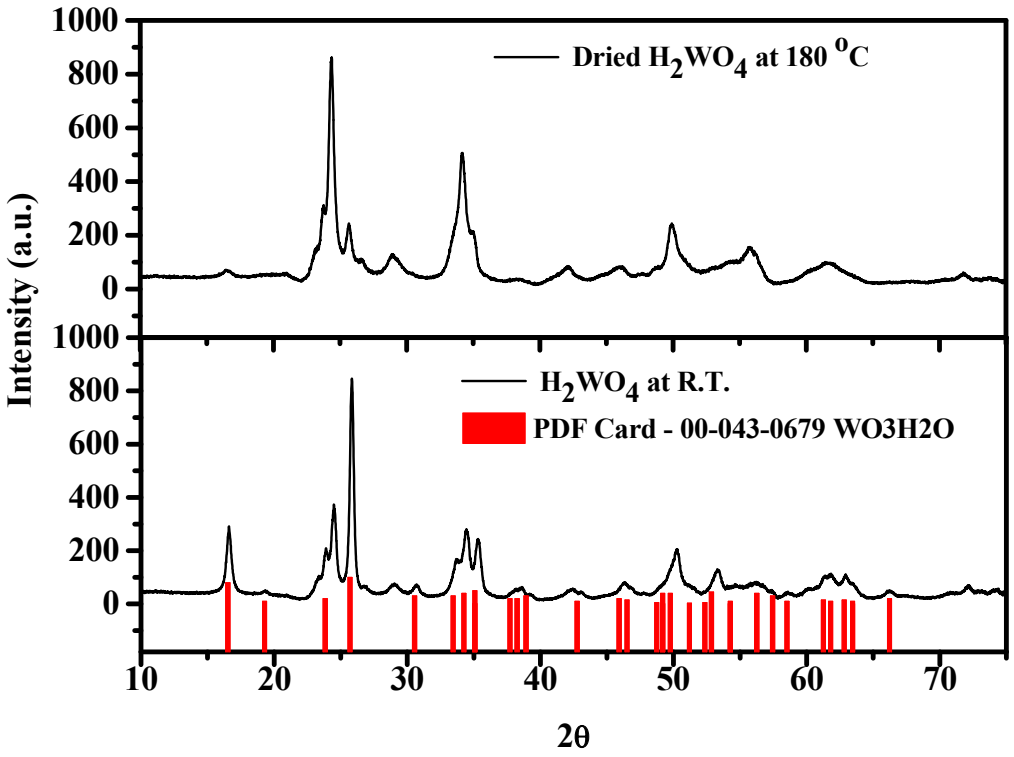

Figure 2- 7. XRD patterns of undried and dried tungstic acid

As expected, partial dehydration of tungstic acid causes the intensities of the peaks due to the vibrational modes of water in the infrared and Raman spectra to diminish but not disappear (Figure 8 and 9). At the same there are changes in the vibrational bands for tungsten-oxygen stretching in the infrared spectrum. The original peak for the undried sample at 942 cm^{-1} splits into two bands at 974 and 936 cm^{-1}. The higher frequency peak is indicative of the formation of W=O [119, 120] as tungsten centers lose water. A new band appears at the band appearance at 1740 cm^{-1} that is likely due to a combination band of W-O stretching and OH_2 bending in the newly formed phase.

The ready partial dehydration of tungstic acid suggests that tungstic acid can act as a water source and a catalyst in hydration reactions such as the formation of alcohols from alkenes, ketones from acetylenes, and amides from nitriles. Furthermore, the formation of a phase that is resistant to further hydrolysis and has open sites at tungsten centers opens up possibilities for other Bronsted and Lewis acid-catalyzed reactions.

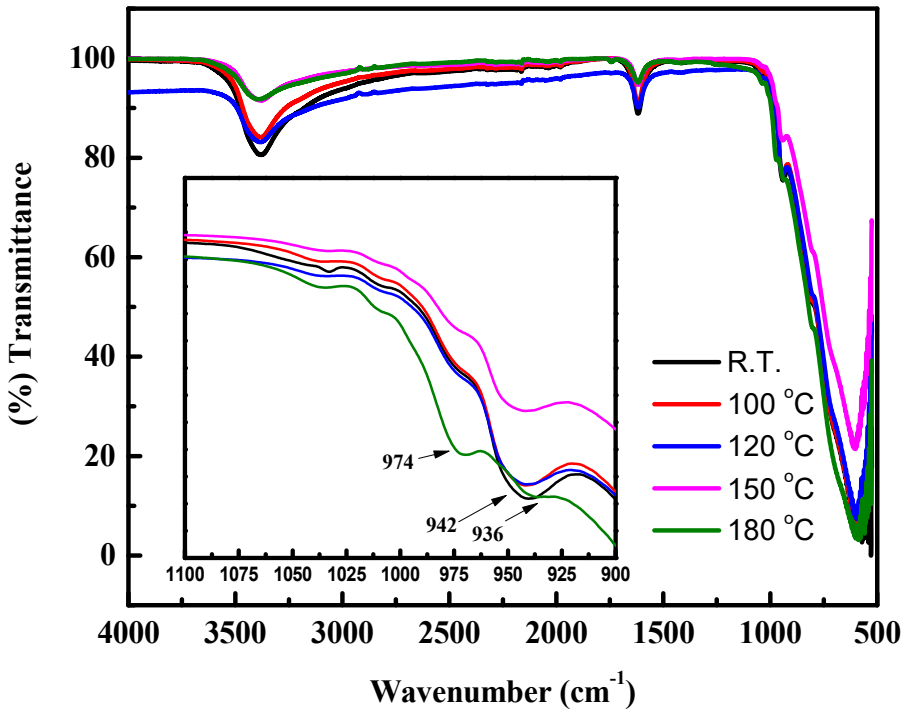

Figure 2- 8. FTIR spectra for the undried tungstic acid and the dried one at different temperatures

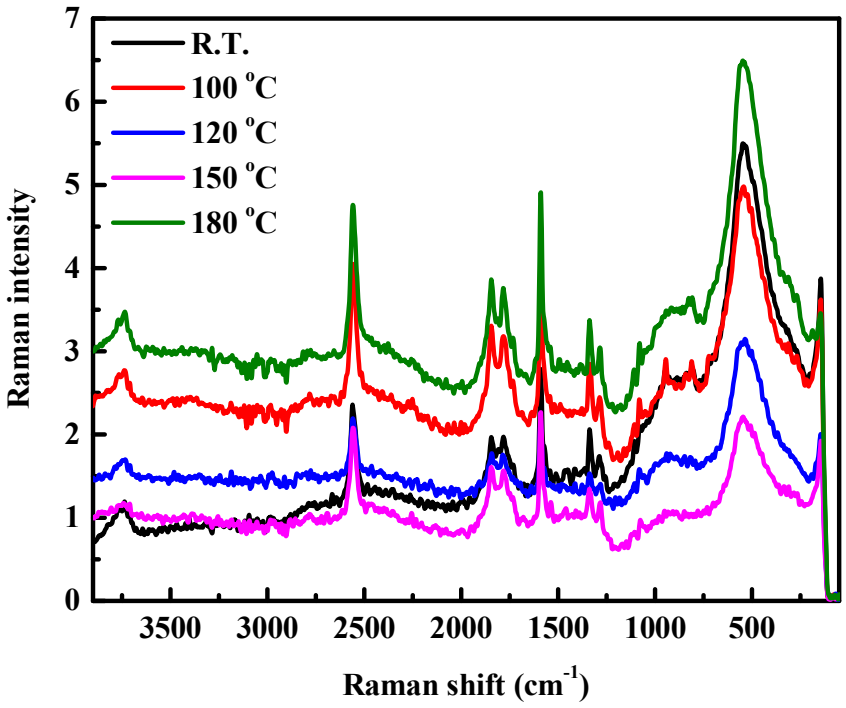

Figure 2- 9. Raman shift spectra for undried tungstic acid and dried ones at different temperatures

3.2.Chemical Transformation of Alkenes using Tungstic Acid

The reactions of various alkenes, includes linear alkenes, cycloalkenes, dienes, and aromatic alkenes, with tungstic acid were explored at 150 ˚C in tubes with a ratio of reactants of 1.5 g H_2WO_4 to 0.15 g substrate and the results of experiments are shown in Table 2.

Table 2- 2. The selected alkenes and products obtained

Substrate	Reaction time (days) at 150 ˚C	Composition of reaction mixture
2-Hexene	1	high conversion with low selectivity
Cyclopentene	1	(19%) and (64%) undefined compounds
Cyclohxene	1	(52%)octahydrocyclopenta[3,4]cyclobuta[1,2]cyclo pentene-1,4-dione, several undefined compounds
1-Methylcyclohexene	1	high conversion with low selectivity
Indene	14	high conversion with low selectivity
Styrene	1	(44%) and (25%) for 1H-indene,2,3-dihydro-1-methyl, several un-identified compounds
cis-Stilbene*	2	(27%) trans- stilbene, and (45%) dimerized compounds

Most alkenes reacted with tungstic acid to produce a large number of products, most of which could not be identified by search/match of the mass spectra versus the NIST database. In some cases, there were only a few major products with many by-products while in others the numerous products were produced in similar low yields. In the case of 2-hexene, over 31 peaks were observed. The only matches were for a small peak identified as 6-dodecene However, by examining the parent ions of the mass spectra, it was determined that seven of the compounds had molecular masses twice that of the starting materials and thus can be identified as dimers, likely various isomers of dodecene.

Heating cyclopentene to 150 ˚C with tungstic acid produced at least 15 products but there were two major products (64.52% and 19.86% integrated peak areas) that appear to be isomers of cyclopentenyl cyclopentane. Among the minor products identified was the oxidation product from the latter compound, 2-cyclopentyl cyclopentanone. There was no decalin detected despite the fact

that this was the major product from reaction of cyclopentene with tungsten hydrogen bronze. Instead, tetrahydronaphthalene was produced suggesting that decalin or a decalin-like product (e.g. octalin) was formed and then dehydrogenated to the aromatic system. Notably, the color change of the tungstic acid to green is indicative of a redox reaction.

The highest yielding product from the reaction of cyclohexene with tungstic acid at 150 ˚C was 1-cyclohexylcyclohexene produced by acid-catalyzed coupling of two cyclohexene molecules. This only accounts for about 53 % of the integrated area as there were a large number (31) of small peaks. Many of these were oligomer that occurred in bands of trimers, and tetramers. For example, 1,1':4',1''tercyclohexane was identified in the products. Two isomers of bicyclohexyl benzene were identified. These presumably arise from dehydrogenation of tricyclohexyl but, alternatively, benzene could be produced by dehydrogenation of cyclohexene leading to the production of the benzene derivatives by acid-catalyzed electrophilic aromatic substitution. The first pathway may be more likely since there are traces of five more partially dehydrogenated cyclohexene trimmers that are not aromatic systems. Presumably they are randomly dehydrogenated on different ring to give two cyclohexene groups linked to one cyclohexyl group. It appears that once oligomerization reaches the trimer stage, the low volatility of the compounds lead to residence times on the tungstic acid surface for slower dehydrogenation reactions to take place. A possible tricyclohexylbenzene derivative may have also been present based on examination of the mass spectrum with m/e = 324 amu (corresponding to 4 cyclohexenes minus 4 hydrogen atoms) and a benzyl radical in its fragmentation pattern. Products from hydration of cyclohexene (cyclohexanol) and 1-cyclohexylcyclohexene (1,1'-bicyclohexyl-2-ol) were also observed. The oxidation product, 1,1'-bicyclohexyl-2-one was also detected.

Methylcyclohexene reacted similarly to cyclohexene in some respects but there were no particularly dominant products. There were mainly two bands of products with retention times from 20 to 25 minutes and 38-40 minutes that can be broadly classified based on mass spectra as dimers

and trimers, respectively. Again, dehydrogenation of the oligomers also occurred. There were 57 peaks total in the GC/MS trace with perhaps 10 being dominant in terms of integrated peak area. Between the bands of trimers, there was a low intensity band of hydrated dimers with the identification based on the parent ions in the mass spectra. There were 20 peaks with parent ions that corresponded to quadruply dehydrogenated trimers and 13 that corresponded to quadruply dehydrogenated dimers. There were also some simple products from hydration of methycyclohexene including methycyclohexanol and its oxidation product methycyclohexanone.

In case of indene, over 18 peaks were observed and three of them with 23.36, 13.83, and 17.64 % integrated peak areas that were identified to be the unreacted starting material indicating only 45.17 % of indene has reacted to produce over 15 observed products peaks. Three minor peaks detected as indanone isomers, the oxidation products of hydrated indene. The major three peaks in regards to their parent ions of the mass spectra had a molecular mass of twice of indene. Therefore by comparing their mass spectra within literature identified as 1,1'-Bi-1*H*-indene isomers, the dimers products of indene. The other several minor peaks were identified as di-, tetra-, Hexa-hydro chrysene isomers (Scheme 1).

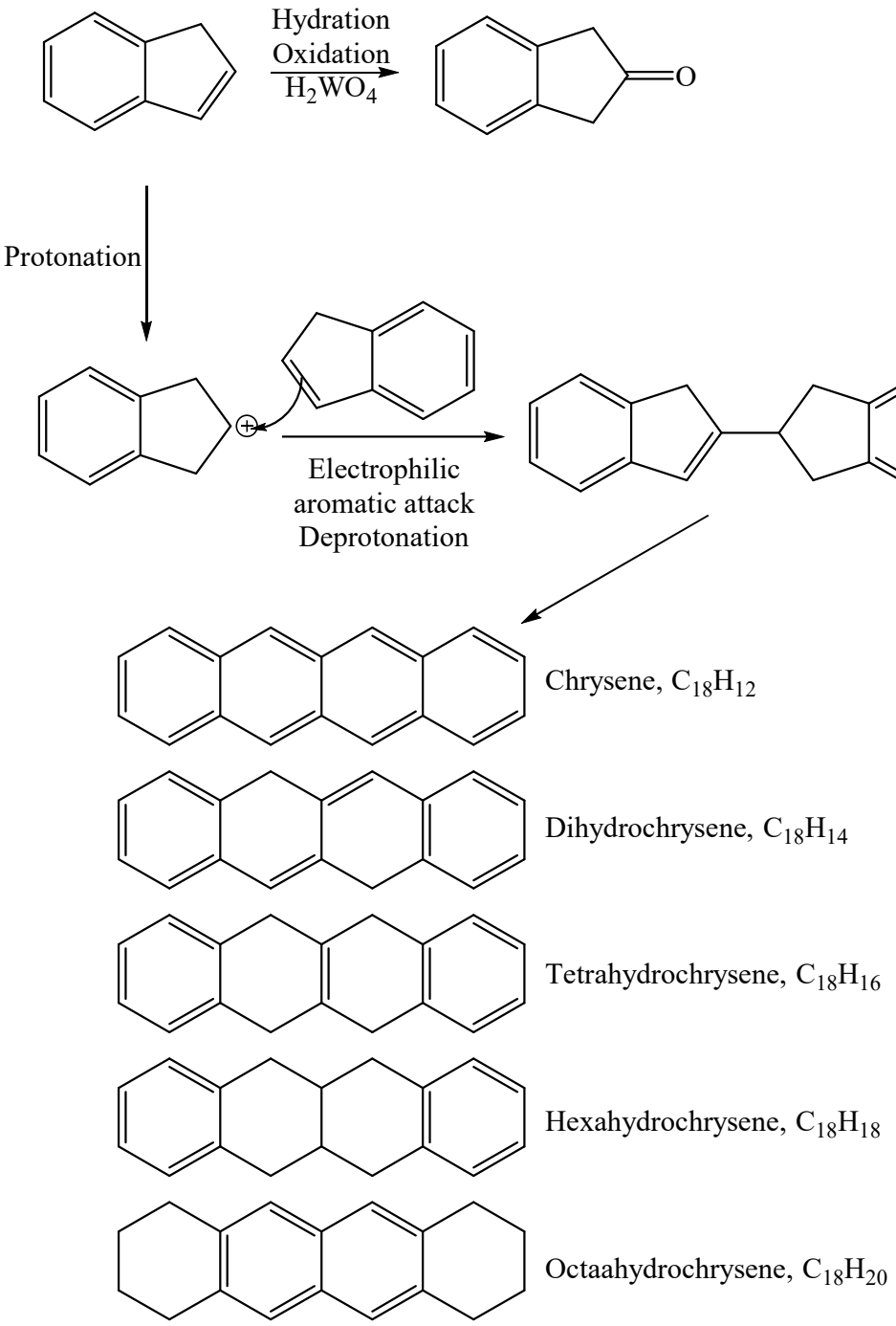

Scheme 2- 1. Indene transformation reaction using tungstic acid

Heating styrene to 150 ˚C with tungstic acid results in formation over of 40 products. The mass spectrum along with several minor products mainly shows two peaks clusters. The first peaks cluster was large in a sense of integrated peak areas and had molecular masses twice that of styrene

large. For the first peaks cluster, several minor products of styrene isomers were detected as 1,3-diphenyl-1-butene. The major two peaks with mass of 208 were identified to be 1-methyl-3-phenylindane isomers. 1-methyl-3-phenylindane which is a dimer of styrene result from protonation of styrene monomer by simply tungstic acid acts as a brønsted acid thus by utilizing a brønsted acid a carbocation will be formed first and then it goes under electrophilic aromatic substation with another styrene molecule producing the dimeric carbocation in which through either intramolecular Friedel–Crafts reaction obtained the 1-methyl-3-phenylindane or proton elimination produced the 1,3-diphenyl-1-butene (Scheme 2). [121] Several minor products of naphthalene were also detected by search/match of the mass spectra versus the NIST database. The second peaks cluster was small in respect of integrated areas to the first peaks cluster and had molecular masses thrice that of the styrene found to be trimeric products isomers arranging from unsaturated terminals to cyclic ones. These trimeric products may be produced by addition to dimer cation to styrene forming a linear trimer cation that by proton elimination produce the unsaturated terminals dimers and/or the cyclic ones (Scheme 2). The observation of aromatic oligomer and trimeric aromatic product results from W(VI) centers dehydrogenated of initially formed hydrated dimeric and trimeric intermediates. [116] A minor peak with 222 molecular mass was observed and by examining the part ion found to be 1,3-diphenyl-2-buten-1-one which is named also dypnone. Worth to mentioned that acetophenone was additionally detected to be one of the minor products. Based on literature dypnone can be obtained through self-condensation of acetophenone using acid catalysts. [122] Therefore, acetophenone was heated to 150 ˚C with tungstic acid and the obtained results show that dypnone was one of the detected products and more detail of this reaction will be described latter within this chapter and the main point is tungstic acid partially hydrate styrene molecules and the oxidized it to acetophenone and through a self-condensation formed dypnone (Scheme 3).

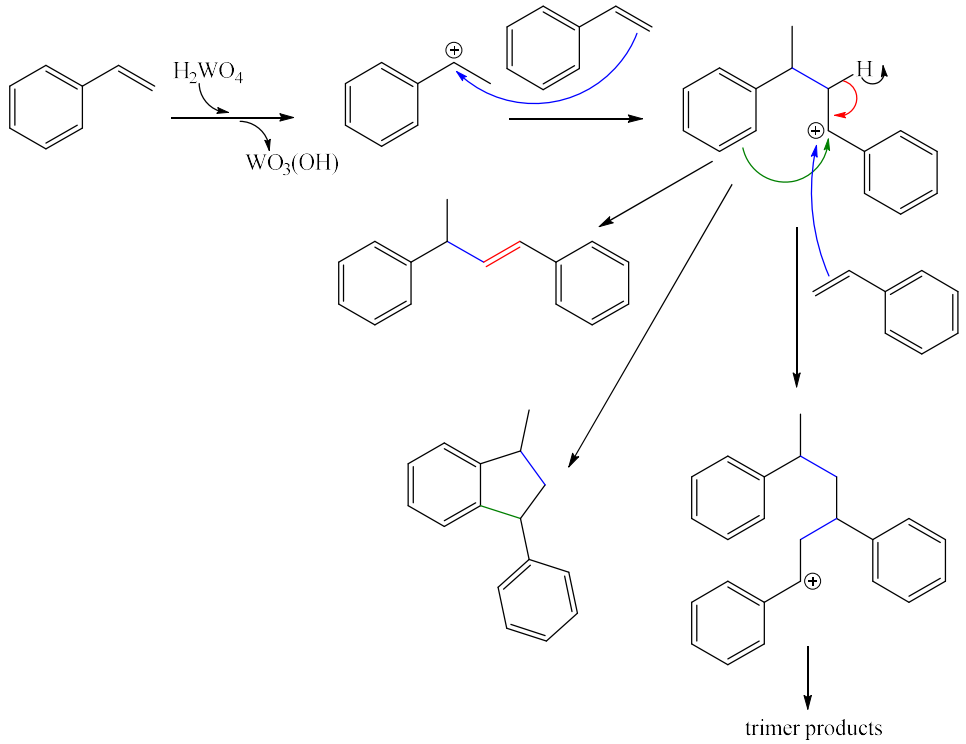

Scheme 2- 2. Styrene transgormation reactions using tungstic acid

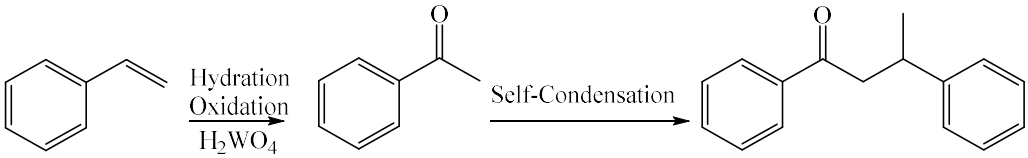

Scheme 2- 3. Dypnone formation from styrene

In this work stilbene was further investigated to utilize the alkene transformation using tungstic acid due to simplicity of following its transformation reactions using GC-Mass spectroscopy. Apblett group previously investigated the transformation reaction of stilbene using tungsten bronze. The reaction of stilbene with tungsten bronze after one day produced dimerized alkene products. The 1,2,3,4-tetraphenylbutene was found to be the major product produced via the reaction of the alkene molecules with the initial radicals that are formed from hydrogen transfer and are stabilized by conjugation with a phenyl group. Scheme 4 shows the proposed mechanism for production of the dimerized alkene.[116] Herein, the reactions of stilbene (0.1 g) with tungstic acid (1.0 g) were carried out for one day at different temperatures (R.T., 100, 120, and 150 ˚C), as

shown in Figure 10, the color of tungstic acid changed with increasing reaction temperatures from bright yellow (R.T.), pale yellow (100 ◦C), light greenish yellow (120 ◦C), to light green (150 ◦C). Colorless needle-shaped crystals were formed at the top of the tubes after slow cooling of the reactions prepared at 120 and 150 ◦C. It speculated that this solid colorless crystal could be the trans isomer for stilbene. GC-MS analysis showed that cis stilbene was converted to the more stable trans isomer as a dypnone the major product. Figure 11 shows that stilbene conversion was low at both R.T and 100 ◦C but significantly higher at 120 and 150 ◦C. To understand the role of tungstic acid in the transformation of stilbene isomers, stilbene was placed at same condition of temperature and time without any tungstic acid amount and the observation was that trans stilbene exists along with cis stilbene in almost same amount when the reaction held with tungstic acid for the R.T and the100 ◦C reactions. In addition, it appears that the amount of trans stilbene increased as the reaction temperatures increased which may suggest whatever phase of tungsten oxide or oxyhydroxide material formed helps the transformation of the isomers. Along with trans stilbene formation for 120 and 150 ◦C reaction temperatures four minor products were detected. One of the detected minor products with short retention time matched the NIST standard for benzaldehyde. The other three detected minor products with long retention time and mass of 360 amu could be identified from their mass spectra (see Figure 12) as tetraphenylbutene isomers (see Figure 13).

Furthermore, the reactions of cis-stilbene with a varied amount of tungstic acid were also performed at 150 ◦C for 24 hours to illustrate the role of mole percent of tungstic acid in the catalytic reaction as shown in Figure 14. From the data, the conversion of cis stilbene increased gradually as the mole percent's of tungstic acid increased and it's seemed that the lower loading percent of tungstic acid might need more reaction time for the reaction to reach the completion. The 150 ◦C reaction with 90.62 mole percent of tungstic acid for stilbene transformation was chosen to demonstrate the reaction time effect. The calculated conversion and area % from GC-MS of the extracts plotted as a function of time as shown in Figure 15. From the trend of the plotted data, the

conversion of cis stilbene increased gradually as the time increased and more than 75% of cis stilbene converted within 24 hours. The maximum conversion of cis stilbene is reached within 5 days (120 hours) producing trans stilbene as a major products with fair amount of benzaldehyde along with other dimers. This result suggest that tungstic acid play a role as a novel and safe solid acid catalyst in solvent-free chemical catalyst for stilbene isomerization reaction and the proposed mechanism shown in Scheme 5. Whereas two mechanisms have been established for alkene isomerization using a homogeneous catalysts, typically rhodium compound used as a catalyst, through the addition of the alkene to a metal hydride forming a metal alkyl followed by hydrogen transfer and elimination, [123] a carbonium ion mechanism using heterogeneous catalysts stated to be a better explanation for the olefins isomerization mechanisms.[124] Tungstic acid basically acts as a Bronsted acid releasing a proton H^+ and Lewis acid accepting an electron pair. The mechanism for isomerization of cis stilbene using tungstic acid to obtain the more thermodynamically stable trans stilbene could be proceed through formation of a carbonium ion intermediate (IV) that is stable enough to formed trans stilbene (VI). This may be an indication that the rate-limiting transfer of a H^+ from tungstic acid to the double bond is involved in accords to work done by Noyce, Hartter, Miles investigatin acid-catalyzed isomerization of cis stilbene using sulfuric acid system. The estimated value of the energy difference between the two conformers has been reported to be 4 kcal. [125] The equilibrium with changing conformation between the cis (IV) and trans (V) of carbonium ion intermediate given in Scheme 5.

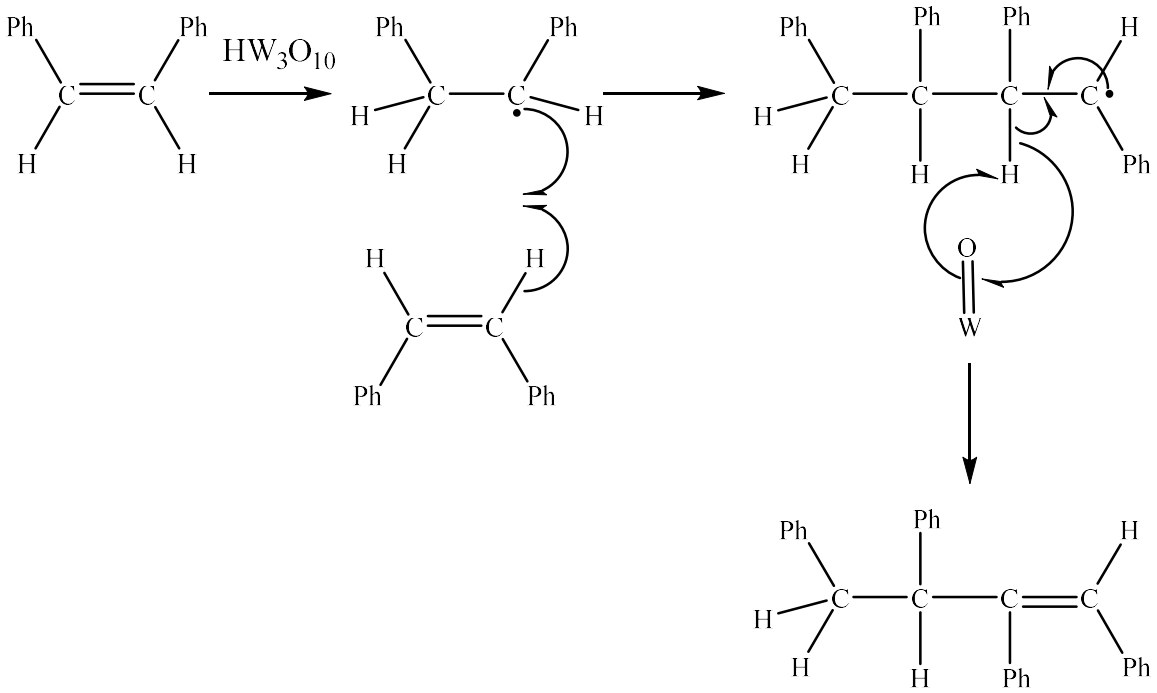

Scheme 2- 4. Proposed Mechanism for Dimerization of Stilbene according to Bollapragada et al., 2003 [116]

Figure 2- 10. Color change of tungstic acid reaction with stilbene for one day at different temperatures; from the left to the right: bright yellow (R.T.), pale yellow (100 ˚C), light greenish yellow (120 ˚C), and light green (150 ˚C)

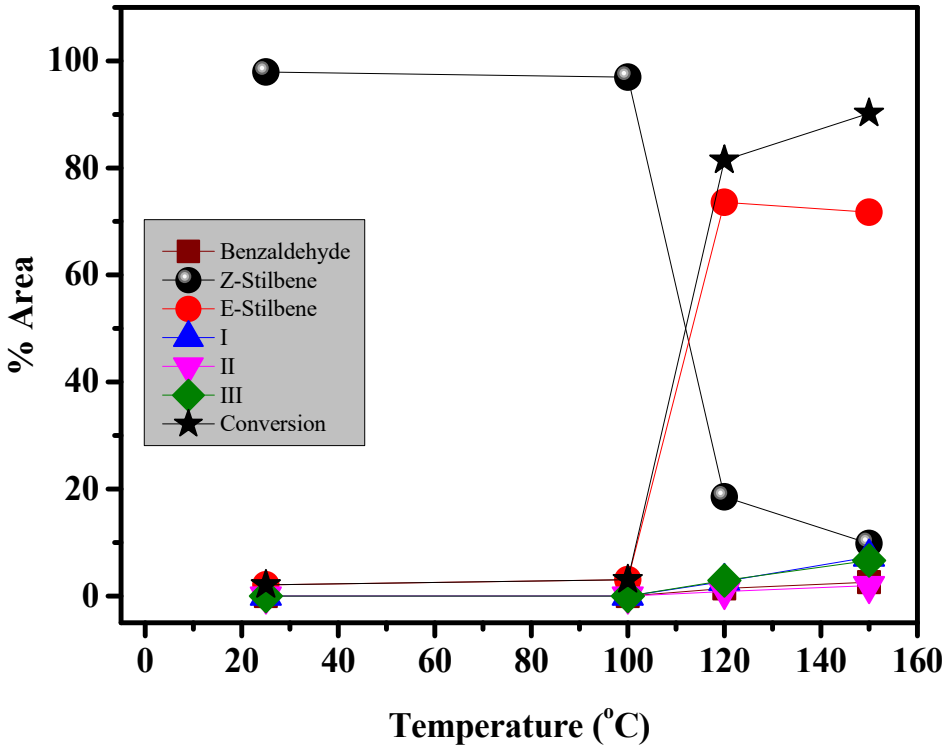

Figure 2- 11. Conversion of Z-stilbene and its products as a function of temperatures

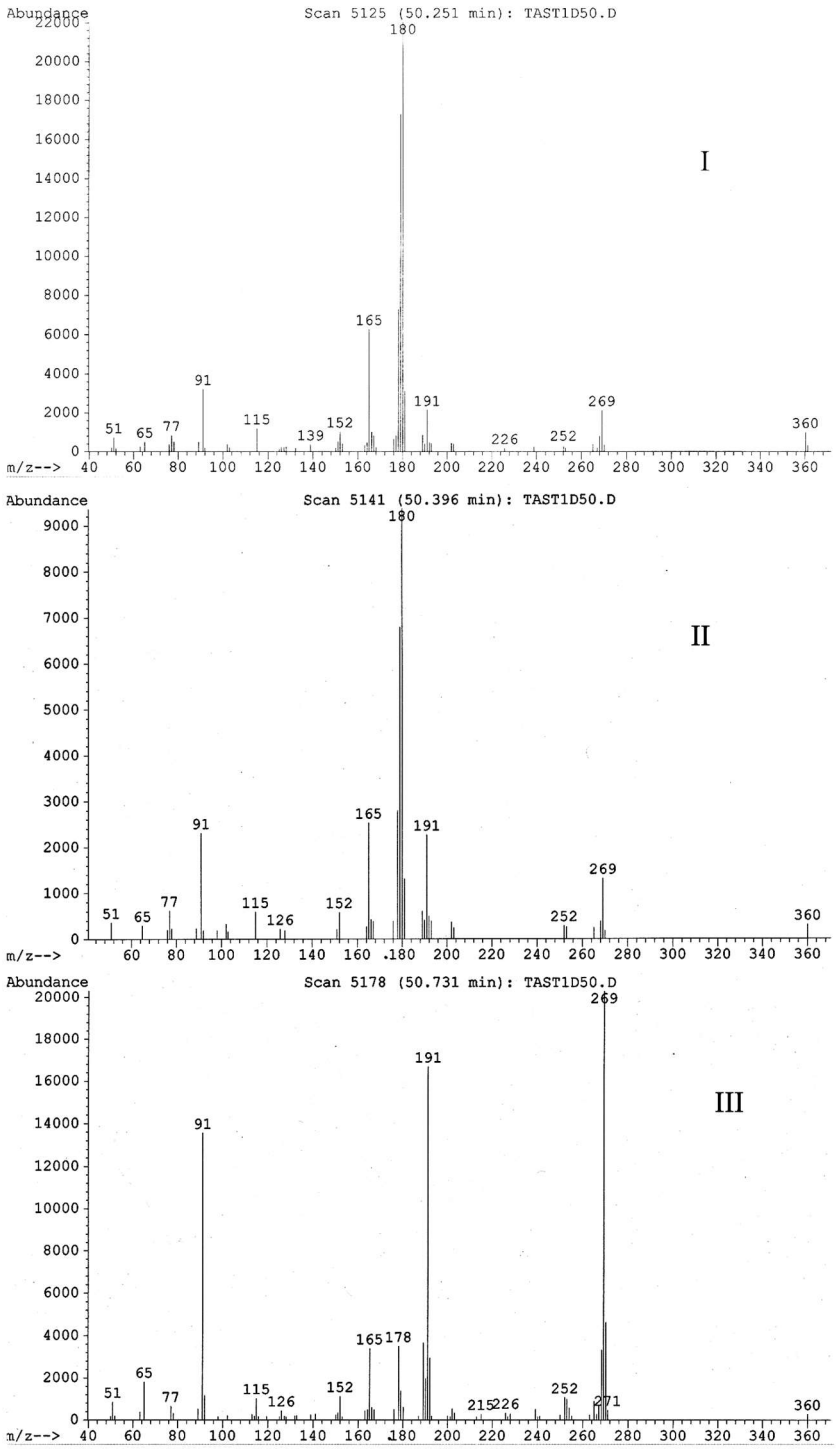

Figure 2- 12. Mass spectra of the dimerized isomers

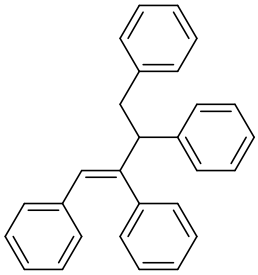

1,2,3,4-Tetraphenyl-1-butene (I or II)

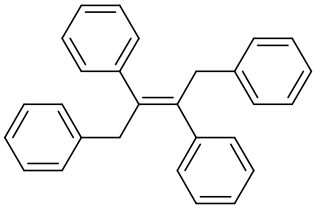

1,2,3,4-Tetraphenyl-2-butene (III)

Figure 2- 13. Dimerized products for stilbene reaction

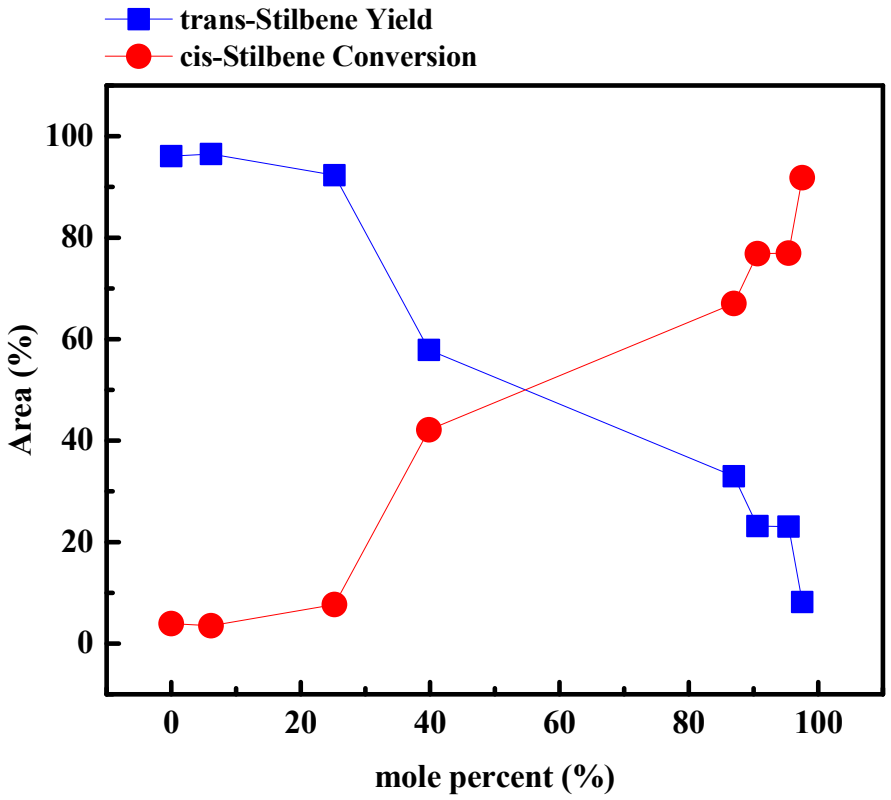

Figure 2- 14. Reaction of cis-stilbene with tungstic acid at 150 ˚C for 24 hour as a function of mole percent of tungstic acid

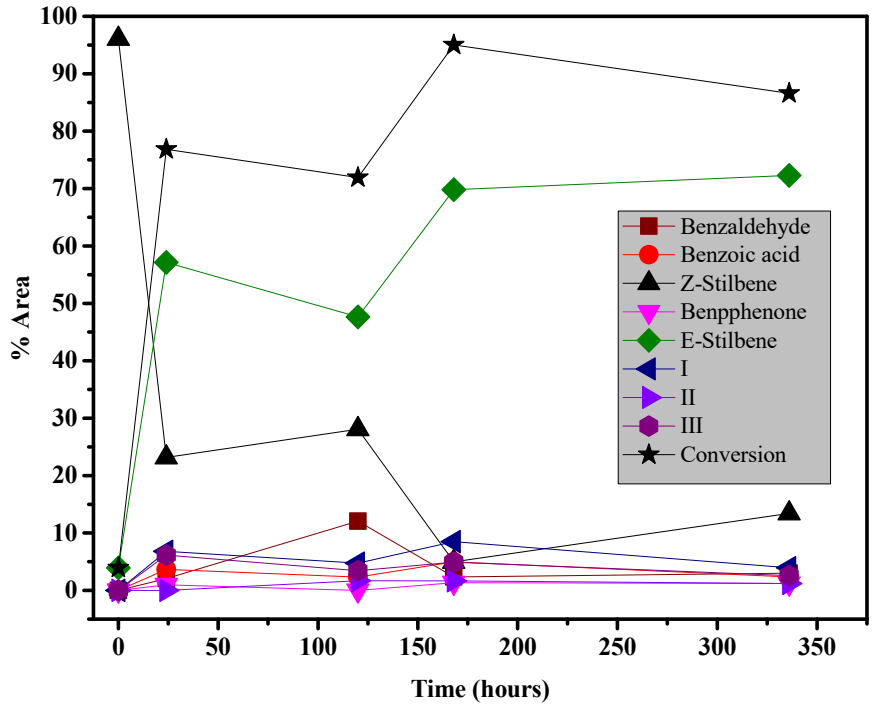

Figure 2- 15. Conversion of Z-stilbene and products yields as a function of time

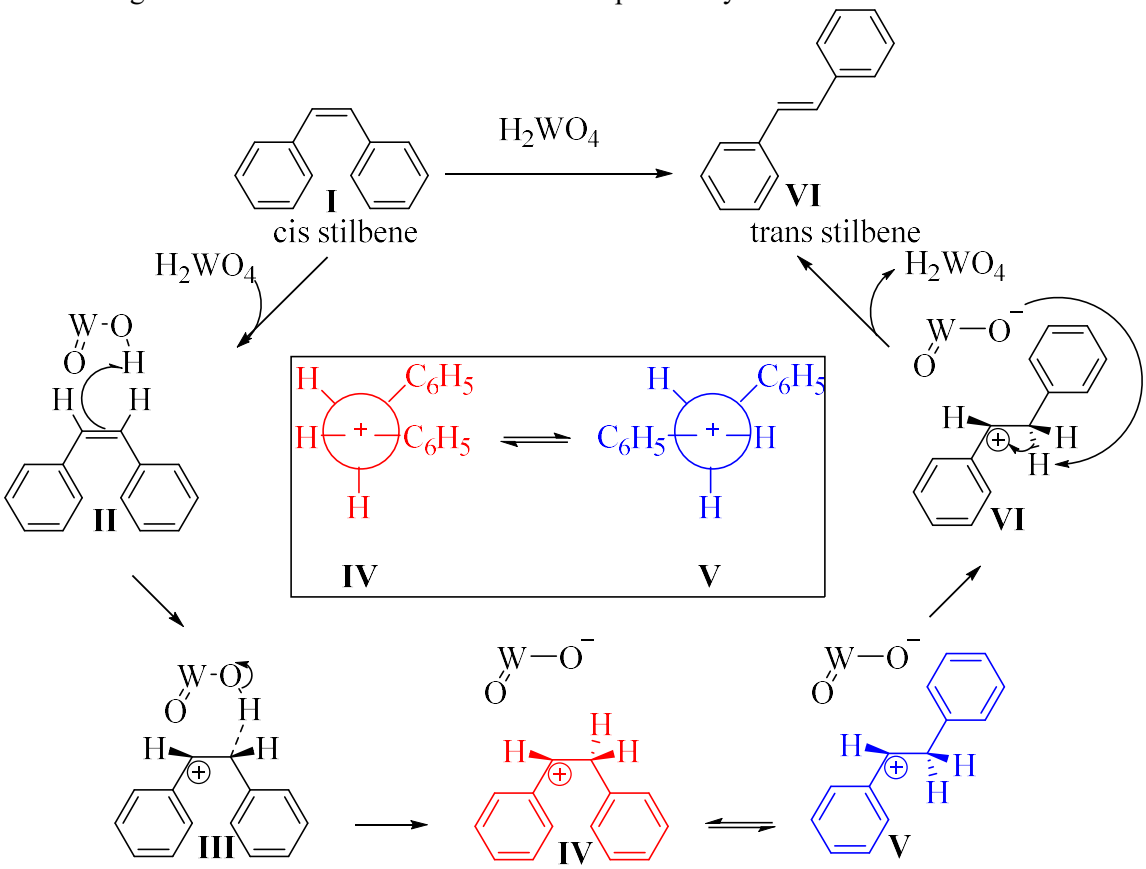

Scheme 2- 5. The proposed mechanism for stilbene isomerization

3.3.Chemical Transformation of Alkynes Using Tungstic Acid

The reactions of various alkynes with tungstic acid were carried out as described in the experimental section and the results of experiments are shown in Table 3. It was found that small changes in the particular substrates leads to major changes in the chemical reactions that take place including hydrogenation, dimerization, cyclotrimerization, oligomerization, and hydration reactions.

Table 2- 3. The selected alkynes and products obtained

Substrate	Reaction time (days)	Composition of reaction mixture
1-Hexyne	2	1,3,5-tributylbenzene, tetracosane*, unidentified compounds
3-Hexyne	14	94% 1,3,5-triphenylbenzene, undefined compounds
4-Methyl-2-pentyne	1	22% 1,2,4-trimethyl-5-(1-methylethyl)-benzene, 11% Hexamethylbenzene, undefined compounds
3,3-Dimethylbutyne	5	84% 1-(1,1-Dimethylethyl)-3,5-dimethylbenzene, 6% hexamethylbenzene, undefined compound
Ethnylbenzene	1	73% acetophenone, 21% 1,3-diphenyl-2-Buten-1-one, undefined compounds
Diphenylacetylene	14	15% benzoic acid, 80% 1,2 Diphenylethanone
(1.5 g) of tungstic acid mixed with (0.15 g) of substrate and heated to 150 °C for all reaction * Tetracosane observed when the reaction temperature was 100 °C		

As shown in Table 3, the GC-MS chromatograms of the diethyl ether extracts of the products from the reaction of terminal alkyne ,1-hexyne, with tungstic acid reactions demonstrate high conversion with low to moderate selectivity. However, depending on the reaction temperature, the resulting products vary. For example, tetracosane, 1,2,3-tributyl benzene, and unidentified compounds, (see Equation 1), were detected in the reaction performed at 100 ˚C while tetracosane was not detected for reactions performed at 150 ˚C. Additionally, the reaction time and tungstic

acid amount were also observed to affect the selectivity of the reactions. When the reaction time at 100 ◦C was increased from 24 hours to 48 hours, the area percentage of tributyl benzene decreased. When the amount of tungstic acid was increased from 3.00 g to 9.00 g, the reaction became more selective toward tetracosane with the area percentage of tetracosane increasing from 18.21 to 30.73 %.

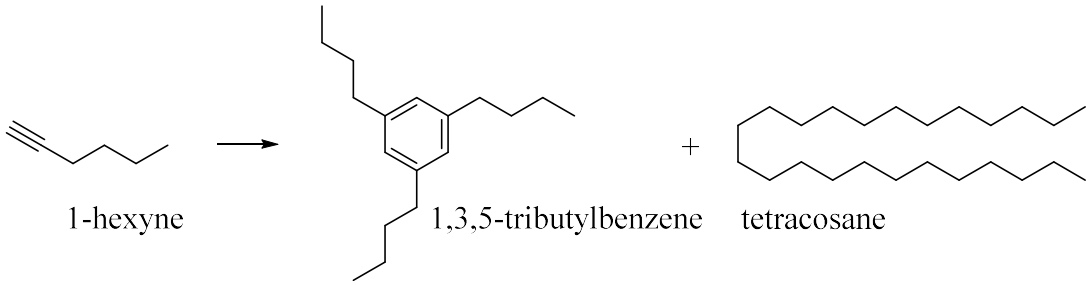

Equation 1. Transformation of 1-hexyne using tungstic acid

The GC-MS chromatograms of the products for the reaction of internal alkyne, 3-hexyne, with tungstic acid at 100 ◦C for 24 hours showed a major peak at low retention time (4.4 minutes) with 86 area percentage with a parent ion of 114 as shown in Figure 16. This major peak did not show a good quality match and it could be 2-hexenoic acid from elucidating the fragmentation of the GC-MS spectra. Performing the reaction at 150 ◦C result in formation of 1, 3, 5-triphenylbenzene with 49 area percentage, see Equation 2. When the reaction proceeds for 14 days the area percentage increased up to 94 % and the GC-MS matched 1, 2, 3- triphenylbenzene as shown in Figure 17.

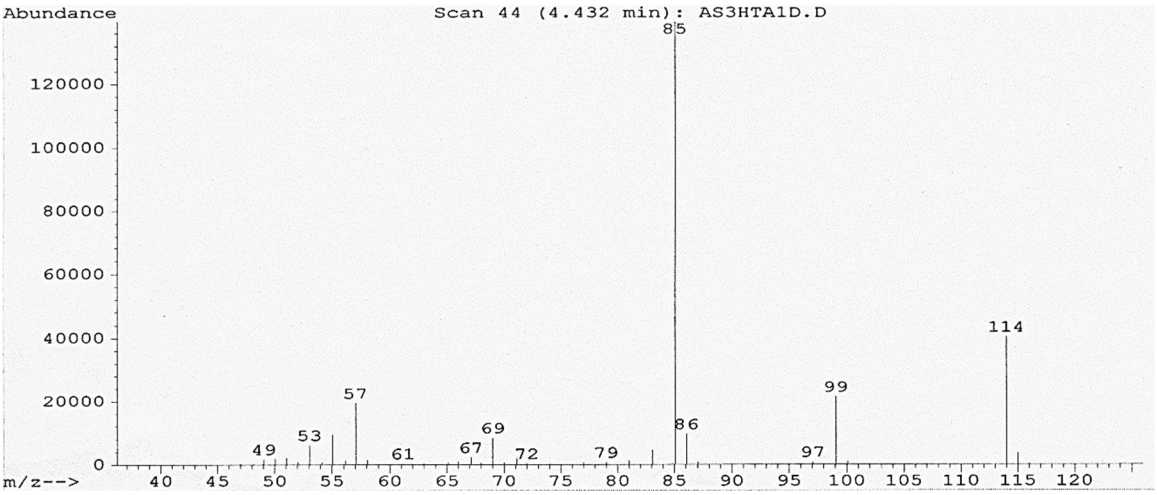

Figure 2- 16. Mass spectrum of the major product of 3-hexyne with tungstic acid reaction at 100 ˚C

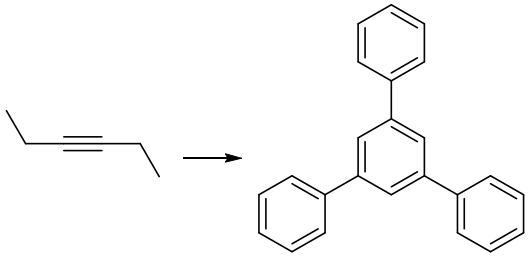

3-hexyne 1,3,5-triphenylbenzene

Equation 2. Transformation of 3-hexyne using tungstic acid at 150 ˚C

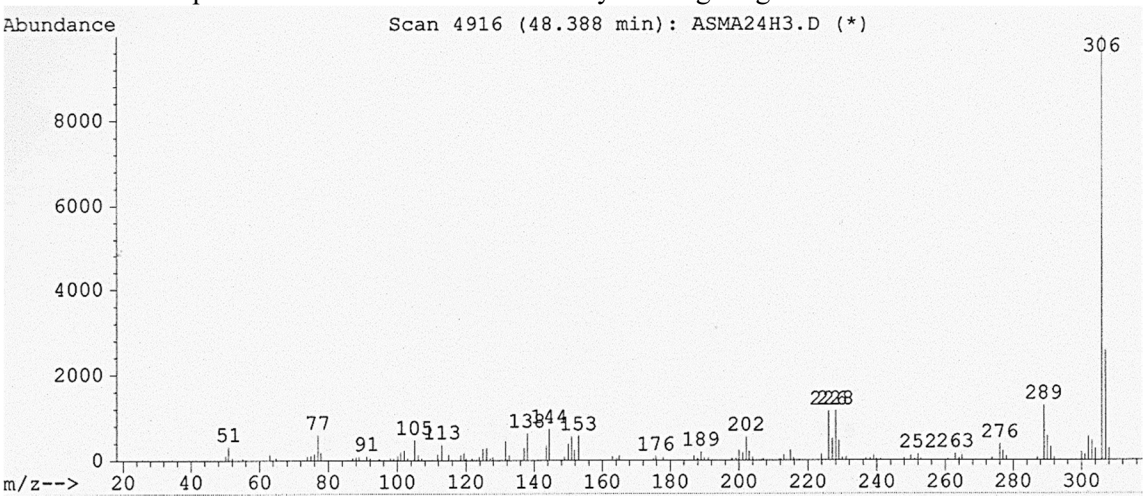

Figure 2- 17. Mass spectrum of major product of 3-hexyne reaction with tungstic acid at 150 ˚C

Tungstic acid is reactivity was also tested with branched alkynes as shown in Table 3. For example, GC-MS analysis of the 4-methyl-2-pentyne reaction mixture displayed a high conversion for the reaction performed at 150 ◦c for 24 hours producing 22% of 1, 2, 5-trimethyl-3-(1-methylethyl)-benzene, 11% of hexamethylbenzene, and several undefined compounds with molecular weight double and triple of the parent substrate as shown in Equation 3. Proposed mechanism is presented in Scheme 6. There are two possible most likely products according to proposed mechanism of this reaction (Figure 18), the 1, 2, 5-trimethyl-3-(1-methylethyl)- benzene (I) and the 1, 3, 5-trimethyl-2-(1-methylethyl)- benzene (II) products. Product II is less sterically likely, but electrocyclic reactions are driven more by electronic factors than steric one. In the transformation reaction of 4-methyl-2-pentyne, tungstic acid undergoes a rearrangement to form dienes that reacted with the another 4-methyl-2-pentyne in a cycloaddition reaction to form a cyclic diene that dehydrogenates to form 1, 2, 5-trimethyl-3-(1-methylethyl)-benzene. These reactions can undergo a Jacobsen rearrangement to produce hexamethylbenzene.

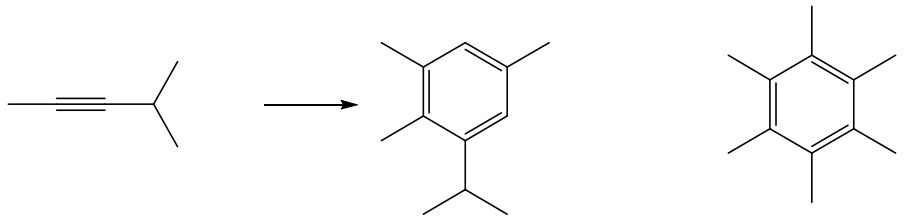

Equation 3. Transformation of 4-methy-2-pentyne using tungstic acid at 150 ◦C

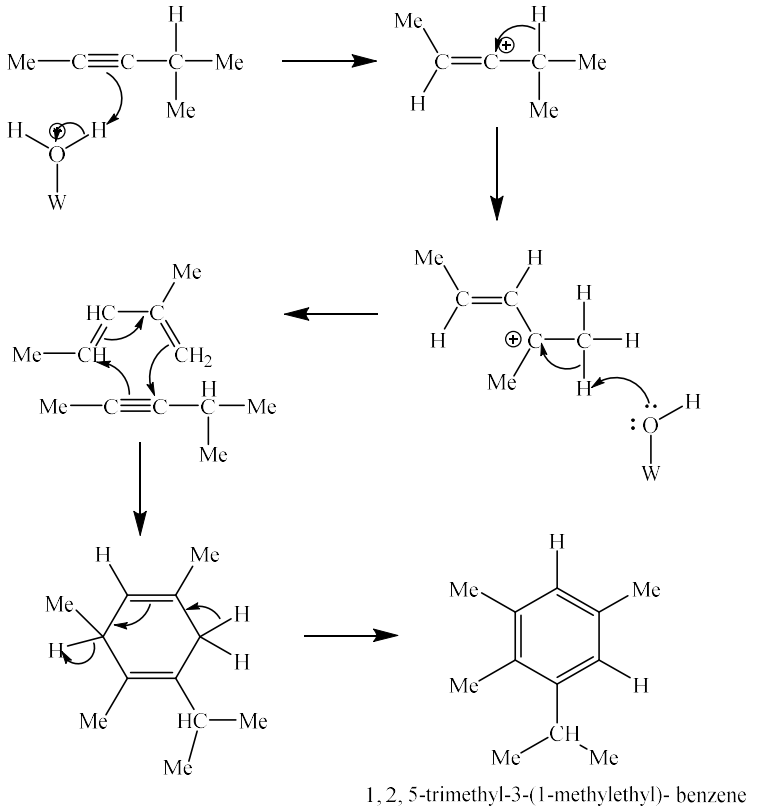

Scheme 2- 6. Proposed mechanisim for transformation of 4-methy-2-pentyne

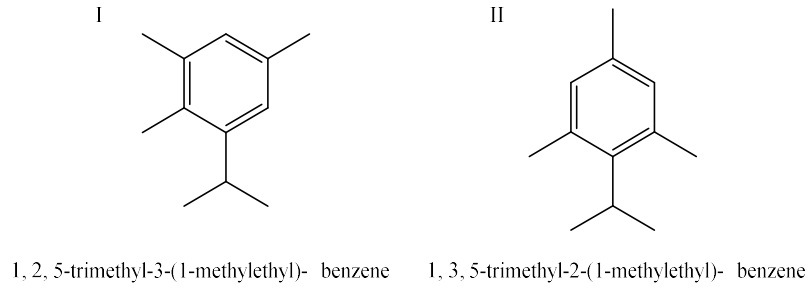

Figure 2- 18.The possible products for 4-methy-2-pentyne ransformation reaction

The GC-MS chromatogram of the 3,3-dimethylbutyne reaction mixture extract showed a high conversion when the reaction was performed at 150 ˚C for 5 days producing 84% of 4-(1,1-dimethylethyl)-1,2-dimethyl- benzene, 6% of hexamethylbenzene, and several isomers have same molecular weight of the major product with 10 % area percentage total as shown in Equation 4. The proposed transformation mechanism (Scheme 7) is likely similar to for transformation of 4-

methy-2-pentyne that involves rearrangement in the carbocation intermediate to form dienes followed by cycloaddition with another 3,3-dimethylbutyne molecule to from the ending product.

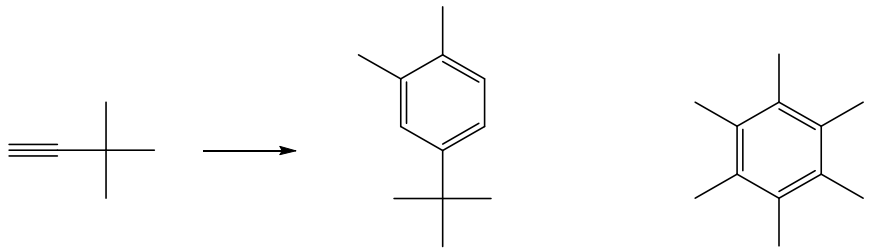

Equation 4. Transformation of 3,3-dimethylbutyne using tungstic acid at 150 ◦C

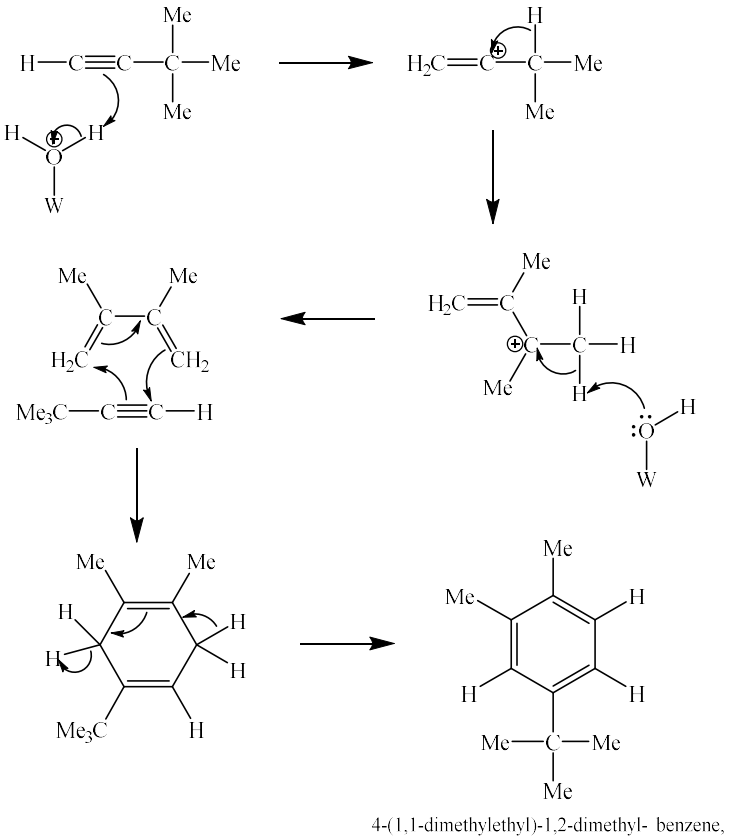

Scheme 2- 7. Proposed mechanisim for transformation of 3,3-dimethylbutyne

The catalytic activity of tungstic acid towards aromatic alkynes were invistigated as shown in Table 3. Phenylacetylene and diphenylacetylene do not react in the same way with tungstic acid as other alkynes. Hydration of ethnylbenzene occurred following Markownikoff's rule producing

acetophenone as initial product. Diphenylacetylene reacted to eventually produce benzaldehyde via several intermediates. The GC-MS of diethyl ether extracts form the reaction of phenyl acetylene with tungstic acid reaction at 150 ◦C for 24 hours showed formation of 73% of acetophenone, 21% of 1,3-diphenyl-2-Buten-1-one (Dypnone), 0.40 % 1,3,5-triphenyl-2,4-hexadien-1-one, 0.60% of triphenylbenzene, and less than 5% of several unidentified compounds. Thus, the result of the reaction of phenyl acetylene with tungstic gave acetophenone as a major product and dypnone, as a minor product. Dypnone conversion and rearrangement to 1, 3, 5-triarylbenzenes was reported previously using p-toluene sulfonic acid as a catalyst.[122, 126] Condensation of acetophenone catalyzed by tungstic acid was found to produce dypnone and 1,3,5-triarylbenzenes. The results suggest that phenyl acetylene was first hydrated by adding a water molecule to the triple bond to give acetophenone. This subsequently self-condensed produce dypnone that then through aldol-type self-condensation and rearrangement of gives triphenylbenzene. This reaction sequence is shown in Scheme 8. Proposed mechanism for transformation of phenylbenzene to acetophenone is shown in Scheme 9.

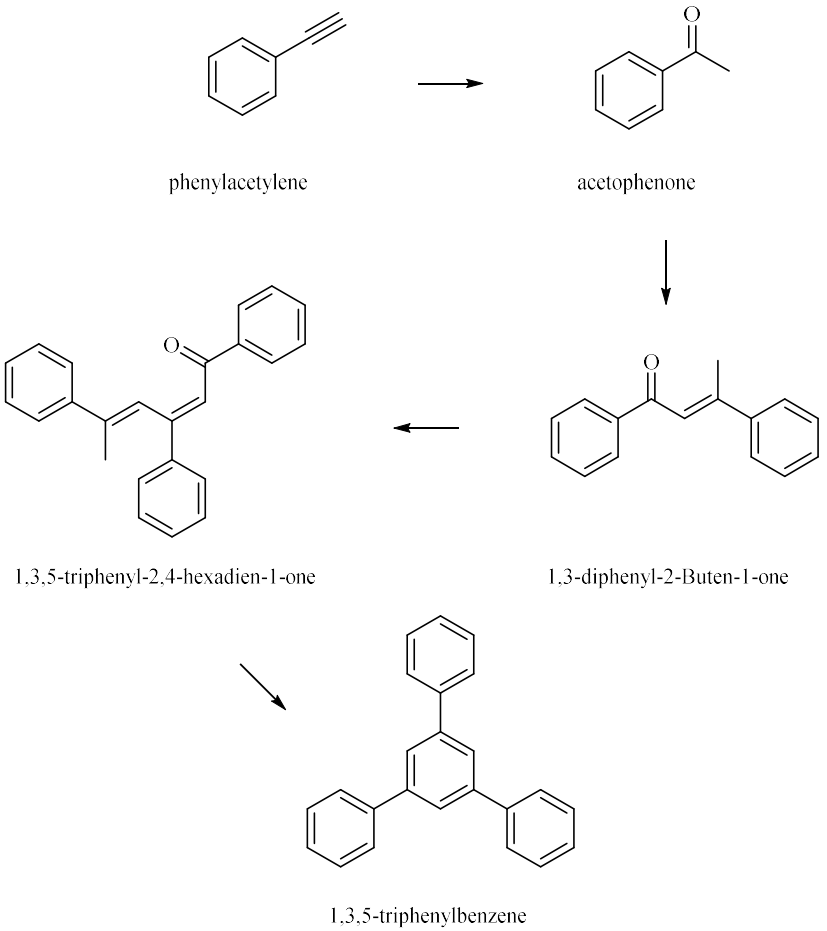

Scheme 2- 8. Transformation of phenylacetylene using tungstic acid at 150 ˚C

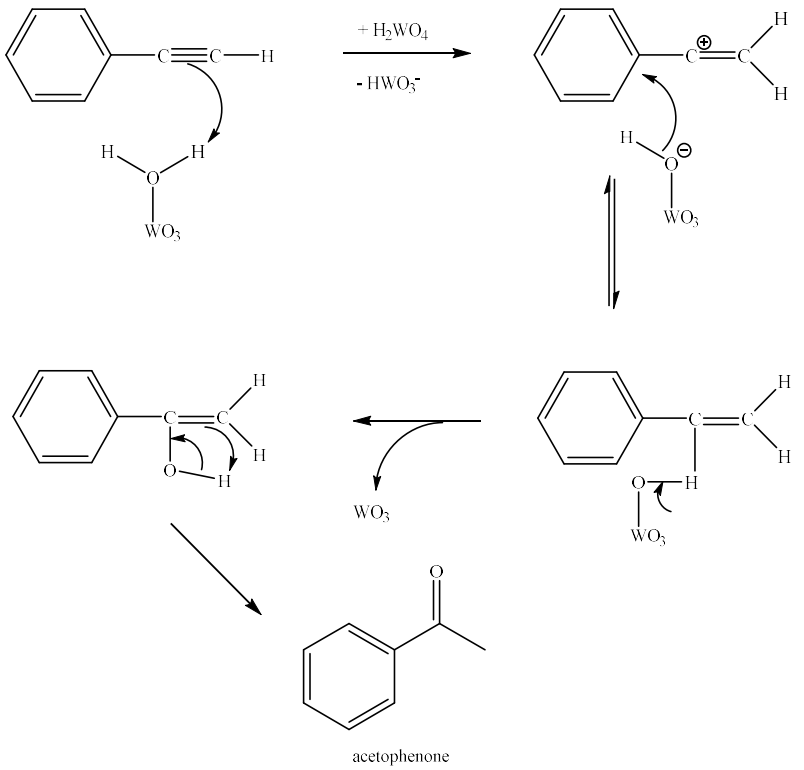

Scheme 2- 9. Proposed mechanism for transformation of phenylbenzene to acetophenone

The GC-MS of diethyl ether extract for the reaction of diphenylacetylene with tungstic acid showed an unusual result via in which benzaldehyde was formed. To investigate this unexpected result, several reactions of diphenylacetylene and tungstic acid were carried out and the results are shown in Table 4. Tungstic acid reacted with diphenylacetylene under the experimental conditions producing carbonyl compounds in fairly good yields. The major products were benzaldehyde, benzoic acid, and benzyl phenyl ketone. As shown in Table 4, the reactions of diphenylacetylene produced varying products depending on tungstic acid loading, and the reaction conditions. The results of the reaction of diphenylacetylene with tungstic acid at for 48 hours as a function of temperature are shown in Figure 19. Conversions were low at 80 $^{\circ}$C and 100 $^{\circ}$C ~ (<12 %) to benzaldehyde and benzoic acid. Similar activities with better conversions and the products were realized at 150 $^{\circ}$C. Furthermore, the amount of diphenylacetylene reagent plays an important role in the diphenylacetylene conversions. Reducing the amount of this reagent results in an increase of

the conversion; for example, mixing 0.015 g of diphenylacetylene with 1.5 g of tungstic acid shows higher conversion compared to 0.15 g of diphenylacetylene. The highest conversion (100%) of diphenylacetylene was achieved when a mixture of 1.5 g of tungstic acid and 0.002 g of diphenylacetylene was heated to temperature 150 °C for 1 day, producing a 86 % yield of benzoic acid. In addition, the amount of tungstic acid also plays a role in this transformation as shown in Figure 20 and Table 4, when a 3 or 6 g of tungstic acid were reacted with 0.15 g of diphenylacetylene for 2 days at 150 °C, high conversions 97 % and 97 % respectively were observed. A poor transformation of diphenylacetylene was observed when the tungstic acid amount is increased higher to 9 g. Although the time of the transformations does not show clear effect on the transformation behavior, it significantly impacts the final products. For example, instead of obtaining a mixture of benzaldehyde and benzoic acid, a mixture of benzyl phenyl ketone (80 % yield) and benzoic acid (15.2 % yield) is obtained from a transformation of 1.5 g of diphenylacetylene (99.91% conversion) using 1.5 g of tungstic acid at 150 °C for 14 days.

Table 2- 4. Diphenylacetylene and tungstic acid reactions

Entry	Tungstic acid	Diphenyl acetylene	Time (day)	Temperature	Diphenylacetylene conversion %	Benzaldehyde yield %	Benzoic acid yield %	Benzyl Phenyl Ketone yield %
1	1.5	0.15	4	100	22.3	1.2	2.3	0.00
2	1.5	0.015	1	150	95.9	33.5	55.2	0.00
3	1.5	0.015	2	150	97.4	38.3	54.3	0.00
4	1.5	0.15	1	150	42.9	17.2	1.1	0.00
5	1.5	0.15	2	150	61.3	30.1	7.5	0.00
6	1.5	0.15	3	150	44.9	18.4	1.7	0.00
7	1.5	0.15	4	150	77.7	8.0	39.7	0.00
8	1.5	0.002	1	150	100.0	11.5	85.8	0.00
9	1.5	0.15	14	150	99.9	0.0	15.2	80.00
10	3	0.015	1	150	96.9	20.7	67.3	0.00
11	3	0.15	1	150	75.4	48.8	7.9	0.00
12	3	0.15	2	150	96.5	36.2	33.9	2.78
13	3	0.15	4	150	53.8	8.1	17.0	0.00
14	6	0.015	1	150	61.1	9.1	27.5	0.00
15	6	0.15	1	150	86.6	44.8	29.7	0.00
16	6	0.15	2	150	97.4	39.4	41.5	0.00
17	9	0.15	4	150	61.3	4.3	27.4	0.00

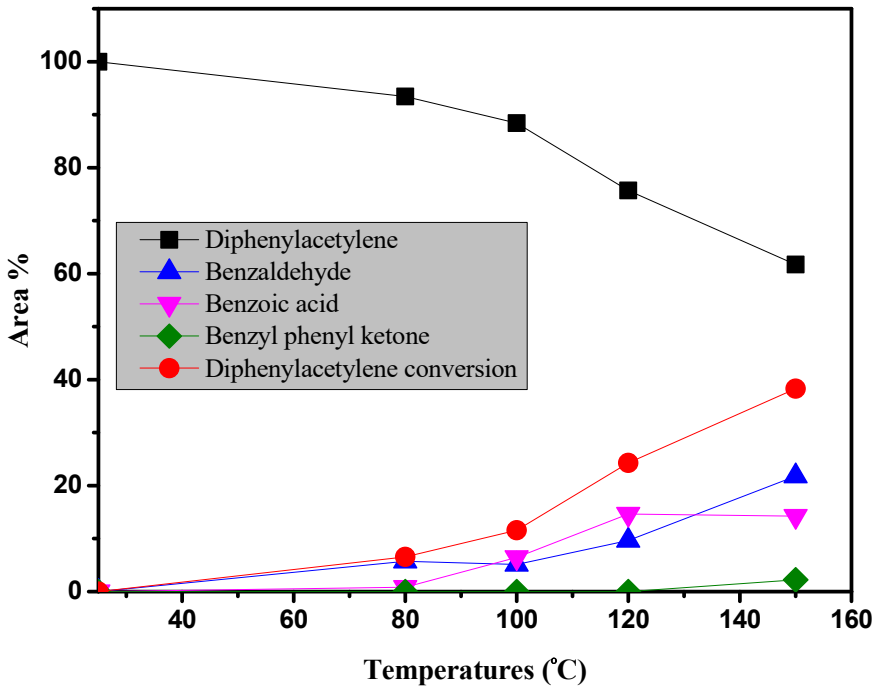

Figure 2- 19. Reaction of diphenylacetylene with tungstic acid for 48 hour as a function of temperature

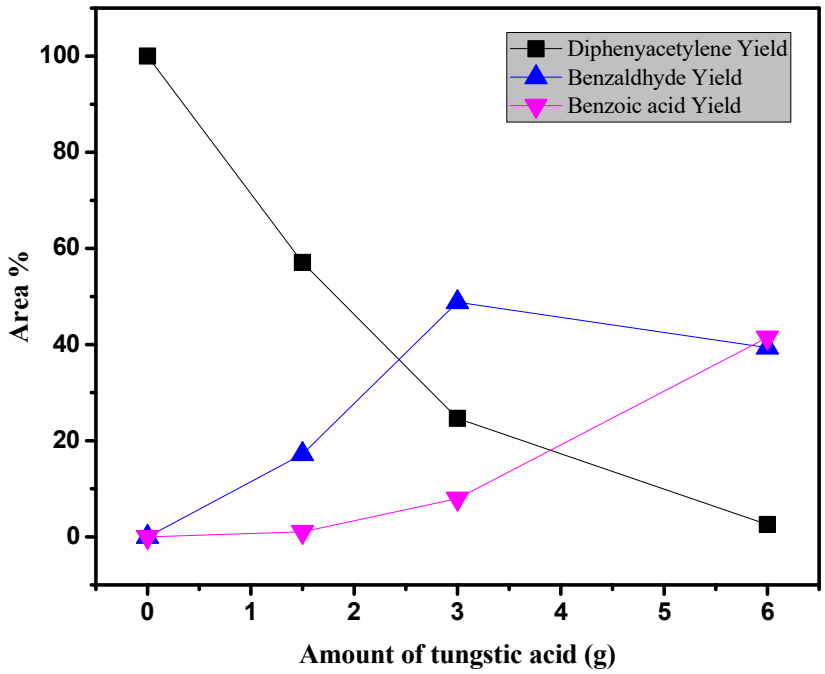

Figure 2- 20. Reaction of diphenylacetylene with tungstic acid at 150 ◦C for 48 hour as a function of tungstic acid amount

Kinetic experiments demonstrated complex catalytic activity of tungstic acid towards diphenylacetylene (Figure 21). Initially, a diphenylacetylene conversion increases rapidly reaching 40% of total conversion within 48 hours. This was associated with a sharp increase in the concentrations of benzoic acid and benzyl phenyl ketone. Beyond this point the diphenylacetylene concentration followed an approximately linear slower decay. From 30 minutes to 24 hours the concentration of benzaldehyde increases dramatically while that of benzoic acid and benzyl phenyl ketone decreases. Beyond 2 days the benzaldehyde drops in concentration while benzoic acid increases. This is likely caused in part by oxidation of benzaldehyde dioxygen. The results suggest a possible mechanism shown in Scheme 10 where benzyl phenyl ketone and benzaldehyde are intermediates and benzoic acid is the ultimate product. Benzoic acid is also a possible product from benzyl phenyl ketone.

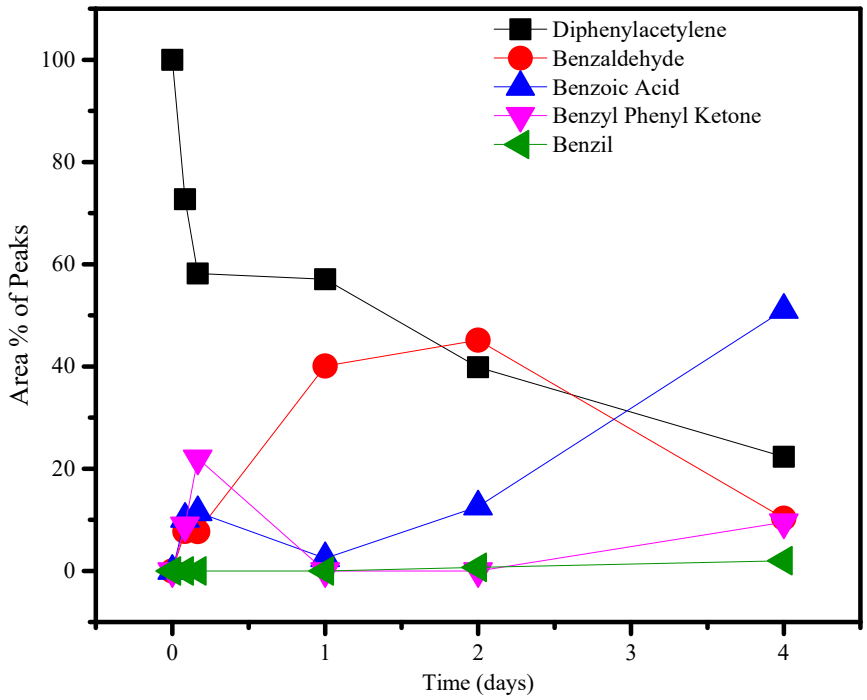

Figure 2- 21.Products and diphenylacetylene conversion vesus time (1.5 g diphenylacetylene, 1.5 tungstic acid at 150 ˚C)

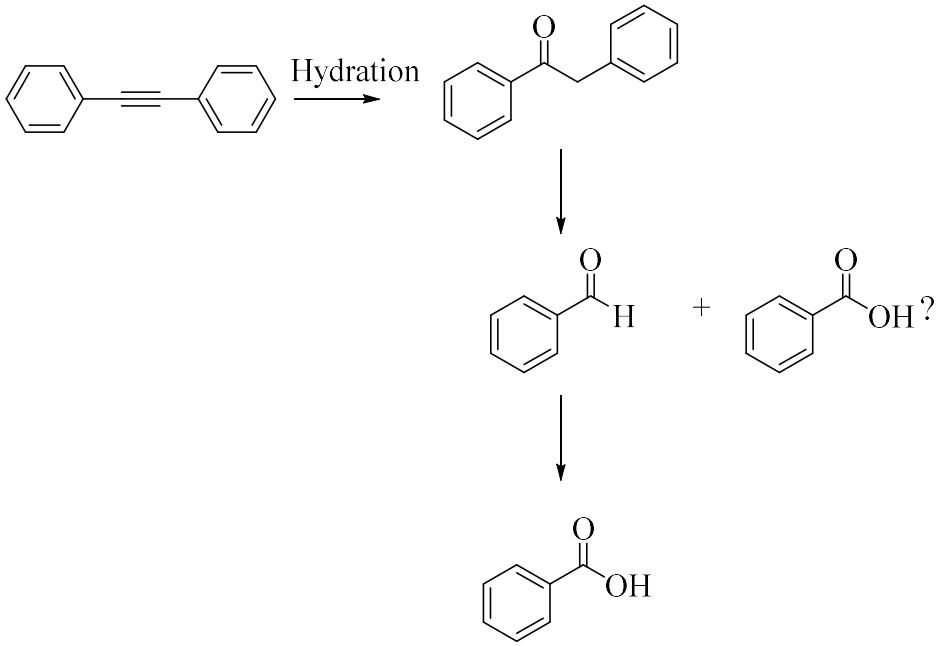

Scheme 2- 10. Possible conversion pathway for diphenylacetylene

A reaction of tungstic acid (1.5 g) and benzyl phenyl ketone (0.15 g) at 150 ˚C for 48 hours gave <35% conversion of the starting material. The products formed were benzoic acid and benzaldehyde as postulated in Equation 5. The tungstic acid changes color from yellow to green, indicating some reduction to W(V). this is in keeping an oxidative cleavage of a carbon-carbon bond in benzyl phenyl ketone. Figure 22 shows transformation of benzyl phenyl ketone as a function of time appears that benzaldehyde is first formed and is then oxidized to benzoic acid. To check if that is the case, benzyl 4- chlorophenyl ketone was reacted with tungstic acid under the same condition. The observed products were benzaldehyde, benzoic acid, and chlorobenzoic acid as Equation 6 illustrates. Therefore, benzoic acid is a result of the further oxidation of benzaldehyde as shown in Equation 7. If the reaction were to produce one equivalent of benzoic acid and one equivalent of benzaldehyde simultaneously, it would be expected that the aldehyde would be formed from the less reduced or benzyl end of the benzyl phenyl ketone. Since benzaldehyde is formed, this implies that both ends of the molecule are converted to aldehydes. The failure to observe chlorobenzaldehyde can be attributed to its high susceptibility to oxidation.

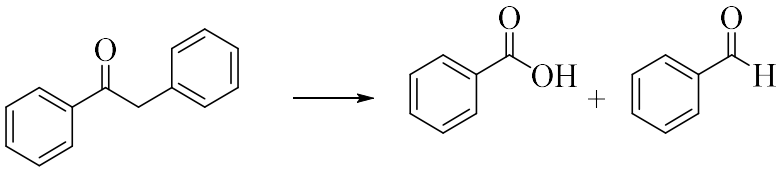

Equation 5. Reaction of benzyl phenyl ketone with tungstic acid at 150 ˚C

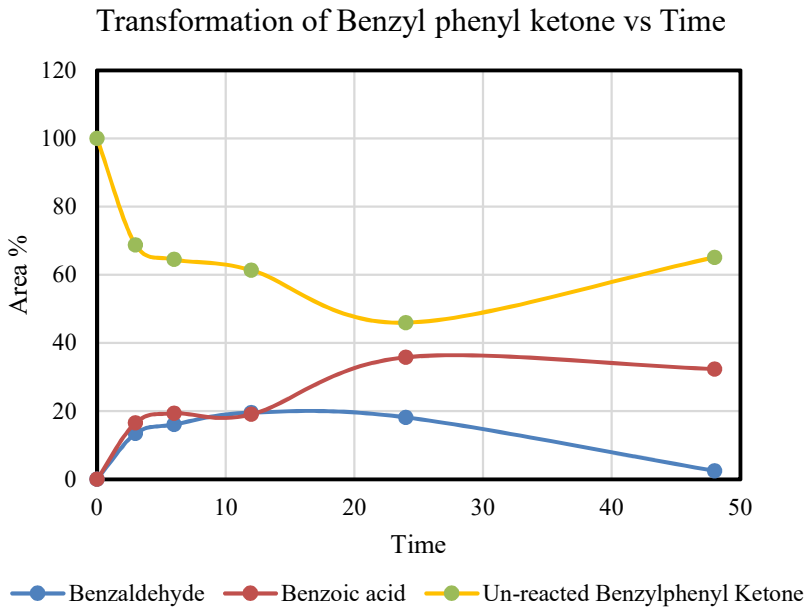

Figure 2- 22. Transformation of benzyl phenyl ketone (0.15 g) using tungstic acid (1.5 g) at 150 ˚C for 48 hours

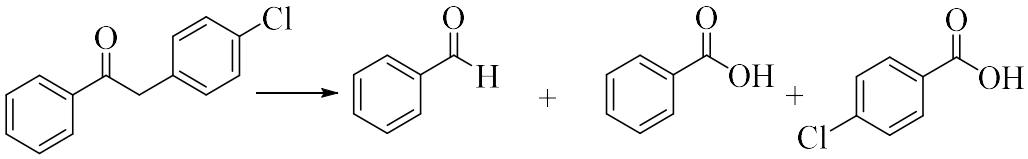

Equation 6. Reaction of benzyl 4- chlorophenyl ketone with tungstic acid at 150 ˚C

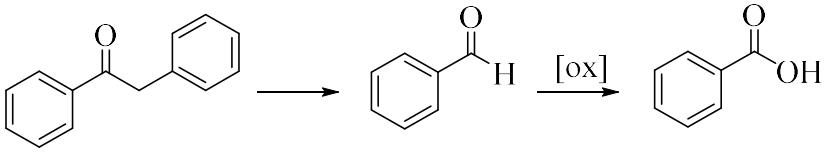

Equation 7. Results of transformation of benzyl phenyl ketone

The oxidation of benzyl phenyl ketone is likely to involve benzoin as an intermediate Equation 8. [127] Therefore, benzoin was reacted with tungstic acid under the same conditions (see Equation 9). The tungstic acid color changed from yellow to bluish-green and the benzoin with

100% conversion gave benzoic acid, benzaldehyde, benzil, and benzyl phenyl ketone products as shown in Equation 9. Both benzaldehyde and benzoic acid are results of oxidative cleavage of benzoin by W(VI), while benzil results from oxidation of the carbon alpha to the carbonyl. Figure 21 demonstrates that benzaldehyde is oxidized further to benzoic acid by W(VI) or O_2. When p-chlorobenzoin (Equation 10) was reacted with tungstic acid, the chlorolable is found in both the benzaldehyde and benzoic acid indicating that selective cleavage of the carbon-carbon bond to an aldehyde and a carboxylic acid does not occur. Instead the reaction must produce both chlorobenzaldehydes and these could subsequently oxidize to benzoic acid. Conversion of benzoin to benzaldehyde is a retro benzoin condensation, observed previously using the enzyme benzoyl formate decarboxylase Equation 11.

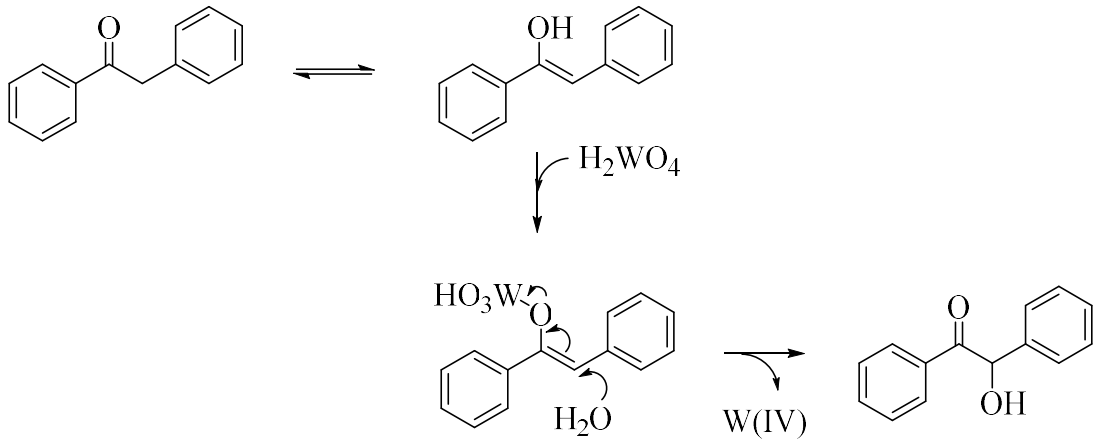

Equation 8. Formation of benzoin intermediate through oxidation of benzyl phenyl ketone with tungstic acid

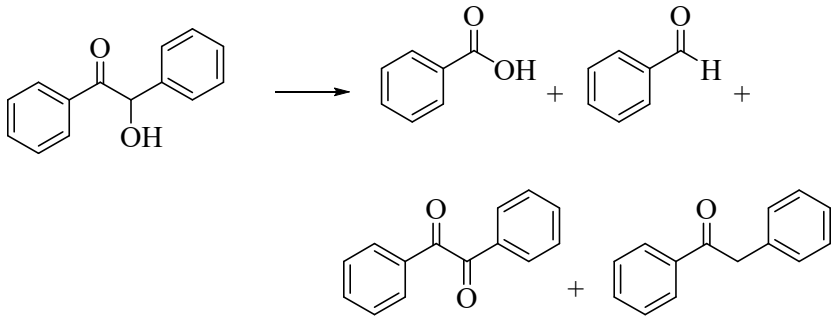

Equation 9. Reaction of benzoin with tungstic acid at 150 ◦C

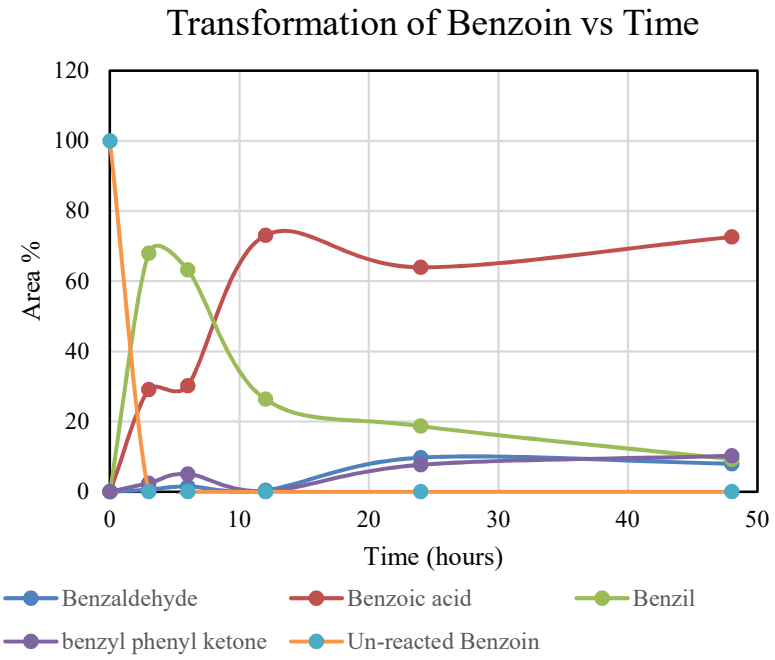

Figure 2- 23. Transformation of benzoin (0.15 g) using tungstic acid (1.5 g) at 150 ˚C

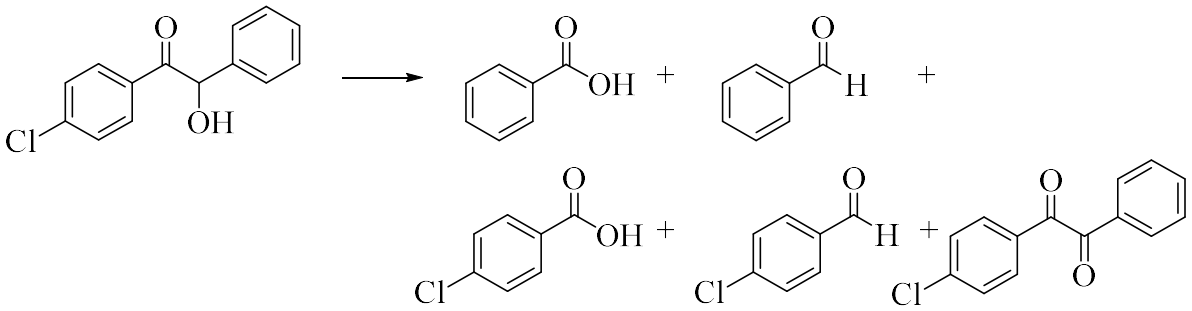

Equation 10. Reaction of p-chlorobenzoin with tungstic acid at 150 ˚C

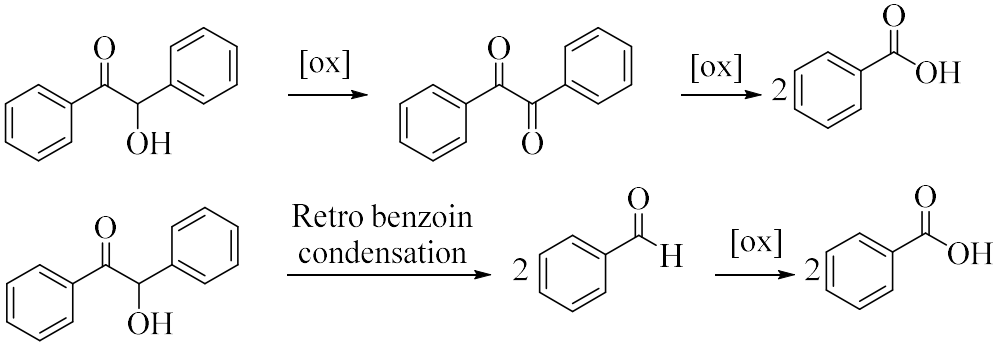

Equation 11. The suggested two pathways of benzoin transformation

P- chlorobenzil arising from oxidation of the benzoin was also observed in the reaction mixture. It is possible that this molecule is cleaved to the carboxylic acids. This possibility was tested by reacting benzil with tungstic acid at 150 ˚C (Figure 24) this reaction produced only benzoic acid (Equation 12). Thus, it can be concluded that benzoin reacts with tungstic acid by two pathways-retro benzoin condensation to benzaldehyde and oxidation to benzoic acid via benzil as shown in Equation 12. Benzil transformed selectively to benzoic acid with <94% conversion. The tungstic acid became dark blue as Figure 25. Indicating the formation of tungsten bronze, H_xWO_3. The same result is observed when the reaction is conducted under N_2, indicating that benzil was cleaved oxidatively by tungstic acid to produce two equivalent of benzoic acid as shown in Equation 13.

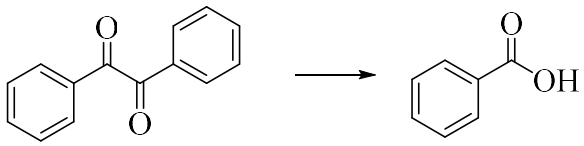

Equation 12. Reaction of benzil (0.15 g) using tungstic acid (1.5 g) at 150 ˚C

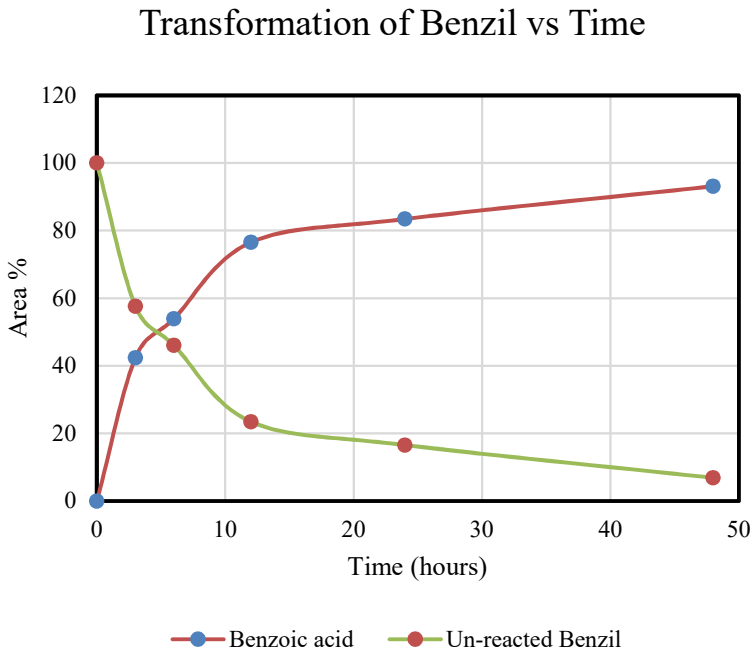

Figure 2- 24. Transformation of benzil (0.15 g) using tungstic acid (1.5 g) at 150 ˚C

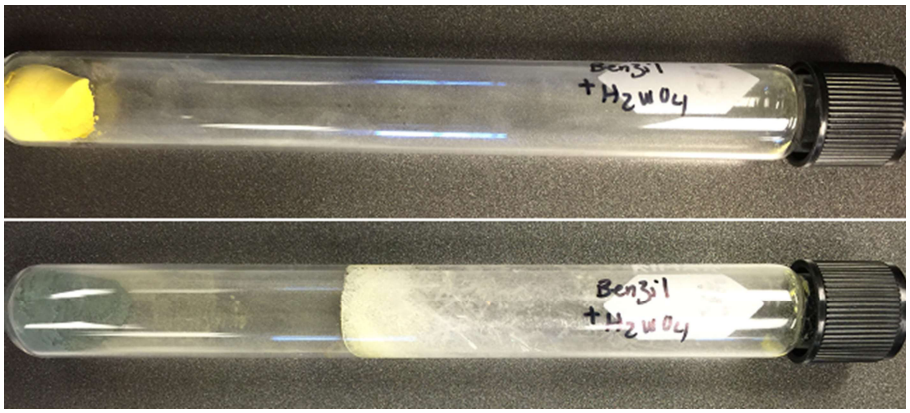

Figure 2- 25. Formation of tungsten bronze from benzil and tungstic acid reaction

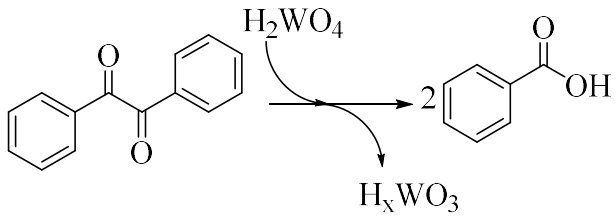

Equation 13. The suggested pathway of benzil transformation

Table 5 summarized the results of the reaction of 0.1 g of diphenyl acetylene and each of the products identified in the reaction mixture with 1 g tungsten acid at 150 ˚C for 48 hours. The reaction of diphenyl acetylene gave benzaldehyde, benzoic acid, and benzyl phenyl ketone. Thus, diphenylacetylene hydration must occur to form benzyl phenol ketone intermediate (Scheme 11). The enol form of benzyl phenyl ketone can then undergo this oxidation of the carbon next to the carbonyl to produce benzoin. This compound is then converted to benzil or cleaved to benzaldehyde. The hydration and oxidation reactions consume the water present in tungstic acid. As a consequence, both the amount of water and the acidity diminish with time. Thus, the reactions become slower and the pathways followed by reaction therefore the products produced vary with reaction time and alteration of reactant ratios.

Table 2- 5. Comparison between the hydration reaction results of 0.15 g of diphenylacetylene and 0.15 g each possible intermediate with 1.5 g tungstic acid at 150 °C for 48 hours

Reagent	conversions %	Benzaldehyde yield %	Benzoic acid yield %	Yield of other compounds %
Diphenylacetylene	38.29	21.81	14.25	2.23 of Benzyl phenyl ketone
Benzyl phenyl ketone	34.85	2..48	32.37	-
Benzoin	100	7.98	72.57	10.20 of Benzyl phenyl ketone 9.25 of Benzil
Benzil	93.12	0	93.12	-

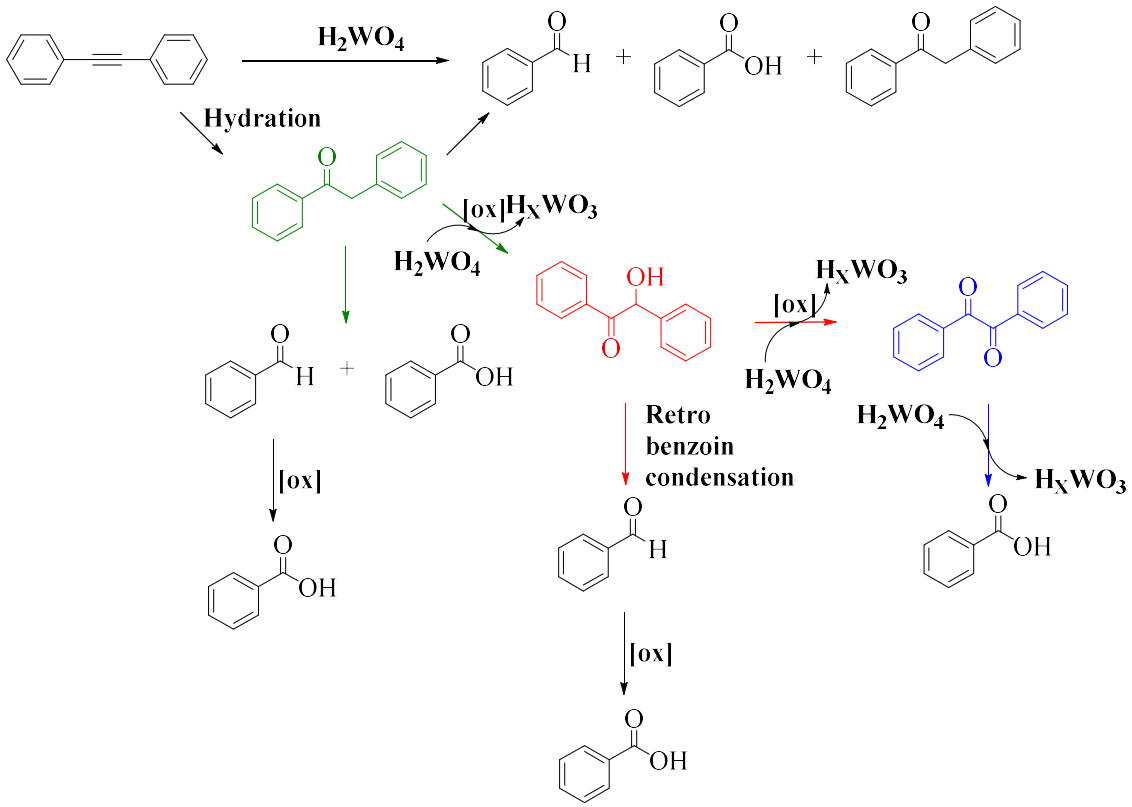

Scheme 2- 11. The proposed pathways of diphenylacetylene transformation using tungstic acid

3.4.Chemical Transformation of nitriles using Tungstic Acid

The reaction of several nitriles with tungstic were carried out at 150 ◦C for 8 hours. The results are summarized in Table 6. The majority of the nitriles produced the corresponding amides in excellent yield via an acid-catalyzed hydration reaction (Equation 14). However, some of the selected nitriles produced a triazine compound in addition to the amide. For example, 2-dichloroacetonitrile produced the 2-dichloroacetamide as a major product in 62 % yield and 2,4,6-tris(dichloromethyl)-1,3,5-triazine in 35 % yield. In a similar manner to molybdenum and tungsten hydrogen bronze systems,[116] the triazine compound is suggested to be the product of cyclotrimerization of the parent nitrile molecules.

Previously, both molybdenum or tungsten hydrogen bronze were found to hydrate nitriles was postulated the acidic hydroxyl groups present on the tungsten and molybdenum hydrogen bronzes serve as the source of water. In the proposed mechanism one metal center is reduced and an adjacent one is oxidized, so that the overall average oxidation state of the bronze catalysts do not change. [116] Although hydration of nitriles using tungstic as a reagent gave similar results, the mechanism of hydration likely involves the water molecules of tungstic acid that serves as a source of water and acidity.

Table 2- 6. The selected nitriles and products obtained

Substrate	Major product	Other products
Acetonitrile	Acetamide (100%)	-
2-Dichloronitrile	2-Dichloroacetamide (62%), and 2,4,6-Tris(dichloromethyl)-1,3,5-triazine (35%)	Unidentified (3%)
2-Trichloronitrile	2-Trichloroacetamide (100%)	-
Isobutyronitrile	Isobutyramide (100%)	-
2-Methylbutyronitrile	2-Methylbutyramide (S and R), 98% total of (52% and 46%)	Unidentified (2%)
Isovaleronitrile	Isovaleramide (94%)	Unidentified (6%)
Valeronitrile	Valeramide (90%)	Unidentified (10%)
Acrylonitrile	Acrylamide (100%)	-

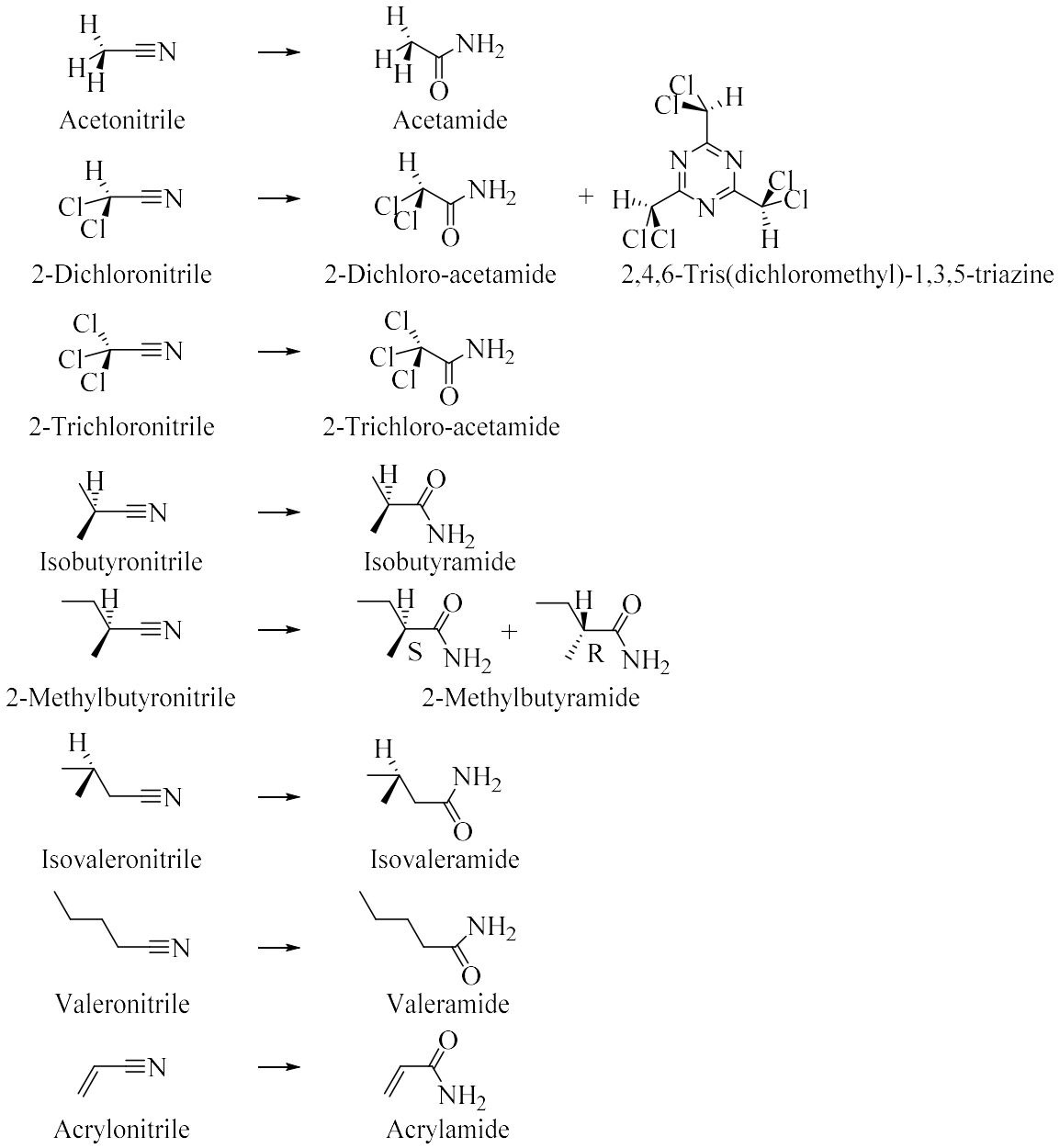

Equation 14. The major products of nitriles and tungstic acid reactions

4. Conclusion:

In its reactions with alkynes, and nitriles, tungstic acid often behaves as a prototypical solid acid catalyst and produces ketones and amides, respectively, via hydration reactions. The tungstic acid acts both as the catalyst and the source of water so that solventless reactions are possible – a major advantage in those reactions that cleanly produce hydrates. The ketones produced follow the Markovnikov rule indicating the formation of a cationic protonated intermediate. In the case of alkenes, hydration was only observed for cyclohexene and methyl-cyclohexene where the corresponding cyclohexanols were formed in low yield. For alkenes, the dominant first step was acid-catalyzed formation of dimers and is some cases higher oligomers. However, cyclopentenes and indenes underwent an unusual where the cyclopentene rings opened up in a dimerization reaction to form two edge-shared six-membered rings to give decalin-like molecules in the case of cyclopentene and hydrogenated chrysene-like molecules in the case of indene. In both cases, tungsten bronze dehydrogenated and aromatized the initial formed materials. For example, hexahydronapthalene and tetrahydronapthalene were observed in the cyclopentene products while chrysene was identified in the indene products. During the dehydrogenation reactions, tungstic acid was converted to tungsten hydrogen bronze, $H_{0.33}WO_3$. Notably, the dimerization of cyclopentenes that are not very useful products from catalytic cracking reactions to decalin-like molecules that can be used in diesel fuel may be attractive to the petrochemical industry. Several unusual reactions were observed in the reactions of alkynes with tungstic acid. Phenylacetylene produces some hydrated product (acetophenone) but also two products from the cleavage of the carbon-carbon triple bond, benzaldehyde and benzoic acid. The acetophenone undergoes subsequent reaction through a series of intermediates to form 1,3,5-triphenylbenzene – a process that is known to occur with acidic catalysts. Through a series of reactions of intermediates and asymmetrically-labeled intermediates with tungstic acid, it was concluded that cleavage of the triple bond to two benzoic acid molecules occurs through benzil as an intermediate while the formation of two benzaldehyde

molecules goes through benzoin as an intermediate. This is the first example of a non-enzymatic retro-benzoin reaction. It was found that the reaction of tungstic acid with benzil is a highly-efficient cost-effective way to prepare tungsten hydrogen bronze. It was also discovered that hexyne isomers, in the presence of tungstic acid, can undergo a rearrangement to dienes that in turn react with the parent alkyne in a cycloaddition reaction to form a diene that dehydrogenates to an alkylated benzene. These reactions are complicated by the fact that the aromatic products undergo a Jacobsen rearrangement to produce benzene and more highly-alkylated products such as hexamethylbenzene. For example, t-butylbenzene can be converted to 1,3-di-t-butylbenzene, and 1,4 di-t-butylbenzene, and 1,3,5-tri-t-butylbenzene. The discovery that tungstic acid is an efficient catalyst for the Jacobsen rearrangement can have important applications in organic and industrial chemistry.Nitriles also undergo cyclotrimerization reactions catalyzed by tungstic acid to form cyclotriazenes. The acetonitrile forms acetamide only, dichloroacetonitrile produced the cyclotriazene product in 35 % yield, while trichloroacetonitrile produced the trichloro acetamide almost quantitatively. Cyclotriazenes have numerous applications in industry, medicine, and as herbicides and corrosion inhibitors. They are often produced using highly toxic phosgene making the approach developed in this research highly attractive. Notably the chlorinated cyclotriazenes could readily be converted to other derivatives. Notably they are used to synthesize a useful family of reactive dyes for covalent attachment to cellulosic materials such as paper and cardboard. While a lot of the reactions investigated in this work produced complex mixtures, it is likely that performing reactions under less forcing conditions could increase selectivity. Furthermore, the partially dehydrated phase derived from tungstic acid could be a more reactive catalyst due to Lewis acidic sites opened up by loss of coordinated water from the tungsten ions. Also, this material may better promote trimerization over hydration reactions. The discovery of the reactivity of ketones towards tungstic acid and the Jacobsen rearrangement catalyzed by tungstic acid should be investigated further since they may be quite useful.

CHAPTER III

SYNTHESIS AND CHARACTERIZATION OF VANADIUM OXIDE BRONZE

1. Introduction:

Layered compounds of vanadium have a wide range of applications such as materials for intercalating organic molecules,[128] ion exchange [129], photo-catalysts [5, 6], gas sensors [14], semiconductors and active materials for batteries [32, 33] or electrochromic/electro-optic devices [21, 23, 33]. Bronzes produced from these layered materials, such as hydrogen and sodium vanadium bronzes, are of interest due to the reversible intercalation of protons or alkali ions into the compound producing electronically conducting materials useful for batteries or electrochromic devices. [1, 21, 48] The coloration under ambient conditions associated with the insertion process are useful for electrochromic displays. [21, 32, 33] The structural features of the alkali metal layered compounds (i.e. the negatively charged layers and the exchangeable alkali ions between the layers) make them efficient sorbents for the removal and safe disposal of radioactive cations. Nanofibers of sodium vanadate for instance has been reported to be an efficient sorbent for removal of radioactive $^{137}Cs^{+}$ and $^{85}Sr^{2+}$ cations from water. [130] Previously, molybdenum and tungsten bronzes were reported to be efficient agents for U, Th, Nd, and Pb removal from water. [131, 132] Most recently, in 2015, the capability for molybdenum hydrogen bronze, $H_{0.57}MoO_3$ to remove chromate from aqueous solution via adsorption-reduction processes was reported. [133] Remarkably, utilizing

molybdenum hydrogen bronze materials as colorimetric, reducing, neutralizing reagent for nitro- and peroxo- groups of explosive materials was successfully accomplished by *Apblett. et. al.*, (2006, 2009, 2011, and 2015). [134-137] Vanadium bronzes have been known to be more electrochemically-stable analogues of the molybdenum bronzes. Nevertheless, to the extent of our knowledge, these materials have not been utilized as colorimetric reducing reagents for peroxide based explosives and this will be discussed in chapter 7.

Vanadium bronze materials can be synthesized using several established methods. Hydrogen vanadium bronze, for example; the hydrogen can be inserted at ambient temperature into vanadium pentoxide to form the corresponding hydrogen vanadium bronze through spillover technique using reducing agents such Zn/HCl in solution or hydrogen gas in the presence of a noble metal as a catalyst. [138, 139] Sodium vanadium bronzes are usually synthesized via two main synthetic routes, the sol–gel and the hydrothermal synthesis methods. In the sol-gel route, sodium–vanadium gels are obtained via hydrolysis and condensation of molecular precursors such as vanadates or vanadium alkoxides and then thermal treatment for water removal.[25, 140-142] In the hydrothermal synthesis route, layered sodium vanadium bronzes are produced by hydrothermal treatment of aqueous solutions of vanadyl sulfate and alkali ions.[25, 38, 143] Additionally, using anionic carboxylates as single-source precursors to obtain metal molybdates and vanadates has been demonstrated to be a successful method to produce nanometric materials. [144-147] Previously, a nanoparticulate suspension of molybdenum hydrogen bronze was synthesized through reduction and refluxing MoO_3 with butanol. [135] As a starting point towards utilizing these vanadium bronze materials for catalytic and sensing applications, the primary purpose of this chapter was to report the preparation and the optimization of reaction conditions for proton- or sodium-vanadium bronzes from redox reaction of vanadium pentoxide a variety of reducing agents.

2. Experimental:

2.1. Material

Commercially available reagents of ACS grade or better were used without any further purification. Vanadium (V) oxide, V_2O_5 (99.6 + %) and ammonium metavanadate, NH_4VO_3 (99 %) were obtained from Aldrich Chemical Company, Inc., sodium dithionite, $Na_2S_2O_4$ (83 %) was received from J.T. Baker. Hydrochloric acid, (HCl) was acquired from Phamaco-Aaper. Zinc metal was obtained from Sigma-Aldrich. Sodium standard (1,000 ppm) was purchased from Solutions Plus. Inc,.Water was purified using reverse osmosis and deionization to a resistance of 18MΩ·cm.

2.2. Characterization techniques

Infrared spectra were recorded on a Nicolet Is50 FT-IR spectrometer from 4000–500 cm^{-1}. The X-ray powder diffraction (XRD) patterns were recorded on a Bruker AXS D-8 Advance X-ray powder diffractometer using copper Kα radiation. Crystalline phases were identified using a search/match program and the PDF-2 database of the International Center for Diffraction Data. UV-VIS spectroscopy measurements were recorded using Cary 100-UV/Visible spectroscopy. Sodium compositions were determined by microwave plasma - atomic emission spectrometry using a Agilent 4200 MP-AES instrument. Particle size analysis using dynamic light scattering (DLS) was performed on a Malvern HPPS instrument.

2.3. Synthetic Procedure for Hydrogen Vanadium Bronze via Reduction of Vanadium Pentoxide with Zinc-Hydrochloric Acid

An attempt to synthesize hydrogen vanadium bronze was done by using Zn/HCl reduction in accordance to the method of preparation $Mo_5O_5(OH)_{10}$.[148] Figure 1 shows the apparatus that was used for the reduction of vanadium pentoxide using zinc-hydrochloric acid. A portion of 10.4 g of V_2O_5 and 6 g of zinc granules were added to a 100 ml of distilled water and stirred in 3-neck round bottom flask. Then 40 ml of concentrated HCl was added dropwise carefully. Hydrogen gas bubbles were produced as byproducts. The Zn and HCl were in a ratio to ensure complete

dissolution of Zn metal and formation of reduced vanadium bronze species. Initially the color was blue then it slowly transformed to a green color and finally to a brown color. To ensure the reaction completion, the reaction solution was kept overnight. The resulting brownish green solid was collected and further washed three times with a 200 ml water each and then dried in vacuum. The yield of the hydrogen vanadium bronze product was 9.34 g (89.81%).

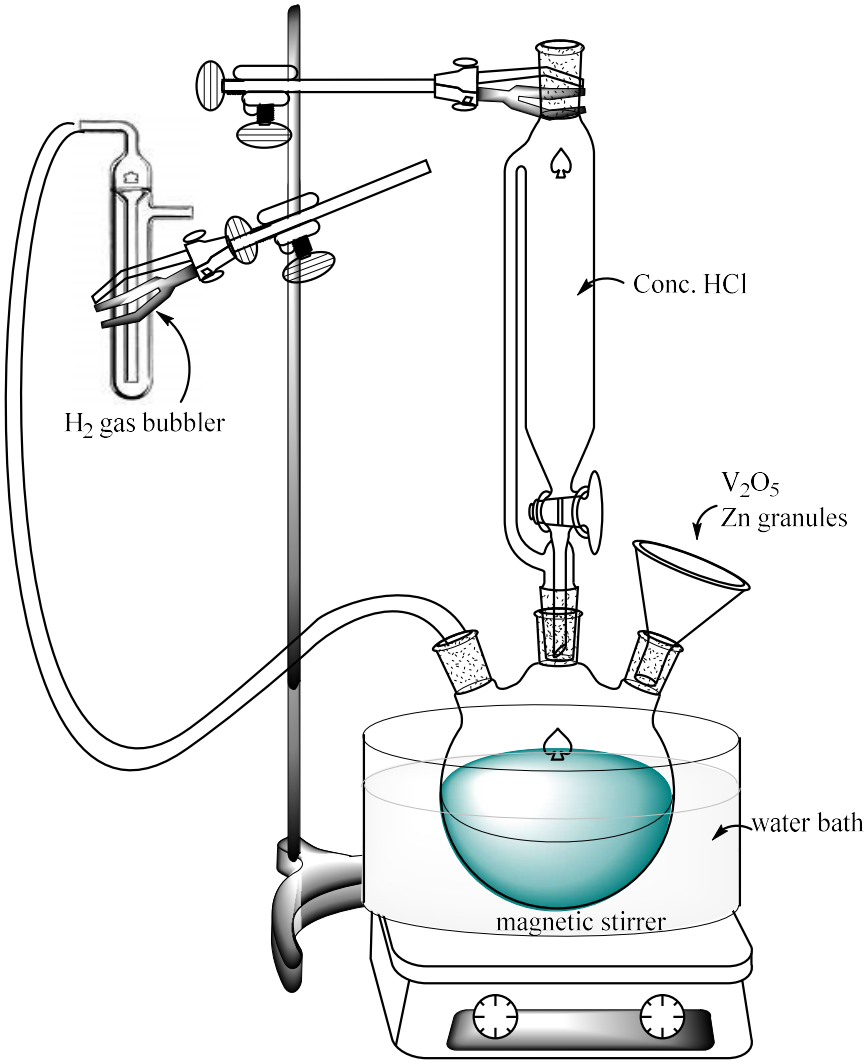

Figure 3- 1.The applied apparatus used in the reduction of vanadium pentoxide using zinc-hydrochloric acid

2.4. Synthetic procedure of Sodium Vanadium Bronze via a Reduction of Vanadium Pentoxide with Sodium Dithionite

Sodium vanadium bronze was synthesized by the reduction of vanadium pentoxide with sodium dithionite. Sodium dithionite was assayed using ion chromatography and found to be 83 % as described by *Materer et.al*, 2012. [149] Vanadium pentoxide was stirred in 125 ml of deionized water and sodium dithionite was added to the vanadium suspension. The color of solution changed immediately from yellow to green to dark blue depending on the amount of sodium dithionite used (see Figure 2). To ensure completion, the reaction was stirred for three days. The precipitate was subsequently centrifuged and the resulting solid was washed with water until the filtrate was clear. The resulting products were then dried under vacuum overnight.

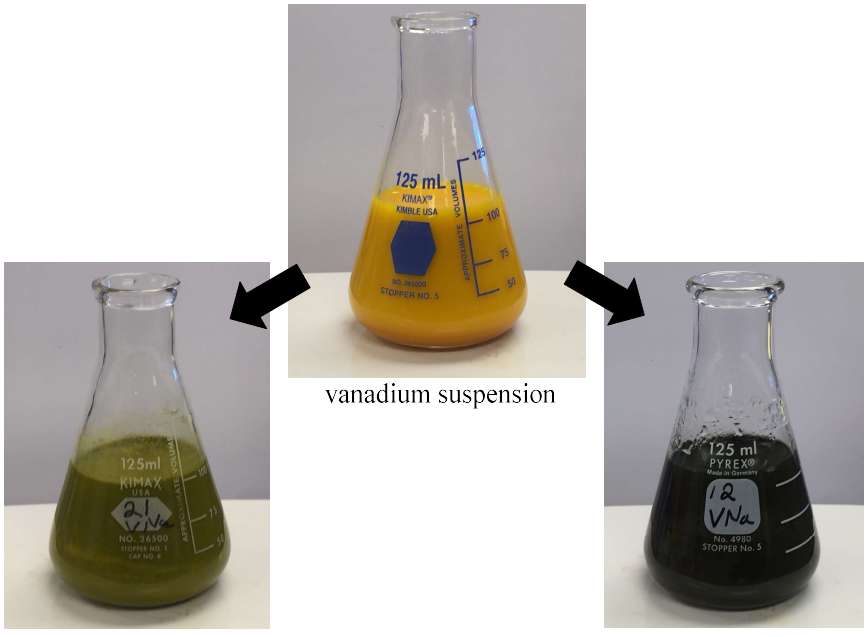

vanadium suspension

green dark blue

Figure 3- 2. Changing color of vanadium suspension by adding varying quantities of sodium dithionite

2.5.Synthetic procedure for Sodium Vanadium Bronze via a Reduction of a Colloidal Suspension of Vanadium Pentoxide with Sodium Dithionite

The colloidal suspension of vanadium pentoxide nanoparticles was synthesized according to method of Biltz with some modifications. [150] Two grams of ammonium metavanadate (NH_4VO_3) was grounds with some water to make a paste. Then 20 ml of 2N hydrochloric acid were added while stirring with a pestle. Once a red precipitate had formed it was filtered and washed with water. The precipitate was then transferred to an Erlenmeyer flask and the volume was adjusted to 200 ml so that the precipitate dispersed to form a red colloidal suspension of vanadium pentoxide nanoparticles. Colloidal solutions of sodium vanadium bronze were synthesized through the reaction of this suspension with sodium dithionite at room temperature. A blue-green jelly piece formed immediately upon adding the sodium dithionite but with continued stirring the gel redispersed to give a stable dark green or blue suspension. The changes of color from red to a dark green and dark blue depended on the amount of sodium dithionite reducing agent (see Figure 3).

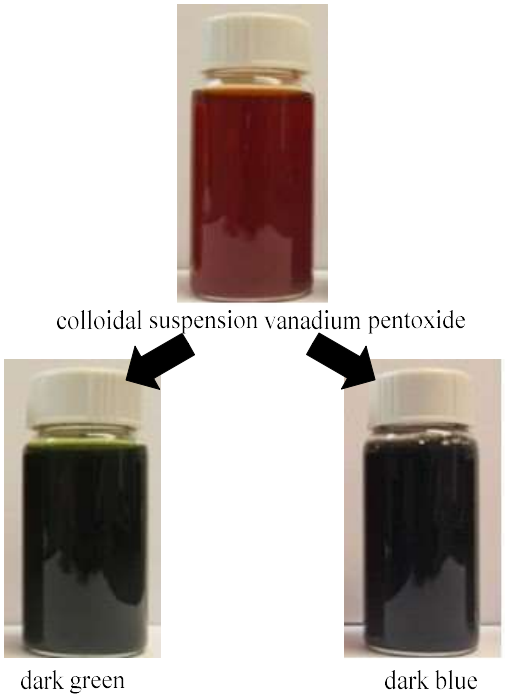

Figure 3- 3.Changing color of colloidal vanadium suspension by adding sodium dithionite

2.6.Determination of Reducing Equivalents by Iodometry

The determination of reducing equivalents of the solid bronze materials was performed using iodometry. Approximately a 0.025 mg of the materials and 10 ml of a 0.01N iodine solution were reacted in scintillation vials and agitated for 2 days in the dark. Triplicate reactions were made for each bronze sample to determine the experimental error. The solutions were filtered through 0.45µm PTFE syringe filter and the residual iodine was determined by UV-VIS absorbance spectroscopy using a Cary 100 Bio UV-Visible spectrophotometer. The absorbance of the iodine solutions was measured at 460 nm in a 1 cm path length cuvette. A calibration curve was made using four different concentrations of iodine solution (Figure 4) The experimental data to determine the reducing equivalents is summarized in Table 1.

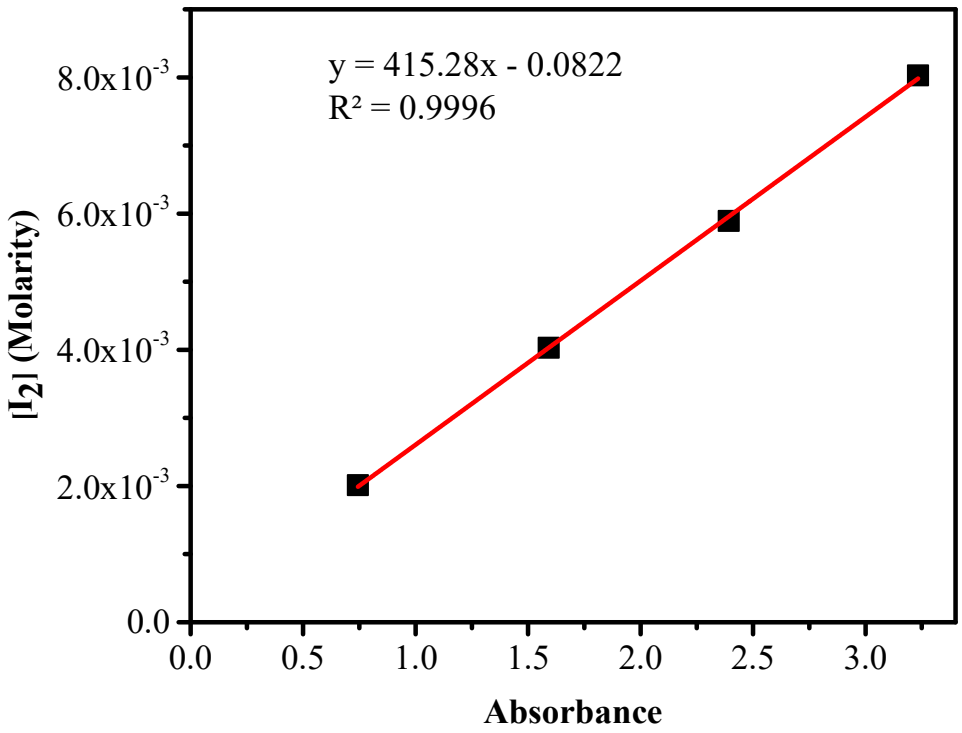

Figure 3- 4. Calibration curve for $[I_2]$ obtained using UV-Visible spectroscopy

Table 3- 1. Determination of reducing equivalents of bronze generated via reduction of iodine

Mole ratio $Na_2S_2O_4/V_2O_5$	Bronze Amount (mg)	$[I_2]$ Solution Volume (ml)	Initial $[I_2]$, (mM)	Final $[I_2]$, (mM)	$[I^-]$, (mM)	Reducing equivalents (mmol)	Reducing equivalents per gram of bronze (mmol/g)
0.17	25	10.69	10	4	6	12	480
0.17	25	10.10	10	3	7	14	560
0.17	25	10.11	10	3	7	14	560
0.25	25	10.06	10	5	5	10	400
0.25	26	10.53	10	5	5	10	385
0.25	26	10.07	10	4	6	12	462
0.50	27	10.06	10	6	4	8	296
0.50	25	10.00	10	7	3	6	240
0.50	27	10.02	10	5	5	10	370

2.7.Determination of Sodium Content

The sodium contents of the bronze materials were determined via microwave plasma-atomic emission spectrometry using an Agilent 4200 MP-AES instrument. To calibrate the instrument, four different concentrations were prepared using a 1000 ppm sodium standard (Solutions Plus. Inc.). The calibration curve was reproduced from the MP-AES as shown in Figure 5. Samples were prepared by dissolving them into a 2% HCl solution. The resulting data are presented in Table 2.

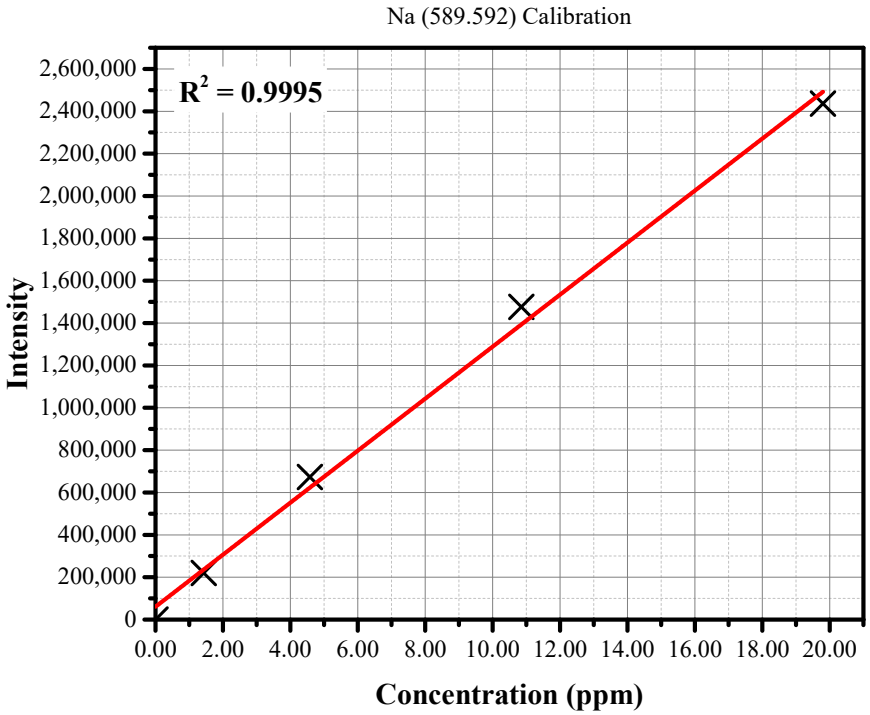

Figure 3- 5. Calibration curve for [Na] reproduced from MP-AES

Table 3- 2. Determination the sodium content of bronze

Mole ratio $Na_2S_2O_4/V_2O_5$	Amount of Bronze (mg)	Solution of 2% HCl (g)	[Na] ppm(mg/l)	mol Na/ mol V_2O_5
0.166	6.000	20.241	4.370	0.117
0.166	7.000	20.067	4.630	0.105
0.166	7.000	20.109	4.530	0.103
0.250	5.000	20.130	4.000	0.127
0.250	6.000	20.148	4.660	0.124
0.250	6.000	20.143	4.460	0.118
0.499	6.000	20.099	5.310	0.141
0.499	6.000	20.038	5.090	0.134
0.499	7.000	20.003	6.030	0.136

3. Results and discussion:

Hydrogen vanadium bronze was synthesized by using Zn/HCl reduction method and characterized as discussed in experimental section. The hydrogen vanadium bronze product was obtained in 89.81% in yield. The loss of hydrogen vanadium product could be as a result of the

solubility of hydrogen bronzes in the hydrochloric acid solution. [151] The reduction of vanadium pentoxide using zinc-hydrochloric acid are presented in Equation 1 and 2.

$$Zn^{o}_{(s)} + H^{+}_{(aq)} \rightarrow H_{(atom)} \qquad \text{Equation 1}$$

$$H_{(atom)} + V_2O_5 \rightarrow H_xV_2O_5 \qquad \text{Equation 2}$$

Hydrogen can be intercalated into vanadium pentoxide lattice either by bonding to vanadium atom forming a hydride bond or by bonding to oxygen forming either –OH or $–OH_2$ groups. Both possibilities can be distinguished by FTIR spectroscopy analysis. [139, 152, 153] Figure 6 shows a comparison between the FTIR spectra of vanadium pentoxide and the hydrogen vanadium bronze. As observed, the characteristic bands of V=O and V-O-V bonds have slightly shifted in comparison to the starting material. Although there was no absorption for an O-H stretching vibration mode at about 3400 cm^{-1}, the absence of any bands between 1060 and 1200 cm^{-1} and the formation of a new band at 1625 cm^{-1} were evidence for hydrogen bonding to oxygen and not to vanadium in agreement with reference [139]. The material was heated in a muffle furnace in air for 12 hours to determine the ceramic yield and it was found to be 99.3 %. The weight loss could be result of both dehydration and dehydroxylation of the hydrogen vanadium bronze. The bronze was analyzed by X-ray diffraction and the pattern is shown in Figure 7. It has been established that the higher hydrogen contents lead to formation of amorphous bronzes and the lower hydrogen content lead to a small change in lattice parameters of vanadium pentoxide.[153] The XRD pattern of the obtained bronze matched mainly with crystalline orthorhombic vanadium pentoxide with a negligible shifts which is expected for lower hydrogen content.[153] Two small peaks were detected that may be due to formation of sodium vanadium bronze. This phase may form due to sodium traces present in the system as a result of impurities in the original solution and the glassware. Determination of the sodium content was performed using a Jenway PFP7 Flame Photometer and was found to be 0.039 of Na per mole of V_2O_5.

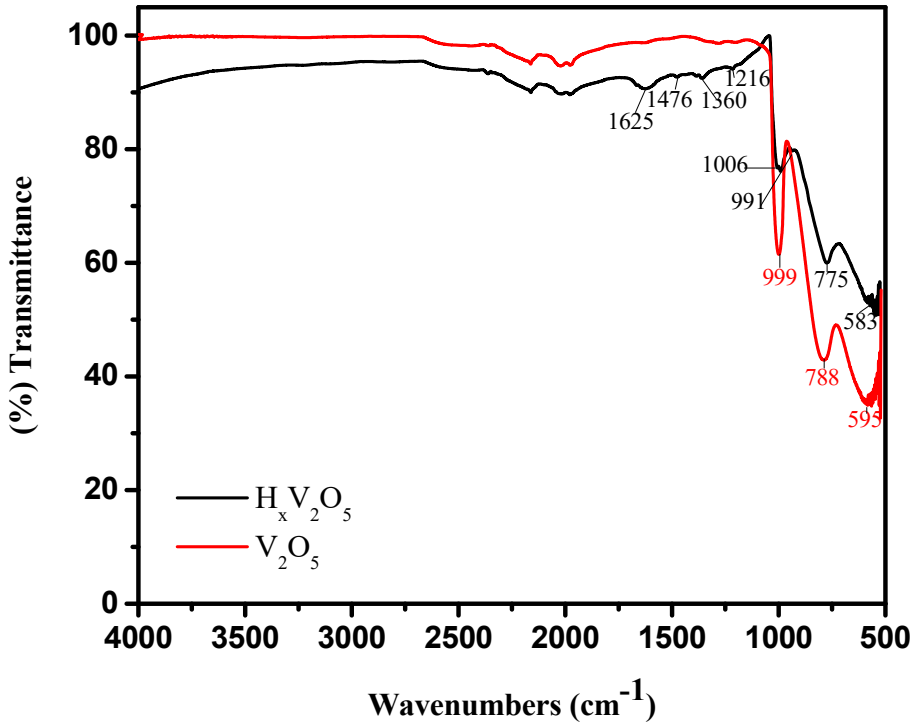

Figure 3- 6. FTIR spectra of vanadium pentoxide and the hydrogen vanadium bronze product

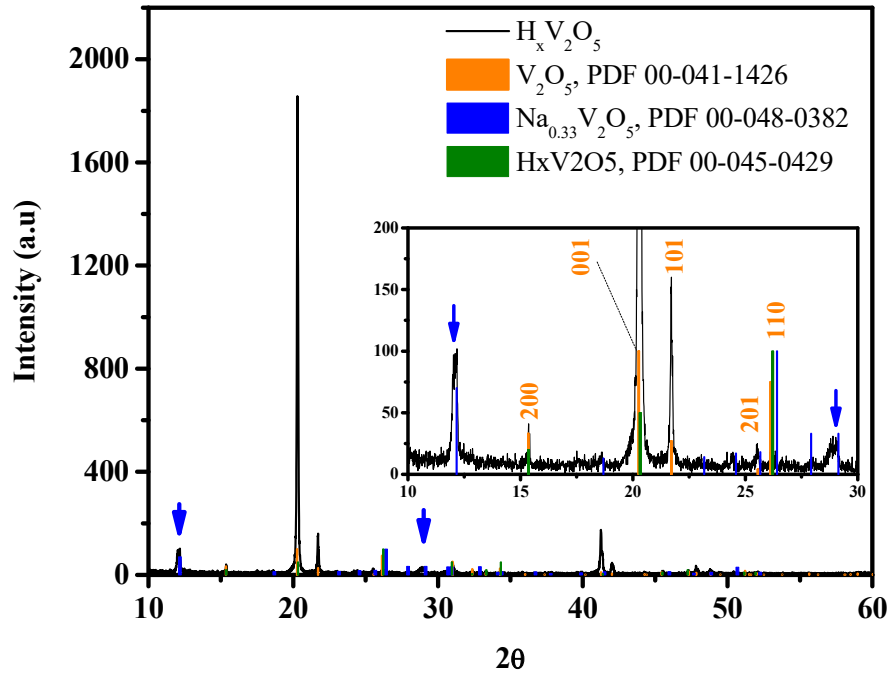

Figure 3- 7. XRD pattern for the hydrogen vanadium bronze

An attempt to synthesize hydrogen bronze was also pursued via using sodium dithionite as a highly soluble strong reducing agent. Varying stoichiometries of sodium dithionite were added

to vanadium pentoxide suspensions. Table 3 summarized the data for pH, filtrate color, product amount and yields for the reduction reaction performed at room temperature for 3 days. Notice that the stoichiometric ratio is defined on the basis of reaction of $Na_2S_2O_4/V_2O_5$ molar ratio (Scheme 1). The observed colors of the reduction reaction are visually different for each molar ratio. These differences reflect the complexity of the reduction reaction associated with proton or sodium insertions to form different vanadium oxide bronzes.[154]

The colors of the resulting solid products are shown in Figure 8. The color variation can be the result of many factors such as: the acid hydrolysis and disproportionation of dithionite, [155] the pH dependence of various vanadium complex species, and the oxidation-reduction potential of vanadium and dithionite ions. [156] The effect of the dithionite to vanadium stoichiometric ratio on the pH and the resulting bronze yield were analyzed and are graphically represented in the 3D surface plot shown in Figure 9.

Table 3- 3. Summary of reactions ratio, pH, filtrate solution color, amount of bronze, and yield for vanadium pentoxide reduction with sodium dithionite at room temperature for 3 days

Mole ratio of $Na_2S_2O_4/V_2O_5$	pH	Filtrate Solution Color	Amount of Bronze (g)	Bronze Yield (%)
0.000	5.50	Yellowish orange	0.000	0.0
0.166	5.32	Blue	1.718	94.0
0.250	4.27	Dark blue	1.699	92.9
0.499	3.90	Dark greenish blue	1.645	90.0
0.999	4.12	Dark greenish blue	1.418	77.6
1.999	4.56	Dark greenish blue	1.034	56.6
3.998	5.18	Dark green	0.590	32.3
5.998	5.02	Bright Yellow	0.200	10.9

Reduction: $V_2O_{5(aq)} + nH^+_{(aq)} + 2e^- \longrightarrow H_nV_2O_{5(s)}$

Oxidation: $S_2O_4^{2-}{}_{(aq)} + 4H_2O_{(l)} \longrightarrow 2HSO_4^-{}_{(aq)} + 8H^+_{(aq)} + 6e^-$

Overall Reaction: $3V_2O_{5(aq)} + Na_2S_2O_{4(aq)} + 4H_2O_{(l)} \longrightarrow 3H_nV_2O_{5(s)} + 2HSO_4^-{}_{(aq)} + (8-3n)H^+_{(aq)}$

Scheme 3- 1. Summary of the reactions for synthesis of vanadium bronze was via reduction with sodium dithionite in a non-buffered aqueous system

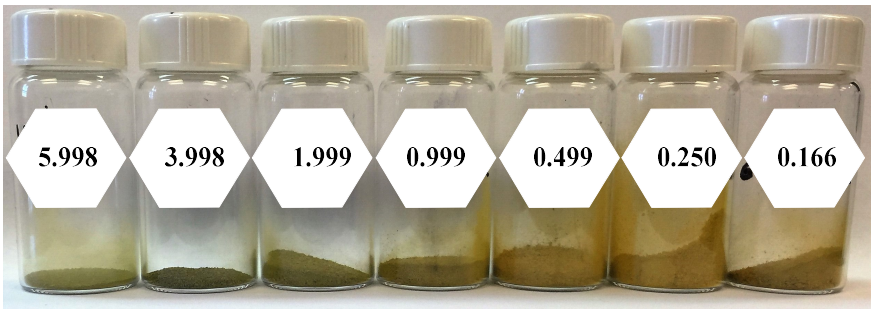

Figure 3- 8. Color change of resulting product with changing $Na_2S_2O_4/V_2O_5$ mole ratio

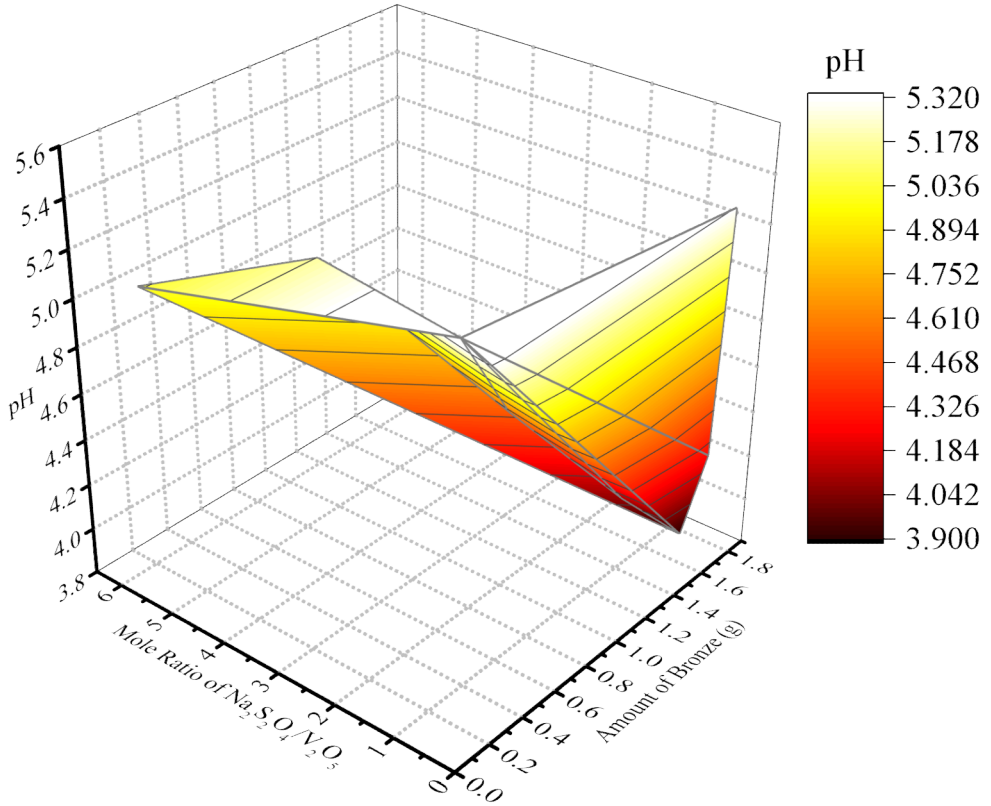

Figure 3- 9. Surface Plot of mole ratio of $Na_2S_2O_4/V_2O_5$ vs pH vs. bronze product yield

The change in pH as a function of mole ratio is shown in Figure 10, and the yield as a function of the mole ratio is shown in Figure 11. The pH data and determined yield indicate that the reaction proceeded through three different trends as the molar ratios changed. In the first trend, pH and yields decreased as the ratio increased. During the second one, the pH increased and yields decreased as the ratio increased while in the third one, little effect of ratio on the pH was observed but the product amount significantly decreased. The chemistry of vanadium in aqueous media known to be complicated since it is affected both by pH and concentration. [156] The first observed trend could be explained by the fact that the more dithionite amount is added to vanadium suspension, the higher the extent of reduction of V(5+) to V(4+) in the solid phase and the higher the release of protons into the liquid phase making the solution more acidic according to Scheme 1. Since vanadium bronze is soluble in acidic media, increasing the reaction mixture acidity result in increasing the solubility of the product, thus reducing. The other observed trends tend to be more complex due to several competitive reactions took place together. Although the reduction of V(5+) is expected to be completed upon the addition of excess dithionite, it accelerates the catalytic reactions of dithionite decomposition to produce thiosulfates, bisulfite, and sulfur. The formation of sulfur was established by visual inspection of the milky appearance (Scheme 2). [157]

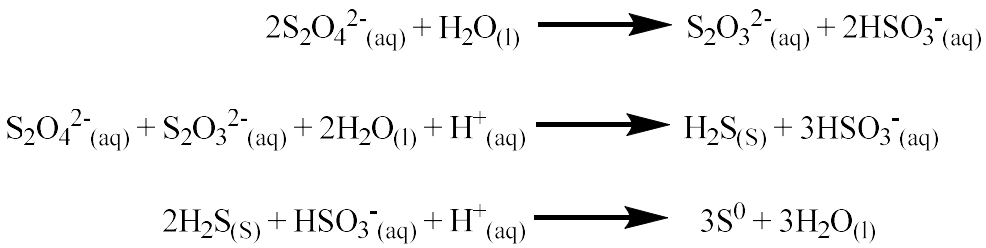

Scheme 3- 2.Summarized the overall equations of acid hydrolysis and disproportionation of dithionite competing reactions

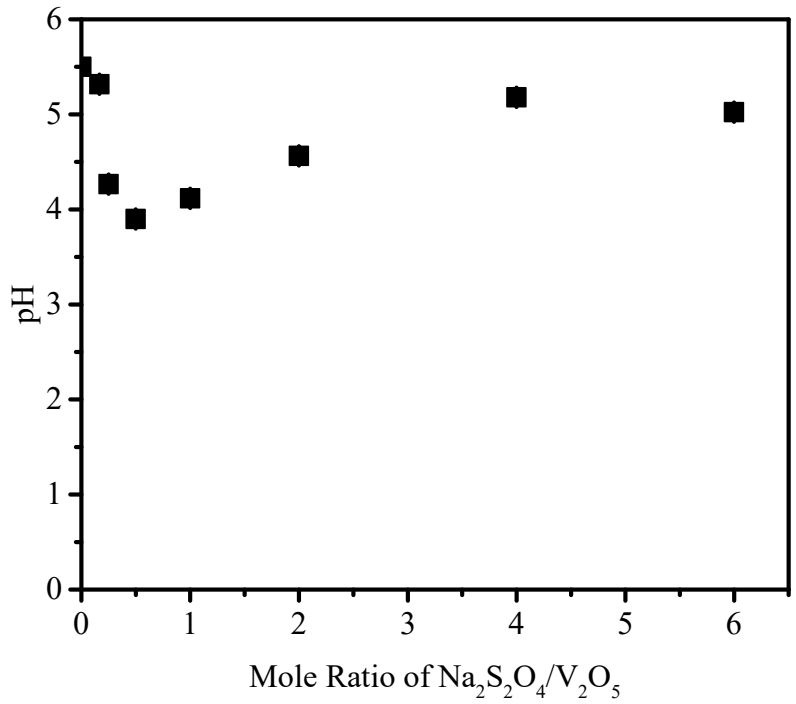

Figure 3- 10. The stoichiometric effect of dithionite to vanadium pentoxide ratio on pH

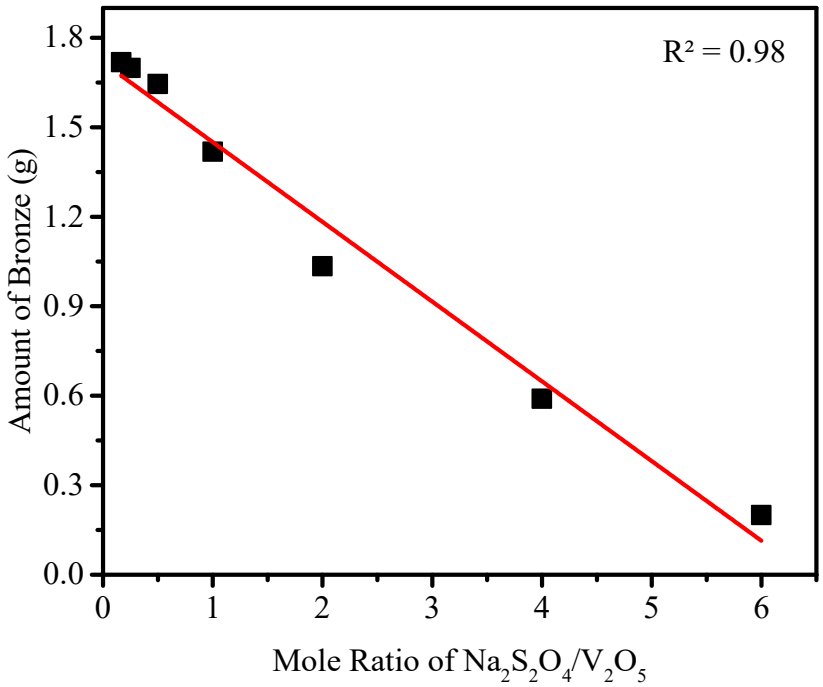

Figure 3- 11. The effect of the dithionite to vanadium stoichiometric ratio on the resulting bronze yield

The resulting solid vanadium bronze product from using (1.00 V_2O_5:0.166 $Na_2S_2O_4$) ratio was characterized using FTIR spectroscopy, and the resulting spectrum is compared to the starting materials as shown in Figure 12. The spectrum of the bronze product is similar to that of vanadium pentoxide. The bands correspond to V=O and V-O-V vibration were slightly shifted and become stronger in the case of the bronze product. This could be the result of the V^{5+} reduction and the incorporation of either sodium or protons into the oxide bronze lattice.[153, 154, 158] There were also broad absorption bands at 3380 and 1625 cm^{-1} attributed to O-H stretching and bending vibrations confirming the presence of water or hydroxyl ions in the vanadium oxide lattice. The FTIR spectra of the bronze solids synthesized with different ratios are presented in Figure 13. Most of the spectra are similar to each other and as higher amounts of dithionite were used in the reduction reaction, the more the intensity of the O-H bands were lowered due to sodium insertion instead of proton insertion. Table 4 shows a comparison of the product yields, pH, reducing equivalents per gram of bronze, and sodium content of the product obtained by reduction reaction of vanadium pentoxide with different ratios of sodium dithionite. As shown, despite the remarkably high yield for the different ratios, as the amount of dithionite increased the lower the yield suggesting loss of vanadium as a vanadyl ion. However, the molar equivalents of sodium in the materials depended on reducing agent amount and were determined. The results suggest the formation of a mixed sodium and proton vanadium bronze since the reducing equivalents are significantly higher than the amount of sodium present.

Further, the materials were characterized by XRD, and were found to match with the pattern of standard crystalline vanadium pentoxide phase with orthorhombic structure (ICDD database PDF No. 00-039-0634) as shown in Figure 14. It has been established that the lower hydrogen content of the green phase of $H_xV_2O_5$ is closely related structurally to V_2O_5 and the higher hydrogen contents lead to formation of amorphous products. [153] A closer look at the XRD patterns of the green products, for example the 1.00 V_2O_5:0.499 $Na_2S_2O_4$ ratio (Figure 15) shows that the

diffraction pattern of the products have peaks that are close to those of vanadium pentoxide, and there are also several peaks that could corresponds to sodium or hydrogen bronzes.

Table 3- 4. Comparison of the product yields, pH, reducing equivalents per gram of bronze, and sodium content of product obtained by reduction reaction of vanadium pentoxide with different ratio of sodium dithionite

Mole ratio $Na_2S_2O_4/V_2O_5$	Yield (%)	pH	Reducing equivalents per gram of bronze (%)	mol Na/ mol V_2O_5
0.166	94.0	5.32	0.822±0.045	0.108±0.007
0.250	92.9	4.27	0.636±0.053	0.123±0.005
0.499	90.0	3.9	0.455±0.099	0.137±0.003

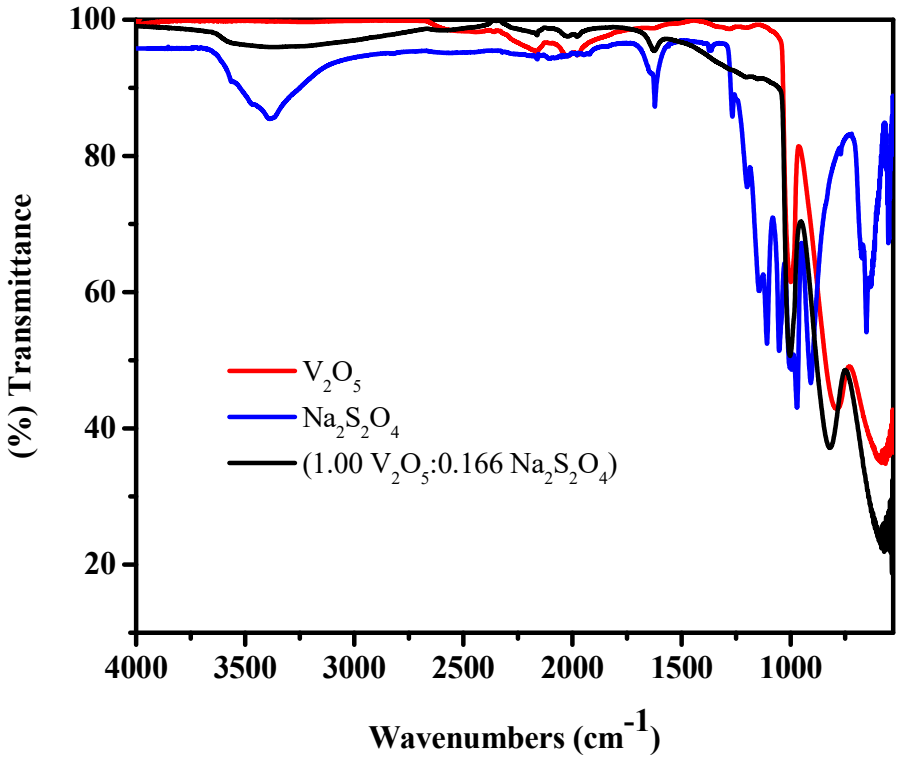

Figure 3- 12. FT-IR spectrum of the obtained $M_xV_2O_5$ solid using $1V_2O_5$:0.166 $Na_2S_2O_4$ ratio, with comparison to spectra of V_2O_5 and $Na_2S_2O_4$

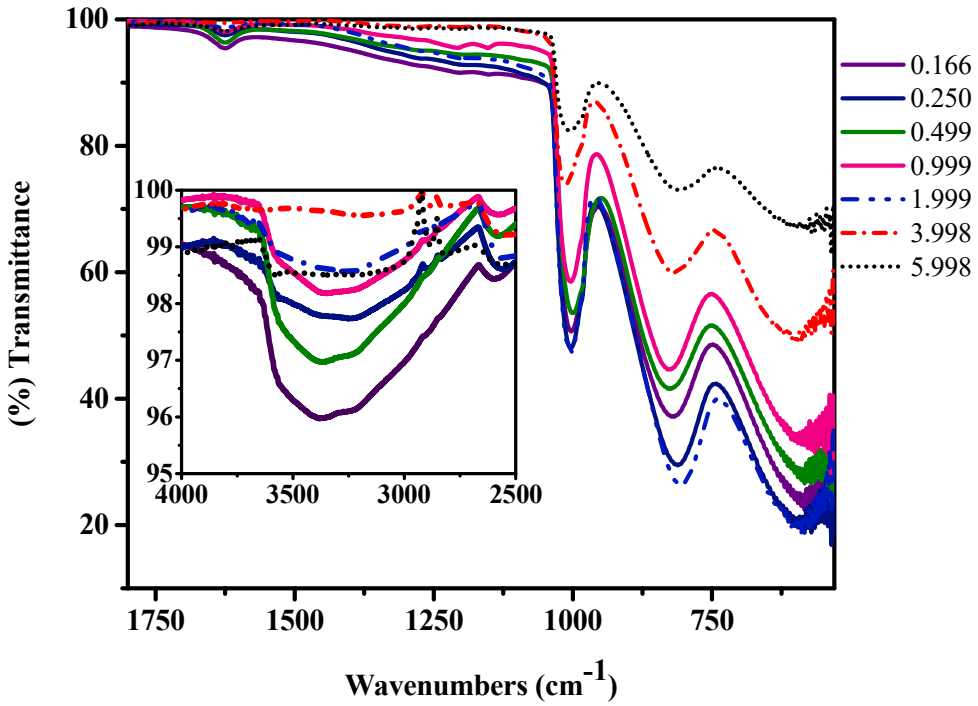

Figure 3- 13. FT-IR spectra of $M_xV_2O_5$ synthesized with different ratios of V_2O_5 and $Na_2S_2O_4$

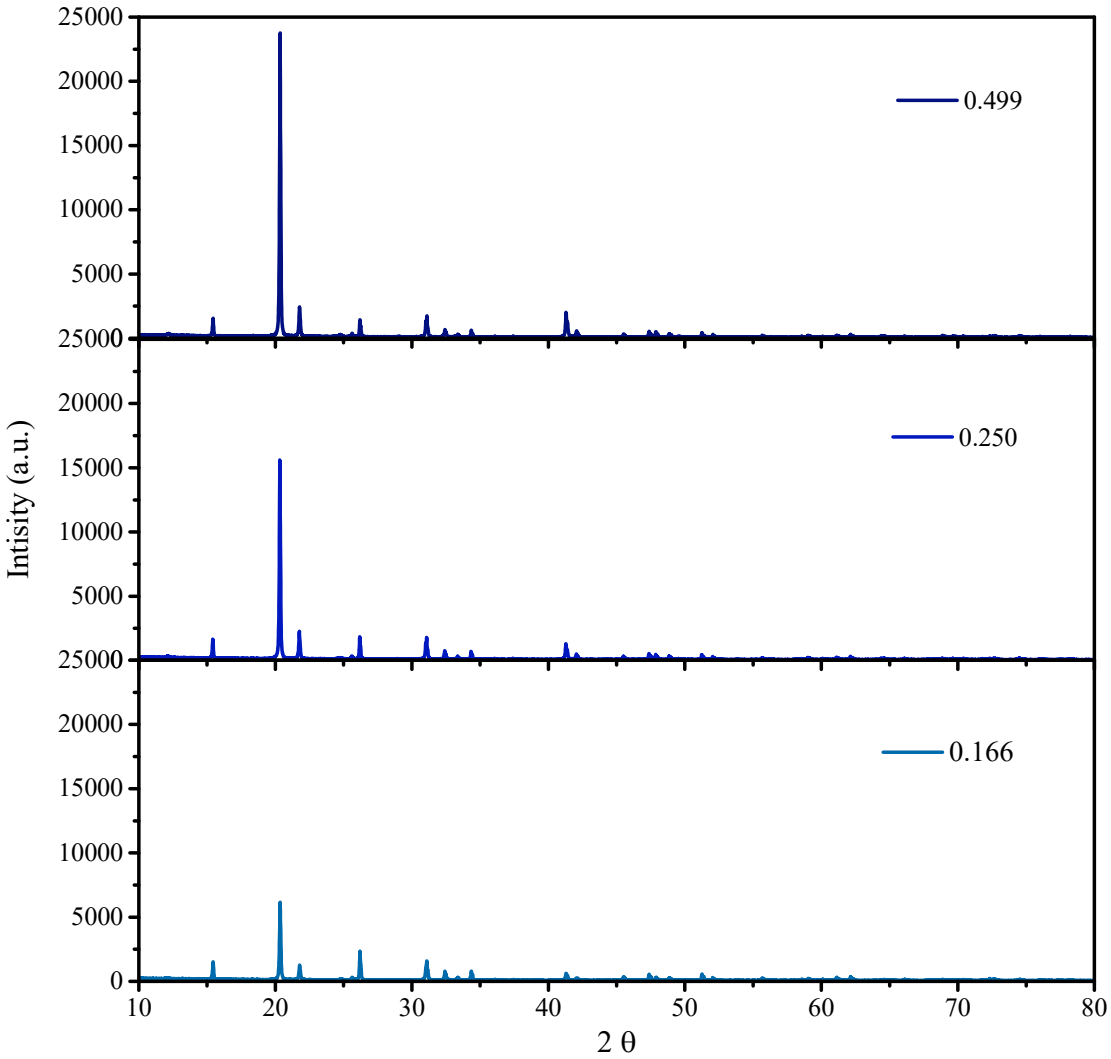

Figure 3- 14. XRD patterns for $M_xV_2O_5$ synthesized with different ratios of V_2O_5 and $Na_2S_2O_4$

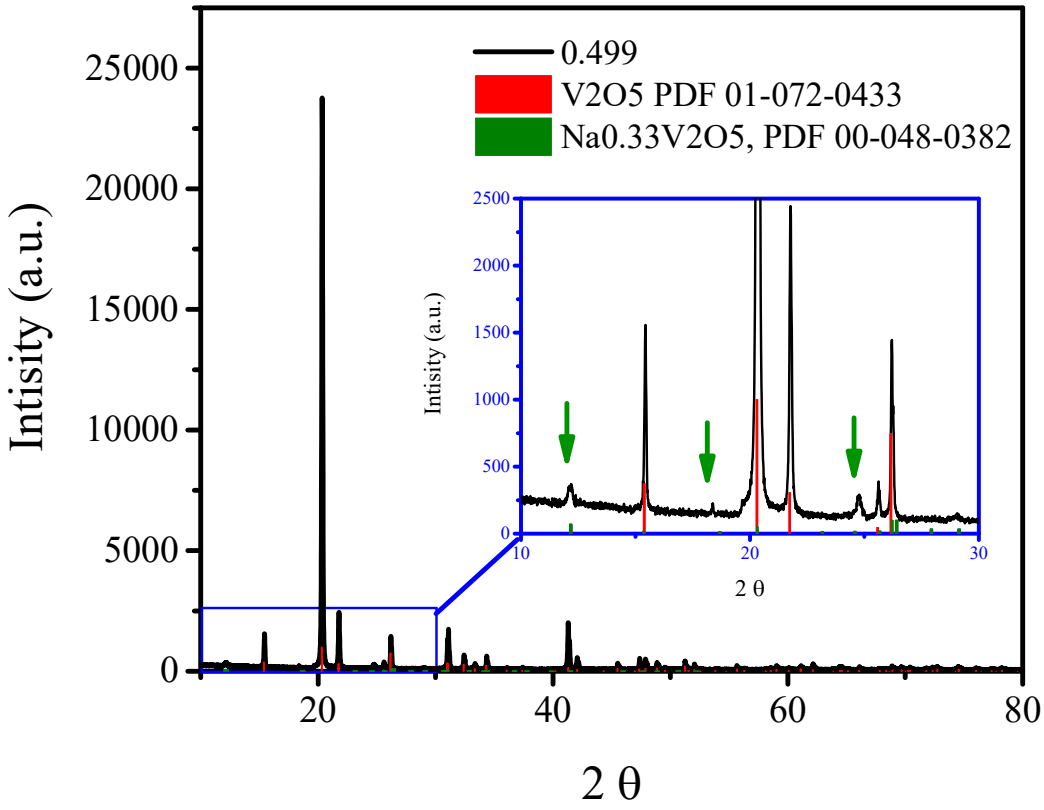

Figure 3- 15. XRD pattern for bronze product synthesized with ratio of $1V_2O_5$: 0.499 $Na_2S_2O_4$

The reduction reactions of the colloidal suspensions were performed with same varying ratios of sodium dithionite to V_2O_5 as was used for the bulk materials. The mole ratios used, pH, and the solution mixture color are tabulated in Table 5. The color of the resulting colloidal bronze suspensions varies with changing mole ratio as seen in Figure 16. The colloidal suspensions were not stable for long and within two weeks the solids aggregated and precipitated.

Plotting the pH data as function of mole ratio (Figure 17) shows that the pH of the colloidal suspensions increased as the sodium dithionite amount increased until a plateau above which little change was observed indicating attainment of the maximum in reducing capacity. The UV-Visible spectra of the suspensions are exhibited in Figure 18. The dark bluish-green colloidal bronze prepared with a $1V_2O_5$:0.166 $Na_2S_2O_4$ ratio displayed characteristic bands for d^1 electron configuration transitions from the $^2T_2$ ground state to ^2E excited state of V^{4+}.[159] The UV-VIS

spectra also show that the more dithionite used, the more [V^{4+}] present up to the ratio of 1 V_2O_5 to 0.993 $Na_2S_2O_4$. The absorbances of the UV-VIS bands for V^{4+} decreased as dithionite was added beyond this point. This was accompanied by the formation of a milky phase believed to be due to formation of sulfur as result of acid hydrolysis and disproportionation of the unreacted dithionite.[155] Notably a new band at 440 nm corresponding to V^{3+} was observed.[159-161] All of these bands disappeared when the 1 V_2O_5 to 5.991 $Na_2S_2O_4$ molar ratio was used.

Dynamic light scattering (DLS) analysis was used to measure the particle size distribution for colloidal suspensions as shown in Figure 19. The particle size distribution of colloidal vanadium pentoxide prior to reduction reaction was a single peak centered around 0.980 nm. Once dithionite was added the particle size grew growth significantly with each increment in the amount of dithionite added. Furthermore, the size distributions became wider and additional peaks at large particle size appeared as aggregation took place. At the highest amounts of this reagent, the particle size distributions were dominated by the high number of very large sulfur particles.

The colloidal bronze materials with reaction ratios less than 1 were dried at room temperature to form very brittle films. The FTIR spectra of these films, shown in Figure 20, were similar to those of the bronzes synthesized from reduction of bulk vanadium pentoxide with sodium dithionite, i.e. the spectra displayed the slightly shifts of the characteristics bands of OH, V=O, and V-O-V vibration in comparison to the original starting vanadium pentoxide material. The higher the ratio, the stronger the bands of the V-O lattice vibrations.

The XRD patterns of the films were also recorded and are shown in Figure 21. The patterns did not match well with any known phases and thus may be either the sodium or hydrogen vanadium bronze, a mixture of the two, or more likely a mixed sodium/hydrogen bronze. Since sodium bronze considered more soluble than hydrogen bronze, the colloidal suspensions were filtered and washed with distilled water. XRD patterns of these purified materials match to mixtures of vanadium pentoxide and hydrogen bronze material as exhibited in Figure 22.

Table 3- 5. Summary of mole ratio, color, and the pH of the obtained solutions for the reduction reactions of colloidal vanadium pentoxide with sodium dithionite at room temperature

Colloidal V_2O_5 (g)	$Na_2S_2O_4$ (g)	Mole ratio	Color once mixing	pH	Color for phase precipitate after two weeks	Yield (%)
20.000	0.000	0.000	Red*	3.40	Orange	99.4
20.041	0.030	0.166	Dark bluish green	5.00	Dark green	97.4
20.027	0.045	0.249	Dark bluish green	4.70	Dark green	70.3
20.069	0.090	0.498	Dark blue	5.10	Dark green	61.3
20.142	0.179	0.993	Dark bluish green	5.90	Mixture of dark color with light milky phases	49.0
20.159	0.359	1.984	Blackish green	5.80	Mixture of lighter dark color with light milky phases	33.5
20.044	0.717	3.991	Black	5.70	Mixture of light blue color with light milky phases	25.8
20.028	1.076	5.991	Black	5.70	Mixture of lighter green and milky color phases	12.9

* The red color remains the same if suspension storage in closed Nalgene bottle for a year, but if it exposed to air it turns to yellowish orange yellowish and precipitates within 2-3 weeks

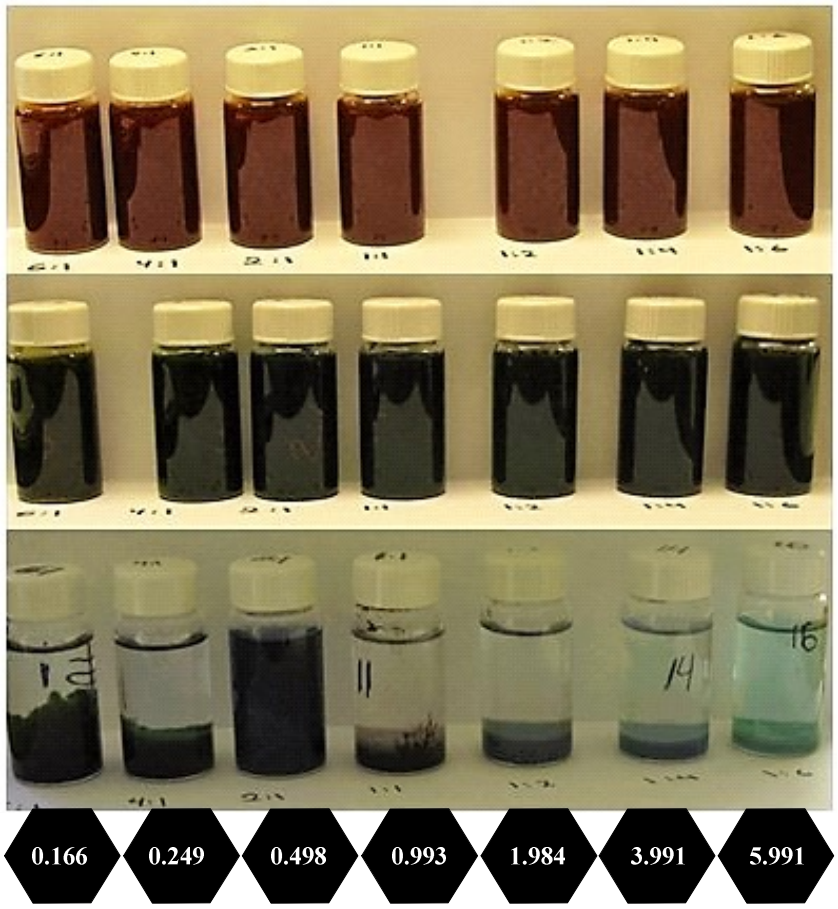

Figure 3- 16. Color change of resulting colloidal bronze suspensions with changing $Na_2S_2O_4/V_2O_5$ mole ratio

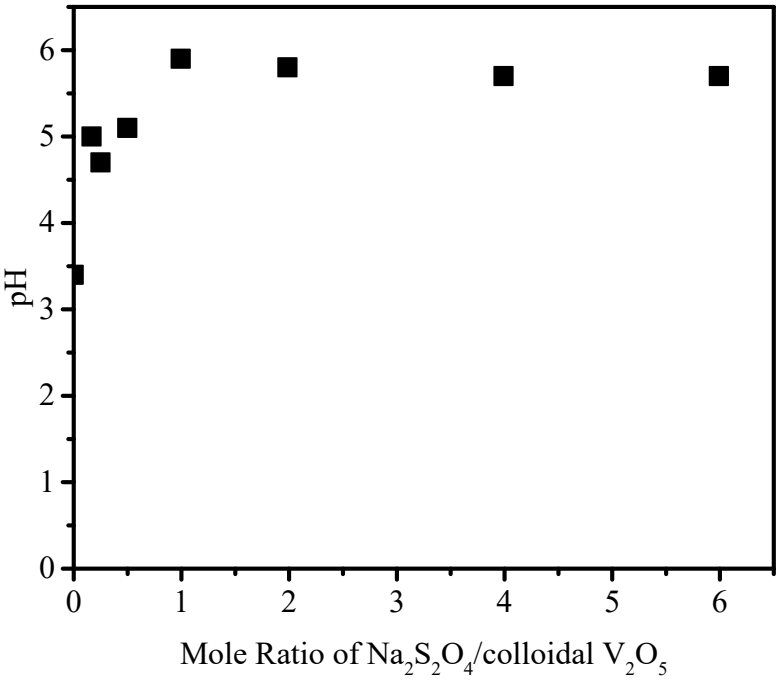

Figure 3- 17. The effect of stoichiometric ratio of sodium dithionite to colloidal vanadium pentoxide on the pH

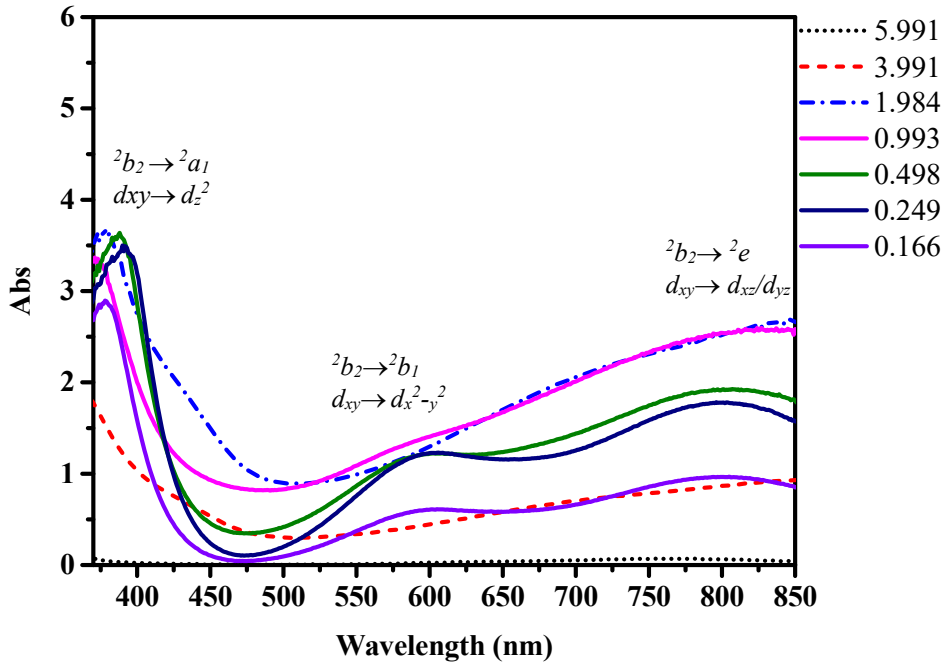

Figure 3- 18. The UV-VIS spectra of the colloidal bronze suspensions

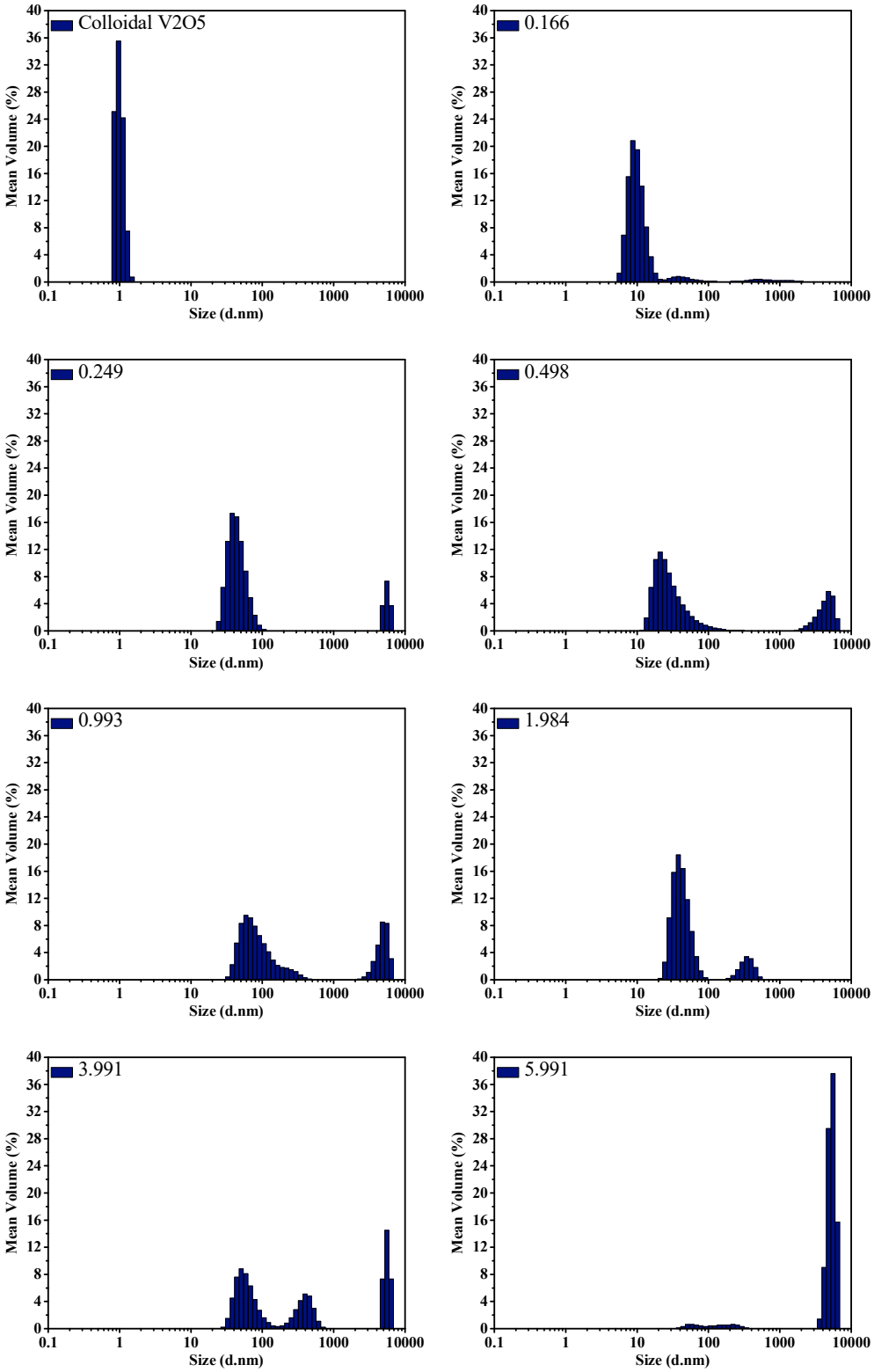

Figure 3- 19. DLS analysis for colloidal suspension of V_2O_5 and obtained colloidal after sodium dithionite reduction

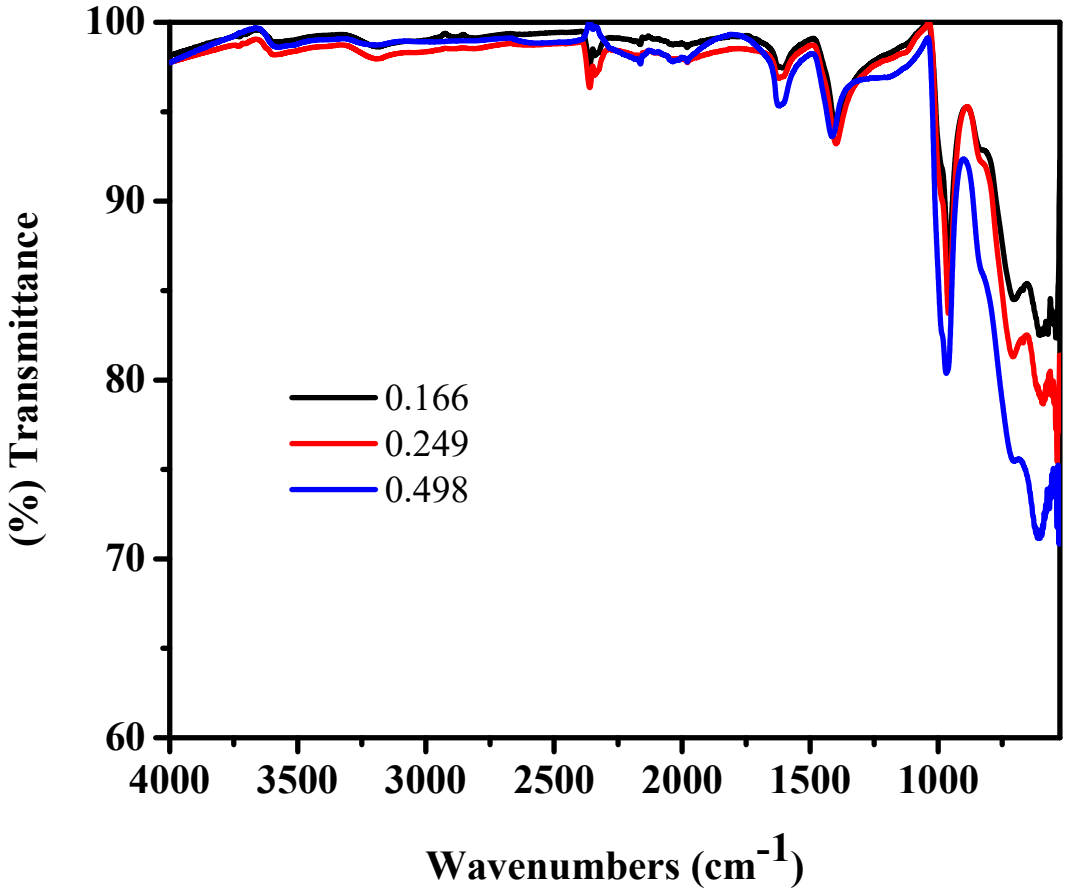

Figure 3- 20. FT-IR spectra of the dried brittle films of $M_xV_2O_5$ synthesized with different ratio of colloidal V_2O_5 and $Na_2S_2O_4$

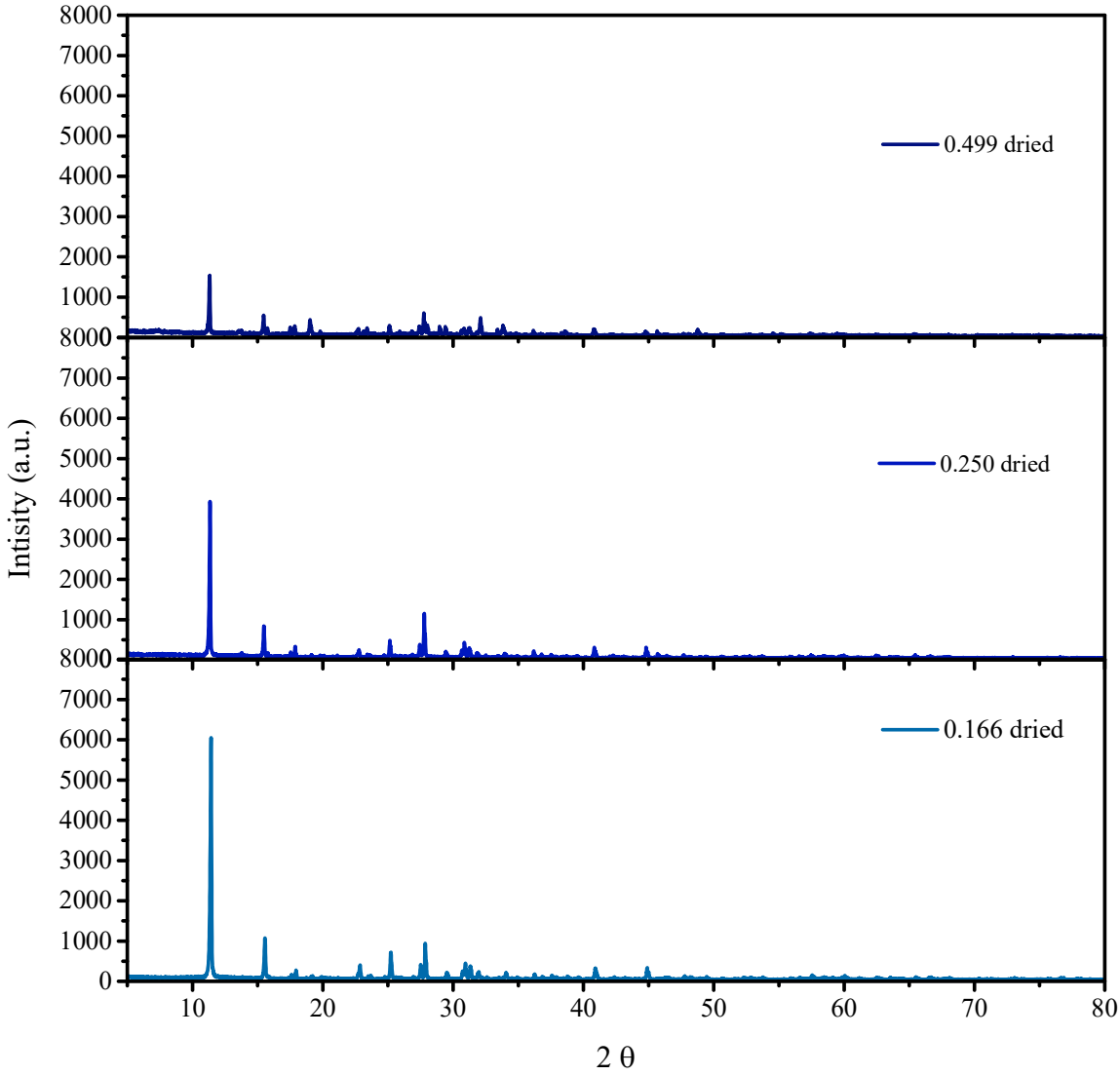

Figure 3- 21. XRD patterns for dried brittle films of $M_xV_2O_5$ synthesized with different ratio of colloidal V_2O_5 and $Na_2S_2O_4$

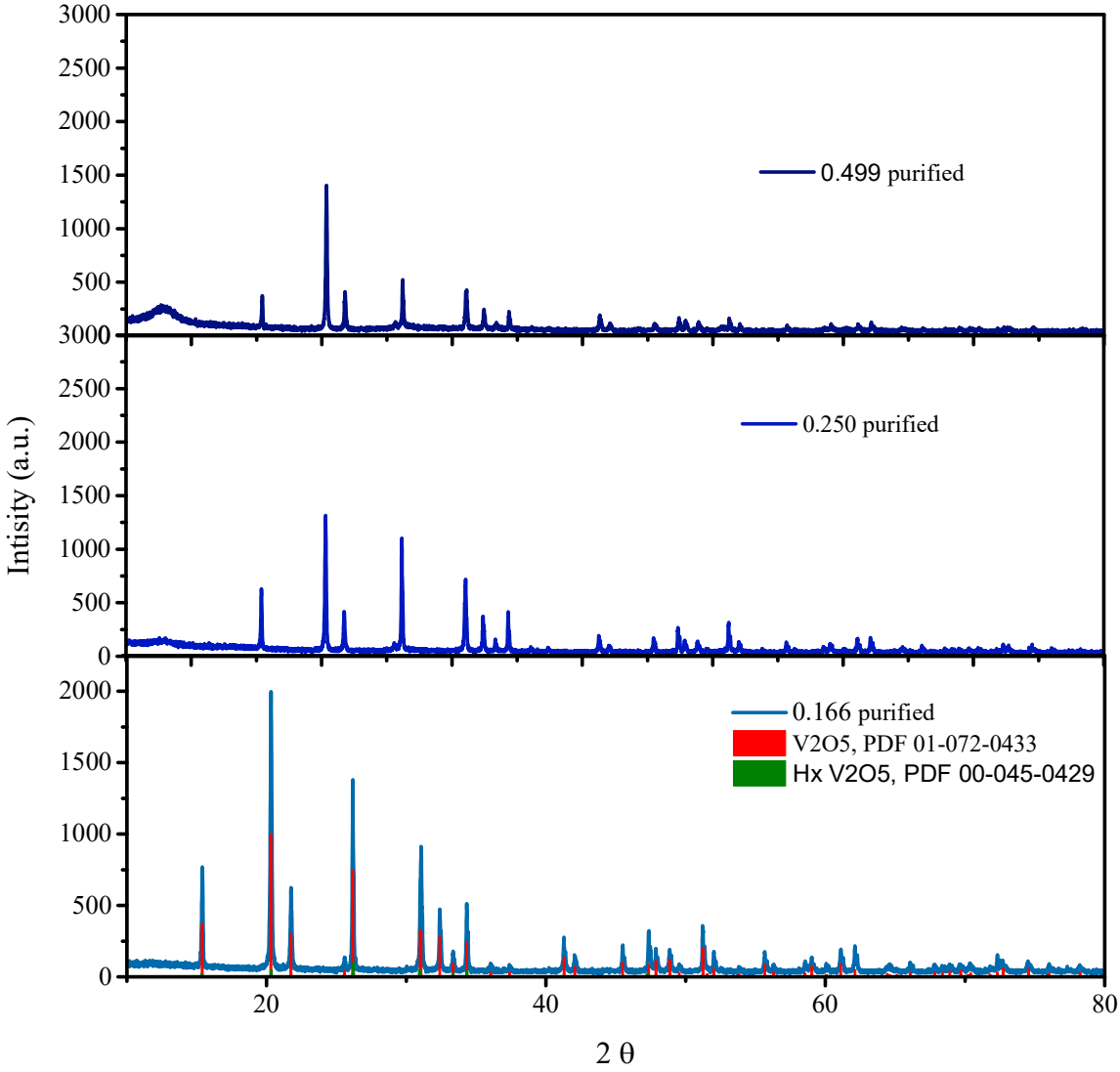

Figure 3- 22. XRD patterns for purified $M_xV_2O_5$ synthesized with different ratio of colloidalV_2O_5 and $Na_2S_2O_4$

4. Conclusion:

Hydrogen vanadium bronze powder was synthesized by reducing vanadium pentoxide with zinc hydrochloric acid. The insertions of hydrogen occurred topotactically in which the resulting bronze retained the original vanadium oxide structure. The XRD pattern also showed the existence of sodium vanadium bronze and the Na trace amount based on flame photometry analysis determined to be 0.039. Reduction of vanadium pentoxide with sodium dithionite produced hydrogen bronze in association with sodium bronze. The reducing capacity decreased with increasing sodium dithionite amount even though the sodium content was raised due the competing reactions. The reactions were pH dependent suggesting that the yields may be improved by performing the reduction reaction in buffered media. Further experiments could be carried out to find the optimum conditions to successfully synthesize sodium vanadium bronze in high yield utilizing different buffer systems. Colloidal suspensions of sodium vanadium bronze were successfully synthesized through reduction of colloidal vanadium pentoxide with sodium dithionite. These colloidal bronzes weren't stable over a long period of time, so further studies to enhance their stabilities could be pursued through addition of stabilizing agents. Moreover, drying of these colloidal materials result in the formation of brittle films that could be utilizing in sensing applications.

CHAPTER IV

SYNTHESIS OF MIXED VALENCE VANADIUM OXYHYDROXIDE AND ALUMINUM VANADIUM OXYHYDROXIDES

1. Introduction:

The intriguing properties of mixed valence vanadium oxyhydroxide and mixed metal vanadium oxyhydroxides resulted in them being the subject of a wide variety chemical studies, [2, 8, 11, 14, 17, 18, 21-27, 32-36, 38-43, 45-47, 52, 53, 56, 58-65, 128-130, 140, 142, 143, 162-167] and several of these reports have been discussed briefly within the introductory chapter. There are a several synthetic routes for mixed valence vanadium oxyhydroxides and mixed metal vanadium oxyhydroxides. Single-crystalline Hollandite-type vanadium (III/IV) oxyhydroxide nanorods, an example of a mixed valance vanadium oxyhydroxide that exhibits semiconducting properties has been synthesized through a simple nonaqueous liquid-phase one-pot route involving the reaction of vanadium oxychloride with benzyl alcohol. [45] Aluminum-vanadium mixed hydroxides, an example of mixed metal vanadium oxyhydroxide that is used as a catalyst for oxidative dehydrogenation of propane, in ammoxidation reactions, and as a precursor for vanadium-aluminum oxynitrides has been prepared via a precipitation method using ammonium metavanadate and aluminum nitrate nonahydrate. [168-170] Even though there are numerous routes for their synthesis, aqueous reactions with minimal byproducts are preferable. The aim of the research reported in this chapter to synthesize and optimize reaction conditions for the synthesis of the mixed valence vanadium oxyhydroxide and

mixed aluminum vanadium oxyhydroxides. Characterization of the precursor materials before and after calcination was also investigated.

2. Experimental:

2.1.Material

Commercially available reagents of ACS grade or better were used without further purification. Vanadium (V) oxide, V_2O_5 (99.6 + %) was obtained from Sigma-Aldrich, oxalic acid was received from Fisher Scientific. Aluminum (III) hydroxide, $Al(OH)_3$ from Sigma-Aldrich. Water was purified by reverse osmosis and deionization to a resistance of 18 MΩ.cm. Vanadium standard (1,000 ppm) is obtained from Ultra Scientific. The aluminum ICP standard (1,000 ppm) was purchased from the Ricca chemical company.

2.2.Analytical techniques

Thermogravimetry (TGA) analyses were performed on a Mettler TGA instrument. Thermal decompositions of experiments were performed in an air atmosphere from ambient temperature to 900 ˚C with a ramp rate at 5 ˚C/min using an alumina crucible. Infrared spectra were recorded on a Nicolet Is50 FT-IR spectrometer from 4000–500 cm^{-1}. The X-ray powder diffraction (XRD) patterns were obtained on a Bruker AXS D-8 Advance X-ray powder diffractometer using copper Kα radiation. Crystalline phases were identified using a search/match program and the PDF-2 database of the International Center for Diffraction Data. Crystallite size of calcined products were evaluated using the Scherrer equation. Scanning electron microscopy (SEM) on a FEI Quanta 600 field emission gun environmental scanning electron microscope was utilized to determine particle sizes and morphologies of the products. Surface areas were determined via nitrogen physisorption using the Brunauer, Emmett, and Teller (BET) method on a Quantacrome Nova 1200. The pH changes over time were measured using ISFET pH Meter, Model IQ125 obtained from mini Lab IQ Scientific, USA. UV-VIS spectroscopy measurements were recorded using Cary 100-UV/Visible spectroscopy. Metal concentrations were determined by microwave plasma -

atomic emission spectrometry using an Agilent 4200 MP-AES. Particle size via using dynamic light scattering (DLS) was performed on a Malvern HPPS instrument.

2.3.Synthetic procedure

2.3.1. Synthesis of Vanadyl Oxalate solution via a Reduction Reaction between Vanadium Pentoxide and Oxalic acid

Vanadyl oxalate solution was prepared via reduction of vanadium pentoxide by oxalic acid in similar fashion to the method described by Jun Liu and his co-workers. [171] An Erlenmeyer flask (1L) with stir bar inside are weighed and then 58.7 g (0.323 mole) of vanadium pentoxide and approximately 300 ml of water were added. The mixture was heated to reflux while stirring. Once the water started to condense at the flask neck, 122 g (0.968 mole) of oxalic acid was added cautiously and gradually. After this addition was complete the mixture was heated for 10 additional minutes. The solution was then stirred for at least 12 hours to allow the reaction to reach completion. Water was then added to the solution so that the total mass of the solution was equal to 1000 g. Finally, the solution was filtered and collected.

2.3.2. Synthesis of Mixed Valence Vanadium Oxyhydroxide

A solution of vanadyl oxalate was evaporated to dryness at room temperature to form a glassy solid. The glassy product is then dried further *in vacuum* until it reached constant weight. The resulting vanadyl oxalate precursor was then calcined at different temperatures of 200, 400, and 600 ◦C in air for 12 h.

2.3.3. Synthesis of Mixed Valence Aluminum Vanadium Oxyhydroxide via a Reaction of Vanadyl Oxalate Solution and Aluminum Hydroxide

Varying ratios of aluminum hydroxides were mixed with the vanadyl oxalate solution at room temperature for varying periods of time. The mixtures are separated by centrifugation. The powders were thoroughly washed with distilled water by repeated suspension and centrifugation

and then dried under vacuum. The products were then calcined at 600 ˚C for 12 hours. The amounts of the chemicals and yields of solids are listed in Table 1.

Table 4- 1. Different ratios of aluminum hydroxide were mixed with vanadyl oxalate solutions at room temperature for three days

Starting materials (g)		Reactant ratio V:Al	Reaction condition	Product color	Product Weight	Ceramic yield (%)
VOC_2O_4	$Al(OH)_3$					Oven at 600 ˚C
20	2.013	0.5:1.0	R.T.	Pale Green	2.122	59.5
20	1.006	1.0:1.0	R.T.	Pale Green	1.12	61.7
20	0.503	2.0:1.0	R.T.	Green	0.478	68.7
20	0.253	4.0:1.0	R.T.	Dark Green	0.397	78.7

2.3.4. Synthesis of Mixed Valence Aluminum Vanadium Oxyhydroxide via a Reaction of Vanadyl Oxalate Solution and Aluminum Hydroxide at Reflux Temperature

Aluminum hydroxide (2.013g, 0.026 mole) was added to 40 ml (0.026 mole) vanadyl oxalate. The mixture was heated to reflux for 24 hours. A color change from blue to green was observed. Upon cooling a dark gray solid was isolated by centrifuging, washed, dried to give a yield of 2.781 g. IR(cm^{-1}):3425 (s, br), 1680 (vs, sh), 1420 (s), 1290 (s), 980 (s), 800 (m), 580 (m), 547 (s). The product was calcined at 600 ˚C for 12 hours, the ceramic yield was 62.3 %.

3. Results and Discussion:

3.1. Synthesis of Vanadium Oxalate Solution Via a Reduction Reaction between Vanadium Pentoxide and Oxalic acid

A vanadyl oxalate solution was prepared by reaction of V_2O_5 with aqueous oxalate at 100 ˚C. In this reaction, V^{5+} is reduced to V^{4+} by oxidation of oxalate to produce carbon dioxide (Equation 1).

$$V_2O_{5(s)} + 3\ H_2C_2O_{4(aq)} \longrightarrow 2\ VO(C2O4)_{(aq)} + 3\ H_2O_{(l)} + 2CO_{2(g)}$$ Equation 1

The resulting vanadyl oxalate solution was characterized using UV-VIS spectroscopy. Figure 1 shows UV-VIS spectra of Vanadyl oxalate solution with four dilution factors. Octahedral vanadium (IV) ions, with d^1 electron configuration are theoretically expected to have a transition from $^2T_2$ ground state to ^2E excited state. However, vanadyl ions $[VO(OH_2)_5]^{2+}$ are not octahedral but have C_4V symmetry and more complex UV/VIS spectrum. The observed UV-VIS spectra with 0.8, 0.6, 0.4, and 0.2 dilution factors, DF = ($V_{intital}$/ V_{final}), show three bands at 777, 597, and 367 nm that can be attributed to $d_{xy} \rightarrow d_{xz}/d_{yz}$, $d_{xy} \rightarrow d_{x^2-y^2}$, *and* $d_{xy} \rightarrow d_{z^2}$(see Figure 1 and Scheme 1), respectively. [172] These spectra used to construct a calibration curve for vanadyl oxalate according to Beer's law (Figure 2).

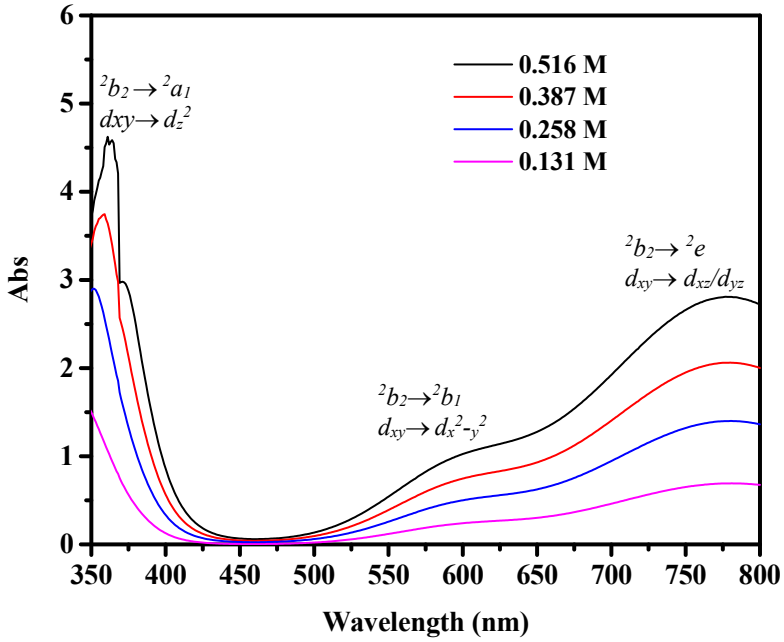

Figure 4- 1. UV/VIS spectra with 4 different concentrations of VOC_2O_4 solution

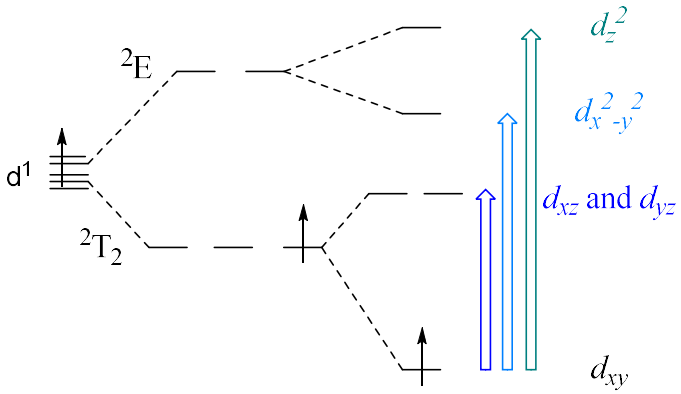

Scheme 4- 1. Schematic representation of (d-d) transitions V^{4+} ion

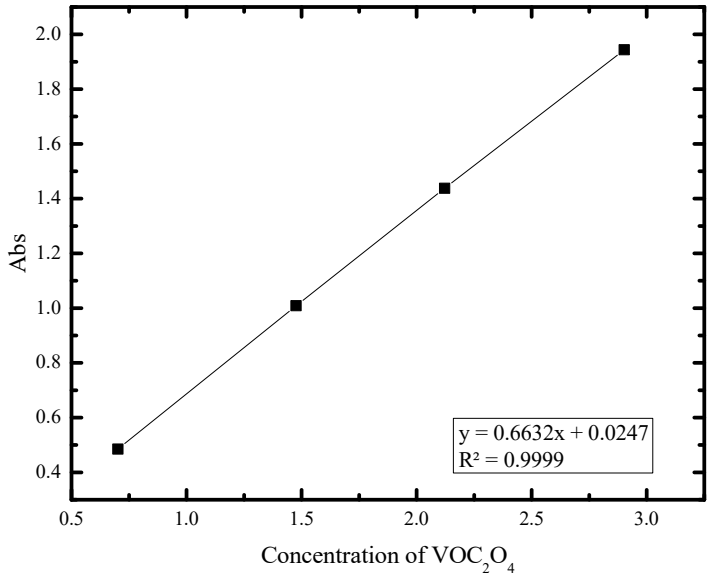

Figure 4- 2. Calibration curve of VOC_2O_4 solution by UV-Visible

MP-AES was used to determine the concentration of vanadium ion in the vanadyl oxalate solutions. Figure 3 exhibits the calibration curve that was generated over the range from 0 to 20 ppm. Typically, a mass of 0.021 g vanadyl oxalate solution was diluted with distilled water to 198.095 g. The vanadium concentration was found to be 0.641 M, close to the theoretical concentration 0.645 M based on amount of vanadium pentoxide used to prepare the vanadyl oxalate solution.

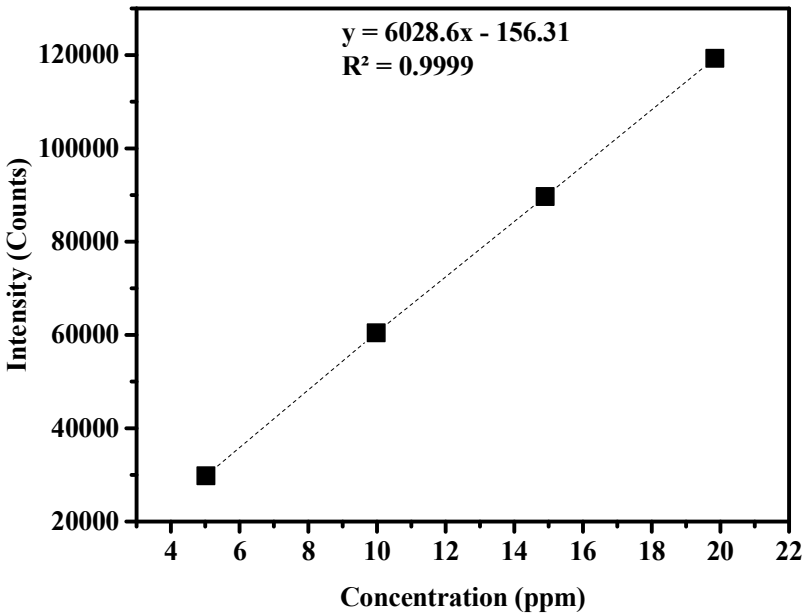

Figure 4- 3. Calibration Curve for vanadium by MP-AES

3.2.Synthesis of Mixed Valence Vanadium Oxyhydroxide

Vanadyl oxalate was isolated by drying its aqueous solution and it was characterized using FT-IR spectroscopy (Figure 4). The strong broad band at 3306 cm^{-1} can be assigned to the stretching mode of O-H in the water molecules. The sharp and strong peak at 1603 cm^{-1} is due to asymmetric stretching vibration of the carbonyl groups of oxalate.[173] The medium vibrational frequency at 1456 and 1305 cm^{-1} can be ascribed to a combination C-O and O-C=O modes. In accordance with literature data [174, 175] the sharp and strong band at 987 cm^{-1} and the weak one at 916 cm^{-1} are characteristic for vanadyl (V=O) stretching vibration in mixed valence vanadium (IV,V) compounds. The absorptions at 805, 621, and 562 cm^{-1} can be attributed to the combination of bending of O-C=O and stretching of V-O modes, respectively. The XRD pattern of the dried sample displayed no peaks attributable to an amorphous phase material.

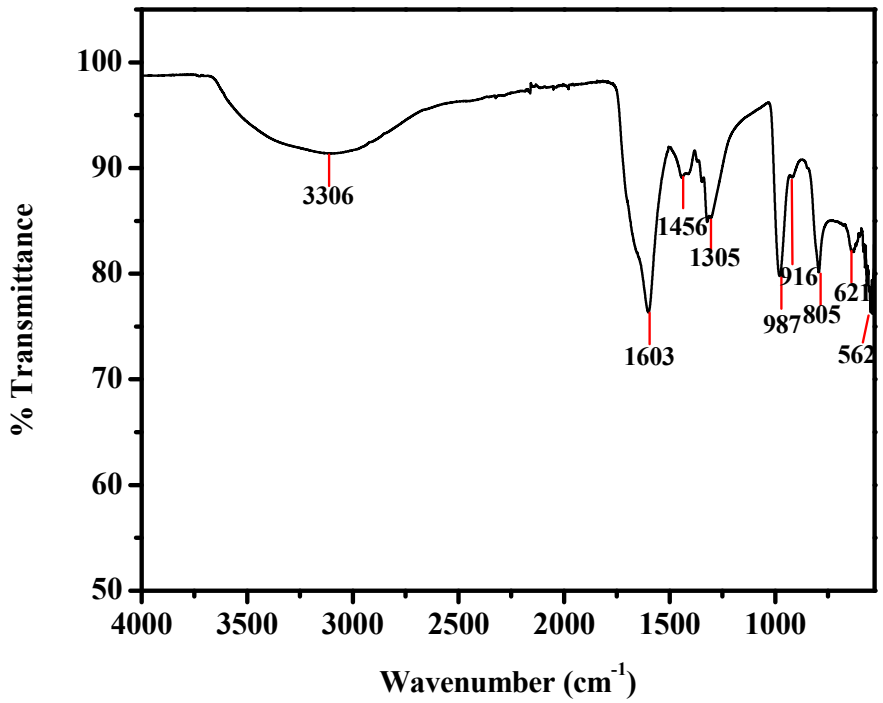

Figure 4- 4.FTIR spectrum for dried VOC_2O_4 product

The thermal decomposition of the vanadyl oxalate was investigated by thermogravimetric analysis (Figure 5). The decomposition occurs in one step with a weight loss of 47.4 %. The onset was 200 ˚C and the decomposition was completed at 300 ˚C. This is accompanied by an exothermic peak observed by DTA and can be attributed to dehydration and decomposition of oxalate. The VO_2 furthers oxidized to V_2O_5 and that explain the slight increase of mass weight in the later stage after 322 ˚C. [171] The formula was calculated from the TGA curve to be $VOC_2O_4 \cdot 0.979H_2O$. Calcination of the dried vanadyl oxalate using a Vulcan Multi-Stage Programmable Furnace, 3-130, under air atmosphere with a rate 5 ˚C/min to 200, 400, and 600 ˚C for 12 hours result in formation of solids with ceramic yields 61.2, 50.2, and 51.7 %, respectively. The final result gives a calculated formula of $VOC_2O_4 \cdot 1.161H_2O$, slightly. The FT-IR spectrum of the calcined products of dried vanadyl oxalate (Figure 6) shows the characteristic vibrational frequencies of vanadium pentoxide (1016 - 996), (775 - 784), (583 – 535) cm^{-1} attributed to V=O stretching of terminal oxygen, V-O-V symmetric, and V–O–V asymmetric vibrations modes, respectively. [176, 177] These

bands become more intense as calcination temperature increased from 400 to 600 cm^{-1}. The formation of the new band at 975 cm^{-1} is attributed to VO^{2+} vibration mode in a new phase that is formed. [178] Figure 7 shows the XRD patterns for the products calcined at 200, 400, and 600 ˚C. The majority of the product phase is amorphous with minority of crystalline phase of vanadium pentoxide for sample calcined at 200 ˚C. The products become more crystalline with increasing calcination temperature as XRD patterns of products calcined at 400 and 600 ˚C illustrated. These patterns matched the orthorhombic shcherbinaite, V_2O_5 phase (PDF-00-01-1426). The pattern for the product obtained from 600 ˚C in Figure 8 shows that there are new reflections at 2θ of 20.51 and 22.02 associated with a slight shift of the (001) and (101) reflections from 2θ: 20.26 to 20.07, and 21.71 to 21.50, respectively. These results may be due to formation of oxide vacancies that is known to occur when V_2O_5 is heated. If so, the new peak does not correspond to known VO_x phases. Notably, there are no reports in the literature for heating vanadyl oxalate as high as 600 C. The surface area for the resulting vanadium pentoxide was found to be 6.3 m^2/g. The ceramic yields, the surface area, the crystallites size, and the color of the products are summarized in Table 2.

Table 4- 2. Ceramic yields, the surface area, the crystallites size, and the color of the products at different calcination temperatures for vanadyl oxalate

Temperatures (˚C)	ceramic yeild (%)	Surface Area (m^2/g)	Crystallitte Size (nm)	Color
25	NA	5.0	NA	dark blue
200	62.50	9.4	NA	dark greenish-brown
400	44.80	17.8	49.18 ± 1.08	yellowish-brown
600	45.00	7.1	51.50 ± 1.23	yellowish-brown

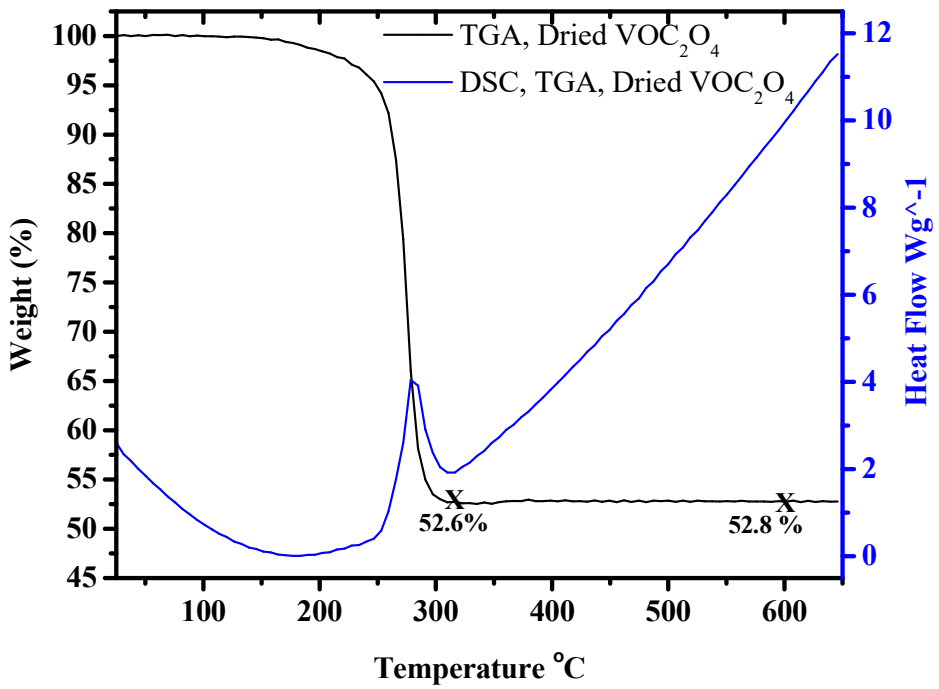

Figure 4- 5.TGA/DSC curves of dried VOC_2O_4 product

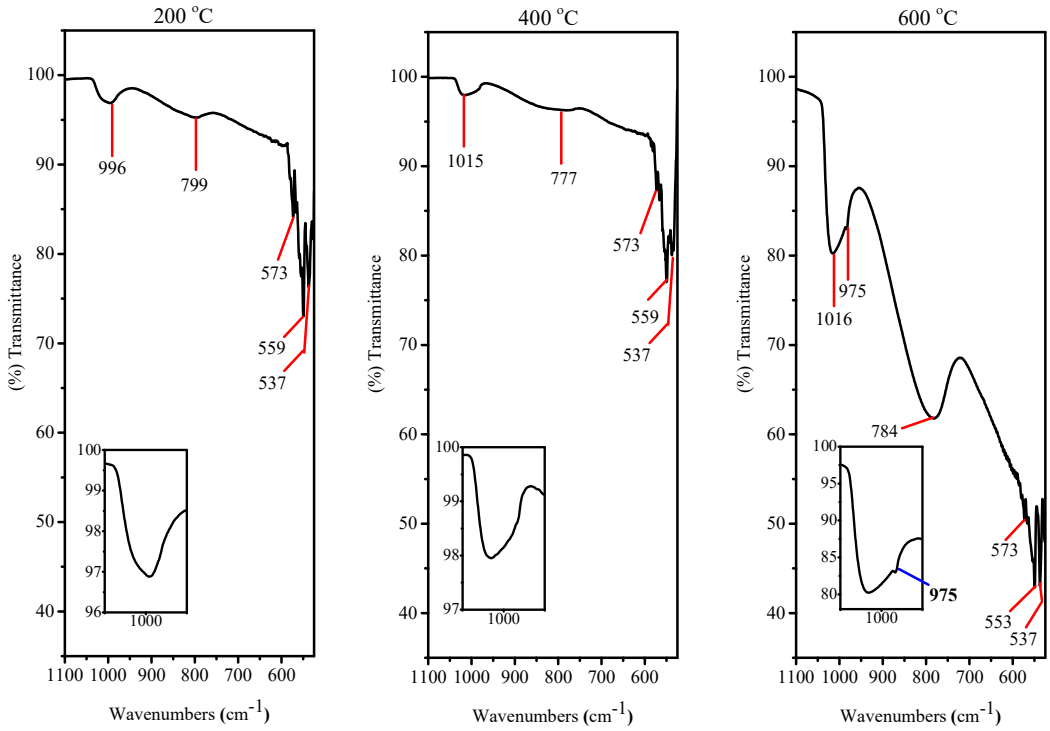

Figure 4- 6. FTIR spectrum of resulting V_2O_5 from calcination of the dried VOC_2O_4

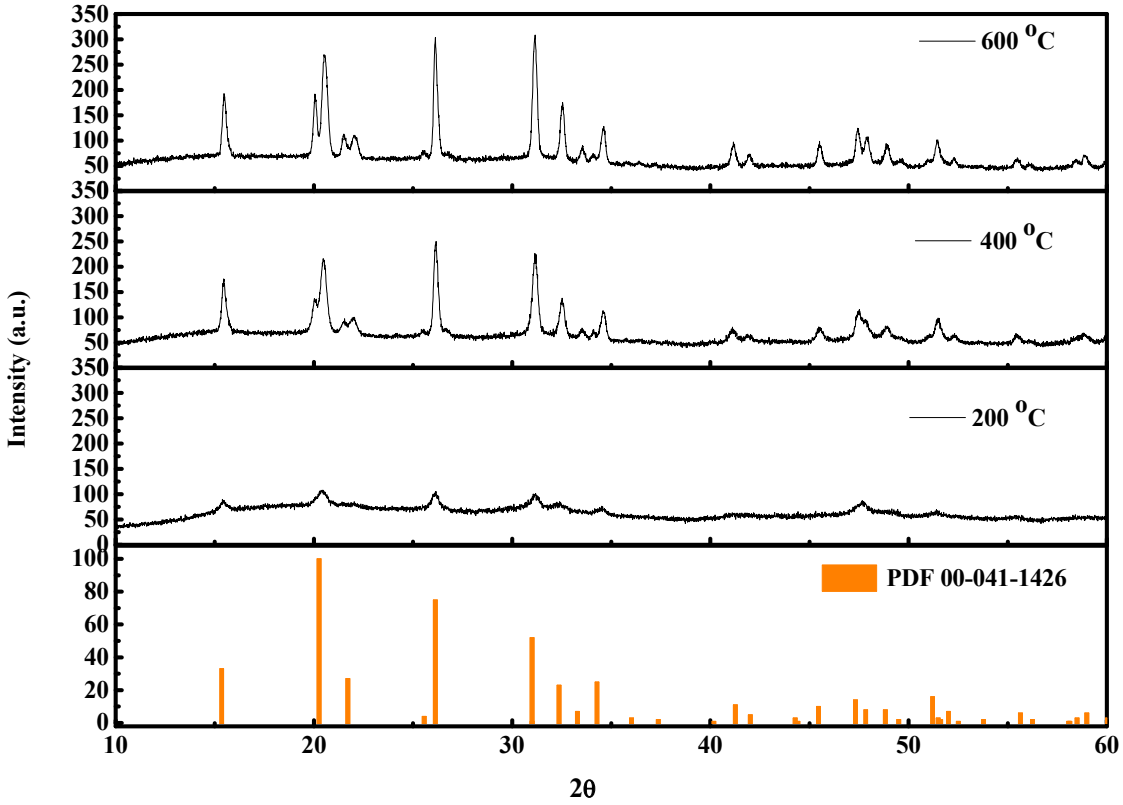

Figure 4- 7. XRD patterns of calcined products of VOC_2O_4 at different temperatures

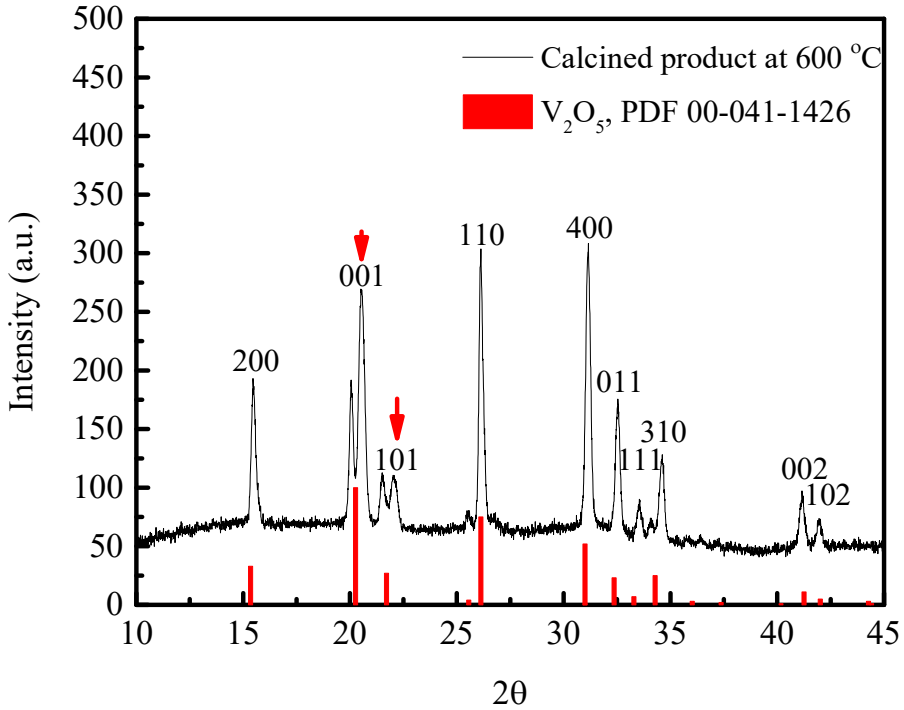

Figure 4- 8. XRD of calcined product of VOC_2O_4 at 600 ˚C

3.3.Synthesis of Mixed Aluminum Vanadium Oxyhydroxide via a Reaction of Vanadyl Oxalate Solution and Aluminum Hydroxide

Aluminum hydroxide was reacted with aqueous vanadyl oxalate at room temperature and under reflux as shown in the schematic representation of the reaction procedures (see Scheme 2).

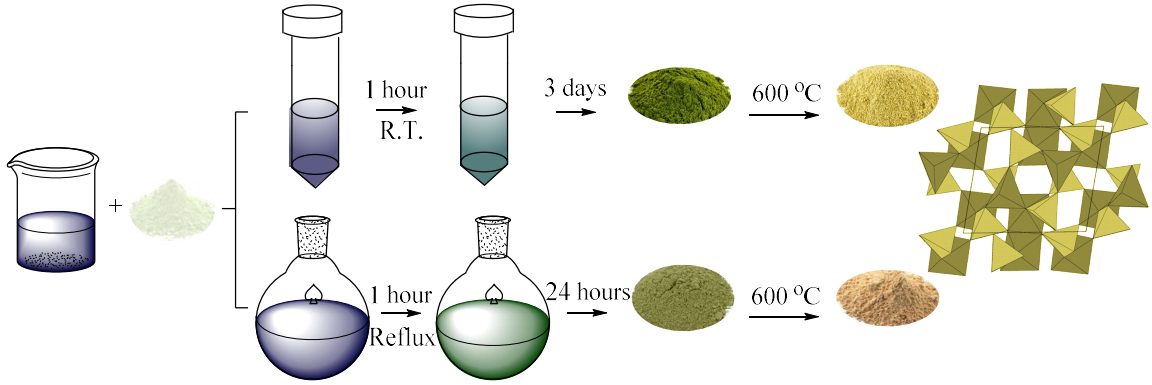

Scheme 4- 2. Representation of aluminum hydroxide and vanadyl oxalate reactions

Table 3 shows the result obtained when varying ratios of aluminum hydroxide were mixed with vanadyl oxalate solutions at room temperature for three days. Also included is the reaction of aluminum hydroxide reacted with vanadyl oxalate with (1.0V:1.0Al) ratio under reflux condition for 24 hours. Table 3 also shows the ceramic yield from TGA thermograms and pyrolysis of products using a Vulcan Multi-Stage Programmable Furnace, 3-130, under air atmosphere.

Table 4- 3. Different ratios of aluminum hydroxide were mixed with vanadyl oxalate solutions at room temperature for three days

Starting materials (g)		Reactant ratio V:Al	Reaction condition	Product color	Product Weight	Ceramic yield (%)
VOC_2O_4 solution	$Al(OH)_3$					Oven at 600 °C
20	2.013	0.5:1.0	R.T.	Pale Green	2.122	59.5
20	1.006	1.0:1.0	R.T.	Pale Green	1.12	61.7
20	0.503	2.0:1.0	R.T.	Green	0.478	68.7
20	0.253	4.0:1.0	R.T.	Dark Green	0.397	78.7
40	2.013	1.0:1.0	Reflux	Dark Gray	2.781	62.3

The change in pH over time was recorded for each ratio and is plotted in Figure 9. The initial pH was 1.8 and it increased as the reaction progressed up to the equilibrium at pH of 3.5. The low initial pH of the solution is due to the acidic $[VO(OH_2)_5]^{2+}$ ions (pK_{a1} = 3.5) and the pH raises as these ions are removed from solution. Since the pKa of $[VO(OH_2)_5]^{2+}$ is 3.5, the expected H^+ concentration for a 0.645 M vanadyl solution is 1.41×10^{-3} M and the corresponding pH is 1.85.

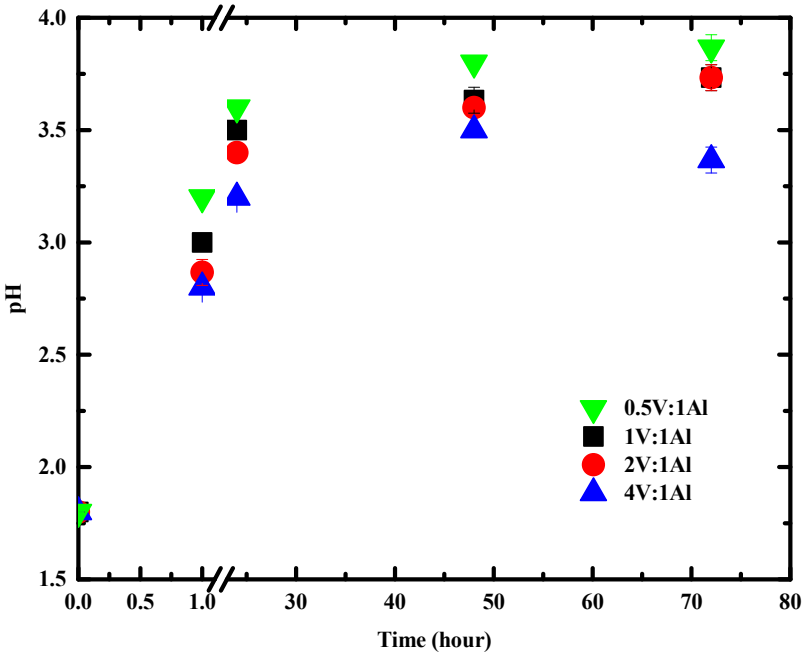

Figure 4- 9. The change of pH over time for alumnium hydroxide and vanadyl oxalate reactions

The solutions with different ratio of vanadyl oxalate reacted with aluminum hydroxide were analyzed via MP-AES to measure the total concentrations of vanadium and aluminum over time (Figure 10 and Figure 11), respectively. The general trend is a rapid decrease in vanadium and an increasing of aluminum concentrations over short period time followed by no or slow decreasing of vanadium concentration that is a corresponded by an increase in aluminum concentration over a short period of time. The concentration gradually changes longer period of time until either equilibrium is reached or the reaction goes to completion. The reaction with a 2.0V:1.0Al ratio is complete after 7 days. The compositions change of vanadium and aluminum in both solution and solid phases over time (calculated from MP-AES data) and provided in Table 4 and Table 5. The kinetics of the reactions were analyzed using zero-order, first-order, and second-order models (Figures 12-14) and (Table 6-8).

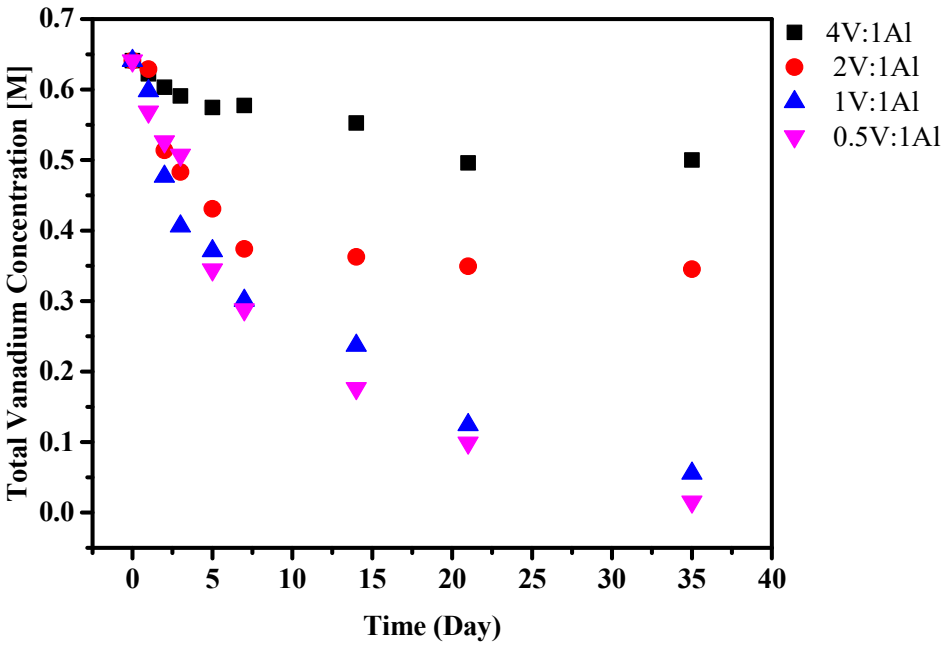

Figure 4- 10. MP-AES analysis of vanadium concentration over time for aluminum hydroxide and vanadyl oxalate reactions

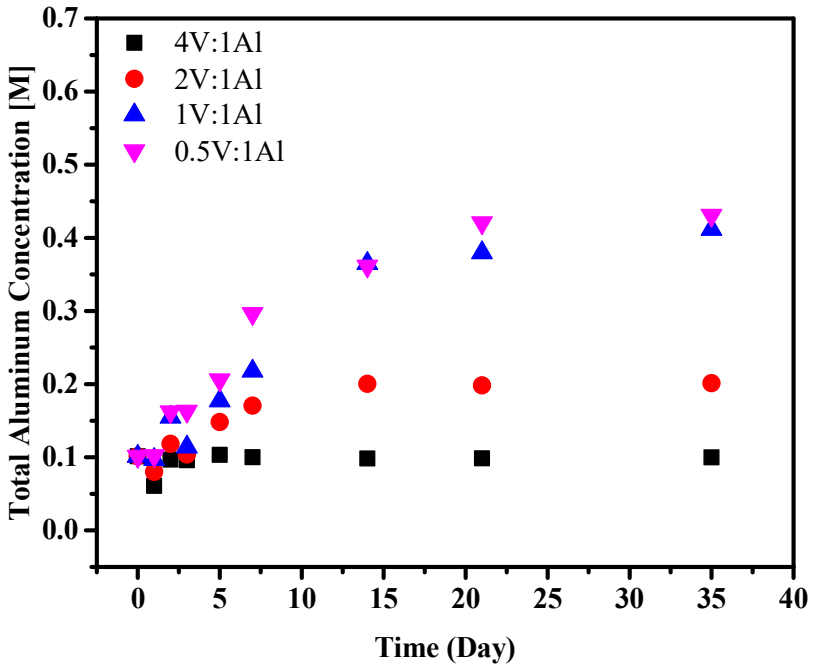

Figure 4- 11. MP-AES analysis of aluminum concentration over time for aluminum hydroxide and vanadyl oxalate reactions

Table 4- 4. The compositions of vanadium and aluminum in solutions (mmole) based on MP-AES analysis

Time (Day)	4V:1Al		2V:1Al		1V:1Al		0.5V:1Al	
	V	Al	V	Al	V	Al	V	Al
0	12.44	1.22	12.44	1.22	12.44	1.22	12.44	1.22
1	12.07	1.94	12.58	1.60	11.96	1.94	11.37	2.05
2	11.82	1.92	10.28	2.37	9.53	3.10	10.52	3.24
3	11.49	2.07	10.35	2.22	8.12	2.28	10.82	3.48
5	11.55	2.00	8.62	2.96	7.43	3.54	6.89	4.12
7	11.05	1.97	7.48	3.41	6.02	4.36	5.76	5.93
14	9.92	1.97	7.25	4.01	4.74	7.30	3.52	7.23
21	10.00	2.00	6.99	3.97	2.49	7.59	1.98	8.41
35	12.44	1.22	6.90	4.03	1.11	8.23	0.31	8.62

Table 4- 5. The compositions of vanadium and aluminum in solid products (mmole) based on MP-AES analysis

Time (Day)	4V:1Al		2V:1Al		1V:1Al		0.5V:1Al	
	V	Al	V	Al	V	Al	V	Al
0	0.00	10.79	0.00	10.79	0.00	10.79	0.00	10.79
1	0.37	11.60	0.24	11.21	0.85	10.87	1.45	10.77
2	0.75	10.88	2.54	10.45	3.28	9.72	2.29	9.57
3	1.00	10.90	3.15	10.74	4.69	10.53	2.67	9.56
5	1.32	10.75	4.20	9.85	5.39	9.27	5.92	8.70
7	1.27	10.81	5.33	9.40	6.80	8.46	7.05	6.89
14	1.77	10.85	5.56	8.81	8.07	5.51	9.29	5.59
21	2.89	10.84	5.83	8.85	10.33	5.22	10.84	4.40
35	2.81	10.82	5.91	8.79	11.70	4.58	12.51	4.20

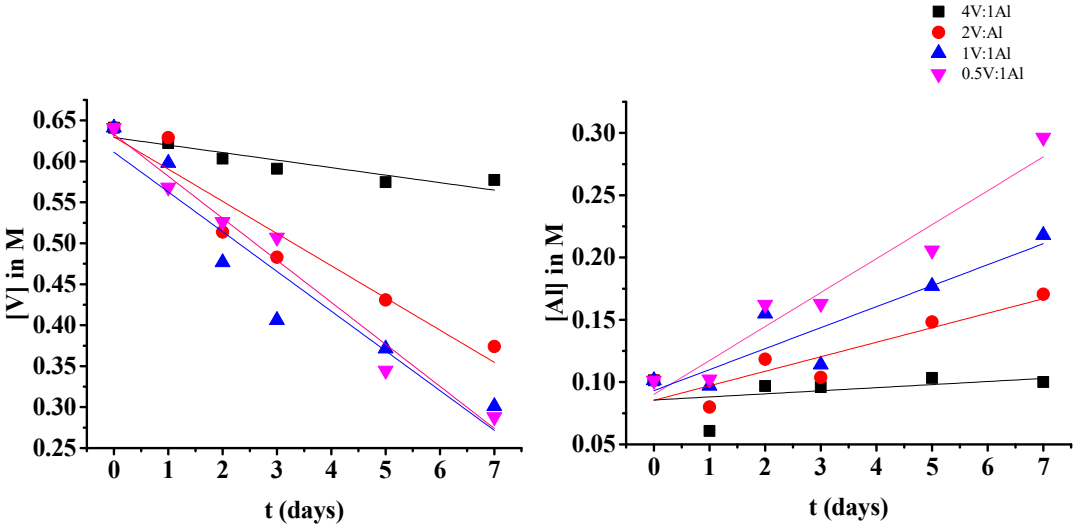

Figure 4- 12. Zero-Order Model

Table 4- 6. Kinetic Data from the Zero-Order Model

V/Al ratio	k	$[V_o]$	R^2	k	$[Al_o]$	R^2
	$M.hour^{-1}$	M	%	$M.hour^{-1}$	M	%
4	0.0092	0.6291	83.98	0.0025	0.0856	16.20
2	0.0393	0.6299	92.58	0.0116	0.0854	82.93
1	0.0485	0.6112	90.97	0.0168	0.0932	83.19
0.5	0.0513	0.6332	97.54	0.0272	0.0901	94.72

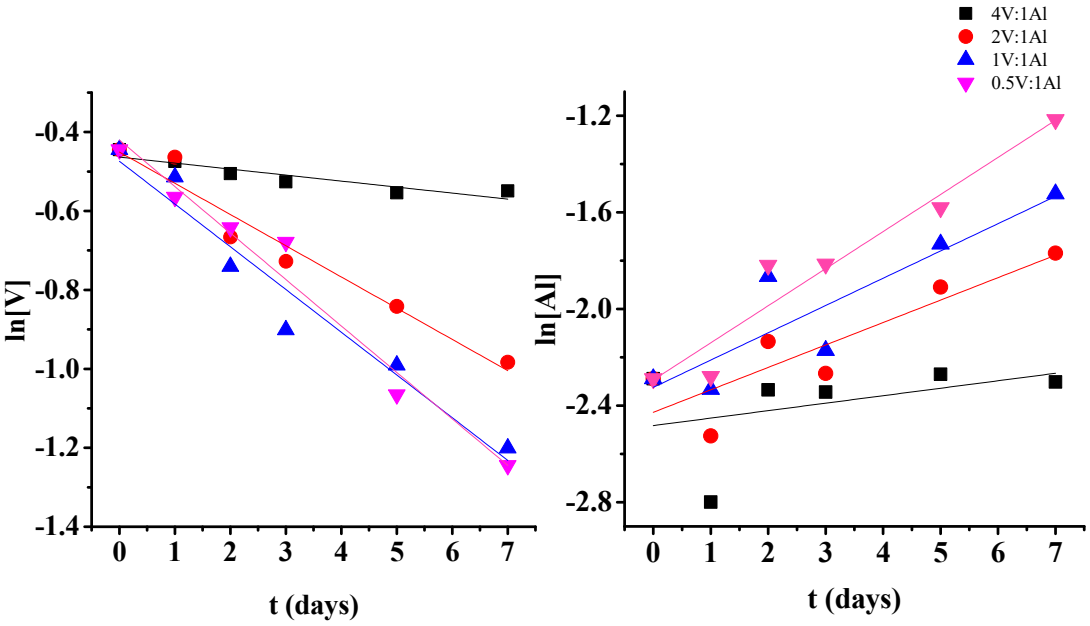

Figure 4- 13. First-Order Model

Table 4- 7. Kinetic Data from the First-Order Model

V/Al ratio	k	$[V_o]$	R^2	k	$[Al_o]$	R^2
	$hour^{-1}$	M	%	$hour^{-1}$	M	%
4	0.0152	0.6291	84.62	0.0309	0.0835	15.84
2	0.0791	0.6372	95.65	0.0929	0.0882	77.73
1	0.1083	0.6225	95.22	0.1129	0.0978	80.37
0.5	0.1177	0.6569	97.19	0.1535	0.1009	94.02

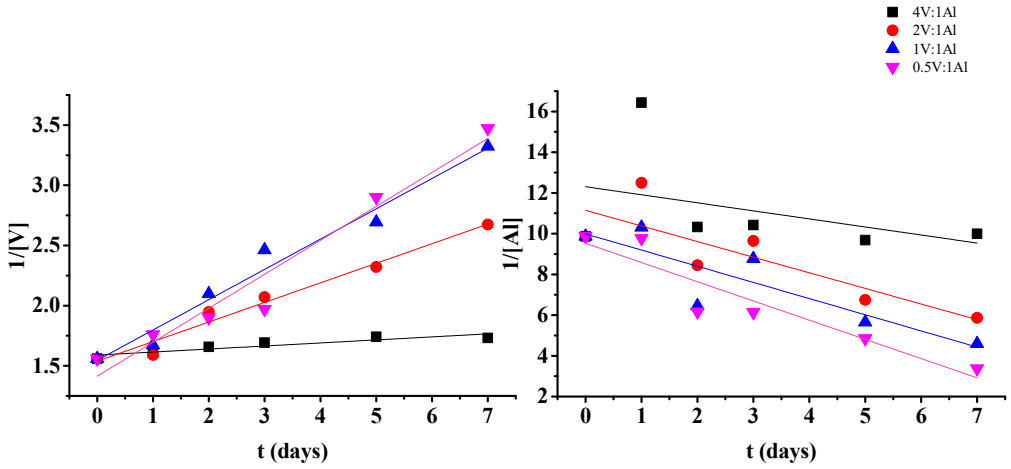

Figure 4- 14.Second-Order Model

Table 4- 8. Kinetic Data from the Second-Order Model

V/Al ratio	k	$[V_o]$	R^2	k	$[Al_o]$	R^2
	M^{-1} $hour^{-1}$	M	%	M^{-1} $hour^{-1}$	M	%
4	0.0252	0.6292	85.23	0.3955	0.0812	15.50
2	0.1626	0.6497	97.56	0.7672	0.0897	70.32
1	0.2517	0.6466	97.43	0.7943	0.1001	46.60
0.5	0.2821	0.7069	95.50	0.9438	0.1049	87.76

The solutions were also analyzed by UV-Visible spectroscopy to determine the concentration of vanadyl ion $[V^{4+}]$ as shown in Figure 15. As it shown with the same dilution of the different ratio solutions, the absorptions of $[V^{4+}]$ are unpredictably increase with increasing aluminum amount expect for 0.5V:1.0Al ratio, x=(Al/V)=2 showing lower absorption. Comparison between MP-AES and UV-VIS data is represented in Figure 16. Plotting total vanadium concentrations from MP-AES verses x; mole ratios, shows as long as the amount of aluminum increased the total vanadium concentration in solutions is decreased due to the precipitation of AlV-product except for 0.5V:1.0Al ratio, (x=2), which could be explained by that the formation of AlV-oxyhydroxide layer on the surface of aluminum hydroxide may prevents the interaction between vanadyl oxalate with aluminum hydroxide core. Comparison between MP-AES and UV-VIS data shows a steady value of V^{4+}concentrations and the significant changes trend of total vanadium from MP-AES is similar to trend of total V^{n+} concentration based on UV-VIS as shown in Figure 17. Total reduced vanadium concentration $[V^{3+}]$ determined by subtraction of total vanadyl consternation from total vanadium concentration and thus based on these observations it seems the aluminum not only acts as a reactant but also as a catalyst for the reduction of vanadyl ion by oxalate as Equation 2 shows.

$$2\,VO^{2+} + C_2O_4^{2-} + 4H^+ \xrightarrow{Al^{3+}} 2V^{3+} + 2CO_2 + 2H_2O$$ Equation 2

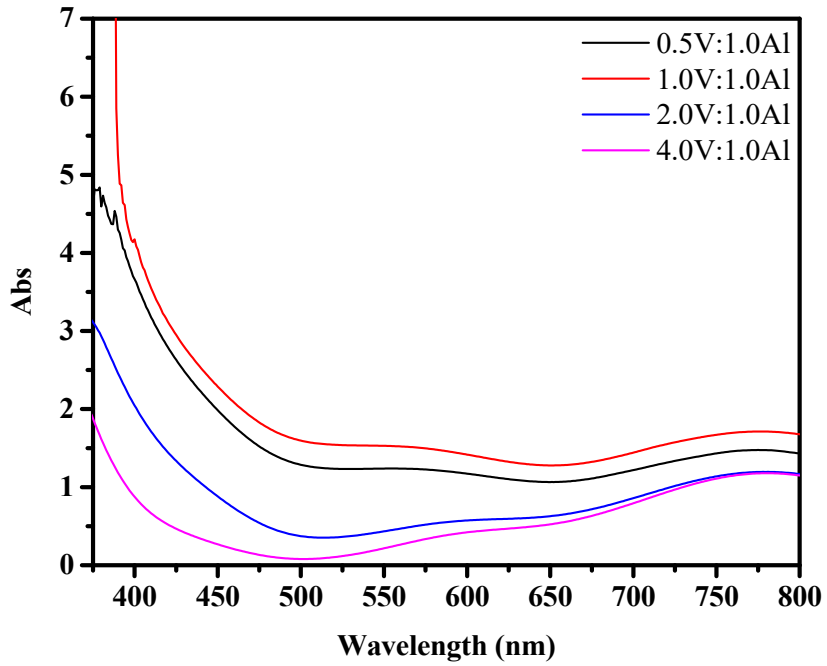

Figure 4- 15. UV-VIS spectra for vanadyl oxalate/ aluminum hydroxide solutions

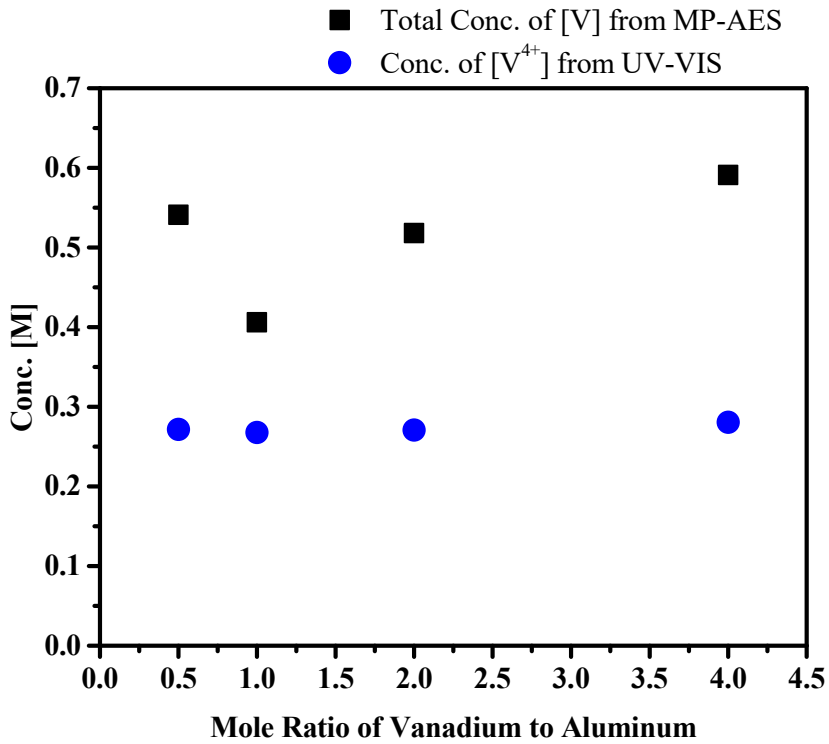

Figure 4- 16. Comparison between MP-AES and UV-VIS data with different mole ratios

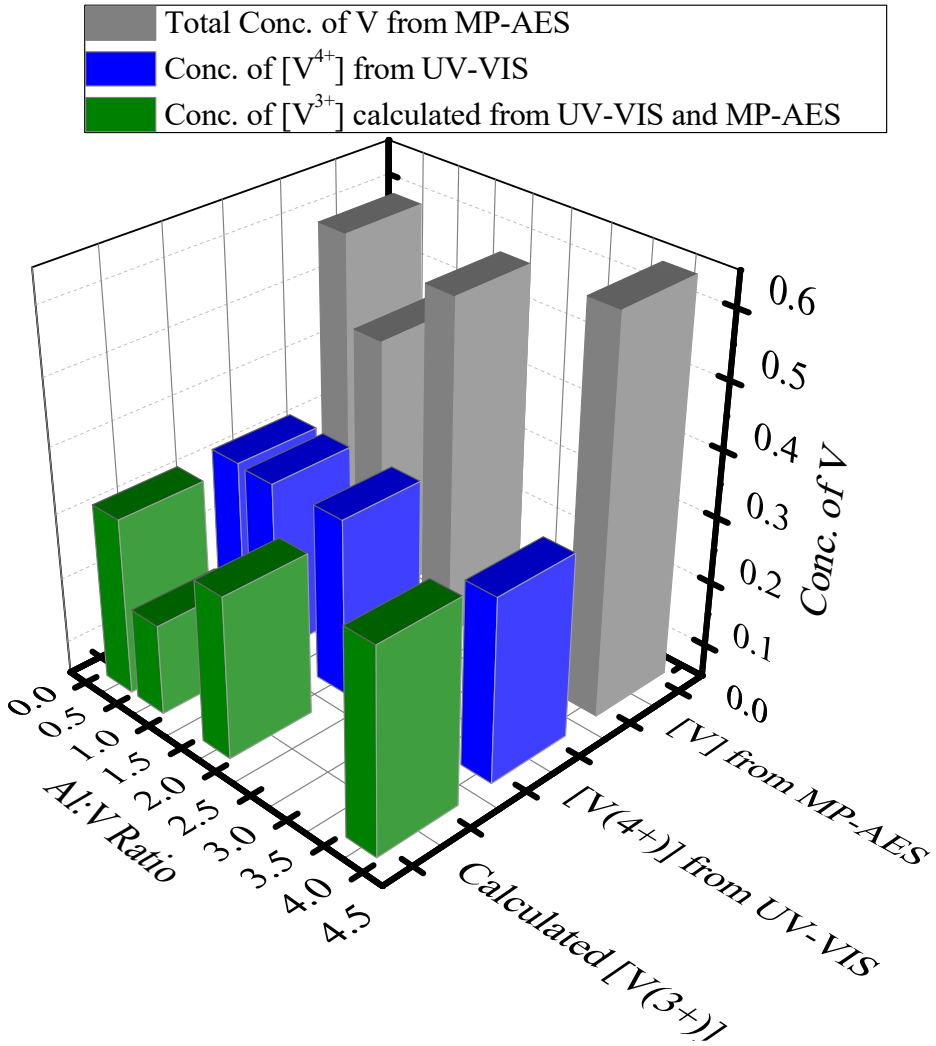

Figure 4- 17. Representation of the data from MP-AES and UV-VIS data for the various molar ratios of vanadium to aluminum

Dynamic light scattering (DLS) analysis was used to measure the particle size distribution of the vanadyl oxalate/aluminum hydroxide reactions (Figure 18). Both the 4V:1Al and 2V:1Al ratios gave a very narrow particle size distribution close to 1 nm in size (0.993 and 0.903, respectively. The later reaction also had a small peak (only 0.1 % of the particle volume) at 6.8 nm. There was a large increase in particle size when the amount of vanadium was decreased to 1 molar equivalents per aluminum. A narrow peak in size distribution centered at 98 nm was observed with no other peaks present. At the 0.5V and 1V to 1Al ratios, only large particles were observed in a bimodal distribution. One peak was observed at 544 nm (56 % of particle volume) and a second

one at 5220 nm that accounted for 44 % of the particle volume. These results indicate that the reaction of vanadyl oxalate with aluminum hydroxide results in fragmentation of the $Al(OH)_3$ particles. As the amount of vanadyl oxalate is increased, the $Al(OH)_3$ particles are broken into smaller particles until clusters around 1nm are formed.

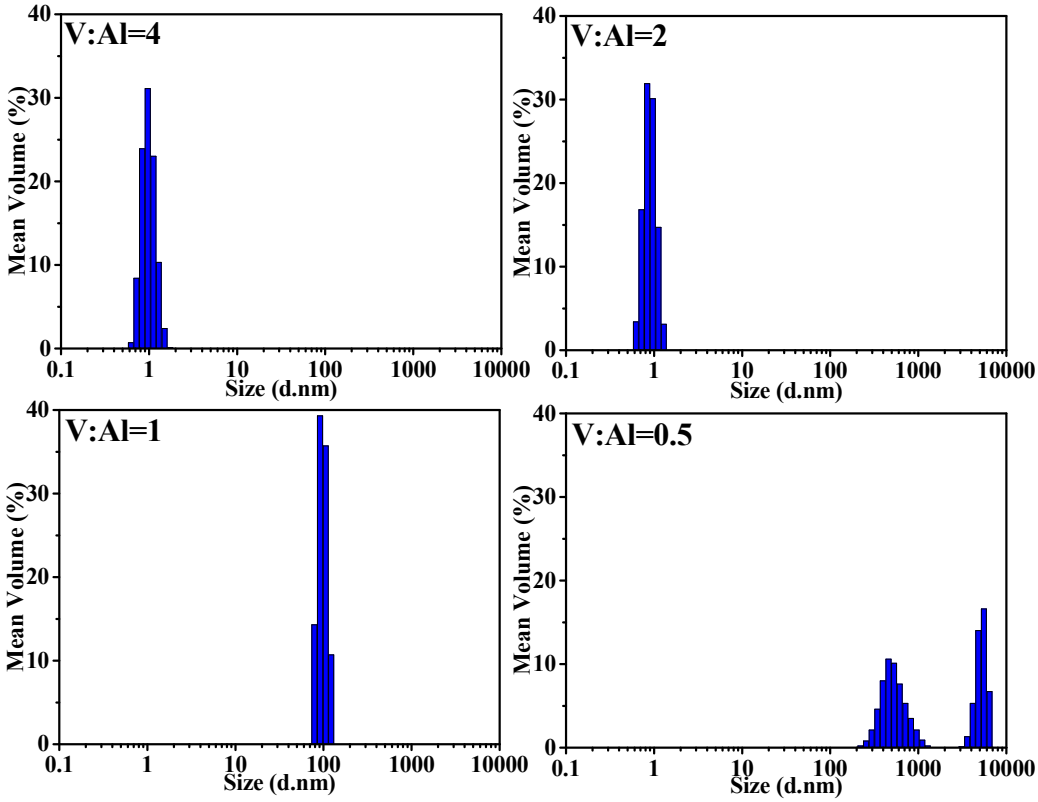

Figure 4- 18.DLC analysis for $Al(OH)_3/VOC_2O_4$ solutions with varying V:Al ratios

The thermal gravimetric analysis of the solid products are shown from Figure 19 to Figure 23. The TGA curves are similar for all of the products except for the 4.0V:1.0Al ratio, which has a lower final weight loss of 84.016% at 600 °C. The ceramic yields obtained based on pyrolysis and thermogravimetric analysis are tabulated in Table 9. For example, the ceramic yield at 600 ˚C of the 1V:1Al product synthesized at room temperature and under reflux are 65.220 and 64.994, respectively. The 34.78 and 35.006 % total weight loss are attributed to two unresolved steps of dehydration and dehydroxylation. Elemental analysis was performed on several samples to

determine whether oxalate or carbonate might be present. Only traces of carbon found: 1.44 % for 2V:1Al product and 1.08 % for the 1V:1Al product produced at room temperature. The solid from the refluxed mixture had a little higher carbon content, 2.93 %. Clearly the trace of carbon cannot be the presence of stoichiometric amounts of oxalate or carbonate. Therefore, it may be attributed to absorbed carbon species on the surface of the oxyhydroxide products. The XRD patterns of all solids indicated that they were amorphous. Considering the TGA data for water and OH content and the amounts of vanadium and aluminum present as determined by MP-AES, an approxiate reaction and formula for the products can be calculated. This is represented in Equation 3. Note that with sufficient excess of vanadium, the aluminum will completely dissolved and product will be $VO(OH)_2$. The possible presence of V^{3+} is a complicating factor that was not considered.

$$x\ VO^{2+}_{(aq)} + 2Al(OH)_{3(s)} \longrightarrow Al_{(2.0-0.67x)}(VO)_x(OH)_{6(s)} + 0.67Al^{3+}_{(aq)} \quad \text{Equation 3}$$

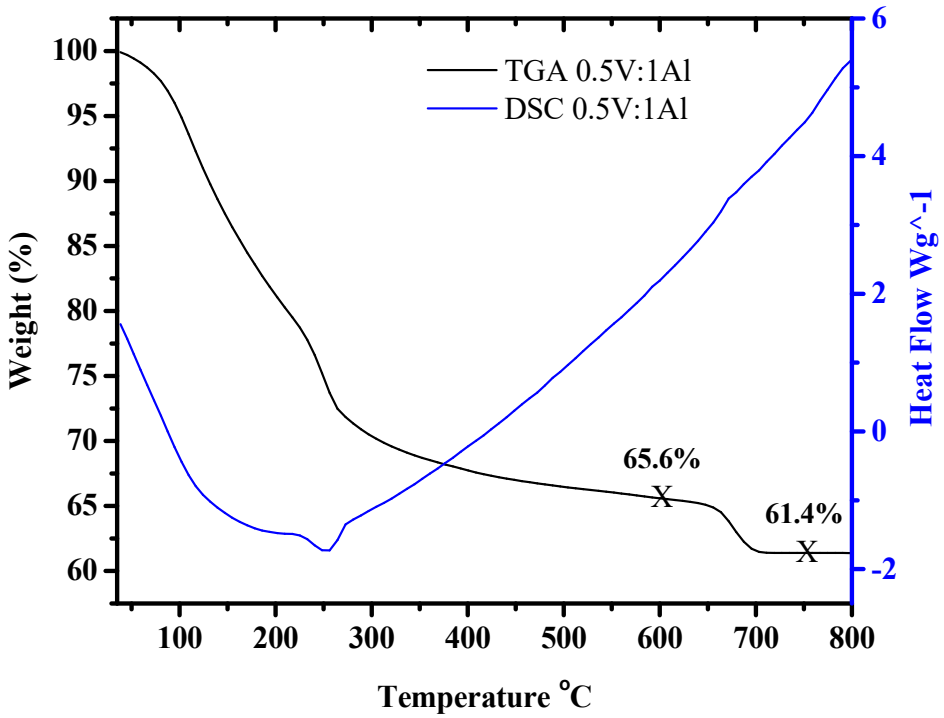

Figure 4- 19. Thermogravimetric curve of the 0.5V:1Al product

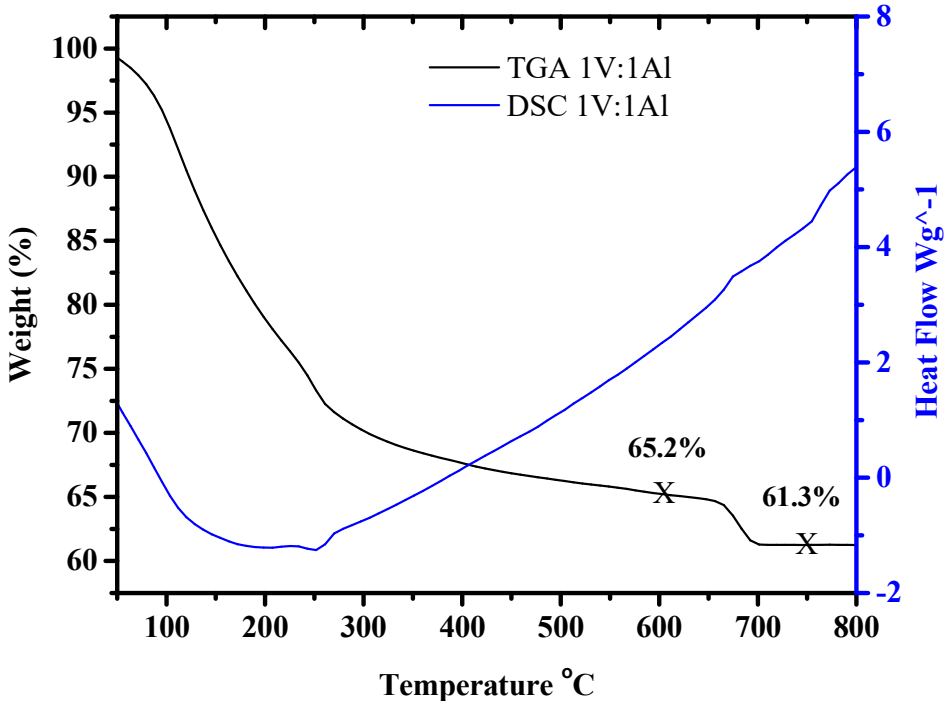

Figure 4- 20. Thermogravimetric curve of the 1V:1Al product

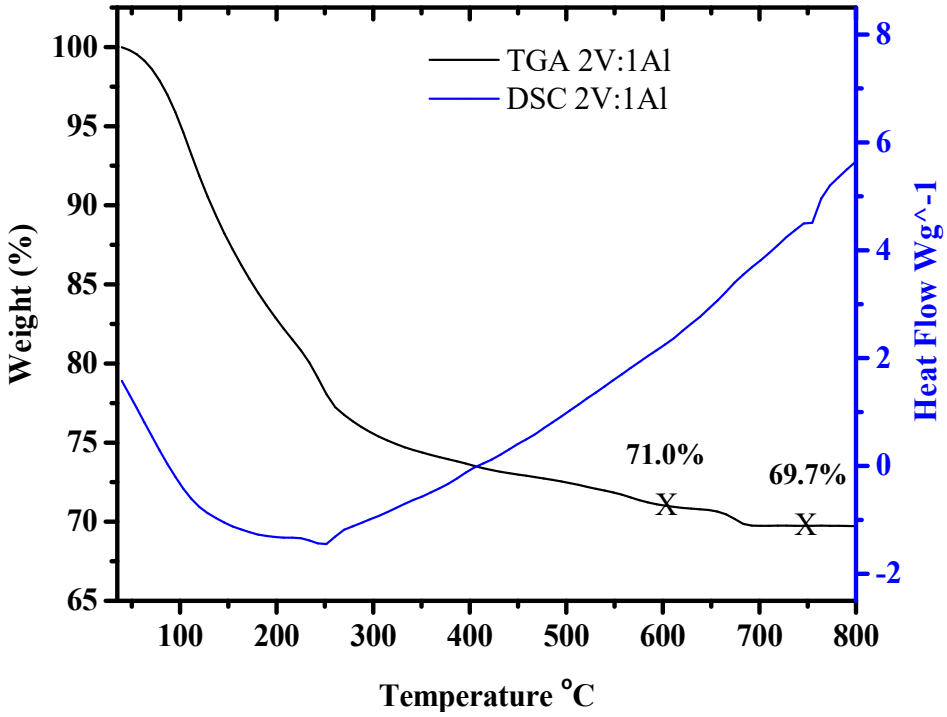

Figure 4- 21. Thermogravimetric curve of the 2V:1Al product

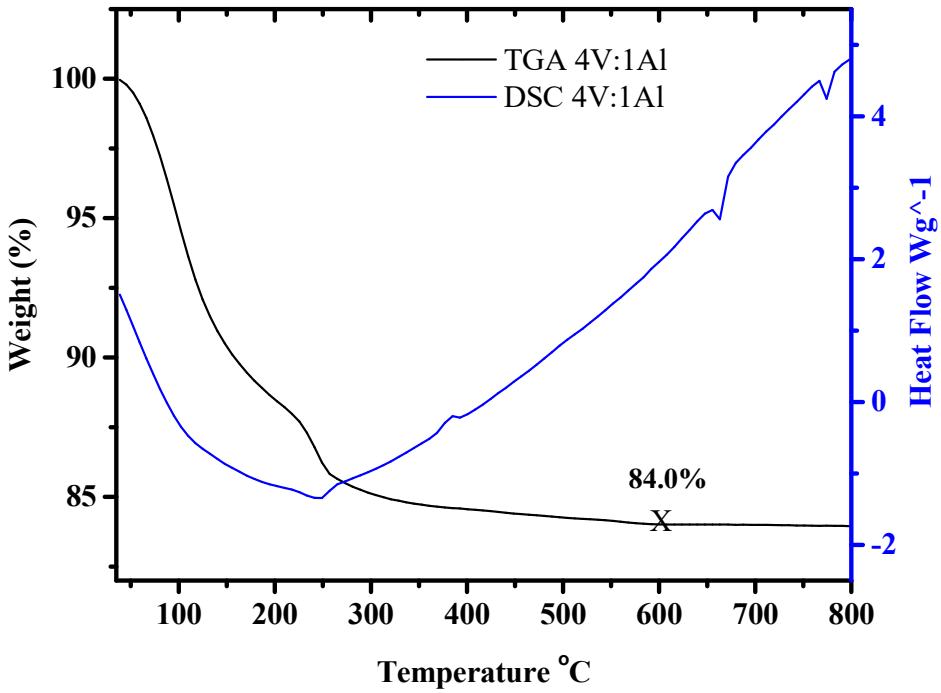

Figure 4- 22. Thermogravimetric curve of the 4V:1Al product

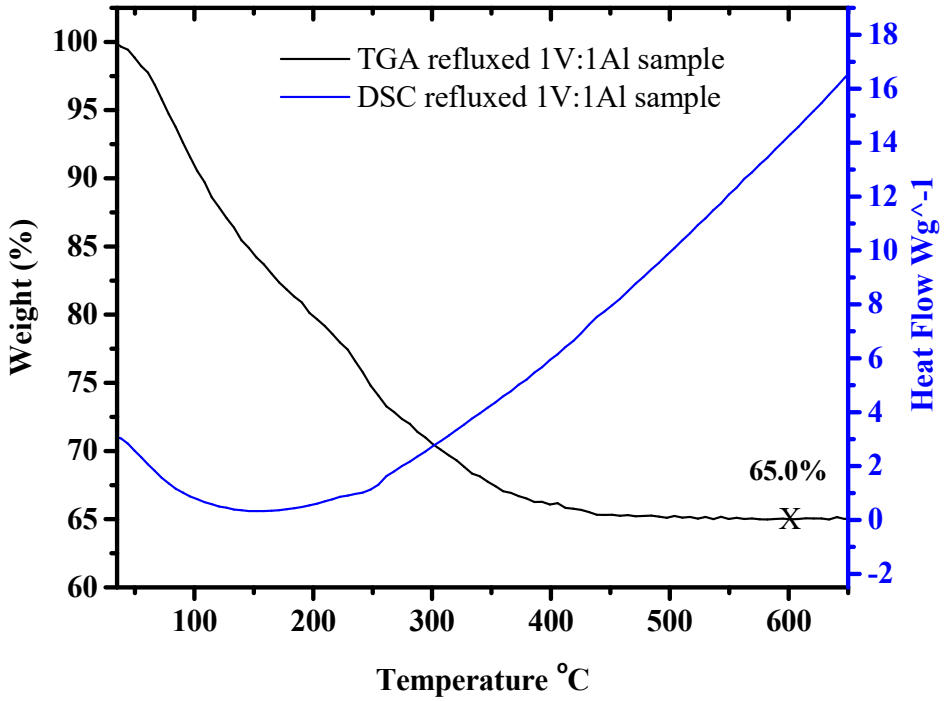

Figure 4- 23. Thermogravimetric curve of 1V:1Al product prepared under reflux

The FT-IR spectra of the products are shown in Figure 24 to Figure 28. The FT-IR spectra display five main vibration bonds in the regions: 3417 - 3436, 1617 - 1420, 1025 - 880, 860 - 670, and 590 - 525 cm^{-1}. The broad band centered around 3425 cm^{-1} corresponds to O-H stretching vibrations of water and hydroxyl ions. The second broad band with medium intensity close to 1620, and 1500 cm^{-1} is due to the symmetric and asymmetric H-O-H and O-H vibration bending modes, respectively.[179] The strong broad bands between 1025 - 880 cm^{-1} are due to V-O and Al-O-V stretching modes. [180] The absorptions bands in the 860 - 670 cm^{-1} range can be attributed to the bridge oxygen asymmetric modes. Peaks in the region below 590 cm^{-1} can be attributed to bridging oxygen symmetric stretching modes.

The stacked plot representation of FT-IR spectra of the oxyhydroxide products is shown in Figure 29. This stacking representation illustrates the effects of changing the V to Al ratios as well as performing the reaction at room temperature or under reflux. The effect of changing V to Al ratio could be followed through V=O stretching of terminal oxygen, the V-O-V symmetric, and TGA refluxed 1V:1Al sample he V–O–V asymmetric vibrational modes, increasing vanadium in the samples causes the bands at 1016, 845, and 584 to shift to 1003, 745, 547 cm^{-1} and become more defined. For the same ratio of reactant, the vibration modes of reaction product under reflux shift to shorter wavenumbers except for the vibration mode at 1620 cm^{-1} which shifts to longer wavenumber. The shift to shorter wave number could be an indication of less reduction of vanadium oxidation state of the product under reflux.[181, 182] The shift of the vibration mode at 1620 cm^{-1} to higher wavenumber may be attributed to more strongly bonded molecules.

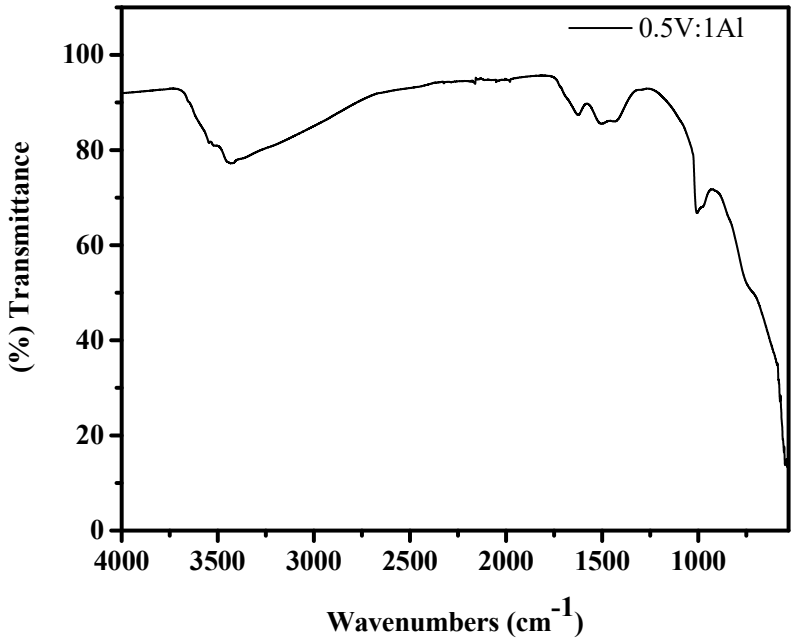

Figure 4- 24. FT-IR spectrum of the 0.5V:1Al oxyhydroxide product

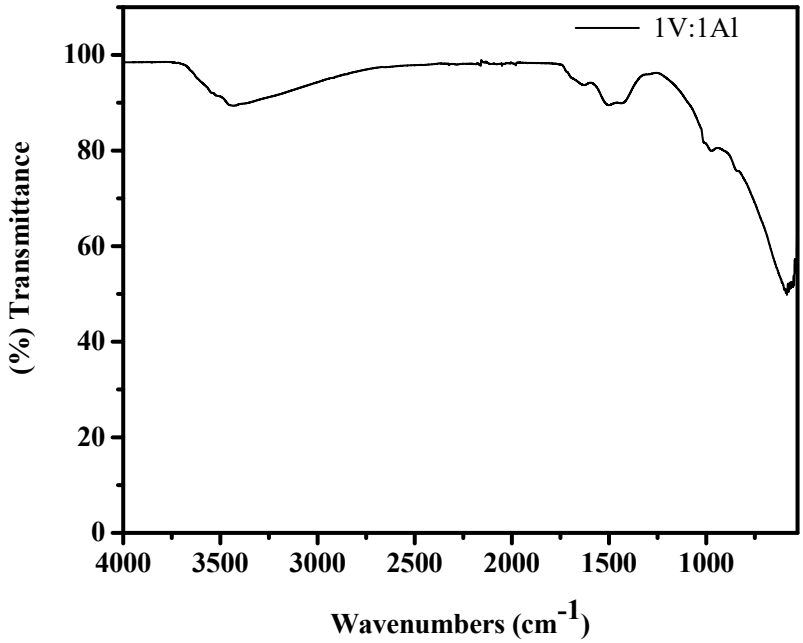

Figure 4- 25. FT-IR spectrum of the 1V:1Al oxyhydroxide product

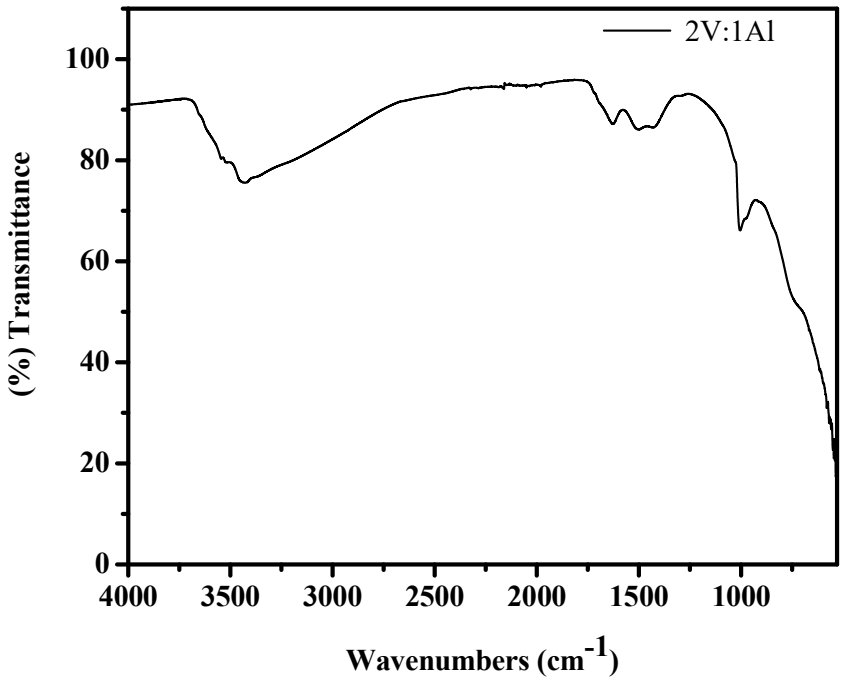

Figure 4- 26. FT-IR spectrum of the 2V:1Al oxyhydroxide product

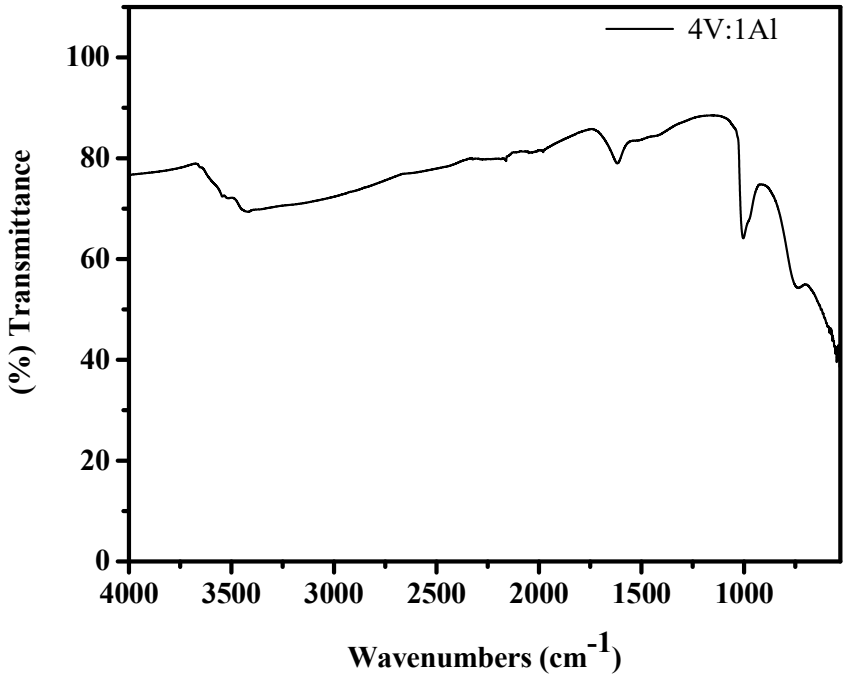

Figure 4- 27. FT-IR spectrum of the 4V:1Al oxyhydroxide product

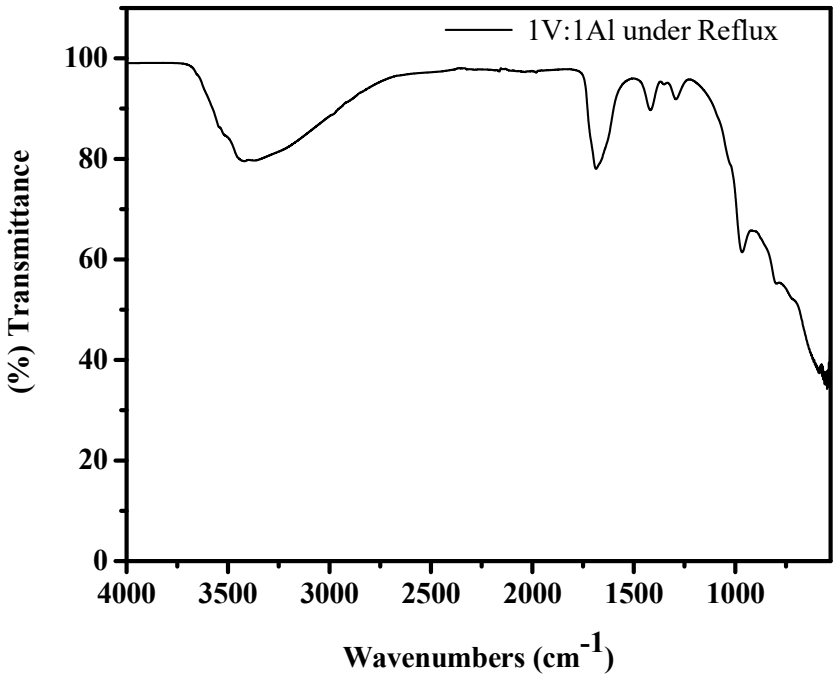

Figure 4- 28. FT-IR spectrum of the 1V:1Al oxyhydroxide refluxed product

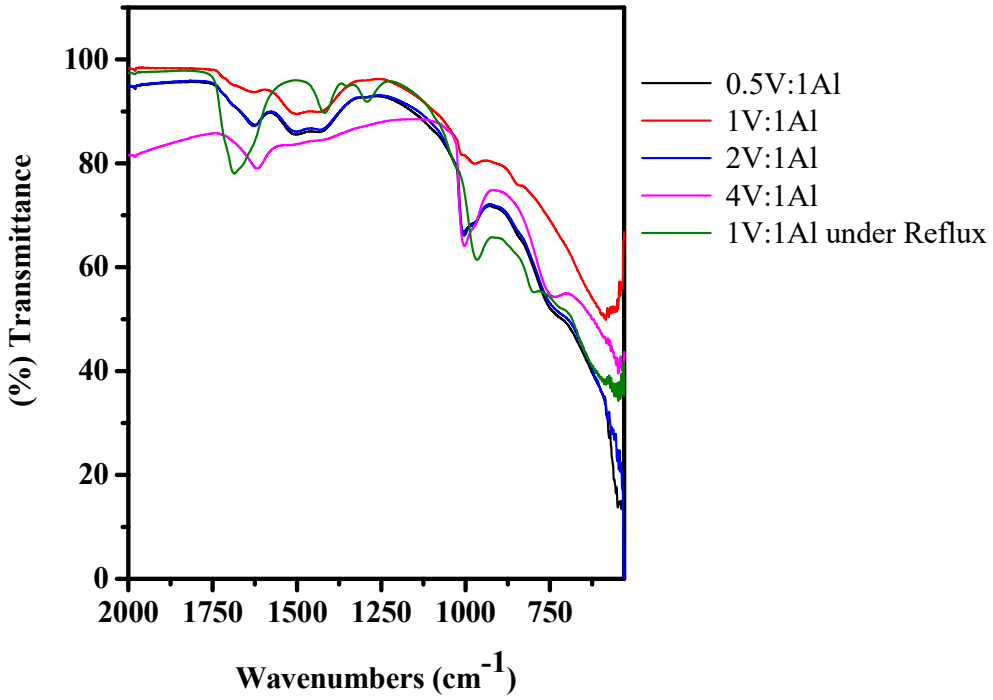

Figure 4- 29. Stack plot the FT-IR spectra of the products synthesized from different ratios

Pyrolysis of the various product was performed using a Vulcan Multi-stage Programmable Furnace, 3-130, under an air atmosphere with ramp of 5 °C/min to 600 °C and a hold for for a 12 hours. FT-IR spectra recorded for the calcined samples are shown in Figure 30 through Figure 34. These show three main absorption bonds in the ranges within 1025 - 880, 860 - 670, 590 - 525 cm^{-1}. These are likely a mix of V-O, Al-O, and Al-O-V vibrational modes. The stack plot representation of the calcined products (Figure 35) shows that the only significant effect of changing the ratio of Al to V is a shifting of the absorption bands at 1015 cm^{-1} to the higher wavenumber 1025 cm^{-1} as the aluminum amount increases. Additionally, the FT-IR of the calcined product from the 1V:1Al reaction performed under reflux had more intense and sharper peaks than the corresponding product from the ambient temperature reaction.

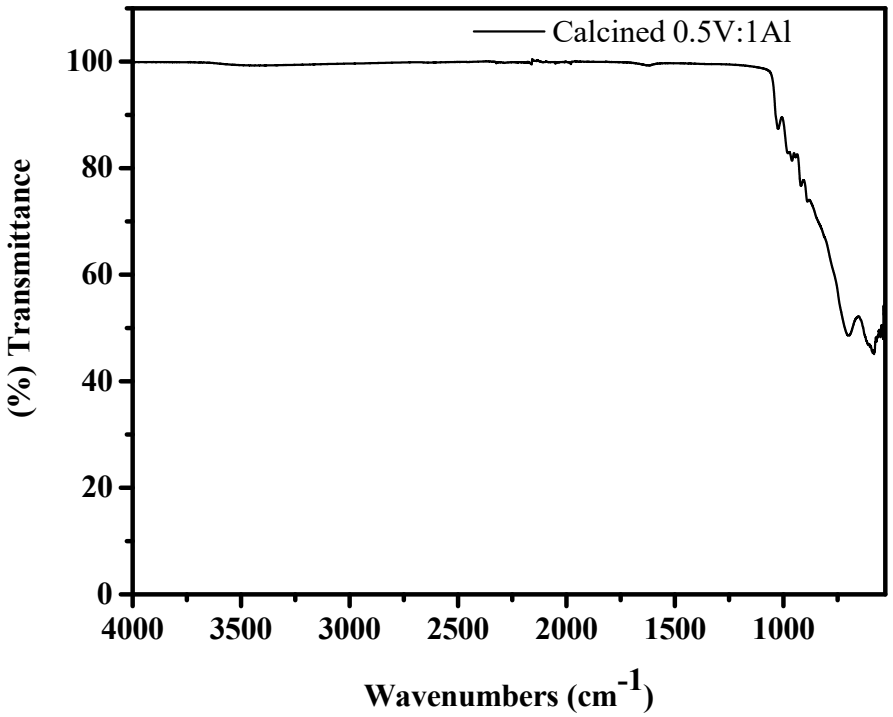

Figure 4- 30. FT-IR spectrum of the calcined product from 0.5V:1Al ratio

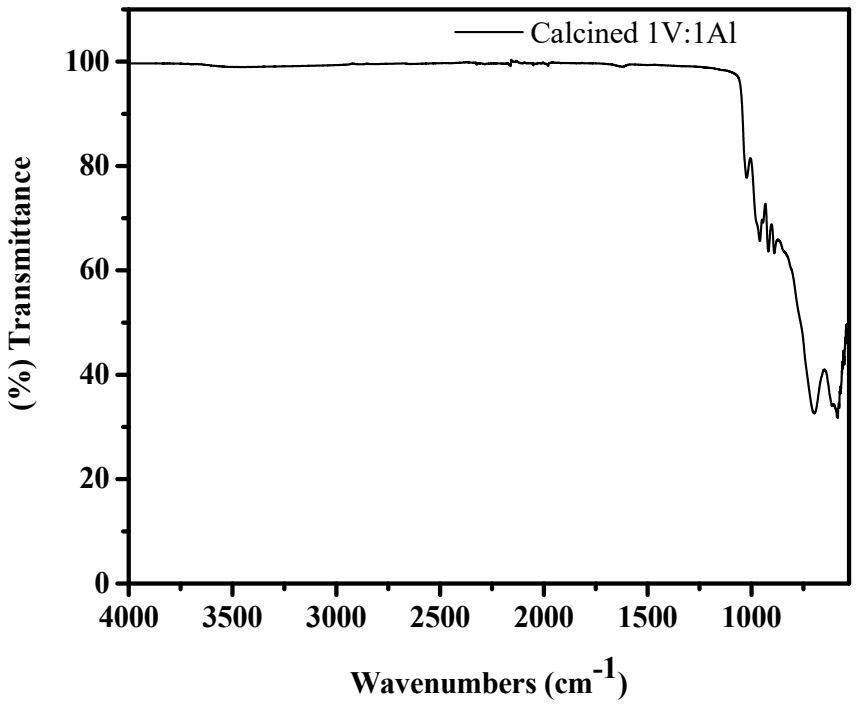

Figure 4- 31. FT-IR spectrum of the calcined product from 1V:1Al ratio

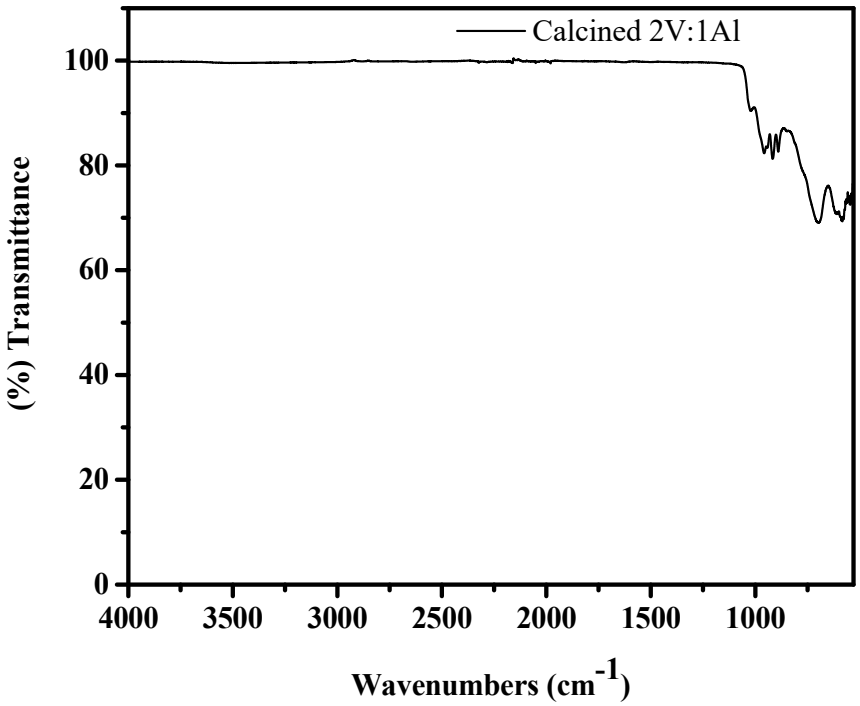

Figure 4- 32. FT-IR spectrum of the calcined product from 2V:1Al ratio

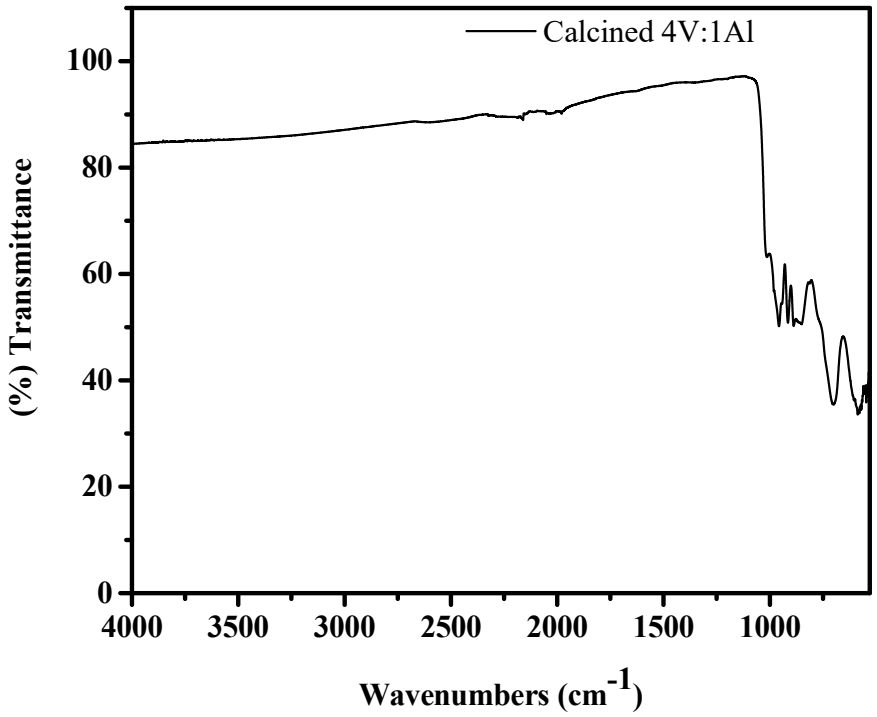

Figure 4- 33. FT-IR spectrum of the calcined product from 4V:1Al ratio

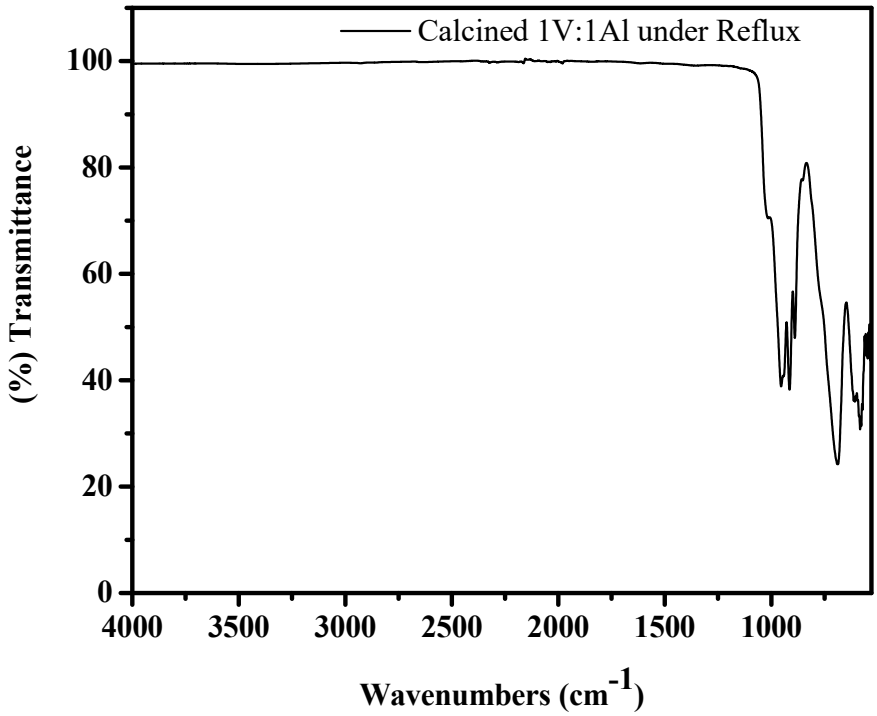

Figure 4- 34. FT-IR spectrum of the calcined product from 1V:1Al ratio under reflux

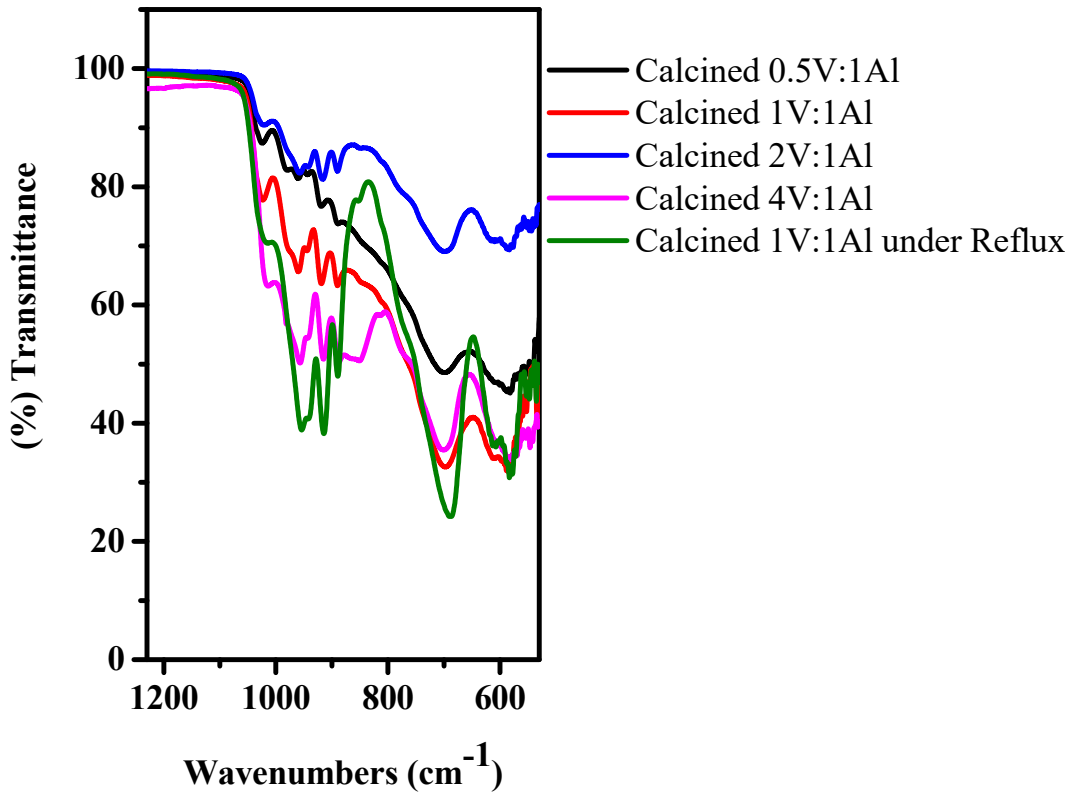

Figure 4- 35. Stack plot the FT-IR spectra of the calcined products synthesized from different ratios of vanadium to aluminum

The X-ray powder diffraction patterns of the solid products show the presence of the triclinic, phase of aluminum orthovanadate, $AlVO_4$ (ICDD #: 01-073-8265, as shown in Figure 36 to Figure 40. However, as shown from the pattern figures and the 3D representation shown in Figure 41 the only phase pure aluminum orthovanadate was obtained by calcination of products resulting from the reaction of aluminum hydroxide with 2 equivalents of vanadyl oxalate at ambient temperature and 1:1 reaction performed under reflux. All other samples also contained aluminum oxide.

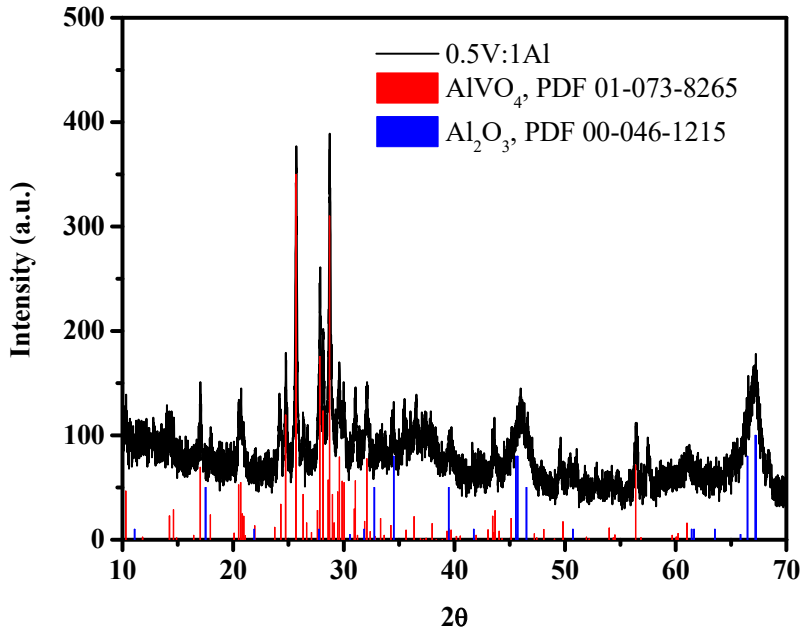

Figure 4- 36. XRD pattern of product formed by vanadyl oxalate (20 ml) and aluminum hydroxide with 0.5V:1Al ratio

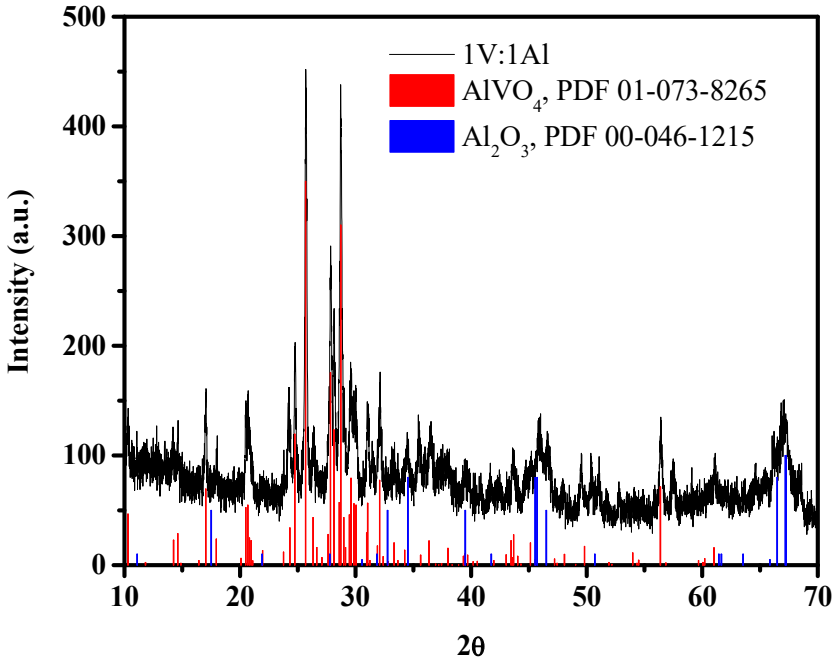

Figure 4- 37. XRD pattern of product formed by vanadyl oxalate (20 ml) and aluminum hydroxide with 1V:1Al ratio

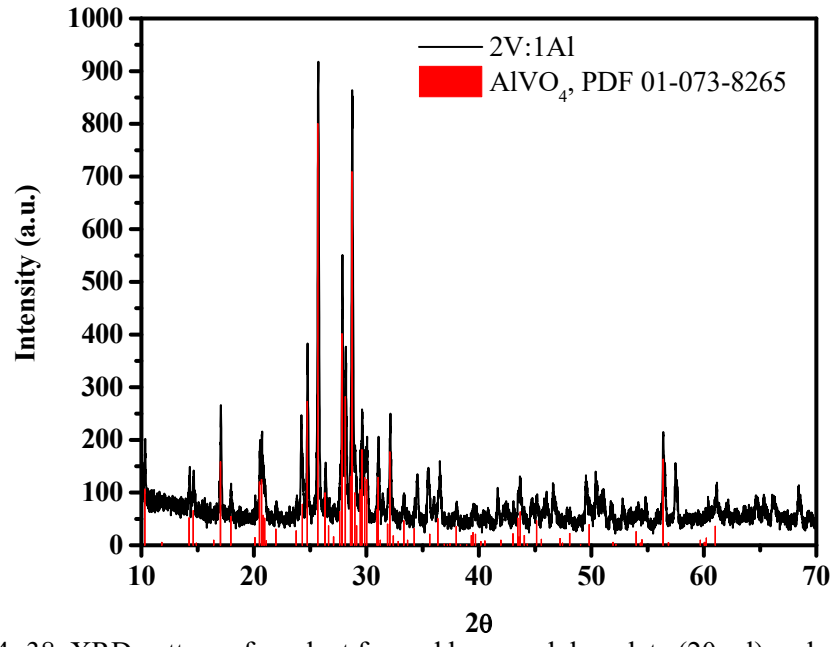

Figure 4- 38. XRD pattern of product formed by vanadyl oxalate (20 ml) and aluminum hydroxide with 2V:1Al ratio

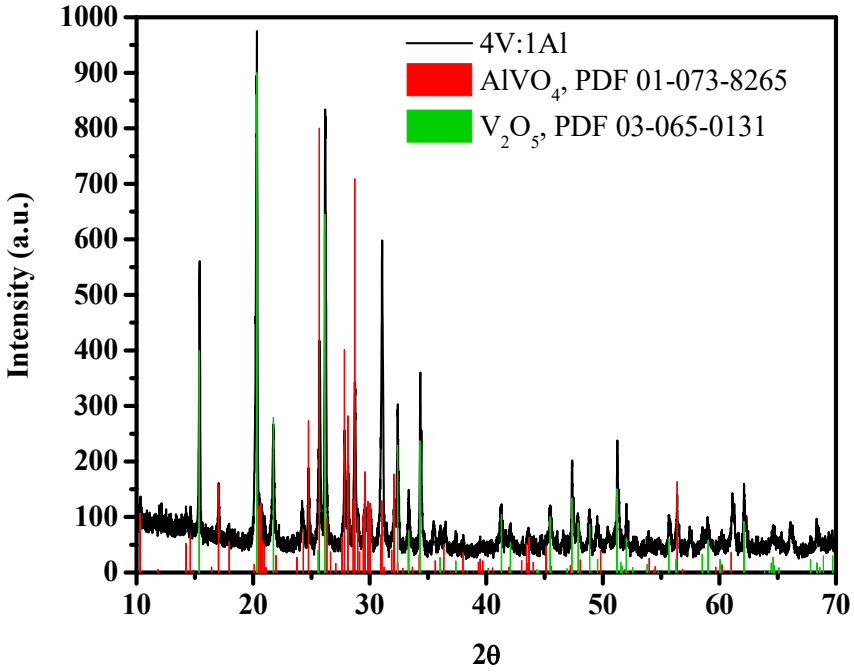

Figure 4- 39.XRD pattern of product formed by vanadyl oxalate (20 ml) and aluminum hydroxide with 4V:1Al ratio

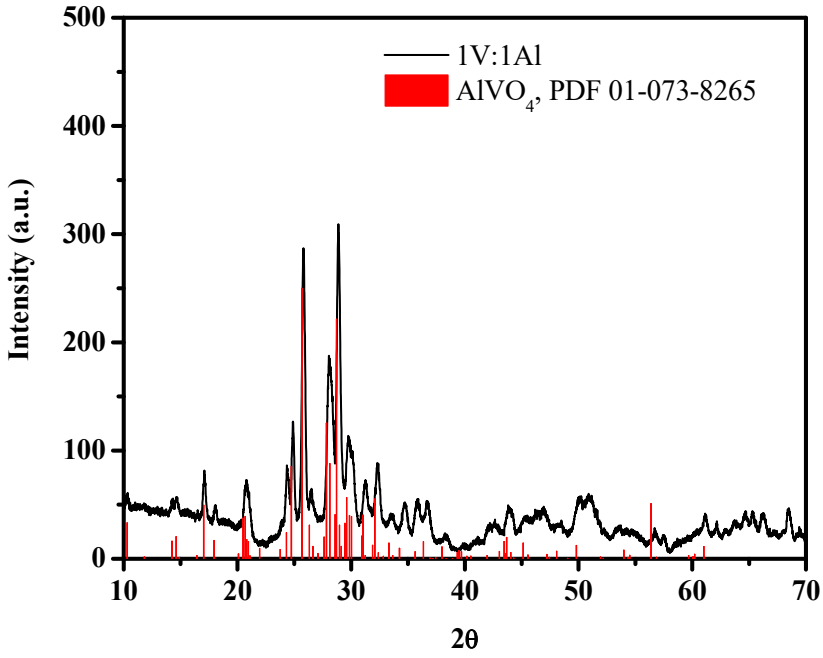

Figure 4- 40. XRD pattern of product formed by vanadyl oxalate (20 ml) and aluminum hydroxide under reflux with 1V:1Al ratio

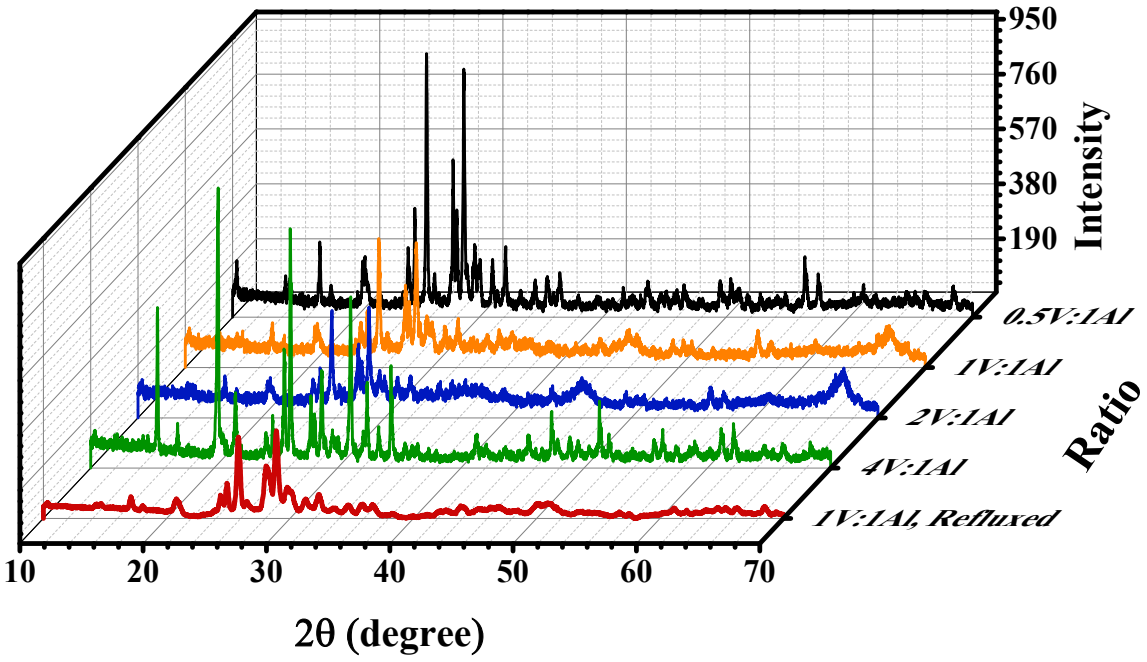

Figure 4- 41. 3D representation of XRD patterns of calcined products resulting from using V:Al different reaction ratios

Figure 42 shows the SEM images for aluminum-vanadium oxyhydroxide precursors synthesized at room temperature and under reflux, before and after calcination. The low magnification images show that the 1V:1Al oxyhydroxide product at room temperature (Figure 42 a) and the 1V:1Al oxyhydroxide product under reflux (Figure 42 b) aggregated in spherical ball shape. The ball shape of the large number of aggregate particles is reduced in size and became fluffier in case of performing the reaction under reflux. This behaviors are shown clearly at higher magnification SEM images of aluminum-vanadium oxyhydroxide precursors at room temperature and under reflux (Figure 42 c and d, respectively). SEM images of obtained aluminum orthovanadtes through calcination of these precursors are shown in Figure 42 e and f. The SEM images indicate that the effect of calcination process on the morphologies in which with increasing temperatures the particles taking a proper shape and the boundaries of particles are well marked. The mean size of those particles for calcined product resulting from precursor formed under reflux is about (98.200 ± 6.279) nm. In addition, as shown in the SEM images for the precursor under reflux with more high magnification (see Figure 43), some small particles tend to assemble into bigger ones and the mean of these smaller size particles is about around 8 nm. EDS spectra are also taken as well as shown in Figure 44, and data tabulated in Table 9. EDS data clearly show that for the room temperature AlV-precursor, the high value of Al account decreased for sample after calcination which indicate that the aluminums on the surface upon pyrolysis of precursors are diffused to form crystalline $AlVO_4$ while for reflux precursor and its calcined products the counts are close to each other and correspond to $AlVO_4$.

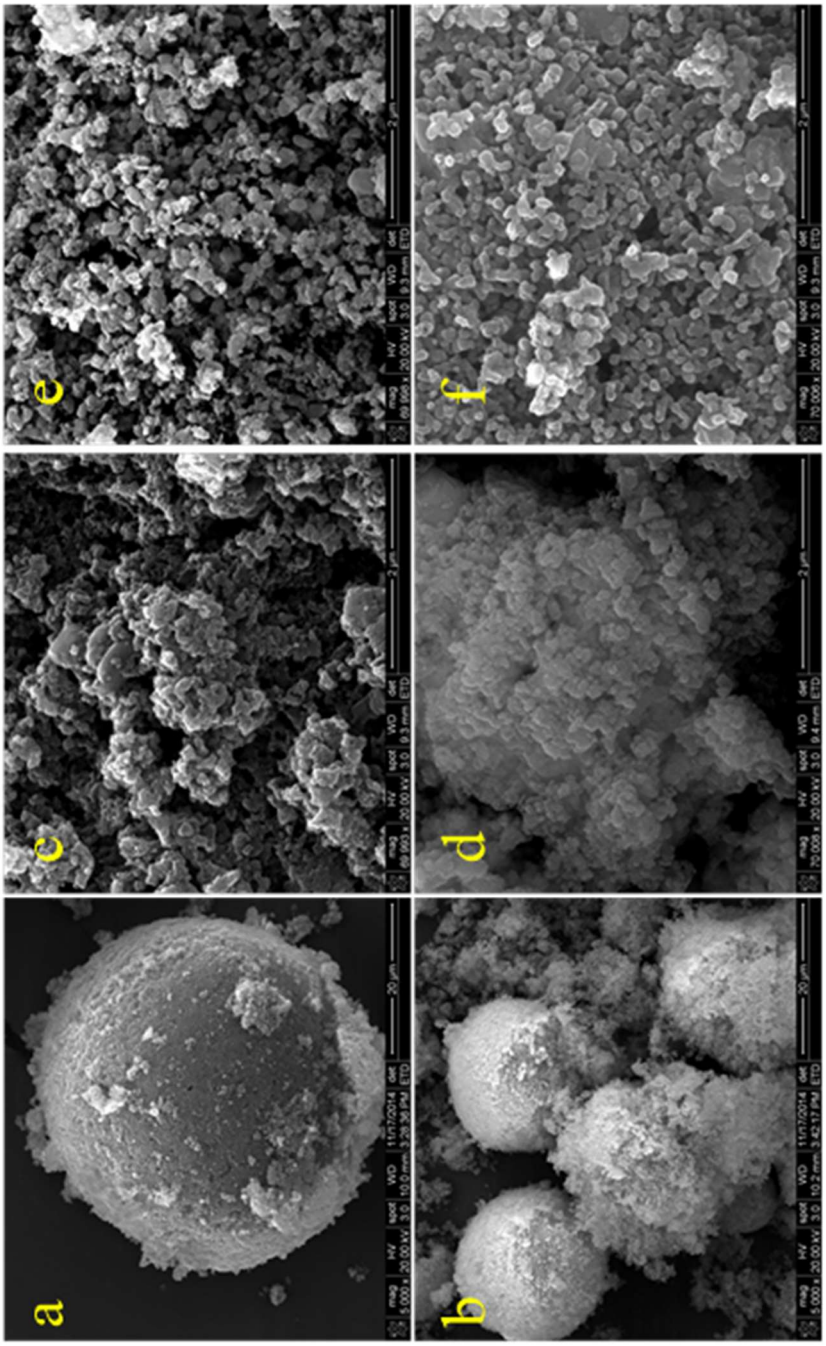

Figure 4- 42. SEM images 1V:1Al oxyhydroxide products synthesized at room temperature (a and c), under reflux (b and d), calcined (R.T.) (e) and calcined (Reflux) (f)

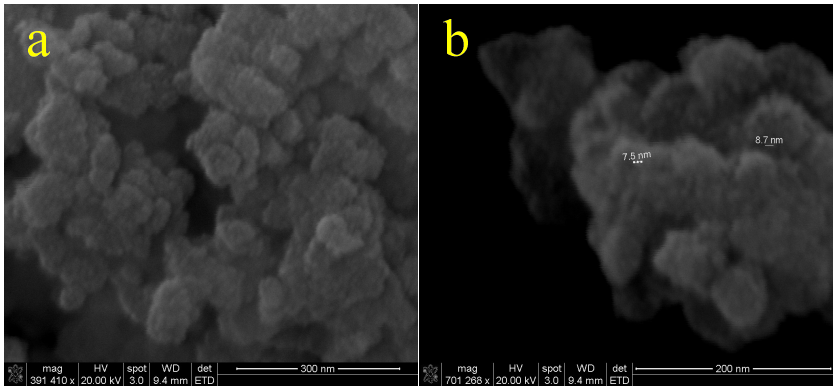

Figure 4- 43. SEM images for the 1V:1Al product under reflux with higher magnification: (a) 391410x (b) 701268x

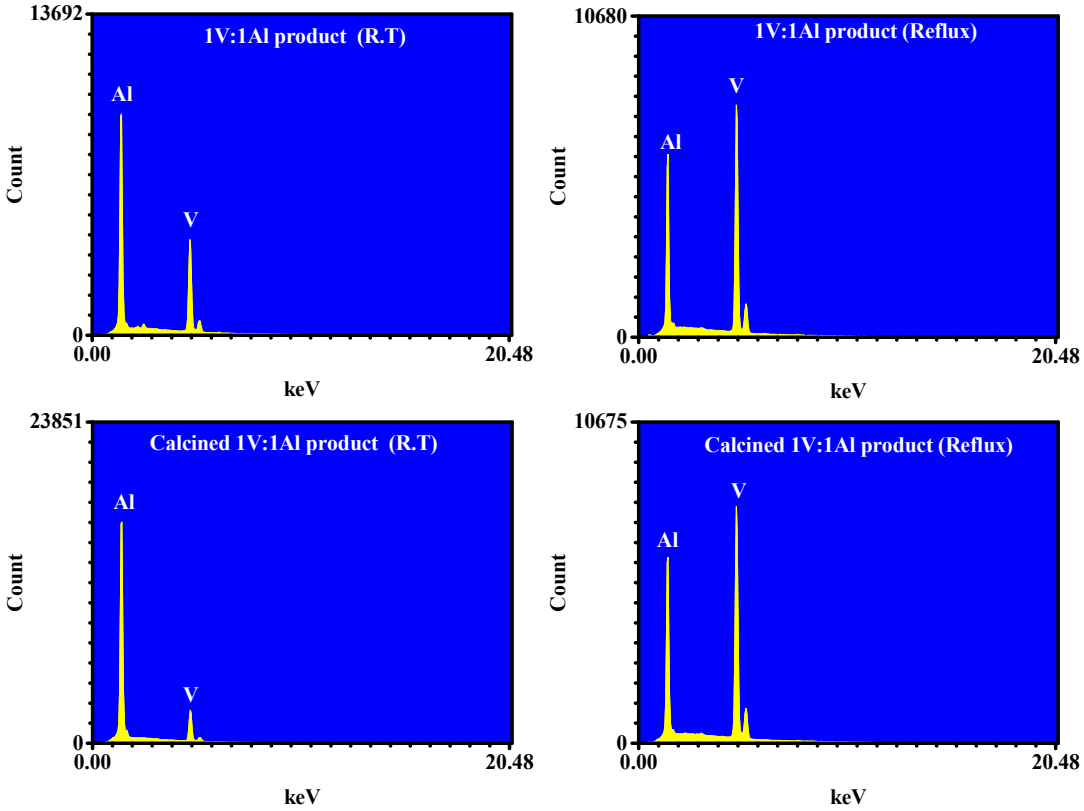

Figure 4- 44. EDS spectra for AlV-products

Table 4- 9. EDS analysis for 1V:1Al products

Sample	Elements	WT%	AT%	Intensity	P/bkg
1V:1Al product (R.T.)	AlL	50.53	65.85	281.161	14.6
	VK	49.47	34.15	156.87	19
1V:1Al product (Reflux)	AlL	27.91	42.23	172.325	11.8
	VK	72.09	57.77	301.447	36.3
Calcined 1V:1Al product (R.T.)	AlL	73.36	83.87	532.982	15
	VK	26.64	16.13	91.334	11.4
Calcined 1V:1Al product (Reflux)	AlL	27.93	42.26	179.883	12.5
	VK	72.07	57.74	314.241	37.1

Surface area of aluminum vanadium oxyhydroxide products and the resulting aluminum orthovanadate products from calcination process were measured using the Brunauer, Emmett, and Teller (BET) method. The crystallite sizes of the materials were calculated using Scherrer equation (see Table 11). The sample produced under reflux displayed a higher surface area and a correspondingly smaller crystallites size after calcination. For both products, calcination markedly lowered the surface area to similar values.

Table 4- 10. Show the surface area measurements of 1V:1Al ratio precursors at room temperatures, under reflux, and the calcined products

Sample	1V:1Al at R.T.	Calcined 1V:1Al at R.T.	1V:1Al under Reflux	Calcined 1V:1Al under Reflux
BET (m^2/g)	41	12	73	16
Crystallite size from XRD (nm)	-	40	-	24

4. Conclusion:

Mixed aluminum vanadium oxyhydroxides were successfully synthesized through reaction of vanadyl oxalate solution with aluminum hydroxide. The effect of reaction conditions, changing reactant ratios and time on the resulting materials have been investigated. Calcination of these obtained mixed aluminum vanadium oxyhydroxide result in formation of aluminum orthovanadate and phase pure of aluminum orthovanadate was only formed for the 2V:1Al ratio. Aluminum plays roles in both formation of the oxyhydroxide and a catalyst for reduction of vanadium by oxalate.

CHAPTER V

SYNTHESIS OF BIMETALLIC VANADIUM OXIDES/OXYHYDROXIDES

1. Introduction:

Metal salts of earth orthovanadate (MVO_4), are used in catalysis [183, 184], gas sensors [185], optical polarizers [186], lithium intercalated electrodes [187], solar cells [188], thin film phosphors [189] unusual magnetic material [190], and many other applications. There are several approaches to synthesize nanostructured MVO_4 materials but hydrothermal [191, 192], and sol-gel [193-195] methods, are most commonly employed. A lot of the preparative methods have drawbacks such as slow diffusion reaction rates and incorporation of impurities.[196] In this regards, low temperature single-source molecular precursor that incorporates the required elements with the correct ratios to synthesis nanomaterials without impurities appears to be more favorable. Previously in Chapter 4, aluminum orthovanadate was successfully prepared via pyrolysis of a mixed aluminum vanadium oxyhydroxide that was synthesized via reaction of aqueous vanadyl oxalate with aluminum hydroxide. Therefore, this chapter reports the synthesis of bimetallic vanadium oxide precursors for MVO_4, M= Zr, Y and La, using oxide precursors as that used for synthesis of $AlVO_4$ described in Chapter 4 in detail. Infrared spectroscopy, thermal gravimetric analysis, and X-ray powder powder diffraction was employed to characterize the precursor compounds and the corresponding metal orthovanadates. The influence of the reaction time, temperature and the precursor's

stoichiometry on the decomposition temperature, particle size, and surface area of resulting metal orthovanadates was investigated.

2. Experimental:

2.1. Material

Vanadyl oxalate solution was synthesized as described previously in Chapter 4. Commercially available reagents of ACS grade purity or better were used without any further purification. Zirconium (IV) hydroxide, $Zr(OH)_4$ (97 %) was obtained from Aldrich Chemical Company. Yttrium (III) oxide, Y_2O_3 (99.9%) was obtained from Johnson Matthey Inc., Yttrium (III) oxide nanopowder, <50 nm particle size is purchased from Aldrich. Lanthanum (III) oxide, La_2O_3 (99%) was purchased from Alfa Aesar. Water was purified by reverse osmosis and deionization to a resistance of 18MΩ.cm. Vanadium Ultra Scientific. Yttrium, lanthanum, zirconium (1,000 ppm) standards were purchased from Ricca chemical company.

2.2. Analysis techniques

This chapter utilizes the same analysis techniques described in pervious chapter 4.

2.3. Synthetic procedure

In a similar fashion to reaction of vanadyl oxalate with aluminum hydroxide, vanadyl oxalate solution was mixed with metal hydroxide or oxide with varying molar ratios at room temperature. Reaction with the ratio of 1V:1M were also performed under reflux. The mixtures were separated by centrifugation and the powders washed thoroughly with distilled water and then dried under vacuum. The resulting products are calcined at 650 °C for 12 hours with heating rate of 5°C/min.

3. Results and discussion:

3.1. Reaction of Vanadyl Oxalate Solution and Zirconium Hydroxide

Reaction of zirconium hydroxide with aqueous vanadyl oxalate solutions were performed at room temperature for 7 days and under reflux for 24 hours for 1:1 molar ratio. The blue color of

the vanadyl oxalate/zirconium hydroxide mixture solution slowly changed to green while mixing at room temperature. Table 1 displays the amount of reactants used. Table 1 also shows the ceramic yield from pyrolysis.

Table 5- 1. Different ratios of zirconium hydroxide were mixed with vanadyl oxalate solutions

Starting materials (g)		Reactant ratio V:Zr	Reaction condition	Product Weight (g)	Ceramic yield (%)
VOC_2O_4	$Zr(OH)_4$				Oven at 650 °C
20.029	4.108	0.5:1.0	R.T	4.134	80.1
20.048	2.054	1.0:1.0	R.T	1.865	81.3
20.029	1.027	2.0:1.0	R.T	0.827	81.2
20.062	0.514	4.0:1.0	R.T	0.377	78.6
39.915	4.108	1.0:1.0	Reflux	4.696	74.0

The changes in pH during the course of reactions are shown in Figure 1. The pH at the beginning was 1.8 and it increased up to average range of pH 2.8 for both the V:Zr ratios of 2:1 and 1:1 reaction, pH 2.2 for the 1:2 reaction, and pH 2.1 for the 1:4 reaction. This increasing in pH is likely due to removal of acid vanadyl complex from water. Figure 2 shows the UV-VIS spectra for the separated solution from vanadyl oxalate/zirconium hydroxide reactions. These displayed the characteristics bands for the vanadyl ion. This indicates the presence of unreacted vanadyl. The absorbance of V^{4+} decreased with increasing amount of use zirconium and this can be seen clearly by plotting the total vanadyl ion concentrations versus the mole ratio employed as shown in Figure 3. There is a linear decrease with increasing $Zr(OH)_4$ reactant due to the formation of number of moles of V^{4+} based on UV-VIS spectra were close to those determined by MP-AES analysis (Table 2) suggesting that the remains unreacted vanadium exists only as V^{4+} ions. Note that the reactions performed at room temperature reach a maximum solution concentrate of vanadium at the 1:1 molar ratio. As the molar equivalents vanadyl oxalate are unreacted, the [V] remans around 0.25 M. Thus, any additional vanadium beyond 1:1 must be incorporated into the solid product.

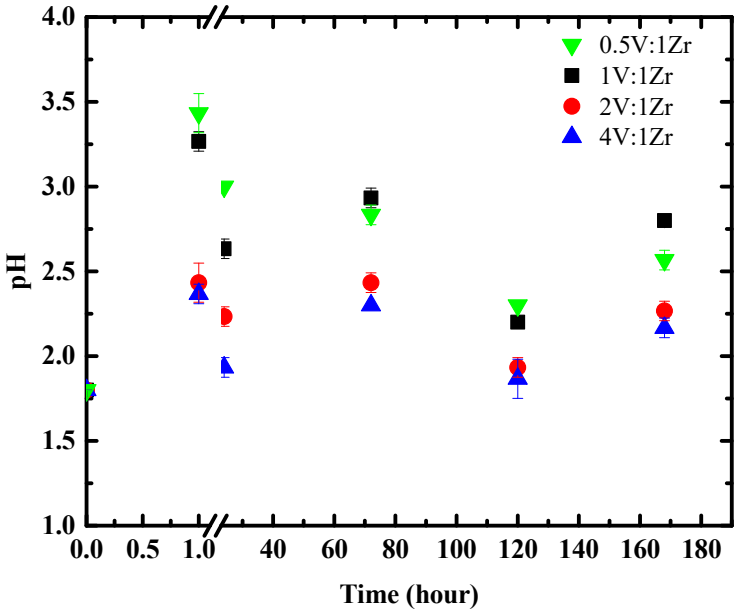

Figure 5- 1. The change of pH over time for zirconium hydroxide/vanadyl oxalate reactions

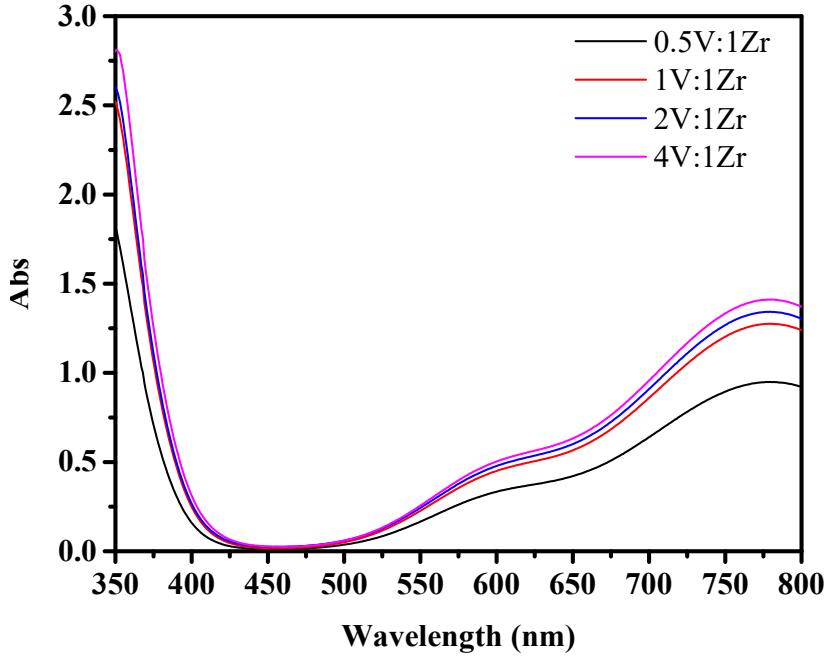

Figure 5- 2. UV-VIS spectra for vanadyl oxalate/zirconium hydroxide solutions

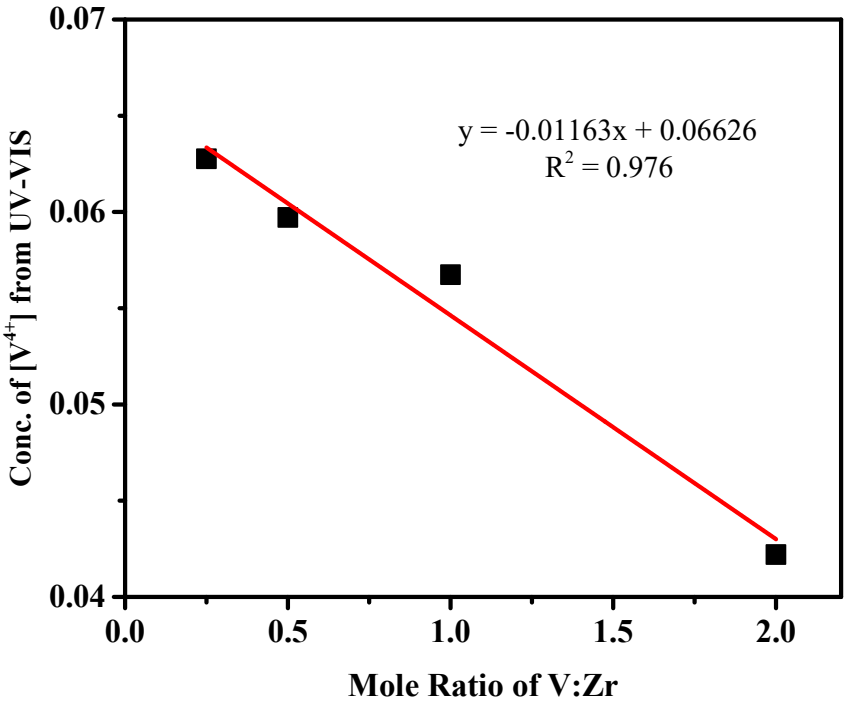

Figure 5- 3. Concentration of vanadyl ions vs V:Zr molar ratios

Table 5- 2. Analytical results to V4+ and total vanadium concentration

Reactant Moles		Reactant Mole Ratios	Mole of V based on MP-AES	Moles of V^{4+} based on UV-VIS
V	Zr	V/Zr		
0.0129	0.0258	0.50	0.0037	0.0034
0.0129	0.0129	1.00	0.0049	0.0045
0.0129	0.0064	2.00	0.0051	0.0047
0.0129	0.0032	3.99	0.0053	0.0049

XRD analysis showed that the products were amorphous (see Figure 4 as an example). Figure 5 shows the FTIR spectra for $Zr(OH)_4$, solid VOC_2O_4, and the reaction products. All spectra have the broad overlapping peaks for hydroxyl groups and water. These mostly occurred at same position except for VOC_2O_4 and the refluxed 1V:1Zr product. The peak at 1600 cm^{-1} in VOC_2O_4 is due to C=O stretching of oxalate is not present in the products indicating that they do not contain oxalate. The peak at 1625 for cm^{-1} due to water and/or Zr-OH bending vibrations is shifted to 1680 and 1690 cm^{-1} for the refluxed product. The peaks at 1545 and 1335 cm^{-1} correspond to vibration

of the bridging hydroxyl groups of $Zr(OH)_4$ [197-199] also disappear during the reaction. Absorption bands at 1025 and 820 cm^{-1} due to V=O and –V-O-V- vibrations [200-202] appeared in the refluxed reaction product. Additionally, new bands were observed in this product at 2990, 1410, 1350, and 1310 cm^{-1} that can be assigned to bridging water and hydroxyl groups. [197-202] The carbon content in the 1V:1Zr refluxed product was 2.03 % indicating that only a small amount of oxalate was present, most likely sorbe on the surface of the product. The thermal gravimetric curves of the products are shown in Figure 6. These all are similar to each other and show two overlapping steps. These are likely dehydration followed by dehydroxylation. For the ambient temperature product, the ceramic yields decreased with increasing ratio of vanadyl oxalate to $Zr(OH)_4$ indicating more extensive formation of ZrV-oxyhydroxide product. The refluxed product has the lowest ceramic yield and therefore the most complete reaction. The total average of the weight loss could be attributed the dehydration and decomposition of oxyhydroxide group (two water molecules lost). It is speculated that the experimental x value in $V_nZrO_2 \cdot xH_2O$ are 1.45, 1.67, 1.70, 1.77, and 2.21 for 0.5, 1, 2, and 4 V:1Zr and refluxed 1:1 product, respectively.

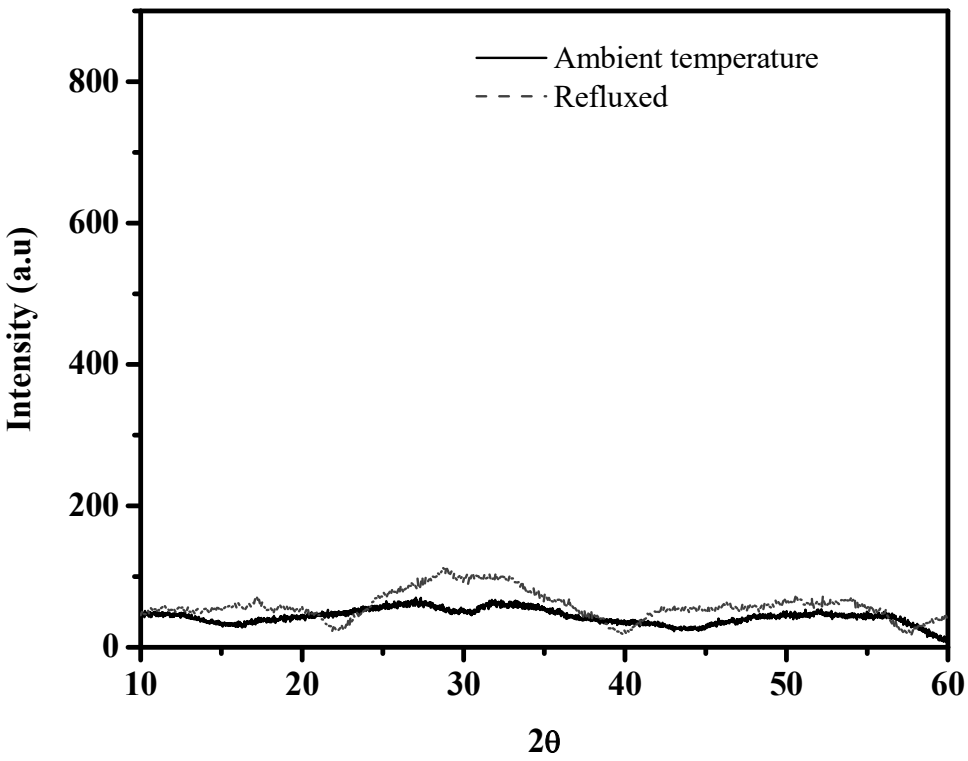

Figure 5- 4. XRD pattern of precursors synthesized from 1:1 vanadyl oxalate and zirconium hydroxide at ambient temperature and under reflux

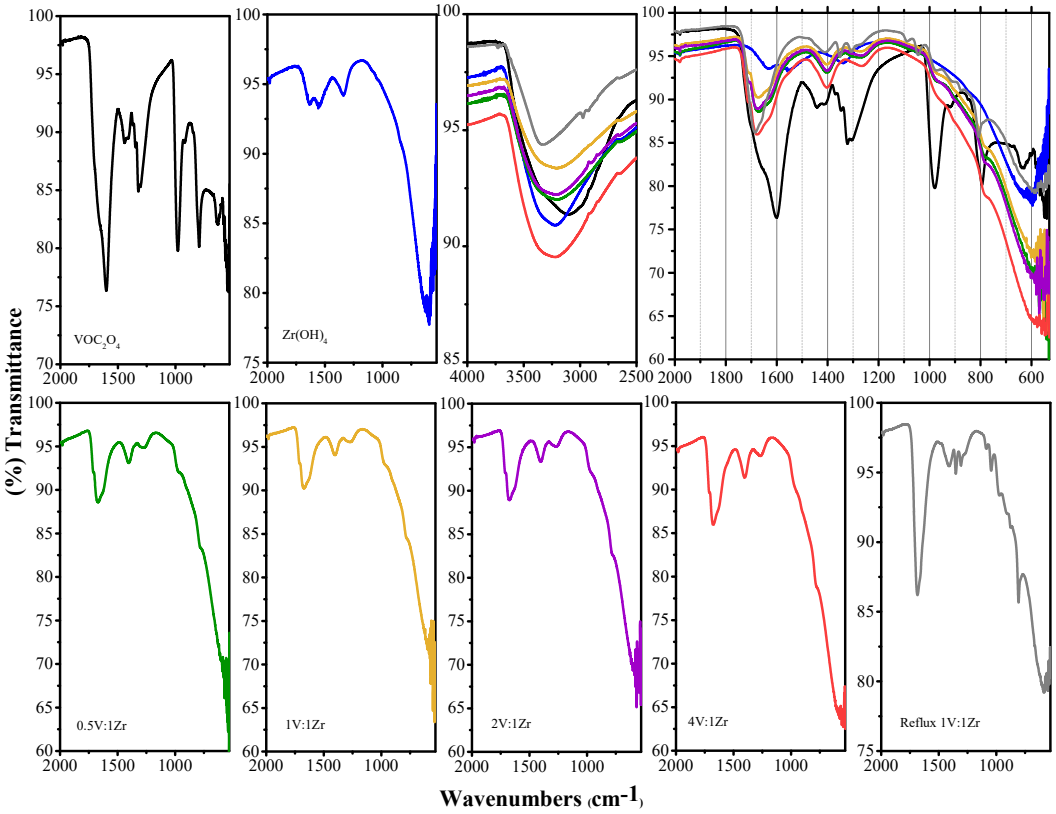

Figure 5- 5. FT-IR spectra of ZrV-products, (The overlapped spectra correspond to the colors of the individual plots)

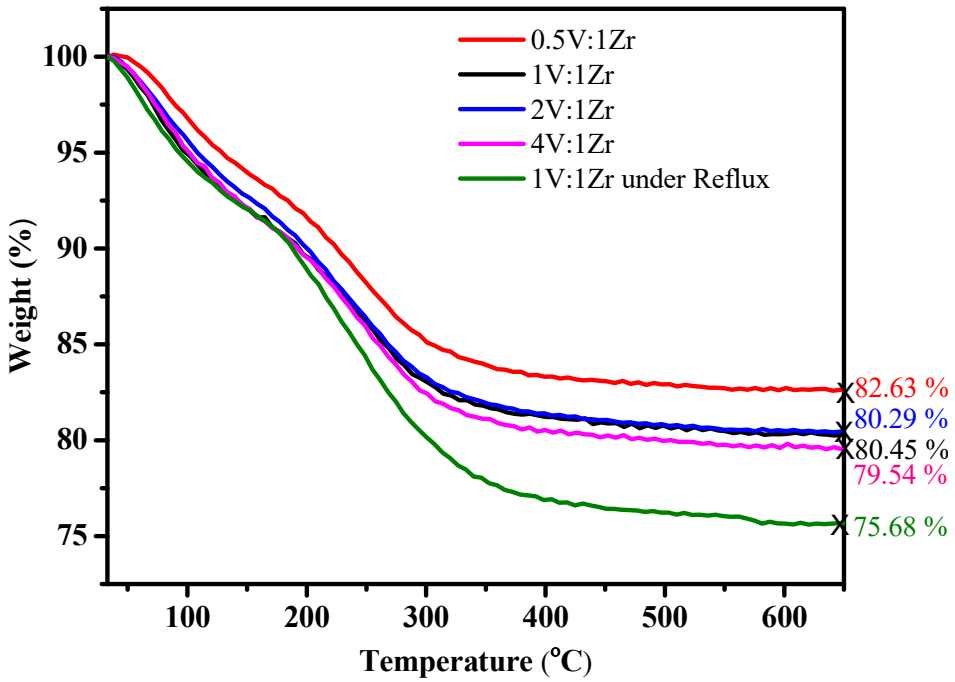

Figure 5- 6. Thermogravimetric analysis curves of the ZrV-products

Figure 7. shows the FTIR spectra of the calcined ZrV-products. All spectra display bands at 580, 980, and 1120 cm^{-1} that can be assigned to vibrational modes of V=O and V-O-V of the vanadium zirconia phase. These bands are more defined and intense and shifted in the calcined product form the refluxed precursor. The bands at 1500, 1418, 1345, and 1025 cm^{-1} could be assigned to V-OH and the sharp band at 775 cm^{-1} to the ZrO_6 octahedra stretching mode.[200-202] Calcination of ZrV-oxyhydroxide products resulted in formation of crystalline materials as shown in Figure 8. The diffractograms were similar for all products with different ratios at room temperature and refluxing of 1:1 ratio reactions in which both tetragonal ($V_{0.1}Zr_{0.9}O_2$) and monoclinic ($V_{0.01}Zr_{0.99}O_2$) phases of vanadium zirconia were detected. These spectra are very similar to the vanadium doped zirconia prepared by the Pechini process. [203, 204] Essentially, there are tetragonal and monoclinic doped ZrO_2 phases present. Calcination of the product from the refluxed1:1 product had a larger amount of the tetragonal $V_{0.1}Zr_{0.9}O_2$ phase and possibly some zirconium vanadate (ZrV_2O_7). Refluxes lead to higher vanadium content and this contributes to the formation of zirconium vanadate (Figure 9). [205] EDS analysis of the 1:1 precursors and their calcined products are shown in Figure 10. Table 3 shows that the as-prepared and calcined product from ambient temperature reaction and the product from refluxing all have approximately 10 mole % of vanadium in keeping with the XRD results. The result for the uncalcined refluxed precursor is high (ca.20%). This is indication of heterogeneity in the sample. Presumably the vanadium rich phase contributes to formation of ZrV_2O_7.

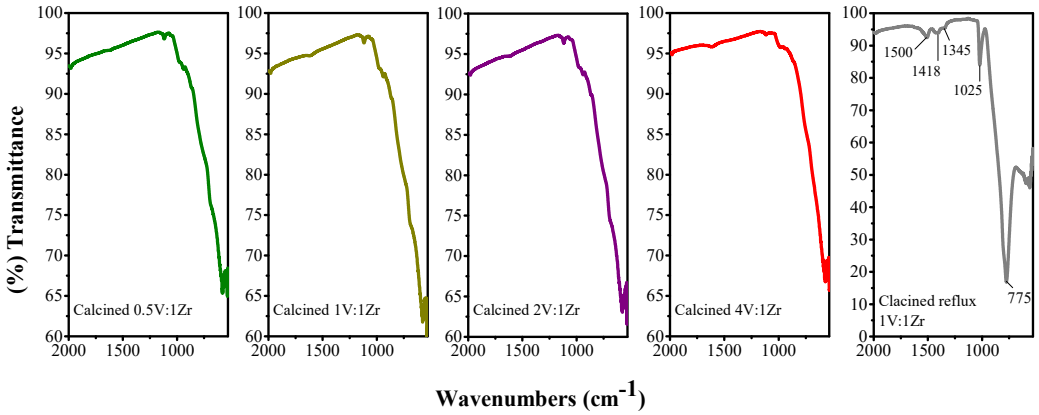

Figure 5- 7. FTIR of calcined of ZrV-products

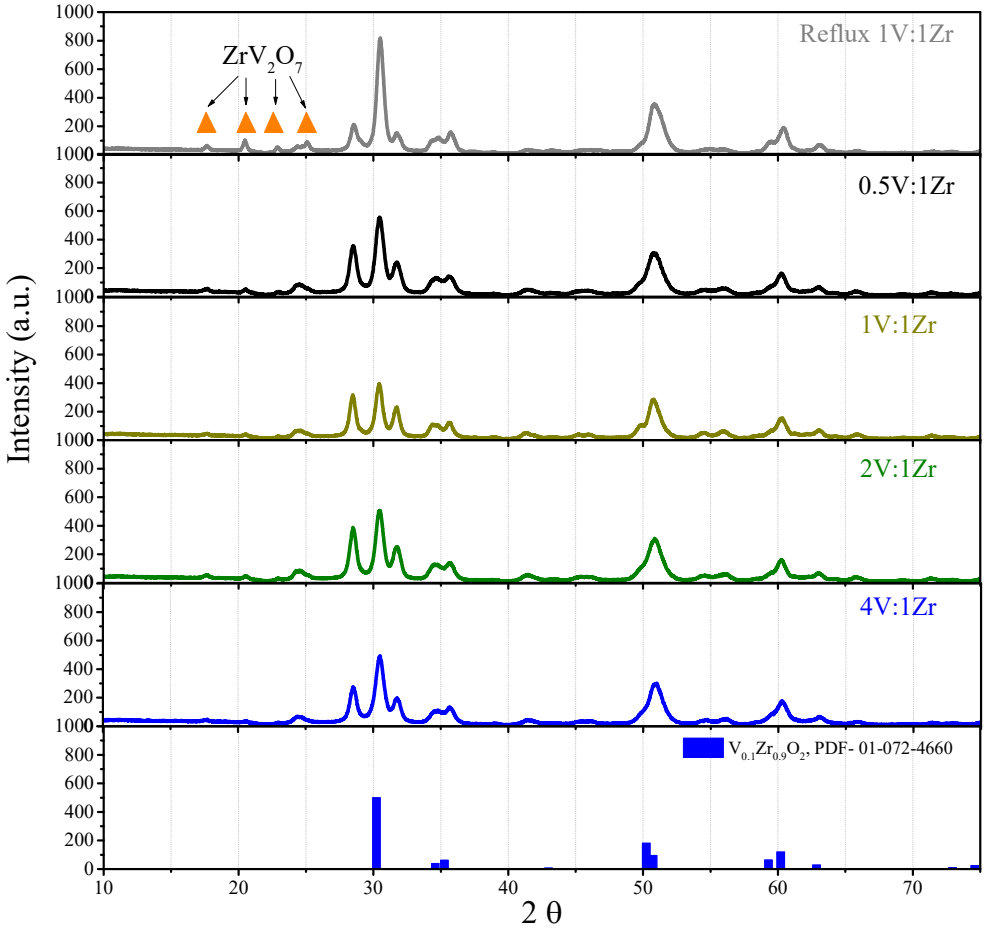

Figure 5- 8. XRD patterns of ZrV-products

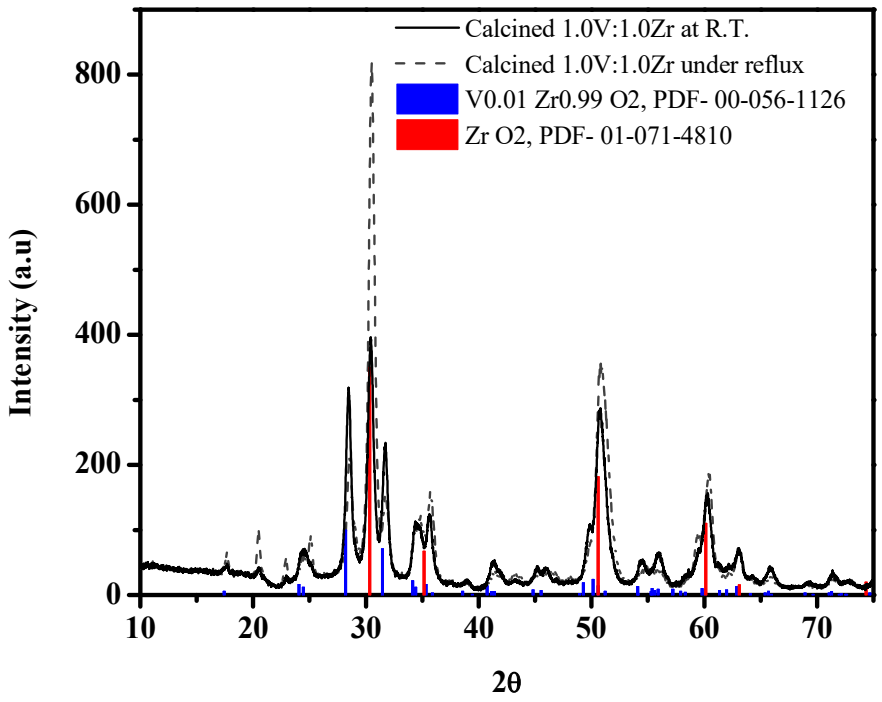

Figure 5- 9. XRD pattern of the calcined ZrV-products

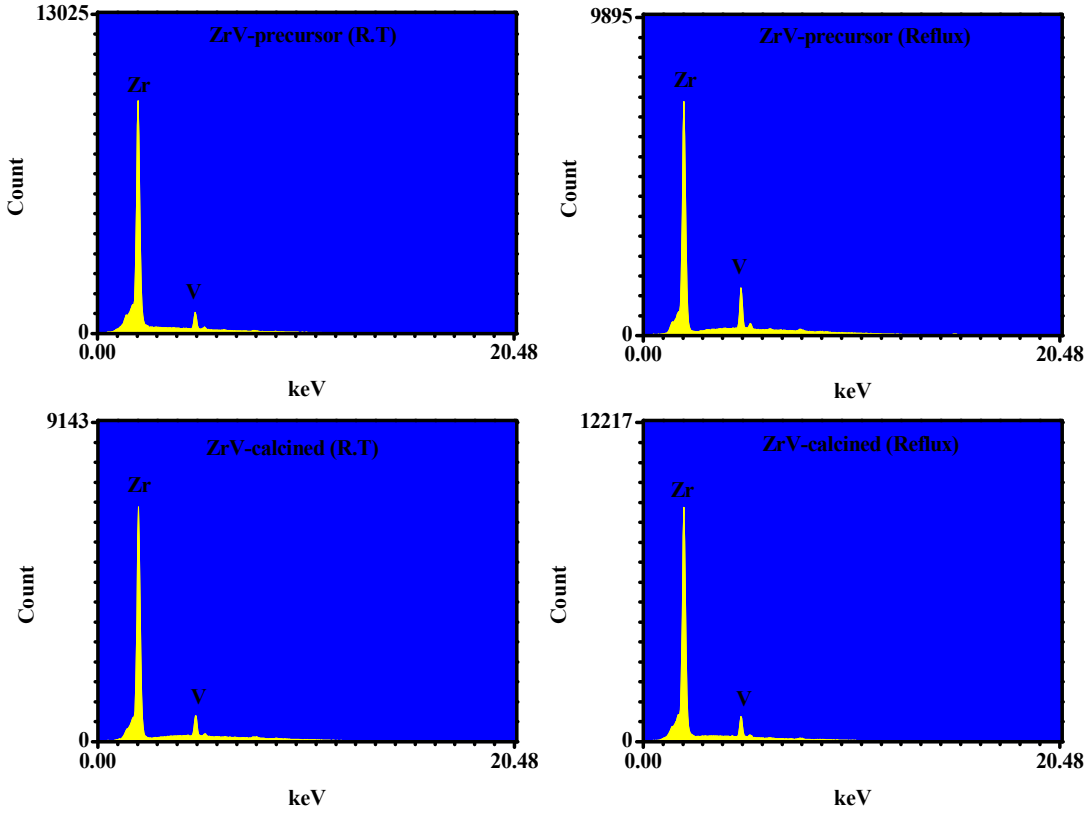

Figure 5- 10. EDS spectra for ZrV-products

Table 5- 3. EDS quantitative analysis for the 1:1 Zr:V

Sample	Elements	WT%	AT%	Intensity	P/bkg
Precursor (R.T.)	ZrL	94.42	90.43	294.907	9.6
	VK	5.58	9.57	27.858	3.2
Precursor (Reflux)	ZrL	87.34	79.39	227.519	26.6
	VK	12.66	20.61	53.614	5.3
Calcined (R.T)	ZrL	93.47	88.89	207.773	23.6
	VK	6.53	11.11	23.238	2.5
Calcined (Reflux)	ZrL	93.75	89.33	281.166	12.3
	VK	6.25	10.67	30.016	2.9

Figure 11 shows the SEM images of the 1:1 precursors before and after calcination. The room temperature produced a product that was co-posed of spherical aggregates of smaller particle (Figure 11 a) and these mostly remained unchanged after calcination (Figure 11 c) although the primary particles grew slightly larger and some smaller aggregates with random shapes formed. On the other hand, the refluxed product was composed of aggregate thin sheets (Figure 11 b) to small monodisperse spherical particles that are aggregated to each other (Figure 11 d). The aggregated particles cumulative in large number of grape clusters shape as seen in Figure 12. Surface areas were measured using the Brunauer, Emmett, and Teller (BET) method and crystallite sizes were calculated using the Scherrer equation and the results are provided in Table 4. The product of the 1:1 reaction performs at R.T. had the highest surface area equal to 254 m^2/g (large number of spherical particles with average of size 43 ± 9 nm based on the SEM image). Surface area data shows the effect of calcination process on the morphologies in which with increasing temperatures resulting in decreasing the surface area.

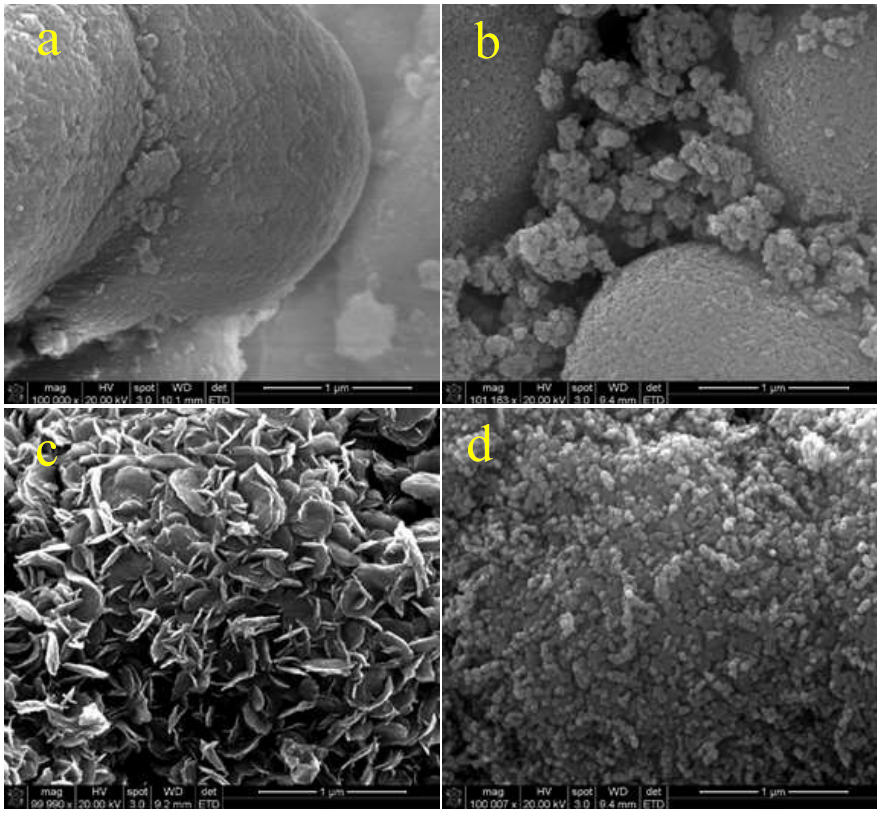

Figure 5- 11. SEM images for ZrV-oxyhydroxide precursor synthesized at room temperature (a), precursor under reflux (c), calcined (R.T.) (b) and calcined (Reflux) (d)

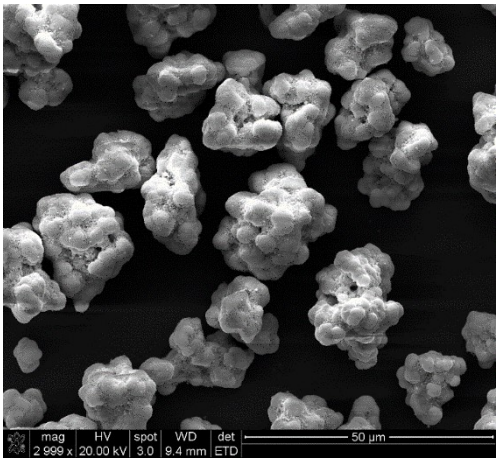

Figure 5- 12. SEM image with low magnification for calcined ZrV-oxyhydroxide precursors synthesized at room temperature

Table 5- 4. Surface area measurements of 1V:1Zr ratio precursors at room temperatures, under reflux, and the calcined products

Sample	BET (m^2/g)	Crystallite size from XRD (nm)	Particle size from SEM (nm)	Particle shape from SEM
1.0V:1.0Zr at R.T.	254	NA	43± 9	Spherical particle
Calcined 1.0V:1.0Zr at R.T.	16	16.0 ± 1.1	60 ± 14	Spherical particle
1.0V:1.0Zr under Reflux	229	NA	310 ± 19	Thin-sheets
Calcined 1.0V:1.0Zr under Reflux	16	14.0 ± 1.3	50 ± 5	Spherical particle

3.2.Reaction of Vanadyl Oxalate Solution and Yttrium Oxide

Reactions of yttrium oxide with aqueous vanadyl oxalate were performed at room temperature for 7 days. In the case of the equimolar reaction, an experiment was also performed at reflux. Table 5 displays ratios of yttrium oxide to vanadyl oxalate that were utilized. Table 5 also lists the ceramic yields from pyrolysis of the solid reaction products at 650 ˚C.

Table 5- 5. Reaction conditions, yields, and ceramic yields

Starting materials (g)		Reactant ratio V:Y	Reaction condition	Product Weight (g)	Ceramic yield (%)
VOC_2O_4	Y_2O_3				Oven at 650 ˚C
20.006	2.912	0.5:1.0	R.T	4.086	81.8
20.084	1.456	1.0:1.0	R.T	2.366	77.8
20.000	0.728	2.0:1.0	R.T	1.269	71.5
20.008	0.364	4.0:1.0	R.T	0.815	62.4
40.000	2.912	1.0:1.0	Reflux	8.096	61.8

The change in pH over time of the yttrium oxide and vanadyl oxalate reactions was recorded and plotted as shown in Figure 13. The pH at the beginning with is 1.8 and it increased up to average range of pH 3.3 for V:Y ratios of 4, 2 and 1, and pH 3.7 for V:Y of 0.5. The pH increase occurs due to removal of acidic vanadyl ions from solution. Figure 14 shows the UV-VIS spectra of the reaction mixtures after solid product removal. The absorptions of vanadyl are decrease with increasing yttrium amount and new unresolved peaks grew in. Notably, isobestic points were observed indicating a reaction where one vanadyl complex is converted to one new vanadyl complex. The total vanadyl ion concentrations from UV-VIS versus the mole ratio of the reaction (Figure 15) shows that as the amount of yttrium increased the total vanadium concentration decreased non-linearly. Table 6 shows the number of moles of V and Y ions based on both UV-VIS spectra at absorbance of λ_{max} equals to 780 nm (for V^{4+}) and MP-AES data using 438.472 and 371.029 nm wavelengths for V and Y, respectively. The number of moles of V^{4+} based on UV-VIS

spectra were close to those determined based on MP-AES analysis. Indicating that only V^{4+} was present in the solution. These solutions are unstable and precipitate after 1 month.

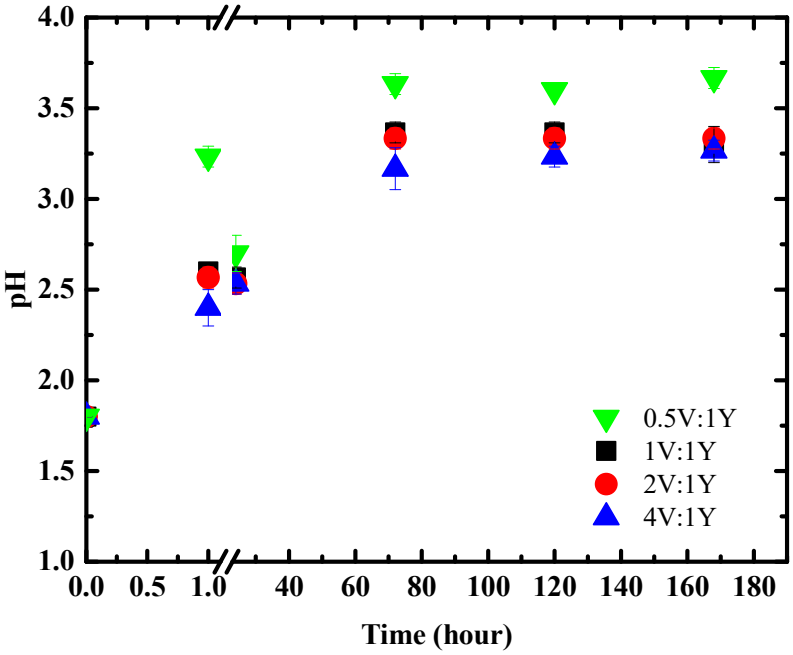

Figure 5- 13. The change of pH over time for yttrium oxide and vanadyl oxalate reactions

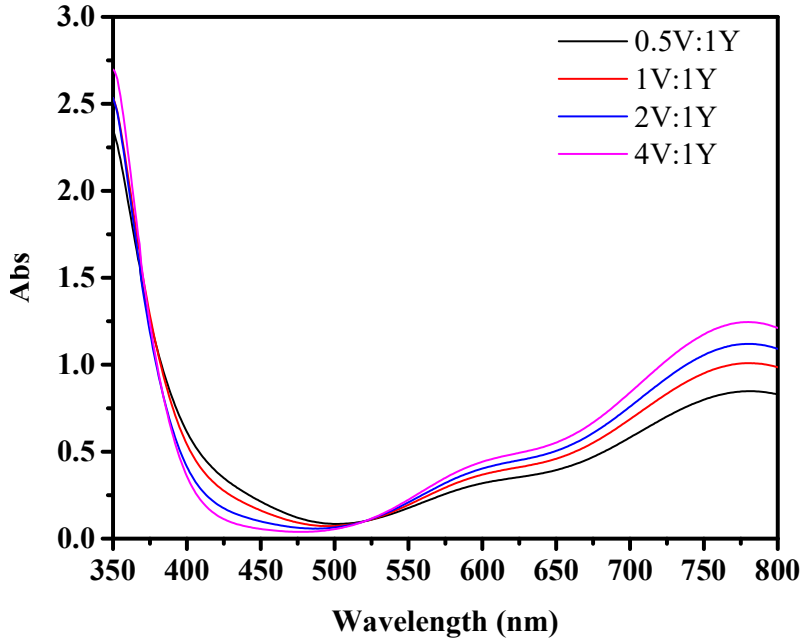

Figure 5- 14. UV-VIS spectra for vanadyl oxalate/ yttrium oxide solutions

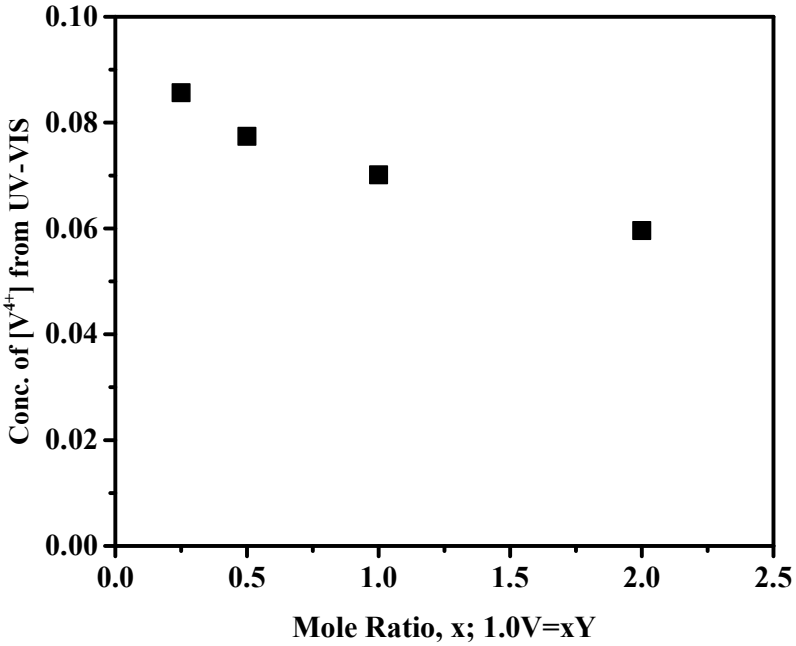

Figure 5- 15. Conc. of vanadyl ion based on UV-VIS data vs V/Y mole ratios, x

Table 5- 6. Comparison between MP-AES and UV-VIS data for the aqueous reaction product

Reactant Moles		Solution Color	Reactant Mole Ratios	Product Moles Based on MP-AES		V^{4+} Moles Based on UV-VIS
V	Y		V/Y	V	Y	
0.0129	0.0258	Colorless	0.50	0.0031	0.0010	0.0031
0.0129	0.0129	Colorless	1.00	0.0037	0.0012	0.0036
0.0129	0.0065	Dark Greenish - Blue	2.00	0.0042	0.0014	0.0040
0.0129	0.0032	Dark Greenish-Blue	4.00	0.0045	0.0016	0.0044

Figure 16 shows the FTIR spectra for solid VOC_2O_4, Y_2O_3, and the reaction products. Characteristic vibration bands for oxalate, Y-O, [206-208] V=O and –V-O-V- were observed. New bands were observed for the yttrium oxide/vanadyl oxalate product obtained produced by refluxing of the mixture. These were at 3598 (s,sh), 1639 (s), 958, 760, and 611 cm^{-1}. The carbon content of the 1:1 products were 4.58 for the room temperature reaction and 7.40 % for the refluxed reaction. Based on these data, it could be that the products contain oxalate. The XRD patterns of the products

(Figure 17) shows unreacted Y_2O_3 of the ambient temperature products. However, another crystalline phase was detected in the product produced with highest ratio of vanadium to yttrium (4:1). The refluxed product had unidentified. Therefore, peaks did not match any patterns present in the ICDD data base may be one or more new phases. addition to remaining yttrium oxide matched with yttrium oxalate for sample with ration 4.0V:1.0Y. XRD pattern for sample obtained under reflux did not match with any crystalline phase which may be form one or more new phases. Thermal gravimetric analysis results for the solid products are shown in Figure 18. The TGA curves are very similar to each other for the ambient temperature products but that of the refluxed product follows a different decomposition pathway and has the lowest ceramic yield. The ceramic yields of the room temperature products are strongly dependent on the ratio of V:Y. This is a reflection of incorporation of oxalate in the solid products.

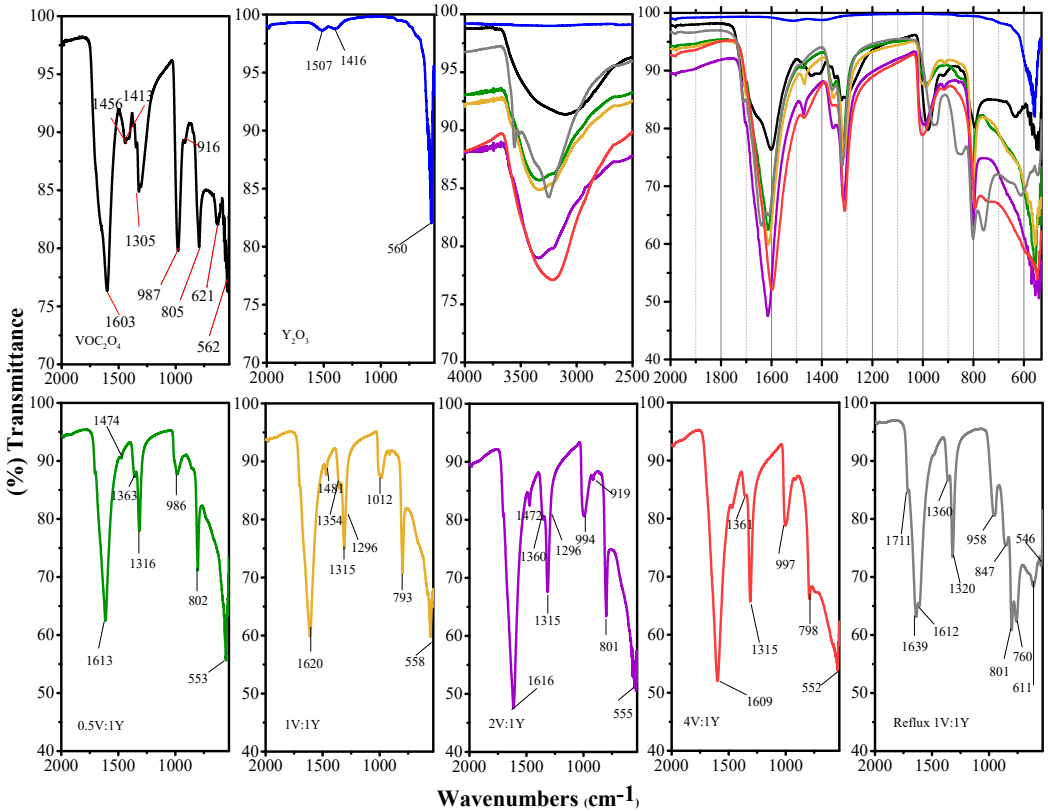

Figure 5- 16. FT-IR spectra of the YV-products, (The colors in the stacked plots correspond with those of the individual plots)

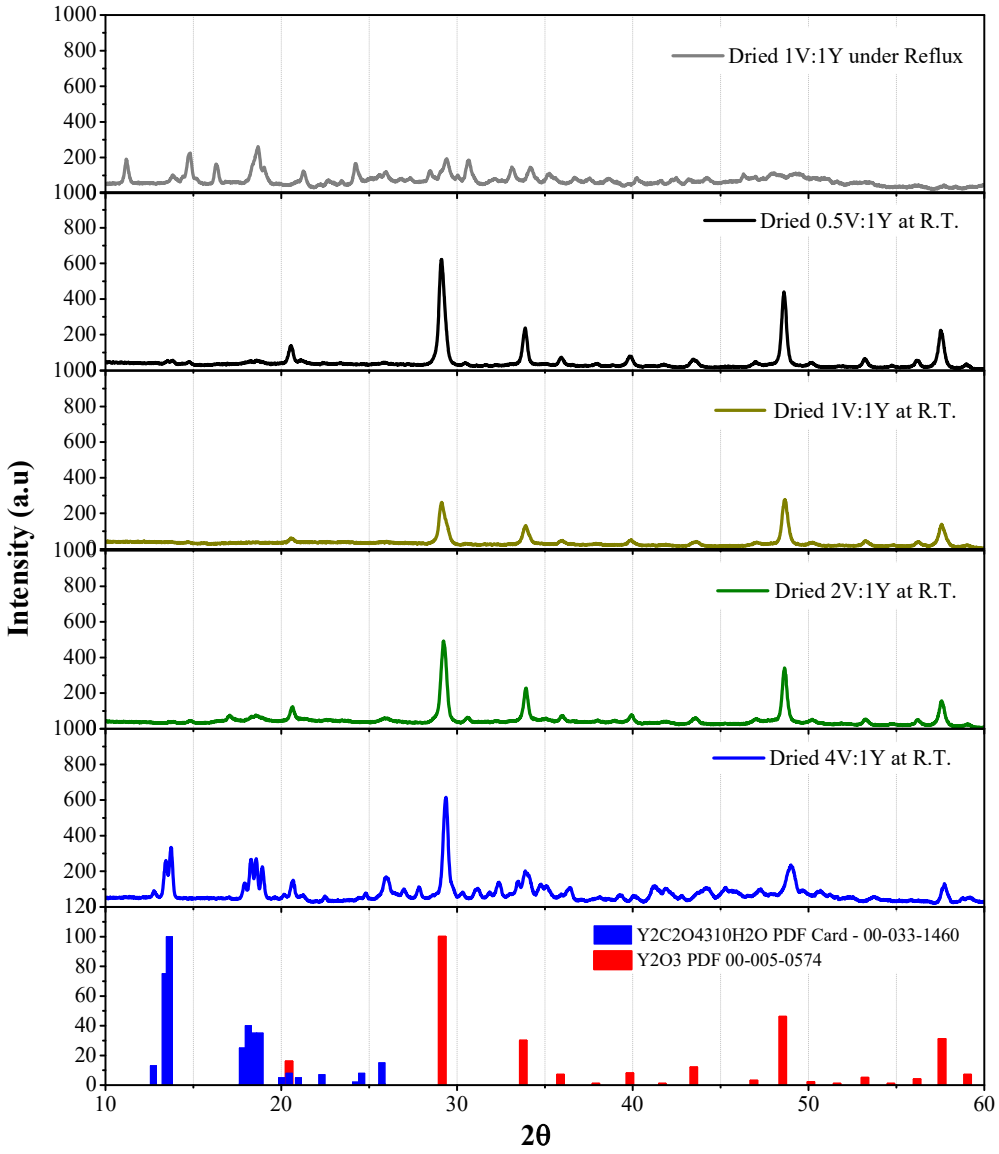

Figure 5- 17. XRD patterns of vanadyl oxalate/yttrium oxide products

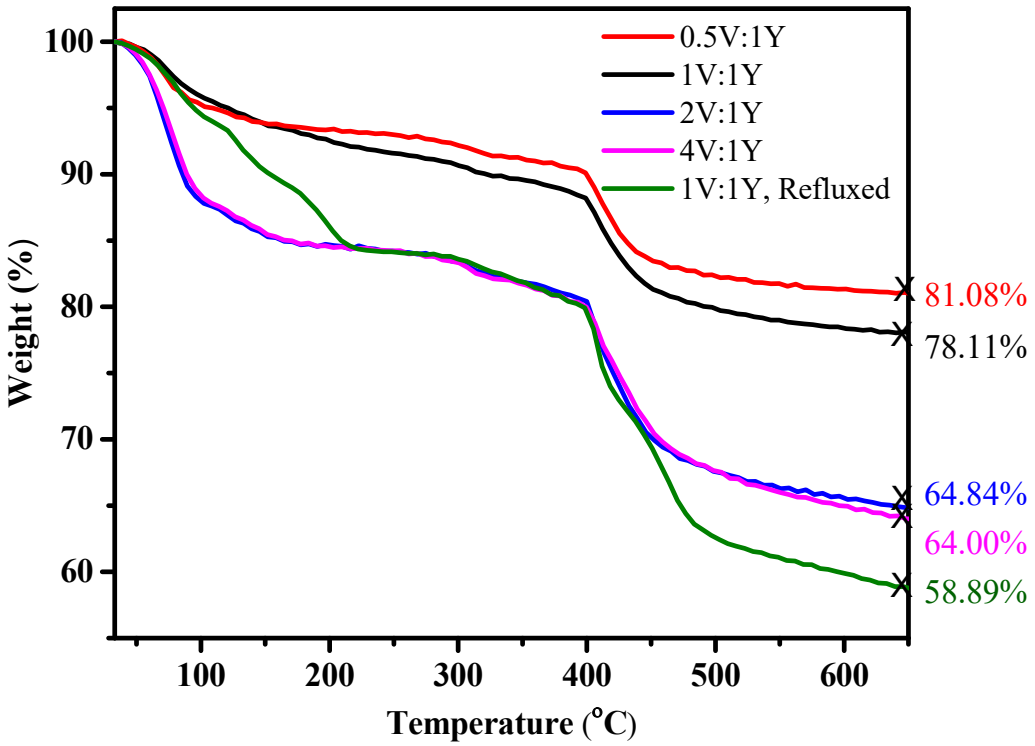

Figure 5- 18. Thermogravimetric analysis curves of the YV products

Figure 19 shows the FTIR spectra of the calcined YV-products. These all spectra display a strong absorption band in the 781-775 cm^{-1} range and a weak band in the 559-553 cm^{-1} range that attributable to V–O and Y–O stretching vibrations, respectively. The later band was observed for samples prepared with 2:1 and 4:1 Y:V ratios at room temperature, and 1:1 ratio under reflux. XRD patterns for the calcined products are shown in Figure 20. Mixtures of tetragonal yttrium orthovanadate, cubic yttrium oxide, and traces of vanadium pentoxide were detected. The SEM images and the EDS analysis for yttrium-vanadium precursors synthesized at room temperature and under reflux, before and after calcination are shown in Figure 21 and Figure 23, respectively. The EDS analysis data are tabulated in Table 7. The SEM image of 1V:1Y product at room temperature (Figure 21 (a)) exhibits a rough bulk surface with sheet-like projections. Calcination caused the particles to become smoother and agglomerate (Figure 21 (b)). The SEM image with higher magnification shows that this smooth surface consists of a large number of aggregated

spherical particles with average size of 40 ± 8 nm that's looks like polystyrene foam as shown in Figure 22. EDS analysis shows that the surface consists mainly yttrium with less than 10% vanadium which slightly increased upon calcination. The SEM image of the refluxed product (Figure 21 (c)) displays a mixture of well-defined particles with small circular thin sheets and large plates. EDS analysis of the small particles show a high content of vanadium with less than 25% yttrium while the large particles have equimolar amount of yttrium and vanadium indicates that these are precursors for yttrium orthovanadate. Calcination of this material result in the production of plateshaped particles of yttrium orthovanadate with well-defined edges. These have an average size of 755 ± 121 nm. The surface areas and the crystallite sizes are summarized in Table 8. Interestingly, the calcined refluxed 1:1 precursor had the highest surface area.

Since the reactions of bulk yttrium oxide with with vanadyl oxalates failed to produce pure compounds, the use of nano yttrium oxide was explore with 1:1 ratio at room temperature and reflux. It was postulated that the smaller size would lead to complete reaction since the vanadyl ions would need to penetrate into the particles with a much smaller distance. The FTIR spectra for the resulting compounds before and after calcination are shown in Figure 24. The refluxed product exhibits similar trends as that prepared from the bulk yttria. Peaks were observed at 3602 (s, sh), 3260 (s, br), 1708 (m), 1611(s), 1353 (w), 1314(m), 944(w), 800,(vs, sh) and 601(s, br) cm^{-1}. In contrast, the room temperature product had stronger bands as can be seen for the peaks at 1608, 1361, and 1316 cm^{-1}. Also the bands at 3207 and 601 cm^{-1} became broader. The calcined samples show a sharp band around 770 cm^{-1}. The XRD patterns for the as-prepared and calcined products are presented in Figure 25 and Figure 26, respectively. The XRD patterns of uncalcined samples did not match known patterns with exception of the product prepare at room temperature which contained a small amount of Y_2O_3. The calcined products at room temperature was almost pure tetragonal yttrium orthovanadate. However, yttrium oxide and vanadium oxide were detected in addition to yttrium orthovanadate phase for the calcined refluxed product. The crystallite sizes of

yttrium orthovanadate synthesized from mixing the reactants at room temperature and of refluxing were determined to be 25.23 and 45.48 nm, respectively.

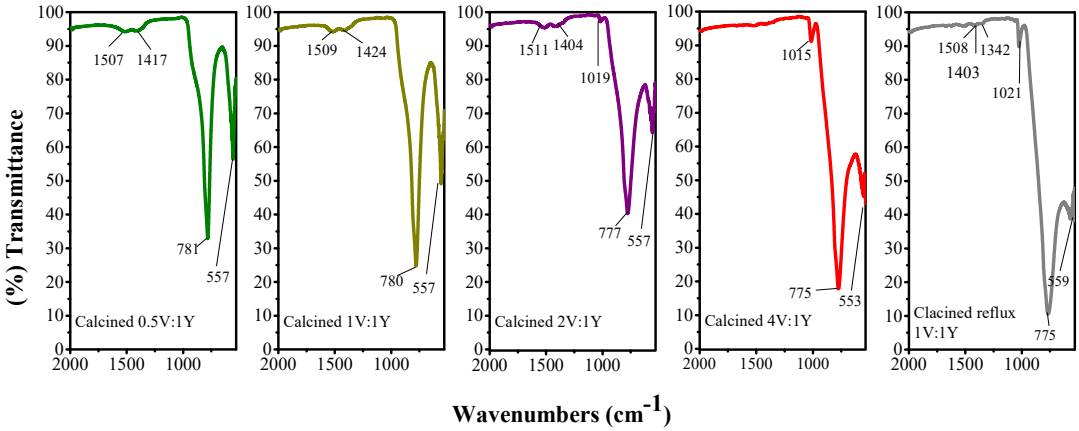

Figure 5- 19. FTIR of calcined products of YV-products

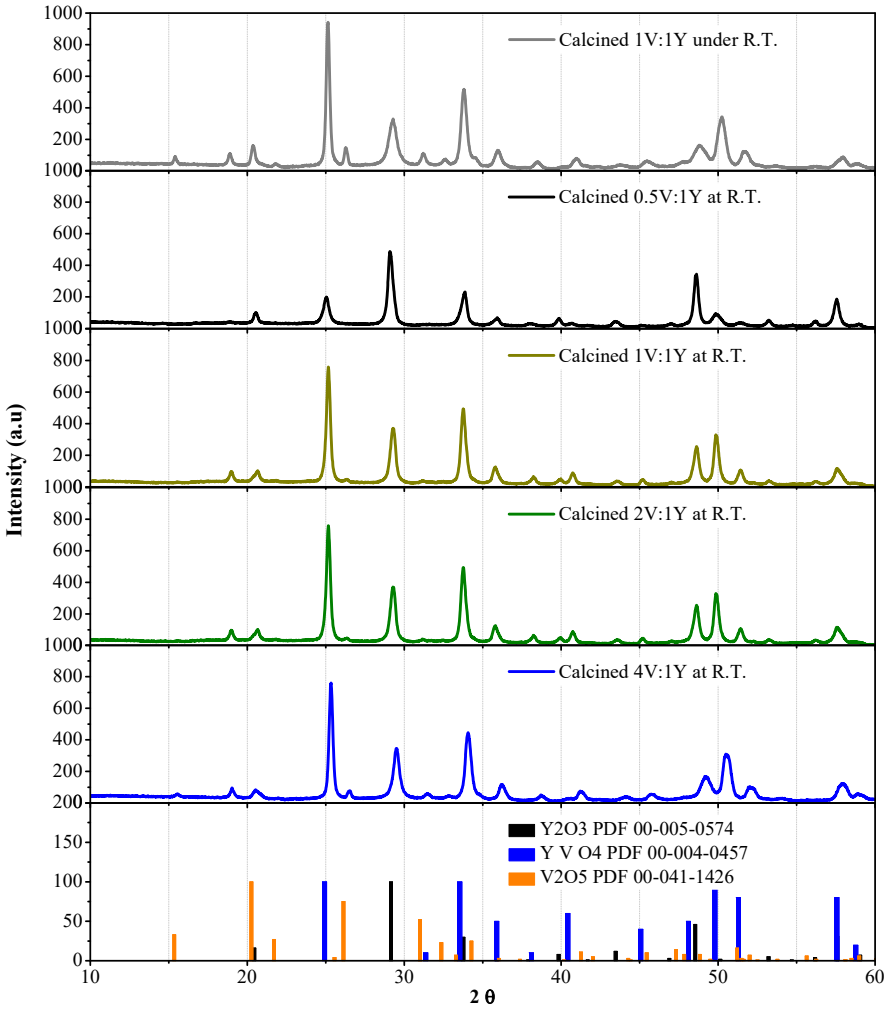

Figure 5- 20. XRD patterns of the calcined YV products

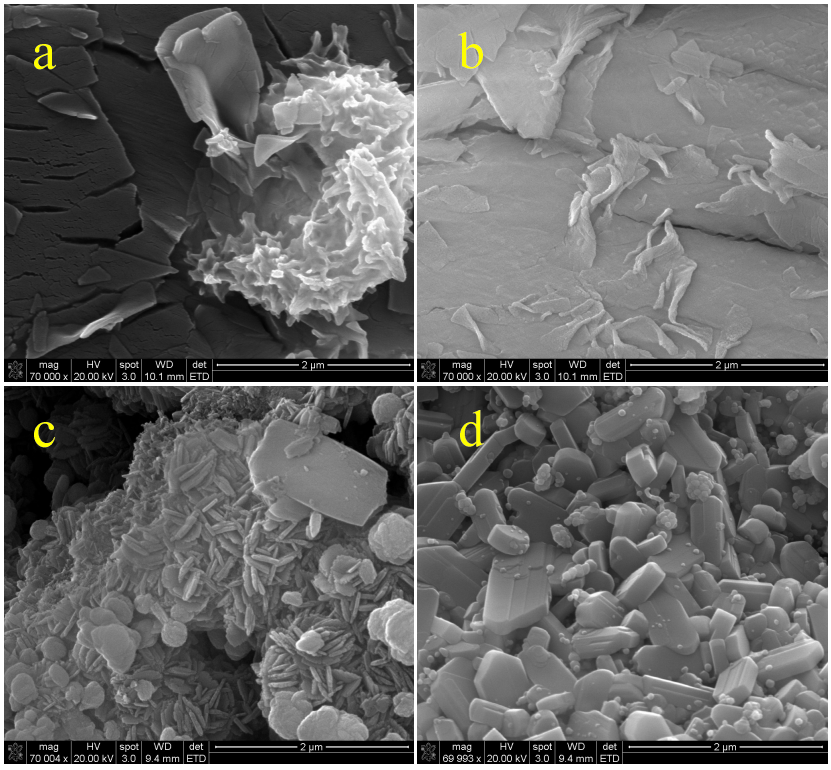

Figure 5- 21. SEM images for YV-precursor synthesized at room temperature (a), precursor under reflux (c), calcined (R.T.) (b) and calcined (Reflux) (d)

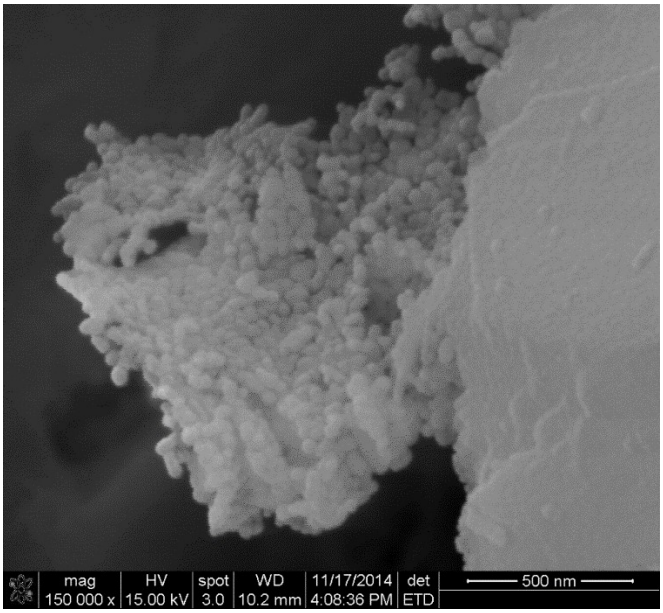

Figure 5- 22. SEM image with higher magnification for the calcined YV-precursor synthesized at room temperature

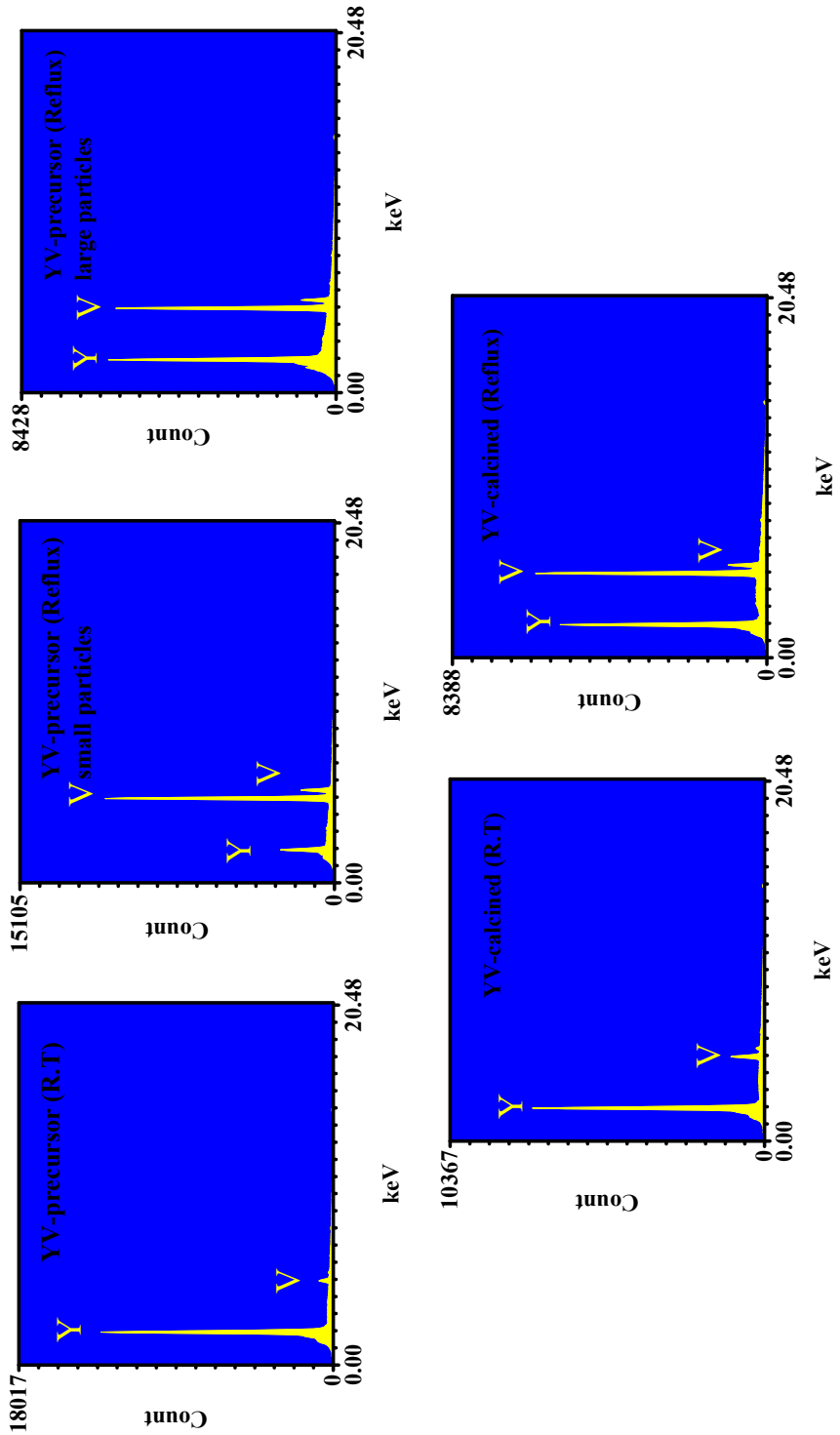

Figure 5- 23. EDS spectra for YV-products

Table 5- 7. EDS quantitative analysis for YV-products

Sample	Elements	WT%	AT%	Intensity	P/bkg
Precursor (R.T.)	YL	96.33	93.76	424.118	17.9
	VK	3.67	6.24	24.678	2.2
Precursor (Reflux) Small particles	YL	23.87	15.23	70.992	4.2
	VK	76.13	84.77	423.35	40.6
Precursor (Reflux) Large particles	YL	55.11	41.29	170.87	5.8
	VK	44.89	58.71	237.95	21.7
Calcined (R.T)	YL	90.32	84.25	239.356	15.1
	VK	9.66	15.75	39.783	5.4
Calcined (Reflux)	YL	54.21	40.42	173.129	8.2
	VK	45.79	59.58	250.57	21.1

Table 5- 8. Surface area measurements of 1V:1Y products at room temperatures, under reflux, and their calcined products

Sample	BET (m^2/g)	Crystallite size from XRD (nm)	Particle size from SEM (nm)	Particle shape from SEM
1.0V:1.0Y at R.T.	45	NA	NA	NA
Calcined 1.0V:1.0Y at R.T.	11	39.2 ± 1.0	40 ± 8	Spherical
1.0V:1.0Y under Reflux	8	NA	292 ± 31	Circular plates
Calcined 1.0V:1.0Y under Reflux	7	46.6 ± 1.9	755 ± 121	Unsymmetrical plates

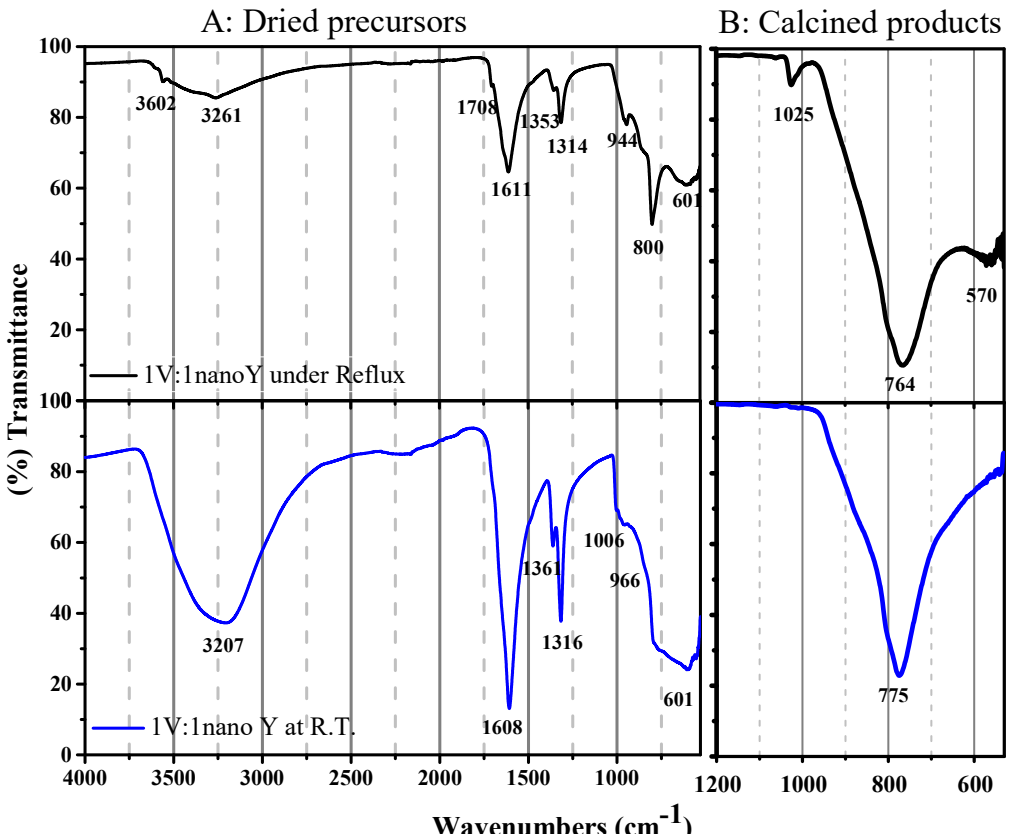

Figure 5- 24. FTIR spectra of precursors synthesized by using nano yttrium oxide and their calcined products

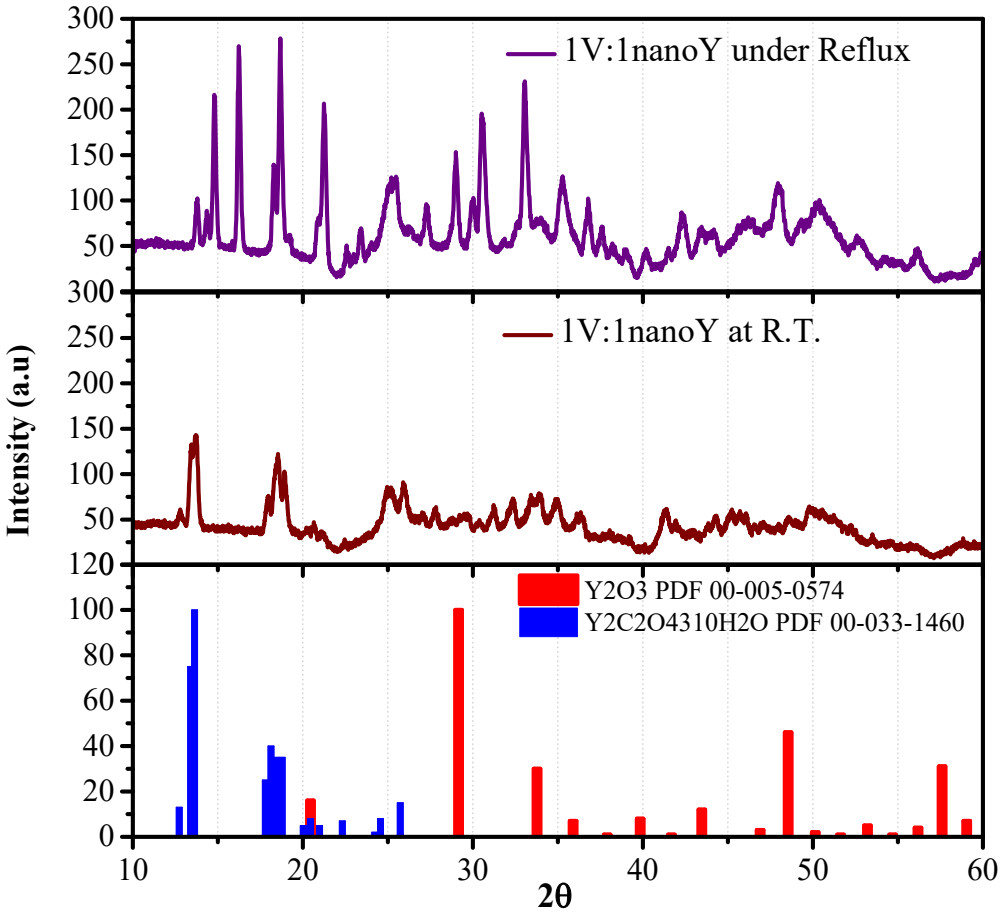

Figure 5- 25. XRD patterns of the precursors synthesized by using nano yttrium oxide

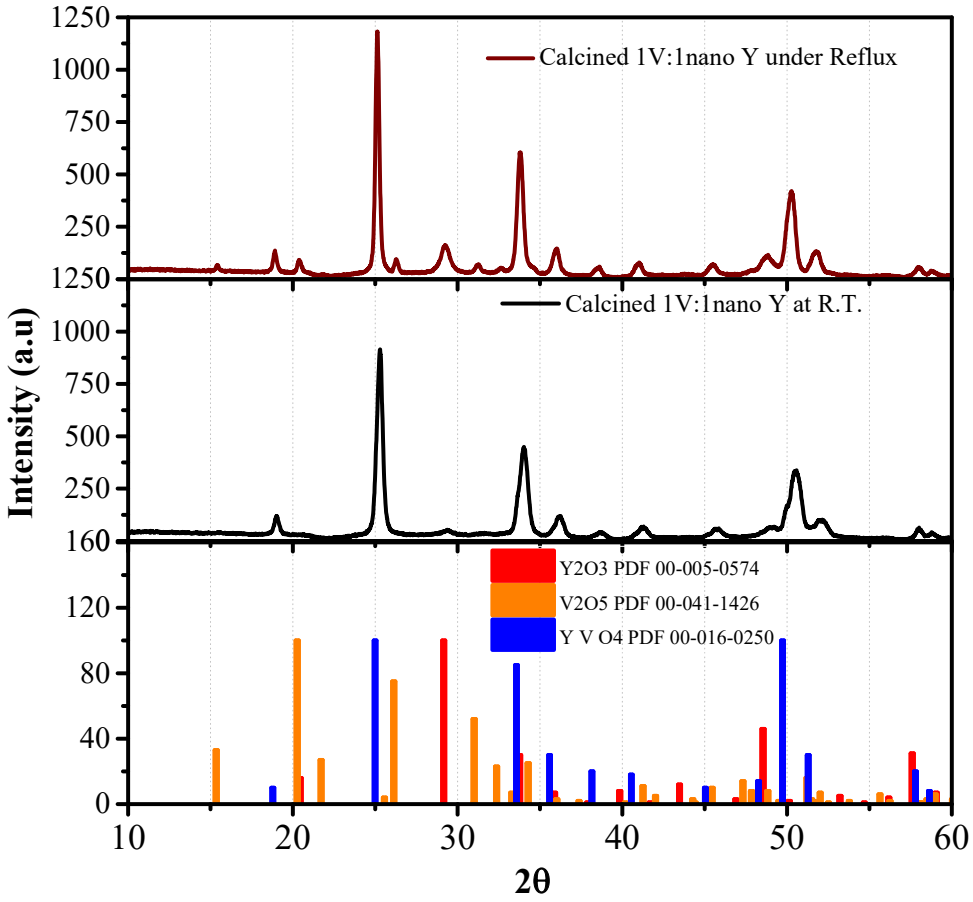

Figure 5- 26. XRD patterns of calcined products of precursors synthesized by using nano yttrium oxide

3.3.Reaction of Vanadyl Oxalate Solution and Lanthanum Oxide

Likewise to the vanadyl oxalate with aluminum, zirconium, and yttrium oxide/hydroxides reactions, lanthanum oxide reacted with vanadyl oxalate solutions at room temperature and under reflux. Table 9 shows the ratios of lanthanum oxide and vanadyl oxalate used for reaction run at room temperature for seven days. The data for the 1:1 reaction under reflux is also presented. The table also includes the ceramic yields from pyrolysis of the materials at 650 ˚C.

Table 5- 9. Conditions used for the lanthanum oxide and vanadyl oxalate reactions and the final ceramic yield

Starting materials (g)		Reactant ratio V:La	Reaction condition	Product Weight (g)	Ceramic yield (%)
VOC_2O_4	La_2O_3				Oven at 650 ˚C
20.017	4.203	0.5:1.0	R.T	6.948	77.9
20.005	2.101	1.0:1.0	R.T	4.734	76.0
20.034	1.051	2.0:1.0	R.T	2.787	72.4
20.018	0.525	4.0:1.0	R.T	1.221	59.3
40.117	4.207	1.0:1.0	Reflux	10.034	62.5

The change in pH over time of the lanthanum oxide and vanadyl oxalate reactions is presented Figure 27. The pH increased from 1.4 up to a plateau at 5.0, 4.4, 3.6, and 2.8 for xV/La ratio of 0.5, 1, 2 and 4, respectively. Figure 28 shows the UV-VIS spectra for the vanadyl oxalate/lanthanum oxide solutions after separation of the solid products. No bands were observed for the 0.5V:1La and 1V:1La ratios. However, for the other two ratios, the characteristics bands of vanadyl ion, (V^{4+}) were detected. The results suggest that with the 1V:1La and 0.5V:1La ratios all of the vanadyl oxalate reacted away. The number of moles of the unreacted V^{4+} for the 2V:1La and 4V:1La ratios found to be 0.0035 (27.13%) and 0.0037 (28.68%) mole, respectively. Determination of number of moles of V and La by MP-AES (see Table 10) were in agreement with the UV-VIS in that vanadium was only detected in the 2:1 and 4:1 reaction mixtures. These were found to be 0.0038 (29.778%) and 0.0036 (27.95%) moles, respectively. The correspondence between the

UV/Visible spectroscopic concentration for V^{4+} and the total vanadium present (from MP-AES) indicates that vanadyl was the only form of vanadium present. A small but almost constant amount of lanthanum is released into solution. Considering the amounts of reagents used and the solution concentrations of vanadium and lanthanum, the solid formed at higher V:La ratios have approximately equimolar amounts of vanadium and lanthanum.

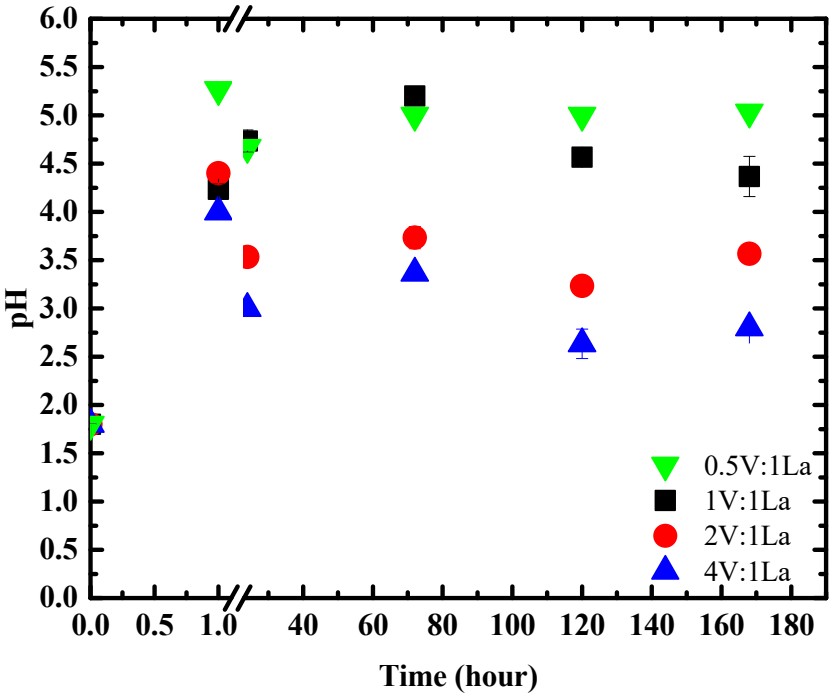

Figure 5- 27. The change of pH over time for lanthinum oxide/vanadyl oxalate reactions

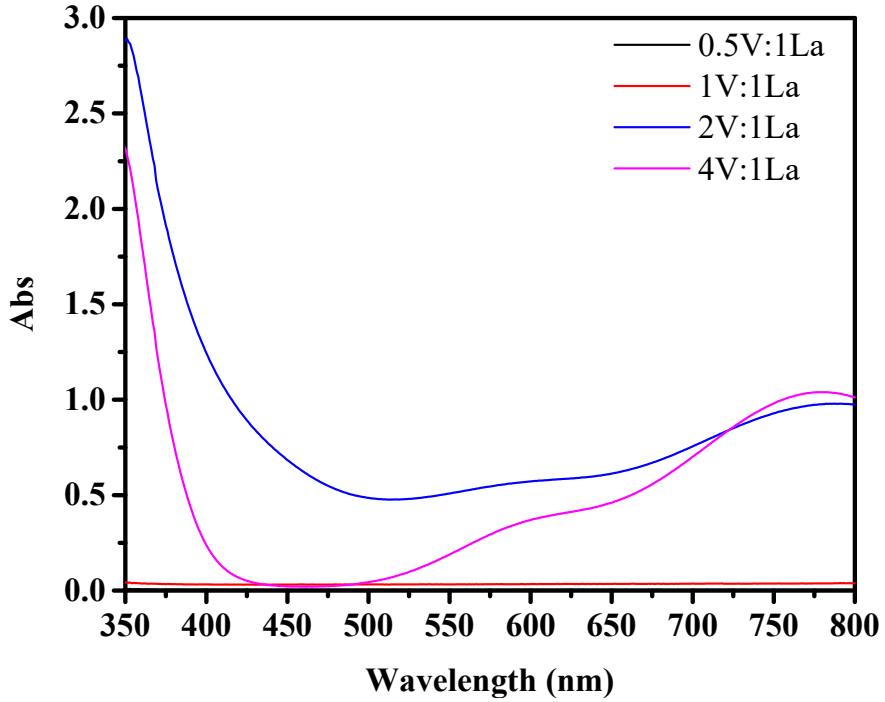

Figure 5- 28. UV-VIS spectra for vanadyl oxalate/ lanthanum oxide solutions

Table 5- 10. Comparison between MP-AES and UV-VIS data with different mole ratios of V:La

Reactant Moles		Solution Color	Reactant Mole Ratios	Product Moles Based on MP-AES		V^{4+} Moles Based on UV-VIS
V	La		V/La	V	La	
0.0129	0.0258	Colorless	0.50	0.0000	0.0001	0.0002
0.0129	0.0129	Colorless	1.01	0.0002	0.0016	0.0003
0.0129	0.0065	Greenish-Blue	2.02	0.0038	0.0013	0.0035
0.0129	0.0032	Greenish-Blue	4.04	0.0036	0.0015	0.0037

Figure 29 shows the FTIR spectra for the starting materials and products. The La_2O_3 spectrum has a sharp strong peak at 3608 cm^{-1} is assigned to the O–H stretching vibration of the adsorbed O–H group. , This is likely a result of $La(OH)_3$ formation since lanthanum oxide known to react quickly with water in the atmosphere to form a new hydroxyl phase. [209] This band in all reaction products disappears for refluxed sample where it is only reduced in intensity. The band at 3106 cm^{-1} of VOC_2O_4 due to the hydroxyl groups of molecular H_2O has shifted to 3250 cm^{-1} in all

the product samples. The bending mode for O–H group of the of starting lanthanum oxide material disappears. The characteristic bands for the oxalate ligand, La-O, V=O and –V-O-V- were observed with slight shifts due to complexation. The XRD patterns of the samples are presented in Figure 30. At low vanadium to lanthanum ratios, the solid products contain lanthanum hydroxide. This disappears for the 4:1 vanadium product but some lanthanum oxalate is observed. The refluxed sample also contains some $La(OH)_3$. It would be appear that the best ratio of V:La might be 3:1. This might reflect the trivalent nature of lanthanum. The thermal decompositions of the samples are shown in Figure 31. The TGA curves are similar to each other but have longer mass losses in each step as the molar ratio of vanadyl oxalate is increases. The thermal treatment corresponding to dehydration and decomposition oxalate groups. The carbon content of the 1:1 product ratio found to be: 4.36 % suggesting that the product contains oxalate ligand. Considering the initial amount of lanthanum oxide and the amount that dissolved, it can be calculated that there are 0.75 molar equivalents of lanthanum ion in the product.

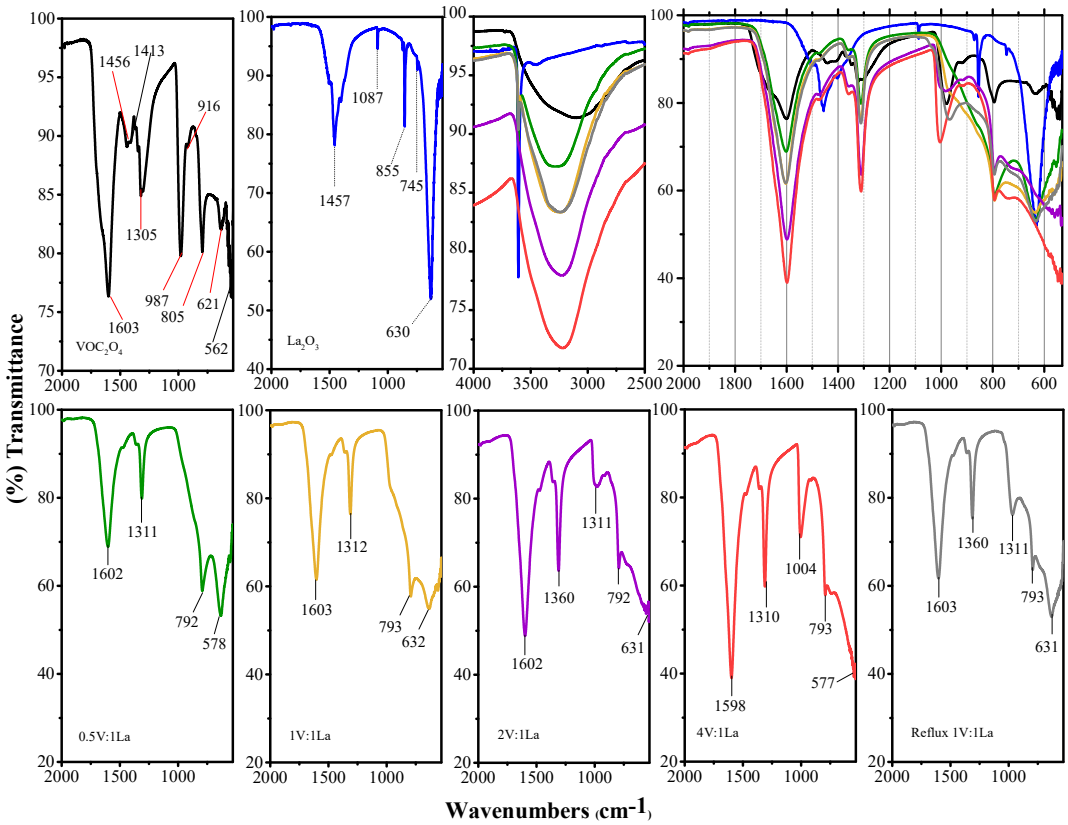

Figure 5- 29. FT-IR spectra of the LaV-products

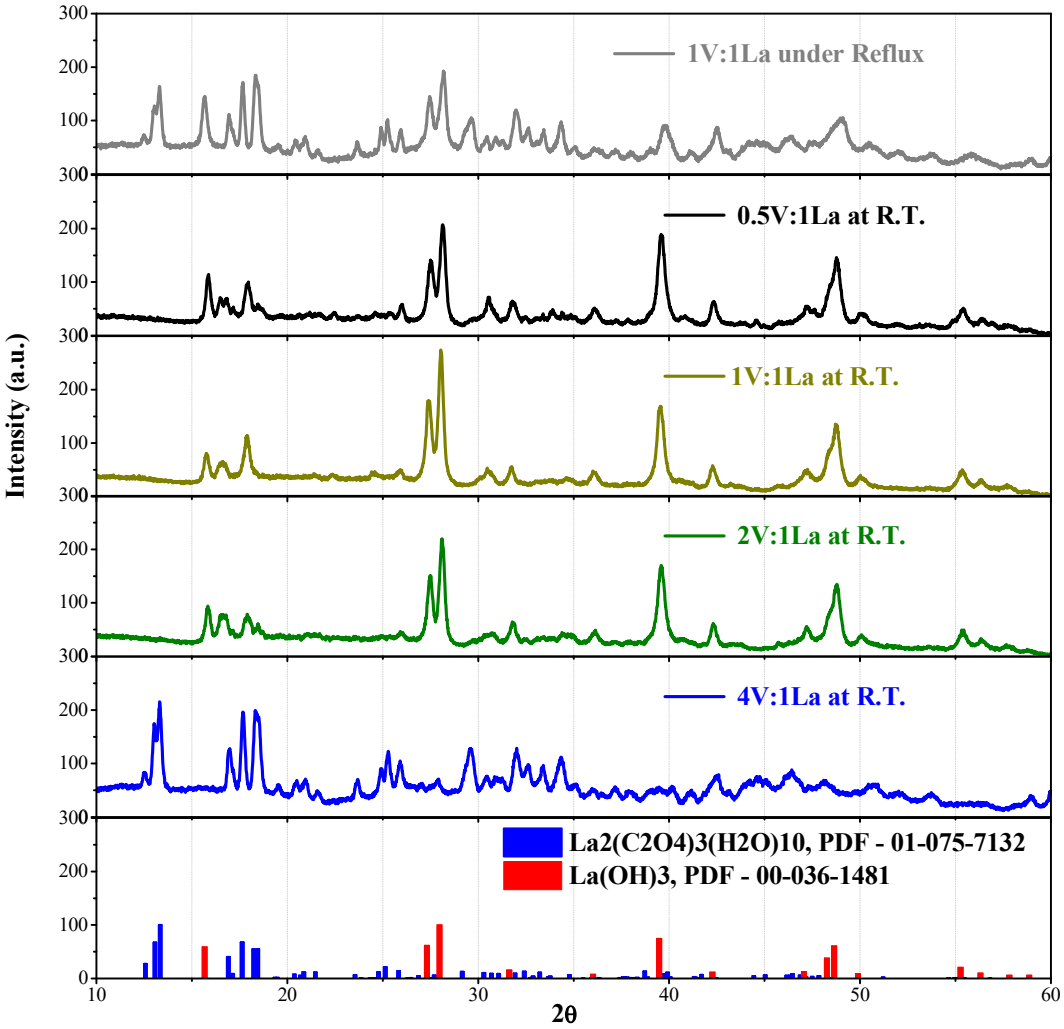

Figure 5- 30. XRD patterns of precursors synthesized from vanadyl oxalate and lanthanum oxide at R.T. and under reflux

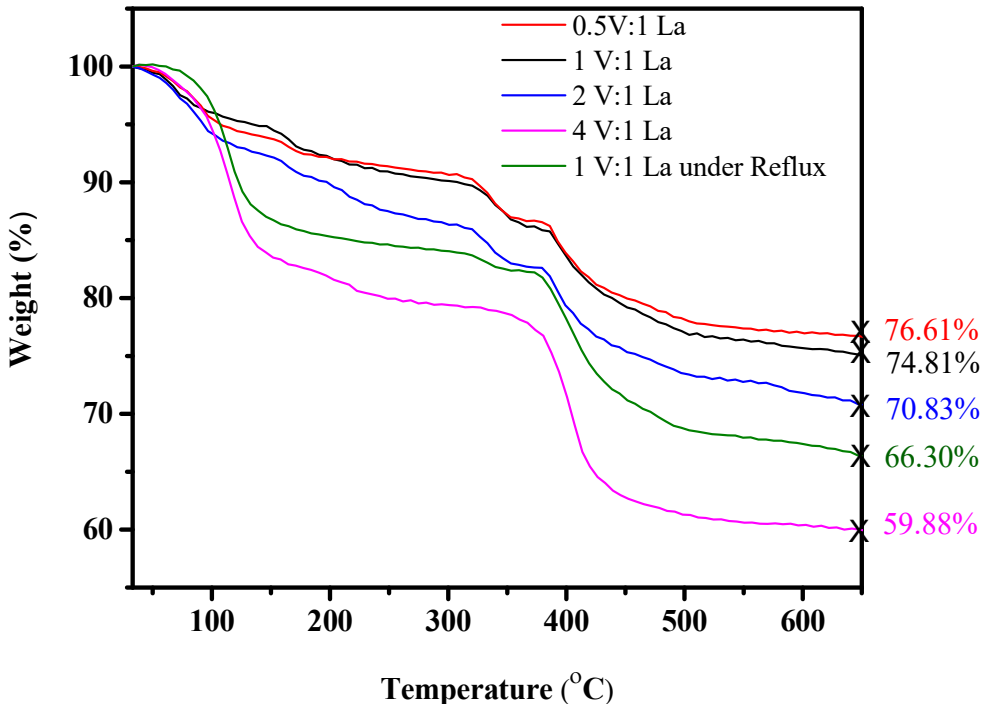

Figure 5- 31. Thermogravimetric analysis curves of the products

Figure 32. exhibits FTIR spectra of the calcined LaV-products prepared under various conditions. The spectra mainly displayed four bands around 1461, 1361, 1086, and 763 cm^{-1} for samples of reaction ratios 0.5V, 1V, and 2V to 1La. Only three bands at 1027, 959, and 565 cm^{-1} were observed for the 4:1. The strong band observed at 763 cm^{-1} is typical of V at the center of distorted tetrahedron of oxygen atoms, tetragonal-$LaVO_4$. [210, 211] In contrast, in the case of the calcined reflux sample, the strong band at 763 cm^{-1} belonging to VO_4^{3-} is split into three bands 954, 914, and 855 cm^{-1} typical of the monoclinic-$LaVO_4$ phase. [210-212] XRD patterns of the calcined products shown in Figure 33 showed that all samples contained monoclinic-$LaVO_4$ (PDF 00-050-0367). The orthorhombic phase of vanadium pentoxide (PDF 00-050-0367) was detected in samples prepared with higher ratios of vanadium. In addition, higher crystallinity was observed with higher vanadium amount. Figure 34 shows the SEM images of the 1:1 LaV-precursors synthesized at room temperature and under reflux, and their calcined products. Figure 35 show the EDS spectra for these samples and the data are presented in Table 11. Surface areas, particle and

crystallite sizes are summarized in Table 12. SEM images of LaV-precursor prepared at room temperature (Figure 34 (a)) and its calcined product (Figure 34 (b)) show particles with similar textured surfaced. However, the EDS analysis showed major changes in the La:V ratio upon heating to 650 ˚C. The surface areas determined to be 5 m^2/g for both samples. The SEM image of the refluxed LaV-precursor, shown in Figure 34 (c), displays a heterogeneous mixture of small and large particles. The small particles have a high vanadium content that is almost equal to the amount of lanthanum, while the large particles have low vanadium content. However, calcination of this precursor resulted in production of a homogenous phase with defined boundaries of spherical shaped particles with 117 ± 36 nm average sizes Figure 34 (d).

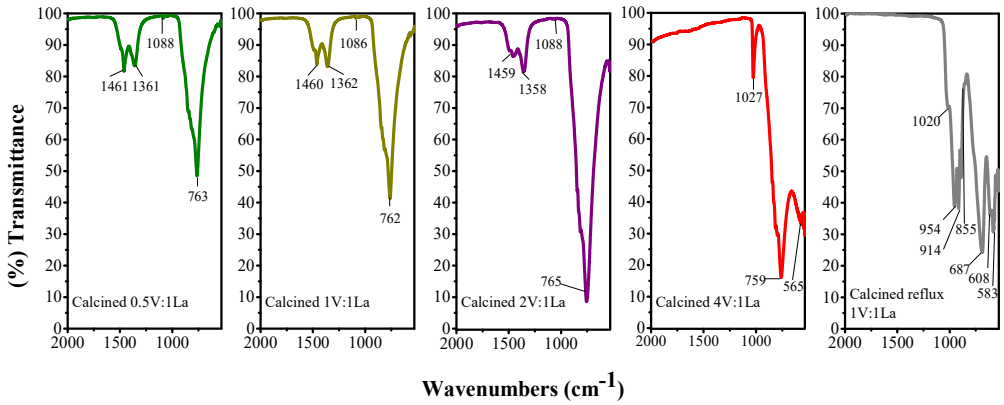

Figure 5- 32. FTIR of calcined LaV products

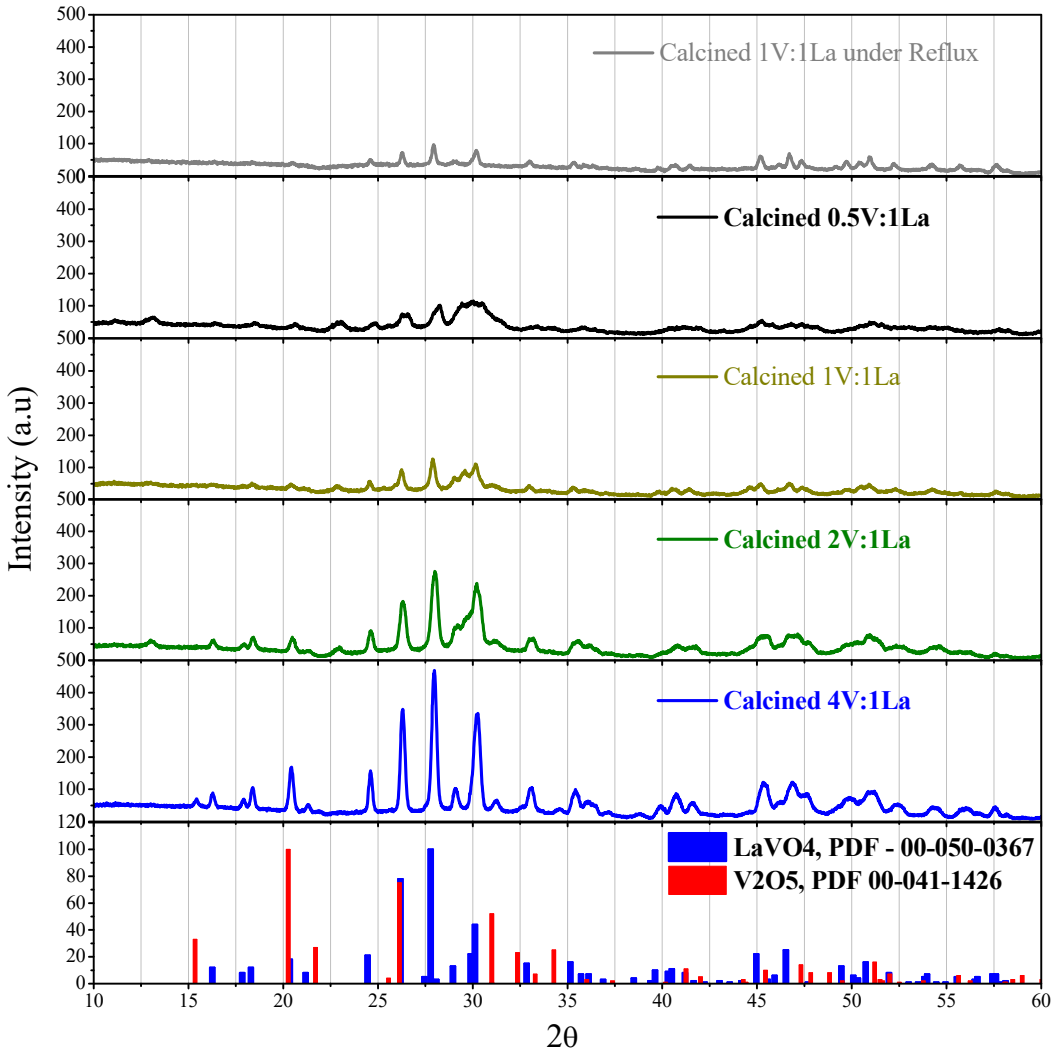

Figure 5- 33. XRD patterns of calcined LaV products

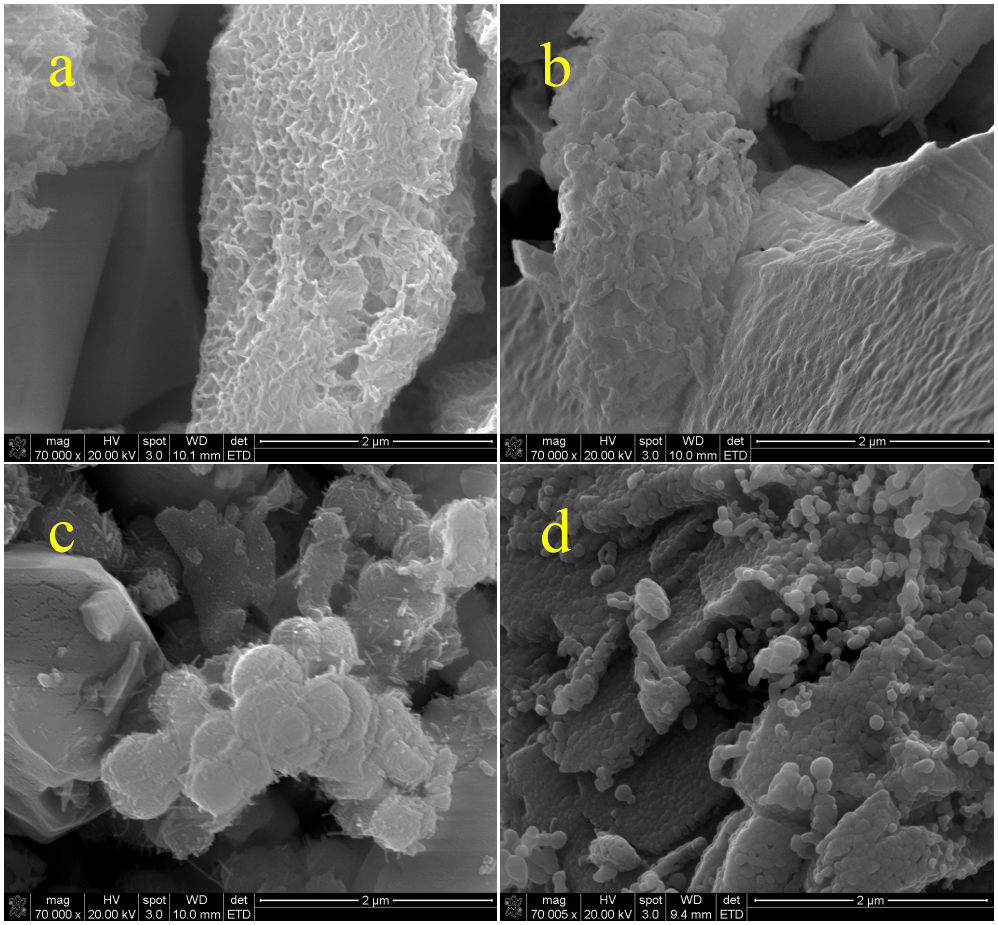

Figure 5- 34. SEM images for LaV-precursor synthesized at room temperature (a), precursor under reflux (c), calcined (R.T.) (b) and calcined (Reflux) (d)

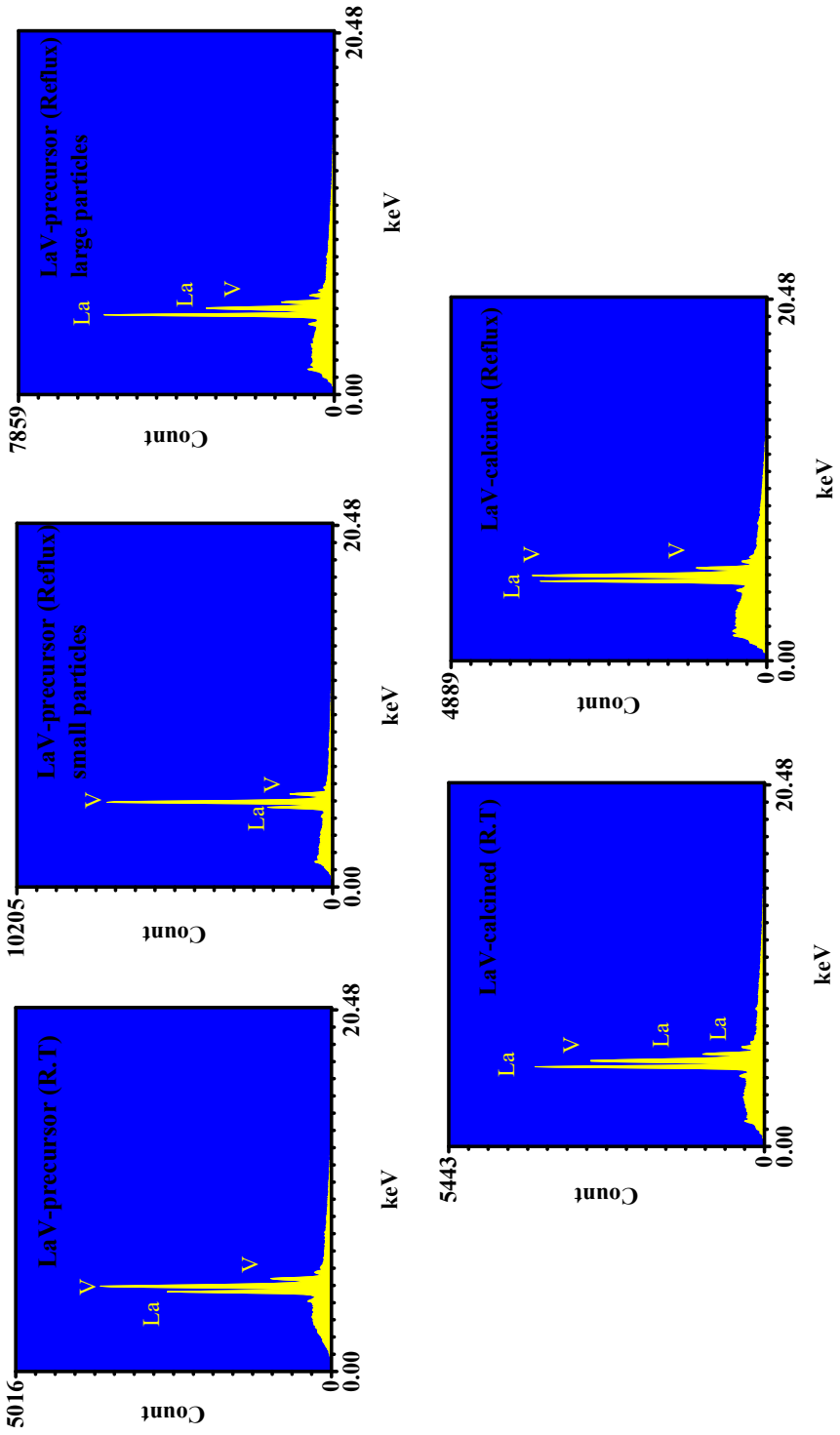

Figure 5- 35. EDS spectra for LaV-products

Table 5- 11. EDS quantitative analysis for LaV-products

Sample	Elements	WT%	AT%	Intensity	P/bkg
Precursor (R.T.)	LaL	69.09	45.05	91.885	8.8
	VK	30.91	54.95	114.227	10.9
Precursor (Reflux) Small particles	LaL	42.85	21.57	73.2.03	5.7
	VK	57.15	78.43	270.73	22.4
Precursor (Reflux) Large particles	LaL	94.65	86.65	170.87	5.8
	VK	5.35	13.35	220.278	11.9
Calcined (R.T)	LaL	84.37	66.44	147.076	10.3
	VK	15.63	33.56	75.801	5.5
Calcined (Reflux)	LaL	78.56	57.33	127.839	6.7
	VK	21.44	42.67	97.014	4.7

Table 5- 12. Surface area measurements of 1.0V:1.0La ratio precursors at room temperatures, under reflux, and the calcined products

Sample	BET (m^2/g)	Crystallite size from XRD (nm)	Particle size from SEM (nm)	Particle shape from SEM
1V:1La at R.T.	5	NA	NA	NA
Calcined 1V:1La at R.T.	5	29.52	NA	NA
1V:1La under Reflux	13	NA	NA	NA
Calcined 1V:1La under Reflux	10	49.91	117 ± 36	Spherical particle

4. Conclusion:

Aqueous vanadyl oxalate was found to react with zirconium hydroxide, yttrium oxide, and lanthanum to produce solids that contain both vanadium and the corresponding metal. The reaction appears not to release significant quantities of metals from the solid reactant so the reaction could be regarded mainly as an acid/base reaction between acidic hydrated vanadyl ions and the oxide or hydroxide groups of the solid reagent. Since the reaction is not surface-limited, the reaction probably follows a dissolution, precipitation mechanism.

Oxalate likely plays a role in this by complexing the metal ion of the solid reactant and pulling it into solution. Support for this hypothesis is provided by the identification of yttrium oxalate and lanthanum oxalate in product mixtures prepared with high vanadyl oxalate (and therefore high oxalate). These oxalate salts are fairly insoluble in water. The actual amount of oxalate in the solids are highest for lanthanum and yttrium but are less than a stoichiometric amount. The pH of the solutions rises during the course of the reaction to between 2.5 and 3.0, depending on the solid reagent used. Under these conditions, hydrogen oxalate will be the dominant species present in solution with some oxalic acid present as well and very little oxalate ion.

As might be expected, the size of the particles of the solid reagent play an important role is the rate and extent of the reaction. Thus, nanometric ytrrium oxide reacted faster and more completely than bulk yttrium oxide. Refluxing makes reactions got much faster but it also alters the product composition and the morphology of the final product.

It is possible with judicious choice of reaction conditions to produce solid products that when calcined form YVO4 and LaVO4, desirable compounds for several applications. In the case of zirconium, incorporation of vanadium is only around 10%, but vanadium-doped zirconium oxide is formed that is a valuable yellow pigment for ceramics. It all cases, it is likely possible to use a small molar ratio of vanadyl oxalate to react with just the surface of the solid reagents so that supported catalysts might be prepared.

There is much future work to be done to determine the scope of the reaction of vanadyl ions with metal oxides and hydroxides. Also, determination of the optimal reaction conditions such as the concentration of vanadyl oxalate, reactant ratios, and temperature to produce the desired materials. Also, it may be possible to employ different vanadyl salts that might avoid formation of undesirable oxalates. Also, the use of different metal oxalates than vanadium might prove fruitful.

CHAPTER VI

REDUCTION OF VANADIUM PENTOXIDE WITH PYURVIC ACID OXIME

1. Introduction:

Vanadium complexes with a variety oxidation states often have insulin mimetic properties useful for treatment of diabetes but they also serve as models for the roles of vanadium compounds in catalytic and biochemical systems, especially vanadium-containing enzymes.[213] In particular, α-oximinocarboxylates salts are of interest due to applications as low temperature precursors for metal oxide ceramics and as efficient chelating agents for a variety of metal ions.[214-217] The metal complexes of α-oximinocarboxylates crystallize in diverse arrangements including monomers, dimers, and polymers. [218, 219] The importance of α-oximinocarboxylates results in part form the two different functional groups, the carboxyl group (COOH) and the oxime (=NOH). Oximes are structurally analogous to amino acids, (see Scheme 1), but have higher ability to coordinate with metal ions due to Lewis acidity of the nitrogen atom and basicity of the oxygen atom in the oxime group (=NOH).[220]

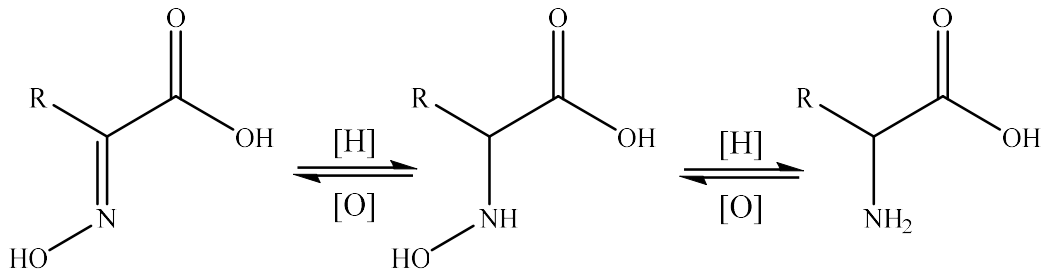

Scheme 6- 1. Oximes structural analogous to amino acids

The salts of α-oximinocarboxylates particularly pyruvic acid oxime (PAO) are useful low-temperature precursors for metal oxide ceramics that can be used to produce high-surface area catalysts, coat heat-sensitive substrates, and synthesize metastable phases with useful properties. [221, 222] It has been demonstrated that thermal decomposition of PAO produces acetonitrile, carbon dioxide, and the corresponding metal hydroxides (see Scheme 2). Depending on the metal further reactions may occur to produce oxides or carbonates.[215, 216, 221, 222]

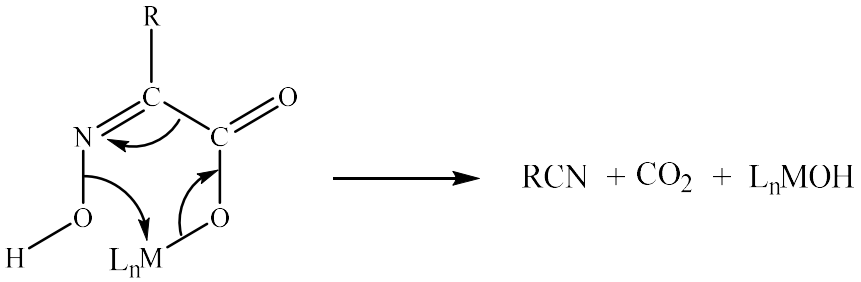

Scheme 6- 2. Thermal decomposition of α-oximinocarboxylates salt

In this chapter, the synthesis and characterization of a vanadium complex of pyruvic acid oxime will be discussed since HPAO is a reducing agent like oxalate, it was expected to reduce V_2O_5 to the vanadyl complex, $VO(PAO)_2$. This could serve as a precursor to V_2O_5 (or VO_2 in an inert atmosphere), LiV_2O_5, and could also react with aluminum hydroxide in the same manner as vanadyl oxalate. The characterization of the precursor and resulting vanadium oxide materials by spectroscopic, thermal gravimetric, X-ray diffraction and electron microscopy will be discussed.

2. Experimental:

2.1.Material

Commercially available reagents with ACS grade purity or better were used without any further purification. Vanadium(V) oxide, V_2O_5 (99.6+ %) and hydroxylamine hydrochloride, $H_2NOH{\cdot}HCl$ (99 %) were obtained from Aldrich Chemical Company, Inc, solution pyruvate $NaC_3H_3O_3$ (99.9 %) was purchased from Chem-Impex Int'l Inc. Lithium hydroxide monohydrate, $LiOH{\cdot}H_2O$ (98%) was purchased from Alfa Aesar, Water was purified by reverse osmosis and deionization to a resistance of 18MΩ.

2.2.Analysis techniques

Infrared spectra were recorded on a Nicolet Is50 FT-IR spectrometer from 4000–500 cm^{-1}. Solution NMR spectra were acquired using a fully automated Bruker AVANCE III HD 400 with Sample Xpress sample changer. Solid state NMR spectra were obtained utilizing a Varian/Chemagnetics CMX-II 300 MHz SSNMR spectrometer. Thermogravimetric (TGA) analysis was performed on a Mettler TGA instrument. Experiment were performed in air or N_2 atmosphere from ambient temperature to 650 ˚C at a ramp rate of 5 ˚C/min. The X-ray powder diffraction (XRD) patterns were recorded on a Bruker AXS D-8 Advance X-ray powder diffractometer using copper Kα radiation. Crystalline phases were identified using a search/match program and the PDF-2 database of the International Center for Diffraction Data. The crystallite size of calcined products was evaluated using the Scherrer equation. Single crystal X-ray diffraction was performed at the University of Oklahoma using a diffractometer with a Bruker-AXS APEX CCD area detector and graphite-monochromated Mo Kα radiation (λ = 0.71073 Å). Scanning electron microscopy (SEM) was used to determine particle sizes and morphologies of the materials using a FEI Quanta 600 field emission gun environmental scanning electron microscope. Surface areas were determined via nitrogen physisorption using the Brunauer, Emmett, and Teller (BET) technique.

2.3.Synthetic procedure

2.3.1. Synthesis of Pyruvic Acid Oxime, CH3C(=NOH)COOH, (HPAO)

Pyruvic acid oxime $CH_3C(=NOH)COOH$ (HPAO) was prepared according to the procedure of Apblett et al. [215, 216] Basically, two solutions were prepared separately; the first one; an 11.004 g (100 mmol) of sodium pyruvate was dissolved in 30 ml of distilled water while the second one consisted of 6.949 g (100 mmol) of hydroxylamine hydrochloride dissolved in 30 ml of distilled water. The two solutions were immediately mixed together and then stirred for 3 minutes. This mixture was placed in refrigerator at 5 ˚C for 2 days. The precipitated HPAO product was collected and then purified by extraction of the HPAO with warm (70 ˚C) absolute ethanol. Evaporation of the solution yielded 9.973 g (96.83 %) of HPAO. Figure 1 showed the IR spectrum of HPAO. IR(cm^{-1}): 3362 (s,br), 3227 (s), 3068 (s,br), 2977 (w), 2895 (st,br), 2696 (w), 2562 (m), 2463 (w), 1779 (w), 1687 (vs), 1651 (s), 1457 (m), 1414 (m), 1376 (w), 1362 (w), 1301 (s), 1174 (vs), 1035 (vs), 987 (m), 881 (s), 814 (s), 758 (m), 700 (vs), 586 (w), 578 (vw), 574 (vw), 563 (w), 549 (w), 543 (w), 529 (vw), 526 (s). ^{13}C NMR (DMSO-d_6): δ (ppm) 165.9 (C=O), 148.7 (C=N), 10.8 (CH_3). ^{13}C ssNMR: δ (ppm) 168.2 (C=O), 151.6, 150.3, and 149.3 (C=N), 11.9 (CH_3).

2.3.2. Synthesis of Vanadium salt of Pyruvic Acid Oxime, $VO(PAO)_2$HPAO (3.000 g, 29 mmol) and V_2O_5 (0.910 g, 5 mmol)) were combined in 125 ml of water. The solution started to turn blue as the V_2O_5 was reduced and $VO(PAO)_2$ was formed. After stirring overnight, the V_2O_5 had completely dissolved, the solution was dark blue, and the pH was 0.9 ± 0.1. Evaporation of the solution produce a slightly hydroscopic dark blue powder. The yield was 3.399 g. IR(cm^{-1}): 3398 (s,br), 3192 (s), 3056 (s,br), 2859 (s,br), 1602 (vs), 1421 (s), 1382 (m), 1352 (vs), 1213 (vs), 1102 (vs), 961 (vs), 887 (m), 841 (m), 789 (s), 766 (m), 747 (m), 703 (w), 639 (vw), 599 (w), 555 (w). ^{13}C ssNMR: δ (ppm) 168.2 (C=O), 151.4 and 150.0 (C=N), 12.1 (CH_3).

3. Results and Discussion:

3.1. Synthesis of Pyruvic Acid Oxime, $CH_3C(=NOH)COOH$, (HPAO)

Pyruvic Acid Oxime, HPAO, was synthesized by reaction of sodium pyruvate with hydroxyl amine chloride (Equation 1). The HPAO was characterized by FTIR and NMR spectroscopy. Figure 1 shows the characteristic FTIR bands of HPAO that are in agreement with the literature. [215, 216] Table 1 presents the ^{13}C solution NMR and solid state NMR chemical shifts in (ppm). The NMR signals of the HPAO are close to those reported in the literature. The solid state ^{13}C NMR of HPAO however shows line broadening and spectral splitting of the ^{13}C-^{14}N dipolar interaction. [223, 224]

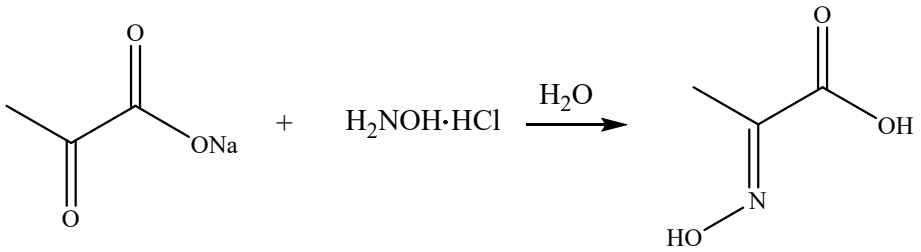

Equation 1. The synthesis of HPAO

Table 6- 1. 13C NMR and ssNMR chemical shift (ppm)

^{13}C NMR (ssNMR)	COO	C=N	CH_3
HPAO, reported [215]	166	148.9	10.7
HPAO, synthesized	165.9 (168.2)	148.7 (151.6, 150.3, and 149.3)	10.8 (11.9)

Figure 2 shows the thermal decomposition behavior of HPAO. The TG curve of HPAO exhibits two weight loss steps, the first step is a rapid weight loss of 4.15 % in the temperature range less than 70 ˚C. The step is an endothermic and corresponds to the dehydration of HPAO. The second step of weight loss of 94.10 % occurs at 167 ˚C and is exothermic are attributed to the decomposition of PAO. No residue was left after 475 ˚C, indicates high phase purity of HPAO, i.e. no residual sodium chloride was present.

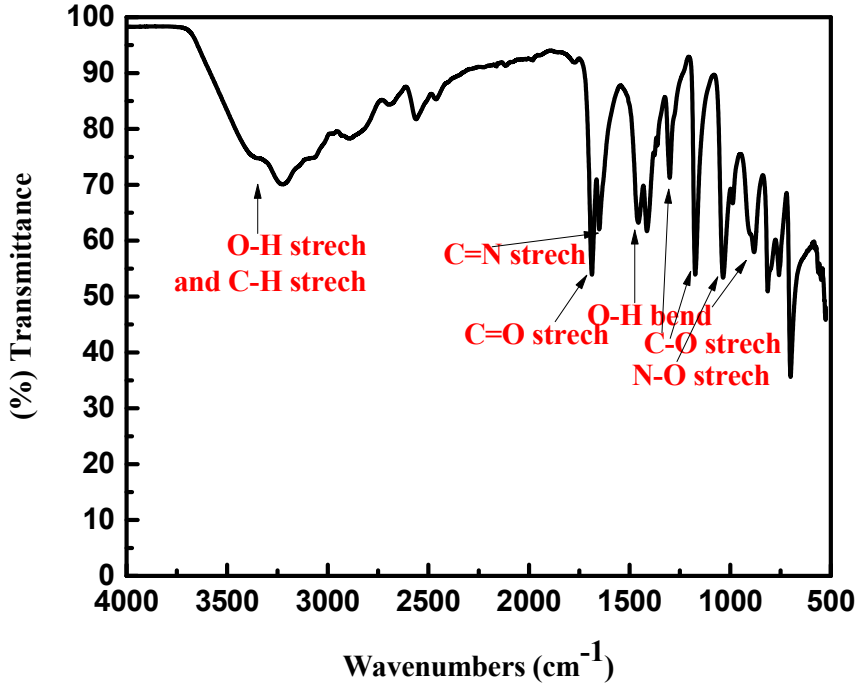

Figure 6- 1. The IR spectrum of HPAO

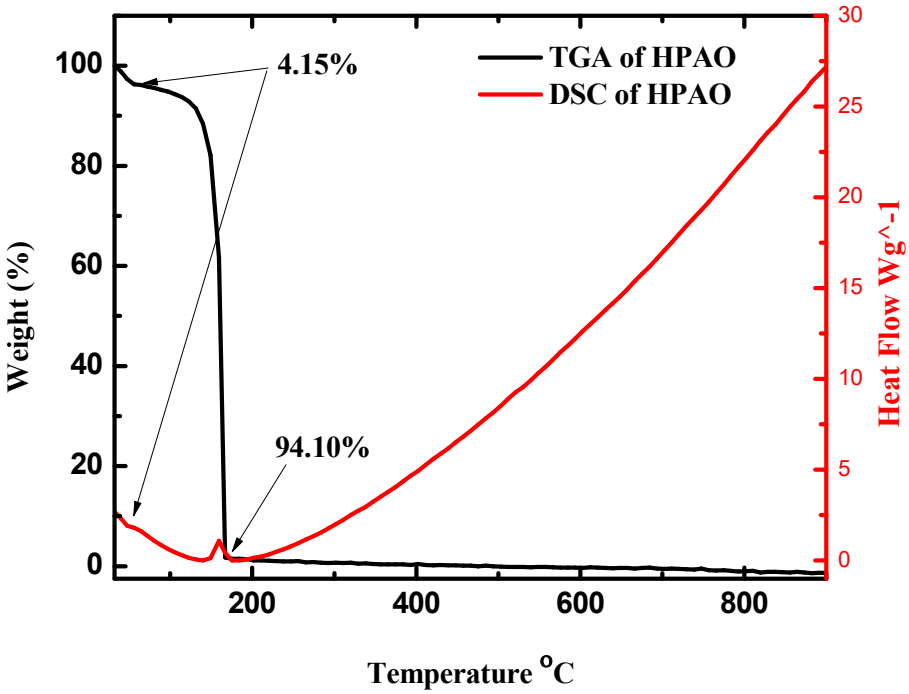

Figure 6- 2. TG-DSC curves of HPAO

3.2.Synthesis of Vanadium salt of Pyruvic Acid Oxime, $VO(PAO)_2$

The vanadium derivative of PAO was prepared by reduction of V_2O_5 and acid/base reaction with vanadium pentoxide as presented in Equation 2.

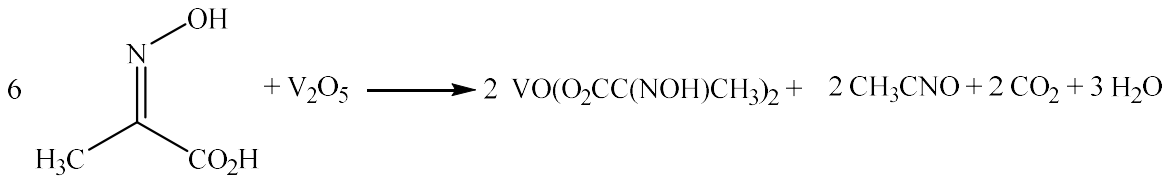

Equation 2. The synthesis of $VO(PAO)_2$

Note that the product is isolated as a hydrate with the approximate formula of $VO(PAO)_2 \cdot 2.5\ H_2O$. The UV-VIS spectrum of the dark blue $VO(PAO)_2$ solution is shown in Figure 3. Three bands were observed at 725, 550, and 400 nm that are attributed in order to $d_{xy} \rightarrow d_{xz}/d_{yz}$, $d_{xy} \rightarrow d_{x^2-y^2}$, *and* $d_{xy} \rightarrow d_{z^2}$ of the vanadyl ion, (V^{4+}), with d^1 electron configuration. [159]

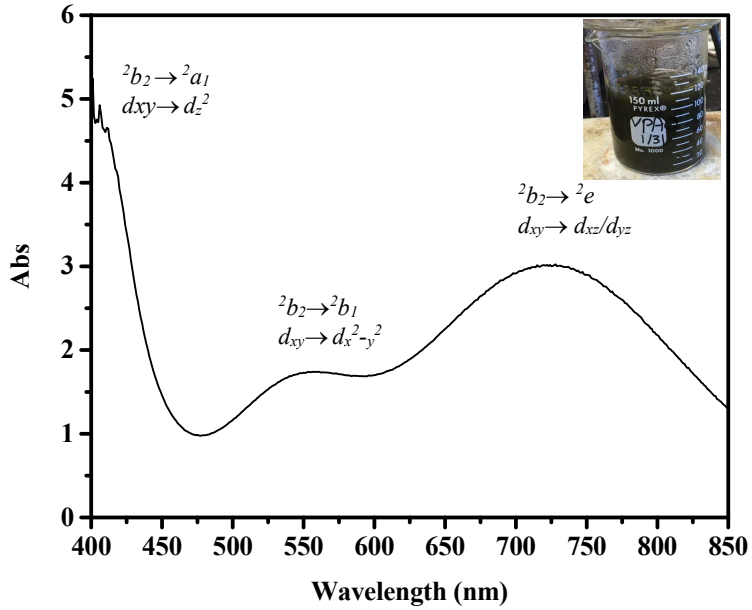

Figure 6- 3. UV-VIS spectrum of $VO(PAO)_2$ solution

Slow evaporation of $VO(PAO)_2$ solution at room temperature results in a formation of hygroscopic dark blue powder of $VO(PAO)_2 \cdot 2.5\ H_2O$. The FTIR spectra of this compound is compared with that of HPAO in Figure 4. It has been reported that the vibrational frequencies of

the asymmetric carboxylate stretch of the IR spectra of the PAO complexes are significantly lowered by 77-95 cm^{-1} compared to that of the parent acid. [215, 216] The decrease of this frequency for the vanadium salt of PAO (Figure 4) is within the reported range (85 cm^{-1}). The decrease may be attributed to the deprotonation and delocalization of the negative charge in the carboxylate ligand and to its coordination to the vanadyl ion. The vibrational frequencies of the oximido moieties in the PAO complexes of the vanadium are not distinguishable since they are overlap with carboxylate stretching frequencies. The vibrational frequencies attributable to the N-O stretch are increased by 77 cm^{-1} in $VO(PAO)_2$ from that observed for the parent acid. This trend is typical for transition metal derivatives of PAO.[215] The new sharp strong band at 965 cm^{-1} characteristic for the vanadyl (V=O) stretching vibration.

The XRD pattern $VO(PAO)_2 \cdot 2.5\ H_2O$, shown in Figure 5, indicates that the product is amorphous. The solid state ^{13}C NMR spectra of HPAO and $VO(PAO)_2$ dried in vacuum at room temperature and at 80 ˚C are shown in Figure 6. The ^{13}C SSNMR spectra demonstrate once again the effect of nuclear quadrupole ^{14}N in the line broadening and spectral splitting of the ^{13}C nuclear magnetic resonance. No major shifts in the COO, C=N and CH_3 signals of the PAO ligand from those of HPAO occurs. This may be a result of the existence of free unreacted HPAO within the product. No signals were detected in the sample of the vanadium complex heated to 80 ˚C. This may be due to decomposition of free unreacted HPAO ligand.

The $VO(PAO)_2$ was reacted with LiOH to prepare a complex where one of the oximes is deprotonated. Such a complex would be a precursor for $LiVO_3$, a useful catalyst and battery materials. is used with expectation that it is act as deprotonating agent. Adding 0.209g of $LiOH \cdot H_2O$ to a solution of $VO(PAO)_2$ caused the solution to slowly turn pale yellow over a period of a day. The final pH was 6.7. After 1 month, reddish-orange block-shaped crystals started to form after slow evaporation of the water at room temperature. After all the water had evaporated, a small amount of black powder was formed in addition to the reddish-orange crystals.

The FTIR spectrum of the crystals, shown in Figure 7, has the characteristic absorption bands for decavanadate anions. The broad bands at 3563, 3489, 3359, and 3173 cm^{-1} regions, and the bands at 1667, 1621, 1599, and 1398 cm^{-1} region can be assigned to asymmetric and symmetric O–H stretching modes and bending modes of the coordination and free water molecules, respectively. The strong bands at 981, 939, 926, 801, 726, and 553 cm^{-1} are due to the stretching vibration of the V=O, (V–O), and (V–O–V) bonds in $V_{10}O_{28}$ clusters. [225, 226]

The crystallographic data and structure refinement are summarized in Table 2. Single crystal X-ray structure determination indicated that the product was $[Na_2(H_2O)_{10}]^{2+}(V_{10}O_{28})^{2-}\cdot 4H_2O$, a novel decavanadate salt. The salt (Figure 8) crystallizes in the triclinic space group P-1. The source of sodium cannot be from impurities associated with HPAO since purity was established. Thus, the sodium likely was extracted from the glass of the reaction vessel. The unit cell is comprised of one hydrated dinuclear sodium cations cluster $[Na_2(H_2O)_{10}]^{2+}$ one decavanadate anion $(H_4V_{10}O_{28})^{2-}$. The coordination environments of the dinuclear Na^+ ions consist of four terminal water molecules and two bridging water molecules that form distorted octahedrons around the Na^+ ions. This is a high unusual arrangement for sodium ions. The $H_4V_{10}O_{28}^{2-}$ clusters are similar to other salts of this ion and consist of closed-packed structures of ten fused VO_6 octahedra. The quadruply protonated decavanadates ion has not previously been reported although a diprotonated cluster has been reported as the sodium salt. [227, 228] Interestingly, the unusual hydrated sodium dimers are just the right size to slot a long side and counter the anionic oxygen on each side of decavanadate. The formation of this compound was due to hydrolysis of PAO ligands and oxidation of vanadium (IV) to vanadium (V) by oxygen gas.

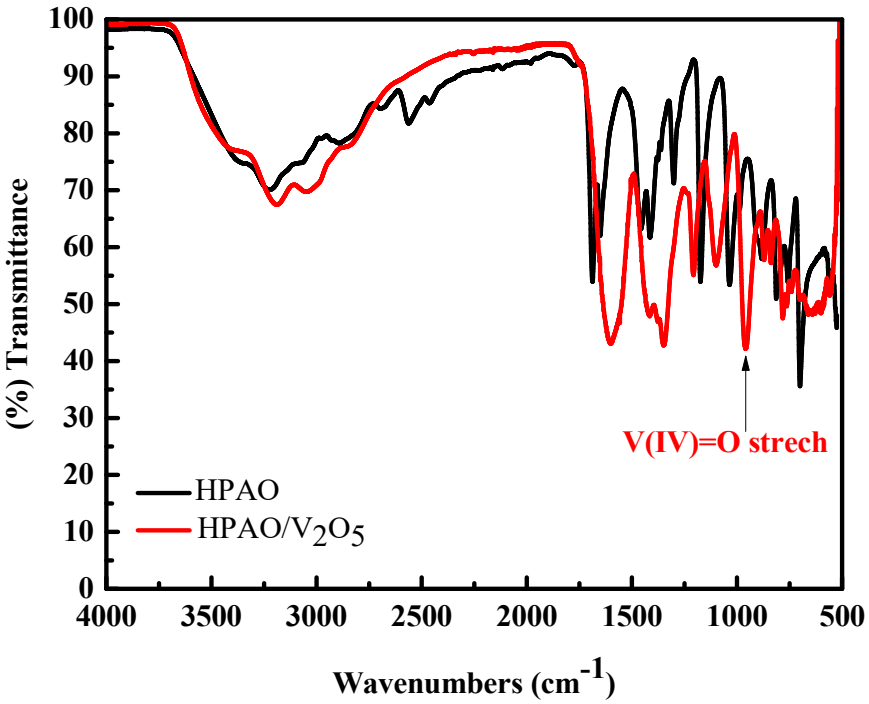

Figure 6- 4. The IR spectra of HPAO and $VO(PAO)_2$ products

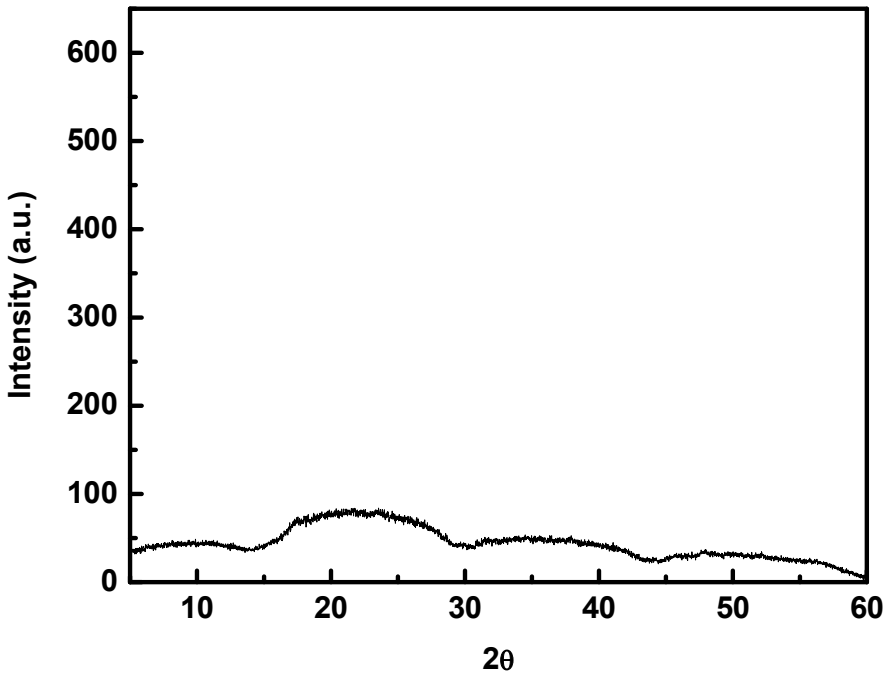

Figure 6- 5. The XRD pattern for $VO(PAO)_2$

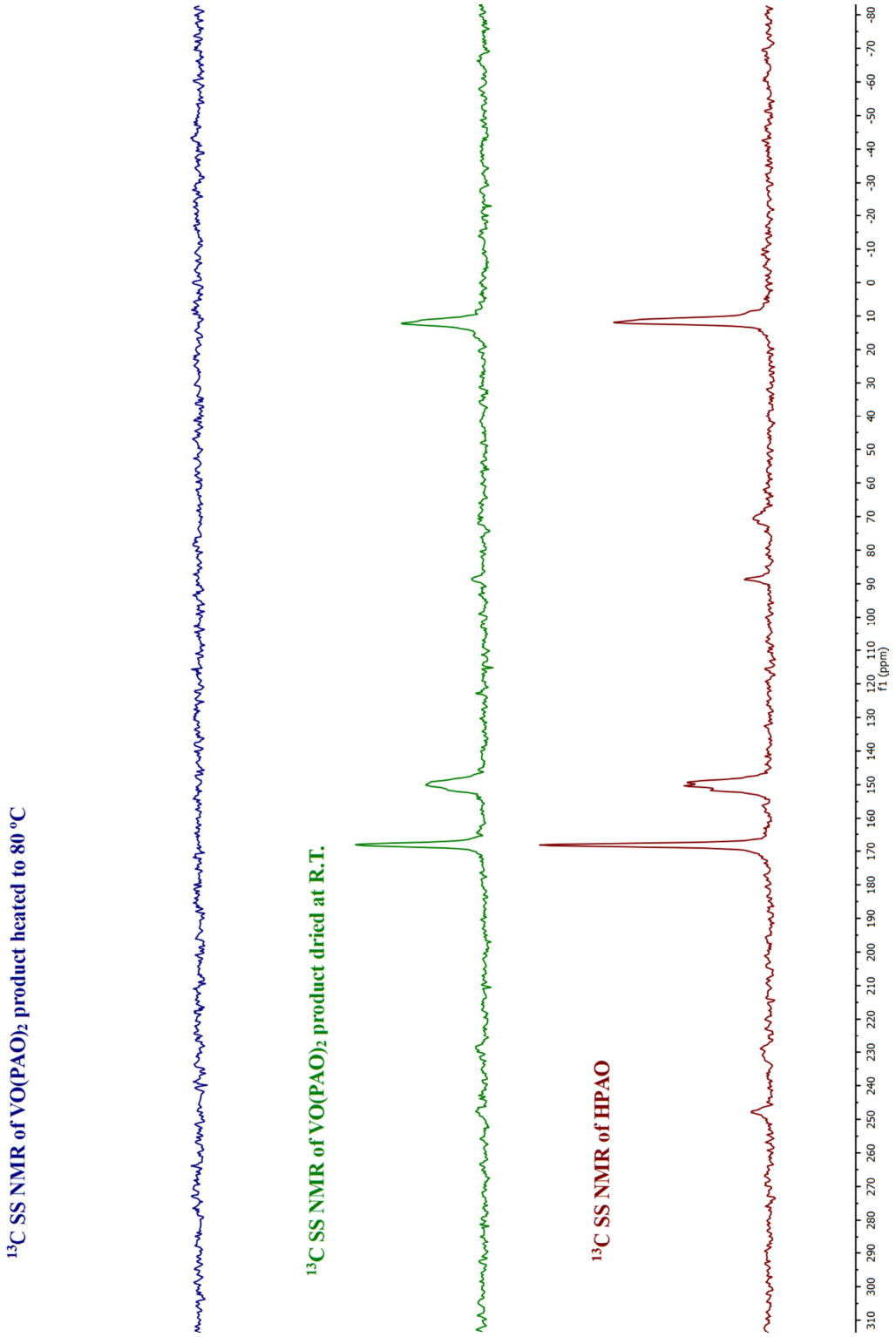

Figure 6- 6. ^{13}C solid-state NMR of HPAO, and VO(PAO)$_2$ products dried at R.T. and 80 ˚C

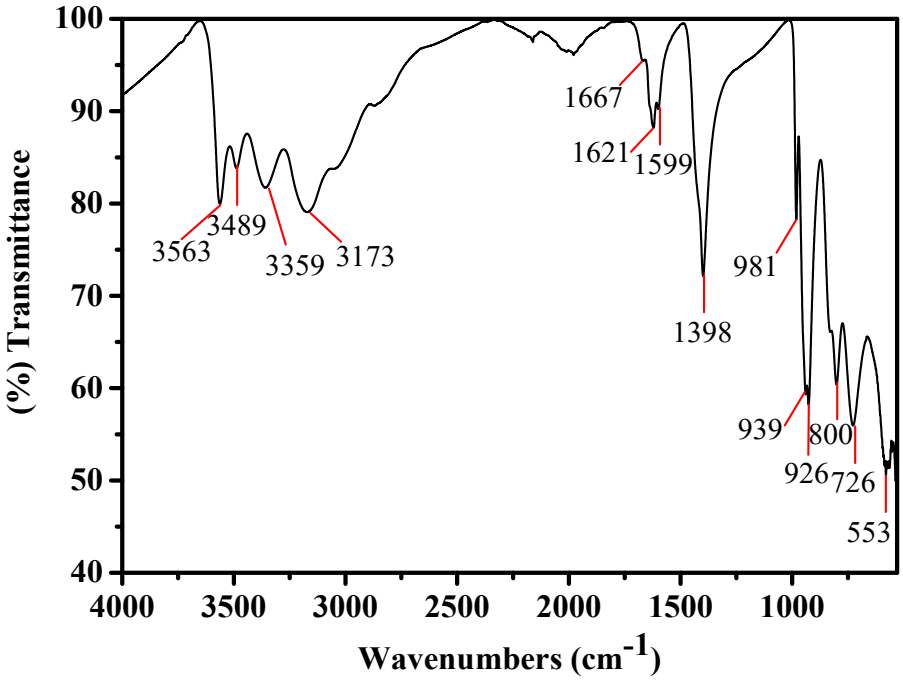

Figure 6- 7. FTIR spectrum of $[Na_2(H_2O)_{10}]^{2+}(H_4V_{10}O_{28})^{2-}$

Table 6- 2. Crystal data and structure refinement for the crystals of VO(PAO)2/LiOH reaction

Empirical formula	$[Na_2(H_2O)_{10}]^{2+}$ $[H_4V_{10}O_{28}]^{2-}$ H_{24} Na_2 O_{38} V_{10}
Formula weight	1187.56
Crystal size	0.34 x 0.27 x 0.25 mm
Crystal system	triclinic
Space group	*P*-1
Unit cell dimensions	a = 8.4482(6) Å α= 68.8943(11)° b = 10.3425(8) Å β= 87.3870(11)° c = 11.2967(8) Å γ= 67.1294(10)°
Volume	843.32(11) Å3
Z, Z'	1
Density (calculated)	2.472 Mg/m^3
Wavelength	0.71073 Å
Temperature	100(2) K
F(000)	616
Absorption coefficient	2.800 mm^{-1}
Absorption correction	semi-empirical from equivalents
Max. and min. transmission	0.541 and 0.449
Theta range for data collection	1.944 to 27.492°
Reflections collected	18845
Independent reflections	3866 [R(int) = 0.0241]
Data / restraints / parameters	3866 / 29 /287
Final *R* indices [I>2σ(I)]	wR2 = 0.0722
R(*F* obsd data)	R1 = 0.0256
Goodness-of-fit (GOF) on F^2	0.999
Observed data [I>2σ(I)]	3523
Largest and mean shift / s.u.	0.001 and 0.000
Largest difference peak and hole ($\Delta\rho_{max, min}$)	0.911 and -0.742 e/$Å^3$

w $R2 = \{\Sigma [w (F_o^2 - F_c^2)^2] / \Sigma[w(F_o^2)^2]\}^{1/2}$

$R1 = \Sigma||F_o| - |F_c|| / \Sigma|F_o|$

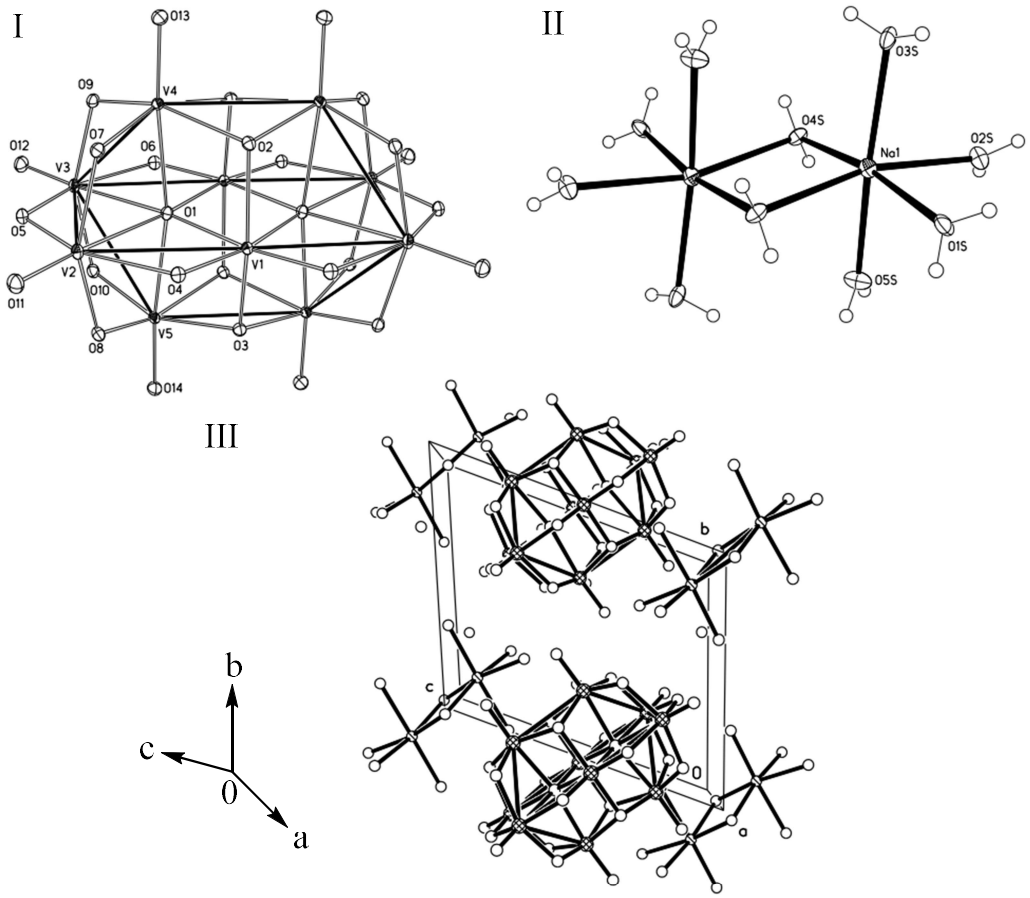

Figure 6- 8. Crystal structure of the $[Na_2(H_2O)_{10}]^{2+}[H_4V_{10}O_{28}]^{2-}$, with displacement ellipsoids drawn at the 50% probability level, thermal ellipsoid plot of cation (i), thermal ellipsoid plot of anion (ii), and the packing diagram (iii)

Figure 9 shows thermal decomposition behavior of $VO(PAO)_2$ in air and N_2. The TGA pattern in air has several overlapped decomposition steps. The first decomposition step bellow100) ˚C and a weight loss of 10 % is attributed to dehydration and is endothermic. The second decomposition step occurs in the range of 150 to 300 ˚C and is also exothermic. This likely due to loss of the first PAO ligand. The third decomposition step from 300 to 520 ˚C is strongly exothermic and due to combustion of the second PAO ligand to yield vanadium pentoxide. The TGA in N_2 is similar to that in air except the final combustion step does not occur so that the final weight loss step tails out to 650 ˚C.

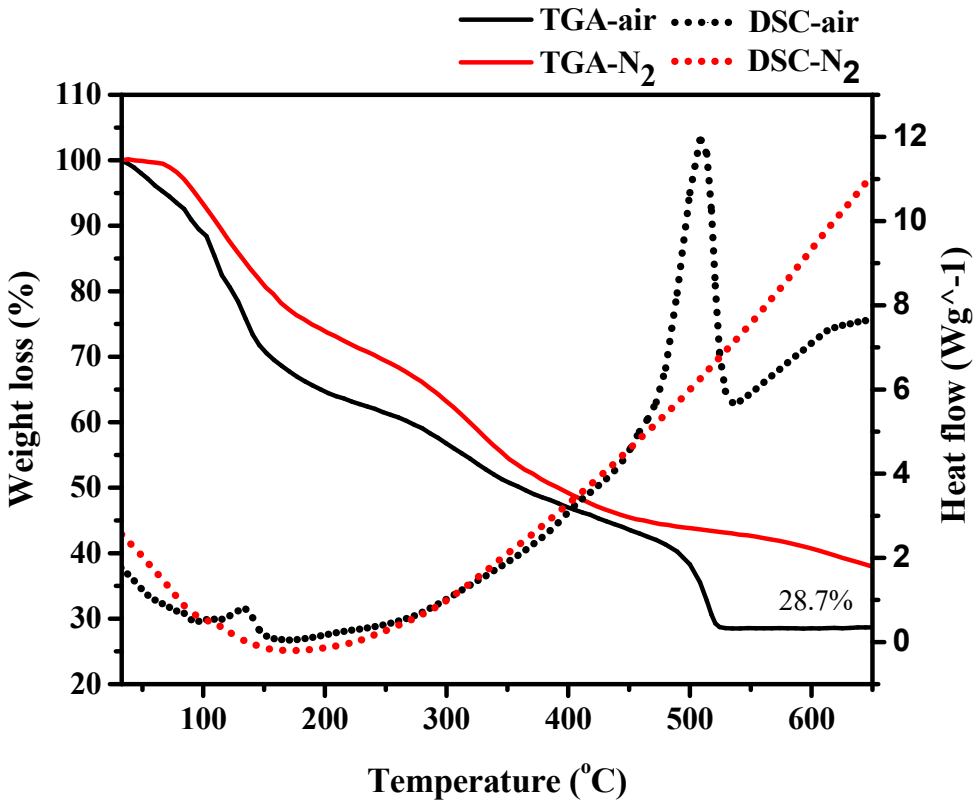

Figure 6- 9. Thermal analysis of $VO(PAO)_2$

The calcination of $VO(PAO)_2$ was conducted at three temperatures (200, 400, and 600 °C) chosen from TGA analysis in ambient air in a temperature programmable muffle furnace, Vulcan 3–130 NDI using a temperature ramp of 5 °C/min, and a hold time of 12 hours. Calcination products were collected after cooling the furnace to 50 °C, at a rate of 10 °C/min. Figure 10 shows the IR spectra of the products produced at these temperatures, the intensity of the characteristic PAO ligand bands decreases markedly upon heating to 200 and 400 °C. New bands are formed that belong to orthorhombic V_2O_5 in the samples heated to 400 and 600 °C. The bands around 814 and 1018 cm^{-1} for calcined product at 400 °C, and 816 and 1026 cm^{-1} for the product at 600 °C can be assigned to the stretching vibration of V=O and asymmetric stretching of the V–O–V bonds respectively. [229] The bands below 600 cm^{-1} correspond to the symmetric stretching vibration of V–O–V bonds. [174, 175, 229] The difference in both spectra is in the sharpness and strength of the

characteristic bands with slightly shifting of their positions upon increasing calcination temperature and that would result from change in V–O bonding due to a change in the V oxidation state. XRD of the products are shown in Figure 11. For the uncalcined product and the calcined materials at 200 ˚C, the XRD are amorphous. At higher temperatures, the XRD pattern match that of orthorhombic phase of vanadium pentoxide, (PDF-00-041-1426) as shown in Figure 12.

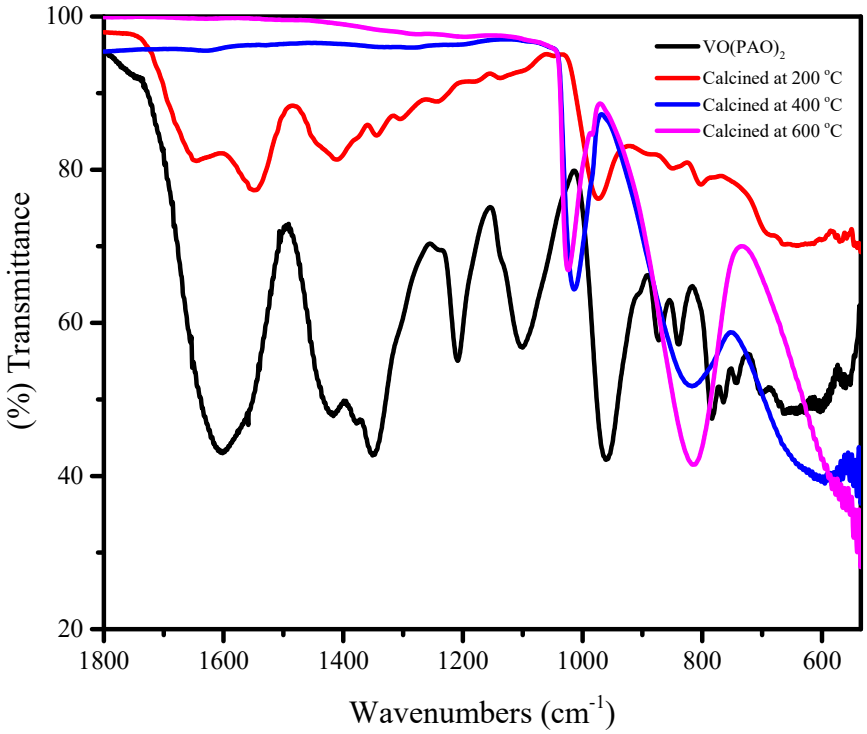

Figure 6- 10. FTIR for $VO(PAO)_2$ and the calcined products at 200, 400, and 600 ˚C

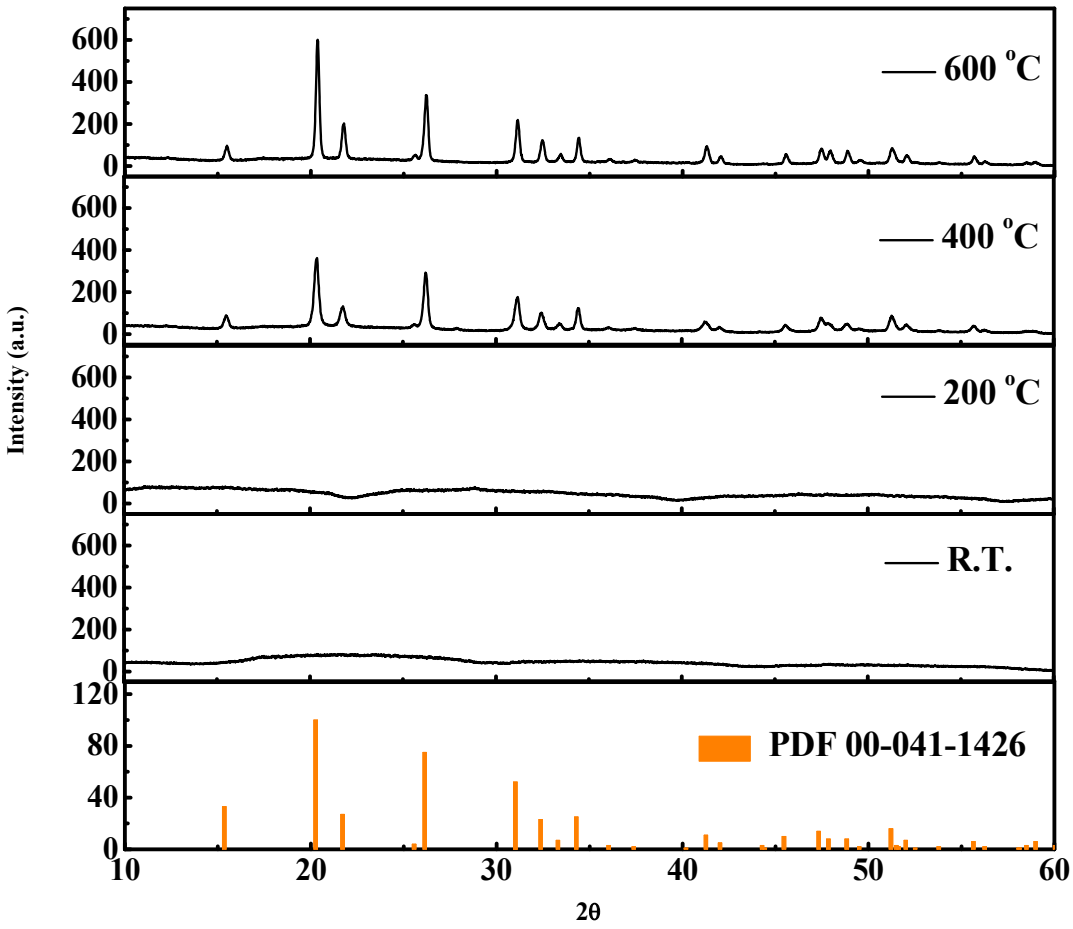

Figure 6- 11. XRD patterns of $VO(PAO)_2$ at R.T, 200 400, 600 ˚C

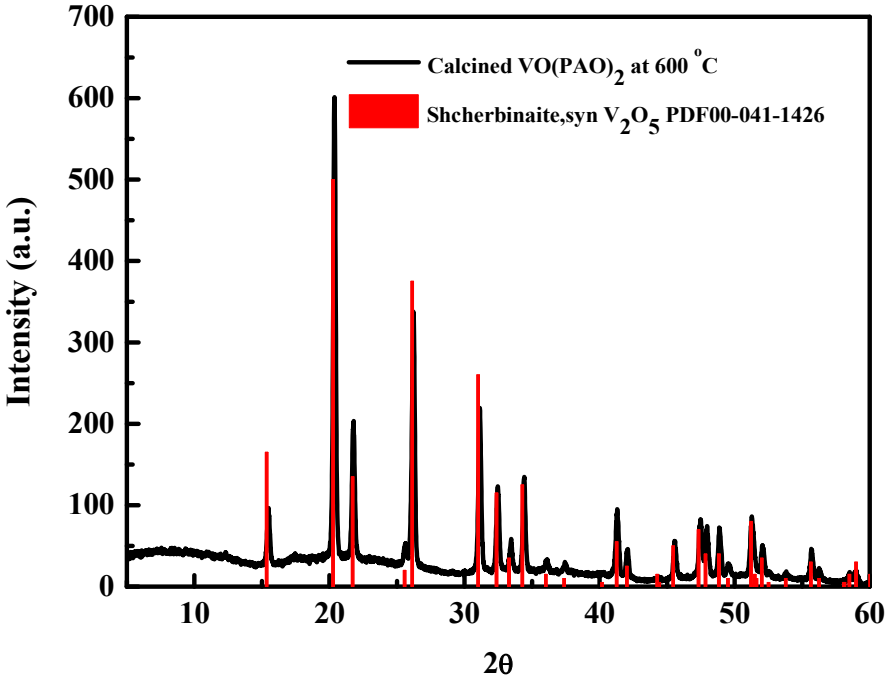

Figure 6- 12. The XRD pattern of $VO(PAO)_2$ product at 600 ˚C

The surface area, crystallites size, and particles size measurements of the products are presented in Table 3. Figure 13 exhibits the SEM images for the calcined products at 200, 400, and 600 ˚C. The surface area reaches a maximum at 400 ˚C (20.9 m^2/g) after removal of the majority of the ligands and before sintering of V_2O_5 occurs. The decomposition of the PAO ligands and dehydration at 200 ˚C appears to create amorphous replicas of the original tubular particle of $VO(PAO)_2$. However, at 400 ˚C crystallization of V_2O_5 has progressed so the tubular particles are covered with small V_2O_5 nanocrystals. Upon heating to 600 ˚C, the V_2O_5 nanoparticles undergo Ostwald ripening that limits itself to the original tabular particle so that the final calcined product consists of smooth tubular particles.

Table 6- 3. Show the ceramic yield, surface area, crystallite size, and particles size measurements of calcined $VO(PAO)_2$ products at 200, 400, and 600 ˚C

Temperature (˚C)	Ceramic yield %	Surface area, BET (m^2/g)	Crystallite size, XRD (nm)	Particle size, SEM
200	75.8	6.2 ± 1.6	NA	NA
400	48.6	20.9 ± 1.3	55 ± 14	Length: (135 ± 26) nm Diameter: (59 ± 13) nm
600	25.8	10.9 ± 1.8	76 ± 11	Length: (2 ± 1) μm Diameter: (391 ± 46) nm

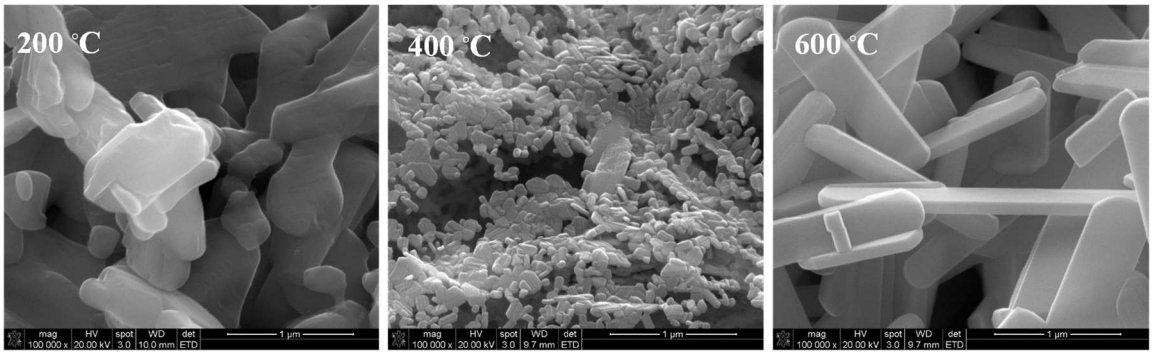

Figure 6- 13. SEM images for the calcined products at 200, 400, and 600 ˚C

Aqueous solution of vanadyl pyruvic acid oxime were reacted with aluminum hydroxide in similar manner to the aluminum hydroxide/vanadyl oxalate reactions discuss in early. A stoichiometric amount of solid aluminum hydroxide (0.780g, 0.01 mole of Al) was added to a vanadyl pyruvic acid oxime solution (0.01 mole of V) and the resulting mixture was stirred at room temperature for 3 day. During that time, the pH increased from 0.9 to 5.4. UV-VIS spectroscopy showed no change in spectra between the starting material and the product (Figure 14), only a decrease in intensity indication of removal of vanadyl ions from the solution. The solution was filtered and the filtrate was dried to produce an off-white powder in a yield of 0.667g (85.51% based on the starting used amount of $Al(OH)_3$). Evaporation of the solution produce 2.316 g of a dark green solid. The FTIR spectra of the products are shown in Figure 15. The spectrum of the dried filtrate displayed the characteristics bands of aluminum hydroxide and adsorbed water. Thermogravimetric analysis confirmed the FTIR result showing that the aluminum hydroxide, with

$Al(OH)_3 \cdot 0.09\ H_2O$ empirical formula, is thermally decomposed to aluminum oxide with a ceramic yield was 64.0% as shown in Figure 16. To confirm this result, pyrolysis of the sample was performed at 650 ˚C for 12 hours to produce a light yellowish powder with 64.4% ceramic yield. The FTIR spectrum after pyrolysis shows absorption bands corresponding to Al_2O_3 as shown in Figure 17. By subtracting the weight of unreacted aluminum hydroxide (0.668 g) from the weight of aluminum hydroxide (0.780 g) it can be calculated that only 14.49 % of the $Al(OH)_3$ reacted with $VO(PAO)_2$. The change of pH could be result of formation of a condensed oxide or oxide/ligand cluster that reduced the $[VO(OH_2)_5]^{2+}$ ions. Alternatively, an acid/base reaction could occur between the OH^- ions of aluminum and either vanadyl ions or PAO ligands to make the dianionic PAO ligand. Notably, $VO(PAO)_2$ is expected to undergo one deprotonation. This would consume 5 mmoles hydroxide-close to the 4.4 mmoles released by $Al(OH)_3$ dissolution. This implies formation $AlV_3O_3(C_3H_4NO_3)_3(C_3H_3NO_3)^{2-}{}_3$. The FTIR spectra of the $VO(PAO)_2$ reactant and the product shows changes in the positions and intensities of C=O and C=N bonds consist with deprotonation of oxime oxygen. [215] changes also occur in the vanadium-oxygen IR absorption bands that indicative of a change in vanadium complexation. The XRD pattern of ALVPAO residue, shown in Figure 18, shows that it's mainly amorphous with several peaks that matched $Al(OH)_3$ (PDF card 00-012-0457). This product was calcined at 650 ˚C for 12 hours with a heating rate of 5 ˚C/min. The ceramic yield of the resulting brown powder was 34.8%. The FTIR of this material is shown in Figure 19. The characteristic stretching vibration of V=O in pure V_2O_5 around ~1020 and 814 cm^{-1} has been split and shifted to lower wave number around 941 and 912 cm^{-1} due to reduction of vanadium species. [229, 230] The bands below 600 cm^{-1} correspond to the symmetric stretching vibration of V–O–V bonds. [174, 175, 229] The FTIR analysis of the pyrolysis products with and without aluminum indicate that aluminum has inserted into the vanadium oxide layers and the suggested product could be $Al_{0.039}V_2O_5$.

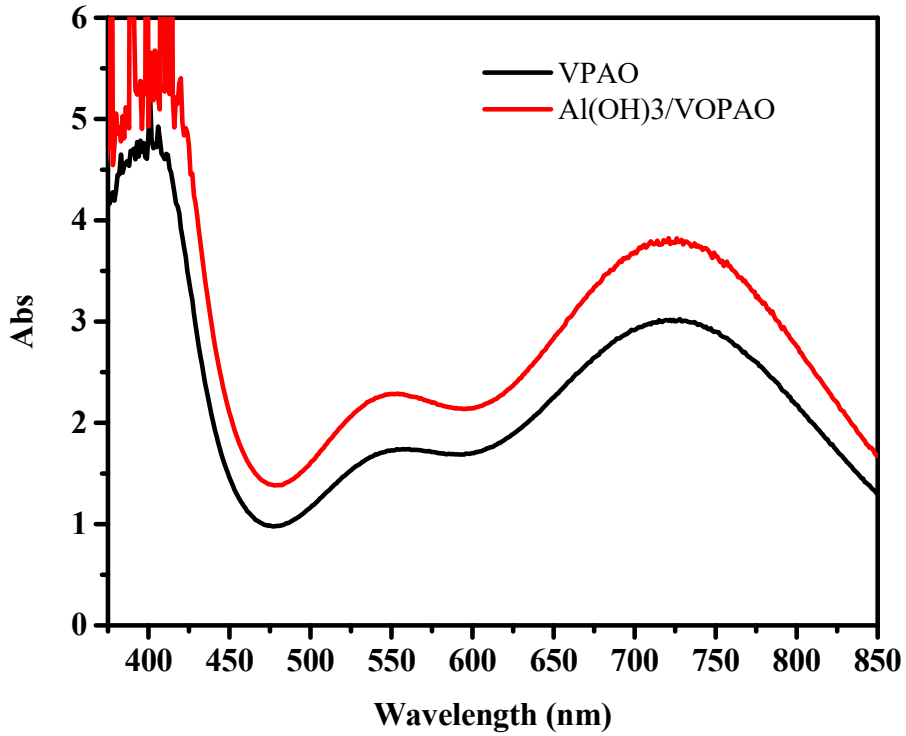

Figure 6- 14. UV-VIS spectra of $VO(PAO)_2$ and $Al(OH)_3/VO(PAO)_2$ solutions

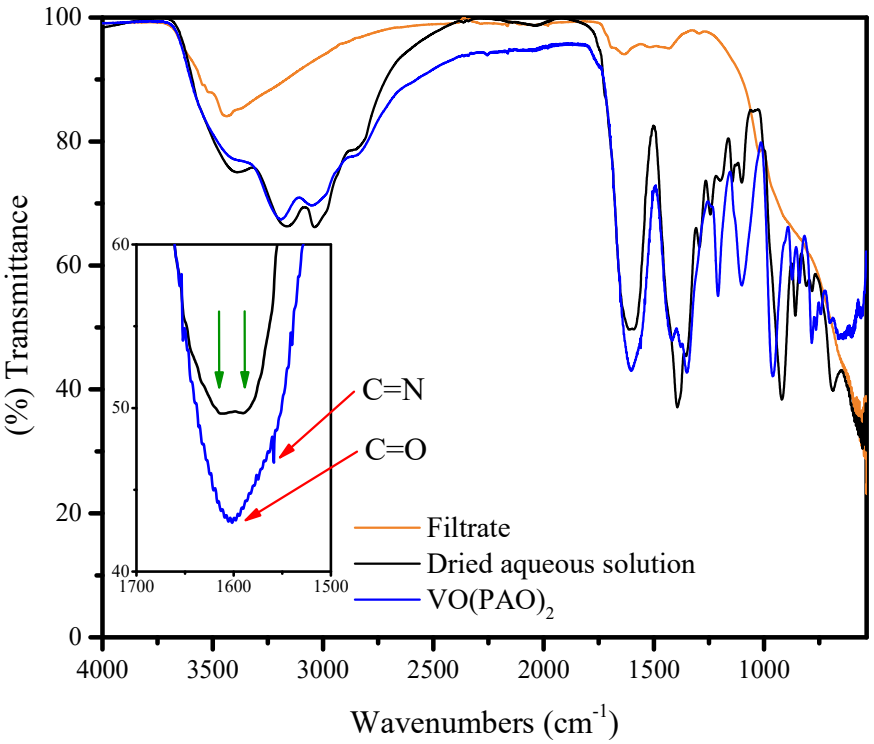

Figure 6- 15. FTIR spectra of dried filtrate and residue in comparison to $VO(PAO)_2$ solid

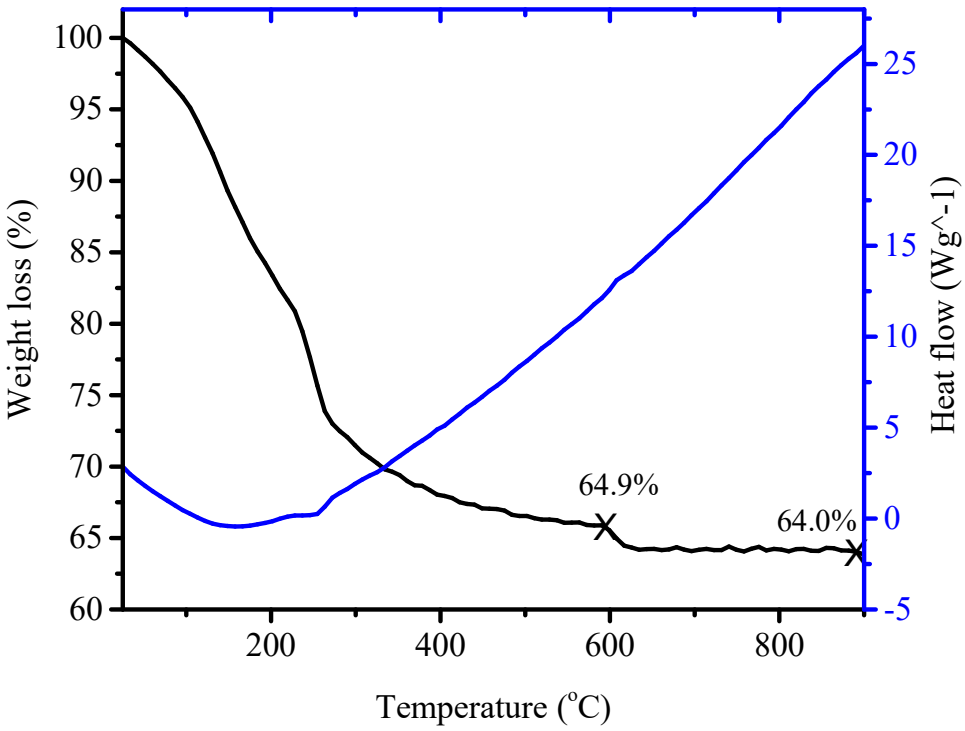

Figure 6- 16. Thermogravimetric analysis of the filtrate from the $Al(OH)_3/VO(PAO)_2$ reaction

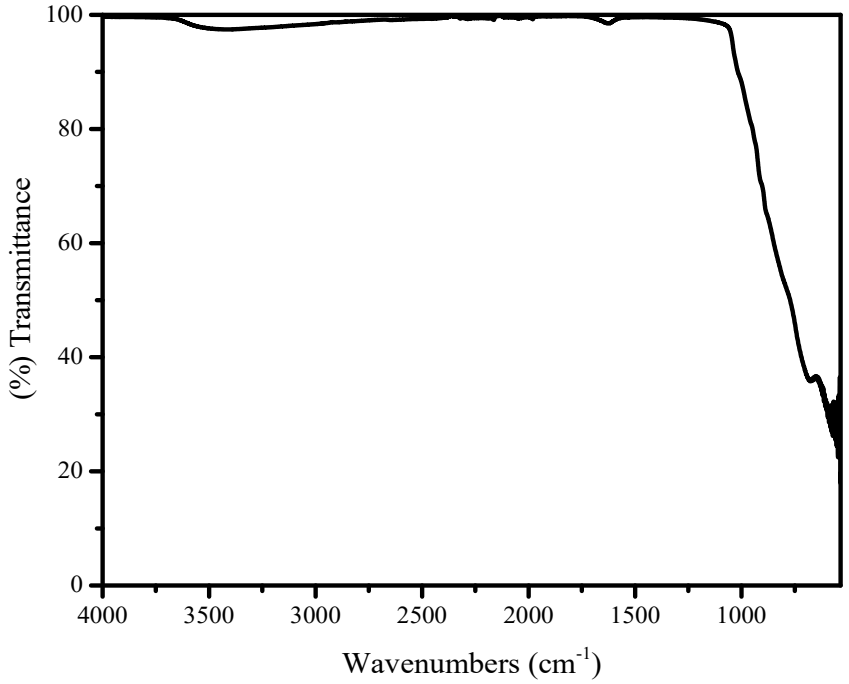

Figure 6- 17. FTIR for Al_2O_3, the pyrolysis of the off-white filtrate

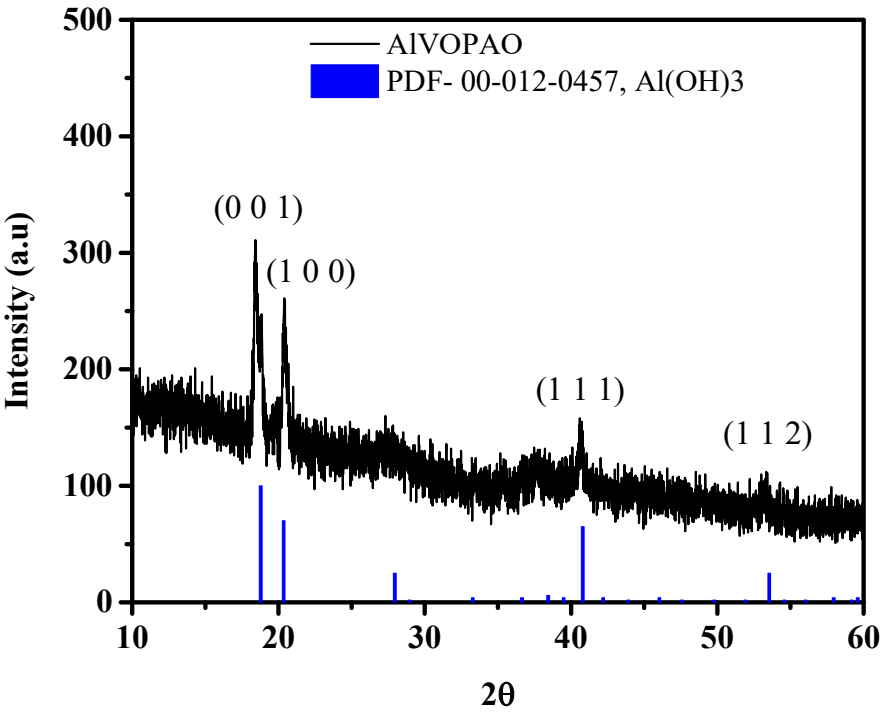

Figure 6- 18. XRD pattern of the dried residue of AlVPAO

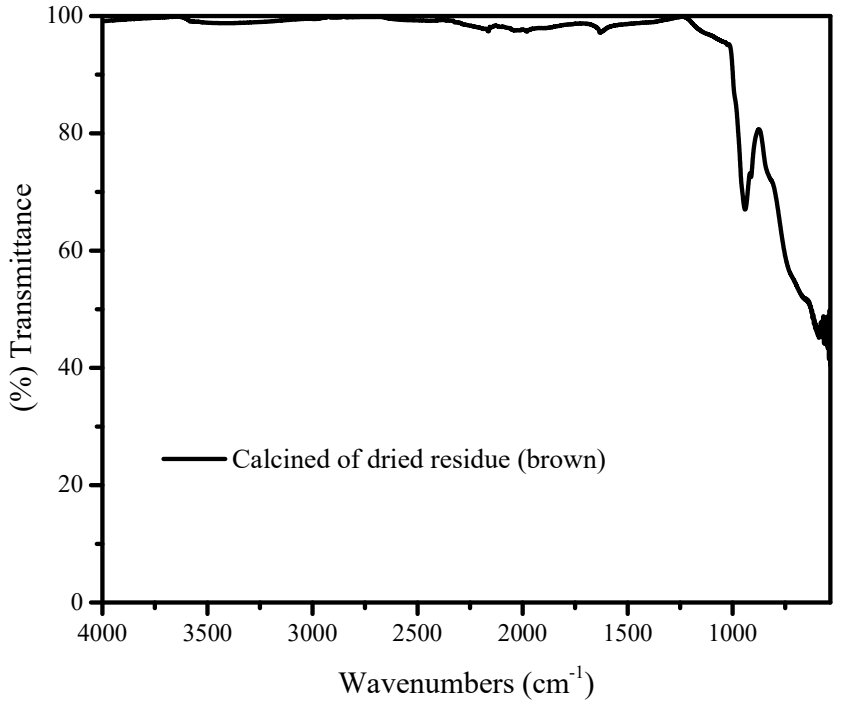

Figure 6- 19. FTIR for $Al_xV_2O_5$, the pyrolysis of the dark green-blackish residue

4. Conclusion:

A drack blue solution of $VO(PAO)_2$ was successfully synthesized through reduction of vanadium pentoxide with pyruvic acid oxime. This solution as synthesized or deposited on a substrate could be utilized for a variety of catalytic and sensing applications as described later in the dissertation. Insertion of aluminum into layered vanadium pentoxide could be pursued by dissolving aluminum hydroxide into a solution of $VO(PAO)_2$ and calcining the product. Investigations and optimizations of the aluminum hydroxide/$VO(PAO)_2$ reaction conditions should be further studied and expanded to other metal salts. $VO(PAO)_2$ was used as a precursor to nanocrystalline vanadium pentoxide which is useful for a wide variety of application. The investigation of other derivatives of α-oximinocarboxylic acids would be use in the catalytic and sensing applications worthwhile.

CHAPTER VII

SENSING APPLICATIONS FOR VANADIUM OXIDES/OXYHYDROXIDES IN BOTH BULK AND NANOPARTICULATE FORMS

1. Introduction:

Hydrogen peroxide, H_2O_2, is the simplest of organic peroxides considered as strong oxidizing and powerful bleaching agents, used in food, medicinal, pharmaceutical, and industrial fields. Peroxides are also useful initiators for some types of polymerization (e.g. epoxy resins used in glass-reinforced plastics). [231-233] The exposure limit of hydrogen peroxide according to Occupational Safety and Health Administration (OSHA) is 1 ppm over an 8 hour a day. [234] Hydrogen peroxides along with other chemicals in presence of acid catalysts known to produce a highly explosives materials. The explosions of peroxides materials have massive negative impacts on the economy and security of the world. [235, 236] Because of the availability of these chemicals, the easy access to their preparing instructions along with the safety challenges associated with their storages, handling, and transportations, several investigations have been conducted for developing new or enhancing the existing technologies. [134, 237-247] Amongst of these successful investigations, the development of the blue nanometric inks that can detect and neutralize peroxide explosive based on colorimetric analyses. [248] These developed oxide bronze materials belong to well-defined, non-

stoichiometric, insertion compounds with general formula $A_xM_yO_z$, where M is a transition metal, A is H^+, alkali metal, alkaline earth metal, and lanthanide, or other metals. Insertion of M (e.g. Na, Li, H) into the lattice Mo^{6+}or W^{6+} oxides and partial one-electron reduction of the host metals to Mo^{5+}or W^{5+} forms colorful molybdenum bronzes (M_xMoO_3), and tungsten bronzes (M_xWO_3). [249-252] These bronzes with their dramatic change in color when exposed to oxidants can be used to detect nitro and peroxide-based explosives. [242, 253] Since vanadium oxides/oxyhydroxides are among the more important catalyst and sensing materials used in industrial processes such as: manufacturing of essential chemicals (e.g. sulfuric acid, phthalic anhydride), and in reducing of environmental toxic gases (e.g. nitrogen oxides from flue gas of power plants) [1, 21, 48, 142, 153], it is suspected that the vanadium bronze would have similar chemistry as molybdenum and tungsten bronzes and would therefore be a good candidate for explosive sensing and catalytic applications. This chapter will report the developments of sensors based on vanadium colorimetric reagent, aluminum oxide TLC slide, thin film and investigate utilizing the colorful materials for sensing hydrogen peroxide.

2. Experimental:

2.1.Preparation procedure of the sensors

2.1.1. Sensors based colorimetric reagents

The synthesis of colorimetric regents of the colloidal V_2O_5/NaS_2O_4 suspension with different ratios and the VOC_2O_4, and its mixed metal solutions were described in the previous chapters. To check for response to hydrogen peroxide, these synthesized colorimetric regents were used as a reagent solutions themselves as well as they have been submerged onto strip, and allowed to air dry.

2.1.2. Sensors based aluminum slide

The colloidal V_2O_5/NaS_2O_4 suspension with different ratios, VOC_2O_4 solution and its mixed metal solutions, VOPAO solution were deposited onto aluminum oxide, TLC sheet perished from Baker-flex, J.T. Baker. TLC sheet was placed into the evaporation dish containing the solution and it was immersed until the solution evaporated. Once the resulting slide obtained its then washed gently with distilled water and dried in air (Figure 1).

Figure 7- 1. precursor deposition process procedure

2.1.3. Sensors based thin film

Vanadium (IV) oxide nanoparticles were synthesized through a homogeneous reduction reaction between peroxovanadic acid and oxalic acid using the method of Guicun Li et. al. [46] Vanadium (V) oxide (V_2O_5) powder (0.036 g) was dissolved in 0.2 mL of a 30% H_2O_2 solution, and then 4 mL of distilled water was added while stirring. Once a reddish-orange solution had formed, 4 mL of a 0.1M oxalic acid solution was then added. The resulting solution was then placed into a stainless steel hydrothermal synthesis reactor. The reactor was maintained at 180 °C for 2 hours and then allow to cool to room temperature. The resulting greenish blue solution was collected and centrifuged. This yielded a dark blueish-green gel that was then dried at room temperature in vacuum to form a dark blue thin film (Figure 2). To check for response to hydrogen peroxide, the synthesized vanadium (IV) oxide nanoparticles gel was deposited onto glass slide. Basically, the gel was allowed to hydrolyze and dried resulting in coating of slide.

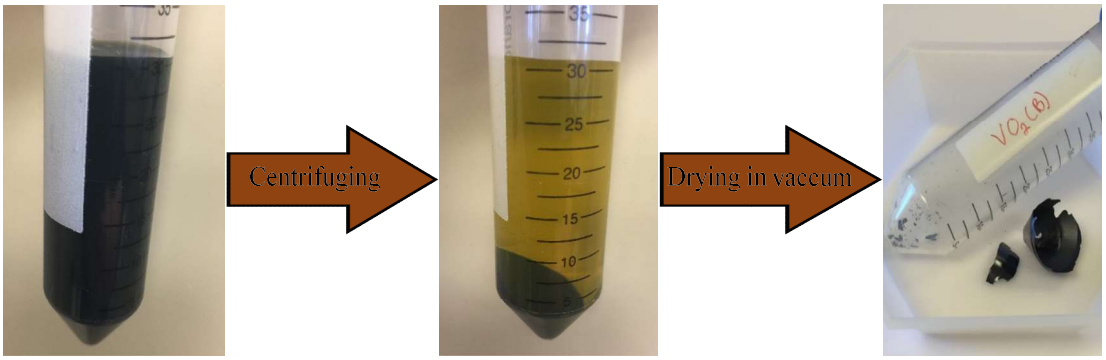

Figure 7- 2. The process to obtain dark blue thin film through centrifuging Vanadium (IV) oxide nanoparticles

2.2.Characterization techniques

The structure of the colloidal suspension and the corresponding thin film as described in the previous chapters has been characterized by ultraviolet visible spectroscopy, dynamic light scattering, infrared spectroscopy, X-ray powder diffraction, and thermogravimetric analysis. The thickness of the obtained thin film was determined by Ektak XT™ stylus profiler. The conductivity of the thin film was measured using impedance spectroscopy, and four-point probe Keithley Instruments 2400 power/source meter.

2.3.Hydrogen peroxide sensing

Hydrogen peroxide solutions of various concentrations were made through dilution of a 35 % hydrogen peroxide stock solution. Then the nanoparticulates solution, their strips, and the manufactured slides were checked for color change after hydrogen peroxide exposure. For the vanadyl oxalate solution Carry 100 UV/VIS spectrometer was used to recorded the spectra after the exposure.

3. Results and Discussion:

3.1.Sensors based colorimetric reagents

The synthesis and characterization of vanadium bronze suspensions with varying the ratios of $V_2O_5/Na_2S_2O_4$ were described in chapter 3. Based on the discussion of their structural characteristics, only 0.166, 0.249, 0.498, and 0.993 ratios had V(4+) ions within the bronze

nanometric matrixes. However, as mentioned earlier the particulates of theses suspension within two weeks are precipitated therefore to test their ability to detect hydrogen peroxide the suspensions were submerged onto test strips. The response toward direct 1% H_2O_2 exposures (Figure 3) were rapid within less than a second. The only difference was excluded to varying color shades along with the different ratios. To enhanced the solutions stabilities and even more their response for hydrogen peroxide detection, these solutions were deposited onto aluminum oxide TLC slides. Direct exposure of slide made up by solution of $1V_2O_5/0.993Na_2S_2O_4$ ratio to 35% hydrogen peroxide resulting in instant color change from blue to bright yellow (Figure 4). Upon exposure to gaseous hydrogen peroxide, the aluminum oxide TLC slides of deposited suspensions with molecular molar ratio of 1.0 V_2O_5 to 0.166, 0.249, and 0.498 $Na_2S_2O_4$ changed from green to yellow in which the intensities are dependent on the deposited molecular mole ratio of each suspensions along with the exposure time as shown in Figure 5 noting this image of hydrogen peroxide exposure as function of time provided by Dr. Materer. In all cases, by utilizing TLC slides of nanoparticulate vanadium oxide bronze the gaseous hydrogen peroxide were given noticeable rapid colorimetric responses. Although the slides show high sensitivity towards detection of hydrogen peroxide, theses slides are not selective since their color change with long exposure to atmospheric air and that due to interference of oxygen from water and other trace gas species.

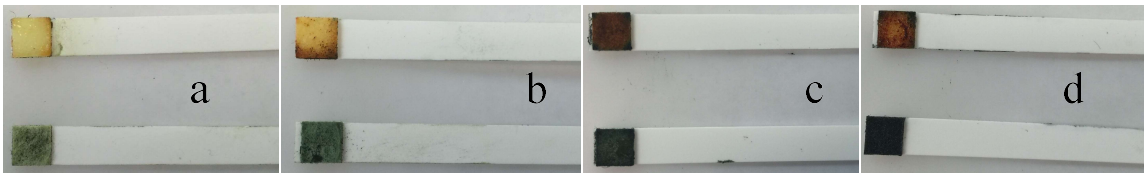

Figure 7- 3. Color change of the vanadyl solution synthesized with $V_2O_5/Na_2S_2O_4$ ratio of 0.166 (a), 0.249 (b), 0.498 (c), and 0.993 (d) deposited test strips after the exposure of 1% hydrogen peroxide

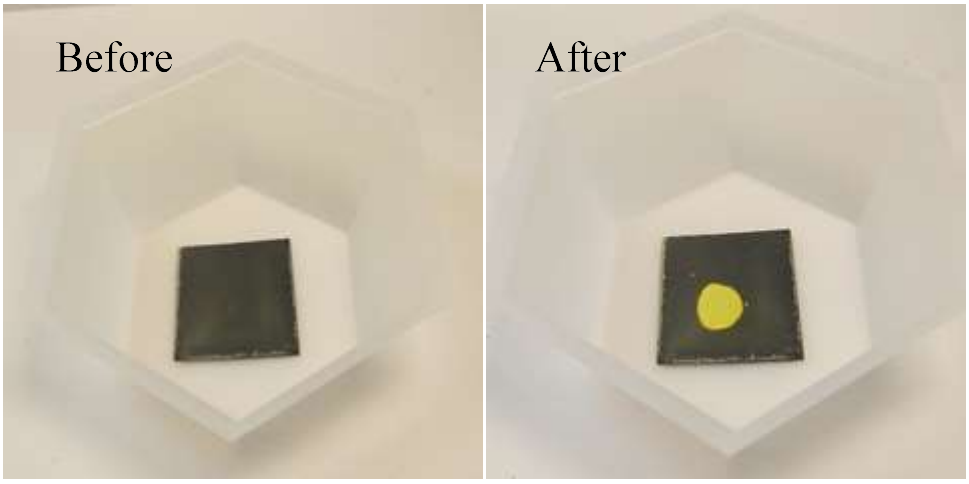

Figure 7- 4. The color change of slide made up by solution of $1V_2O_5/0.993Na_2S_2O_4$ ratio after direct exposure with 35% hydrogen peroxide

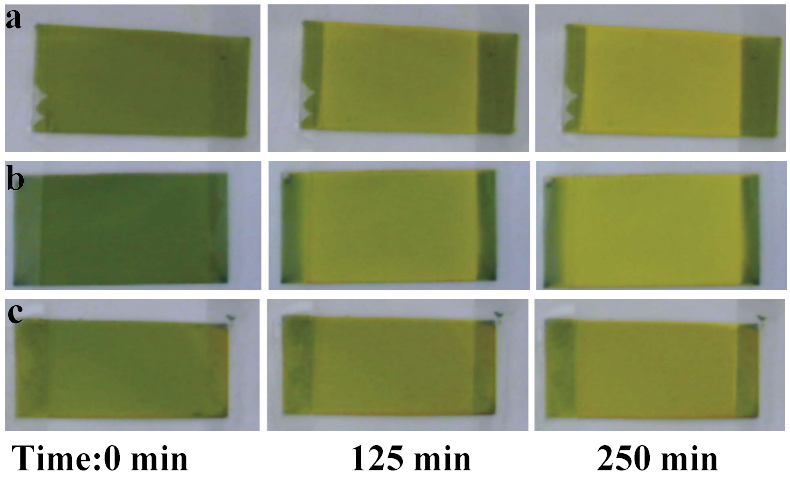

Figure 7- 5. Changing color during sensing hydrogen peroxide vapor as a function of time using aluminum oxide TLC slides of deposited suspensions with molecular molar ratio of 1.0 V_2O_5 to (a) 0.166, (b) 0.249, and (c) 0.498 $Na_2S_2O_4$

The solution of vanadyl oxalate was applied to paper and allow to dry. The paper was then exposed to gaseous of 35 % hydrogen peroxide gaseous for a color change. Basically, the coated paper placed top of bottle jar filled with 5 ml of hydrogen peroxide. The blue color change with less than 10 minutes and turn to the yellow color (Figure 6). This yellow color remained unchanged as long this paper exposed to hydrogen peroxide vapor and when removed it turned to its original

blue color. The solution was also applied to test strip and exposed to 35 % hydrogen peroxide. The color of manufactured strip changes from blue to red with less than 3 seconds and within 7 minutes it became blue once again Figure 7. Moreover, the vanadyl oxalate solution used itself as a colorimetric agent for detection hydrogen peroxide. Basically, a 20 µl of 35 % hydrogen peroxide was added to a 20 ml of the blue agent and the red color appears after 3 seconds and it takes 40 minutes to return to its original blue as seen in Figure 8. The color regeneration was analyzed using UV-VIS spectroscopy. A 4 ml of vanadyl solution was diluted with distilled water to 10 ml. The two cuvettes were filled with 4 ml of the diluted solution; one was used as blank to subtract the ordinal absorption bands and detected any new bands. Upon exposure of the solution to 20 µl of 1 % hydrogen peroxide, the solution turns reddish and a one band with λ_{max} of 440 nm is observed in the UV-VIS spectrum that attributed to the peroxovanadate complex [254] as shown in Figure 9. Plotting the Abs_{440nm} as function of time as seen in Figure 10, this band exponentially declines with time after peroxide exposure regenerating the blue color. Kinetic analysis of the observed data demonstrated that the regeneration of color follows first order kinetic with rate constant of 1.0×10^{-3} s^{-1} and the color regeneration was completed within 40 minutes (Figure 11). This experiment demonstrated the potential for this colorimetric reagent to be used for the detection of hydrogen peroxide vapors and solution phases. In order to further investigate this potential application of the colorimetric reagent, sensing of a 35% H_2O_2 solution was also performed using VOC_2O_4 supported on aluminum oxide TLC sheets. The color changes instantly from dark greenish blue to bright orange within less than 3 seconds and then the orange color fades and returns to dark blue (Figure 12). The observations indicate that the aluminum mixed valence vanadium compounds regenerate itself in similar manner to aqueous VOC_2O_4 solutions and VOC_2O_4–based test strips. Results suggest that a red vanadium (V) peroxide complex forms immediately upon exposure to hydrogen peroxide. This then slowly decomposes to form oxygen and vanadium (IV) oxide as presented in Figure 13.

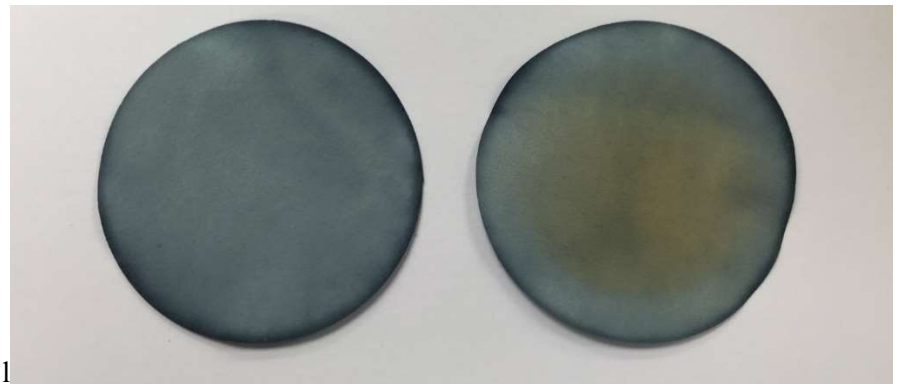

Figure 7- 6. Paper with vanadyl oxalate solution: as manufactured (left); exposed to hydrogen peroxide vapors (right)

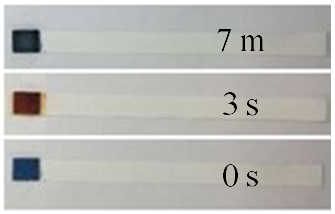

Figure 7- 7. Strip with vanadyl oxalate solution: as manufactured (bottom); exposed to 20 µl of 1% hydrogen peroxide (middle); after the exposure (top)

Figure 7- 8. Changing color during sensing of 35% H_2O_2 solution as a function of time using the blue reagent

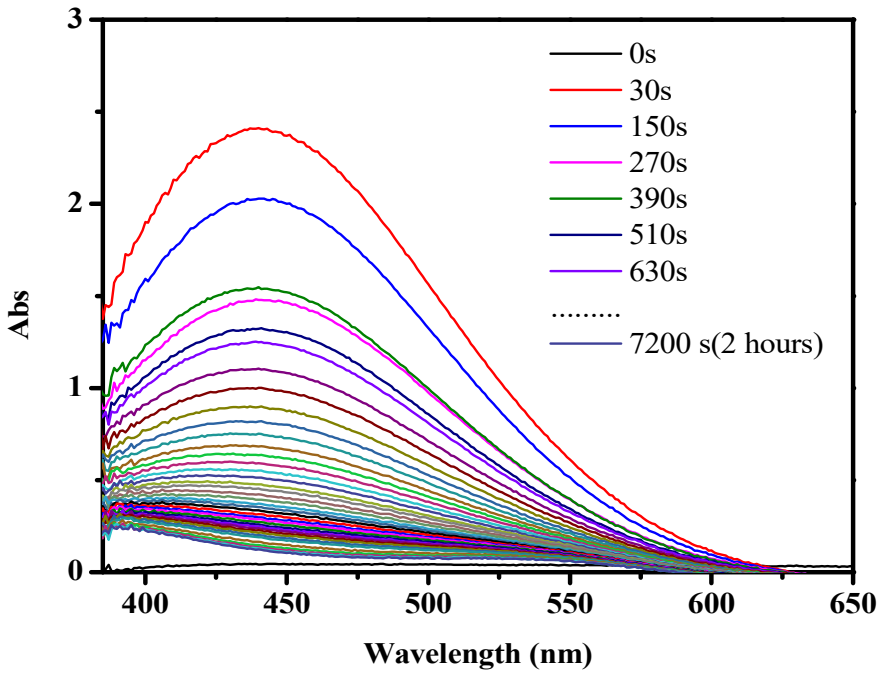

Figure 7- 9. UV-Visible subtracted spectrum of colorimetric reagent prior to exposure to hydrogen peroxide (0s) and colorimetric reagent exposed to hydrogen peroxide as a function of time

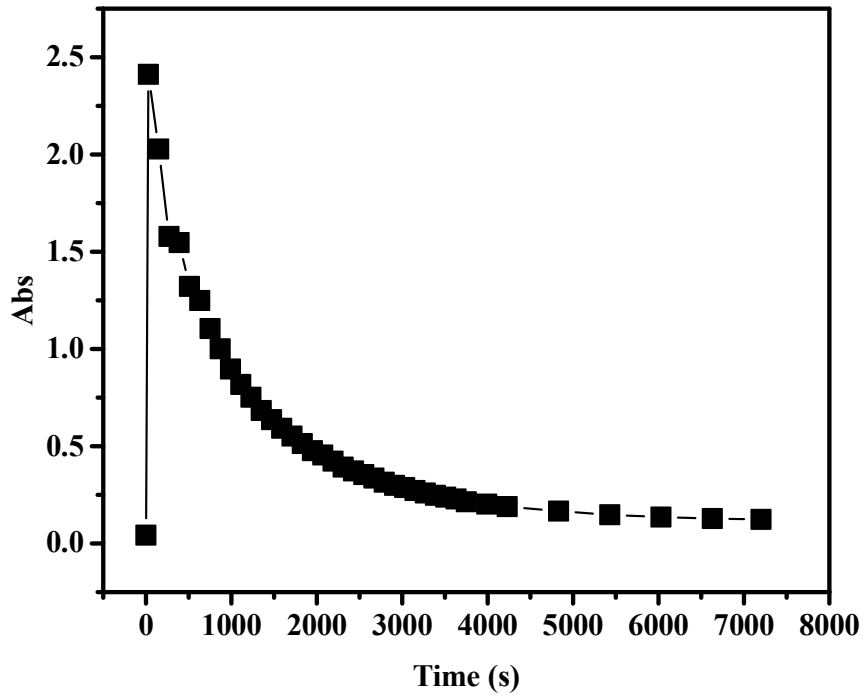

Figure 7- 10. Absorption versus exposure time for the colorimetric regent

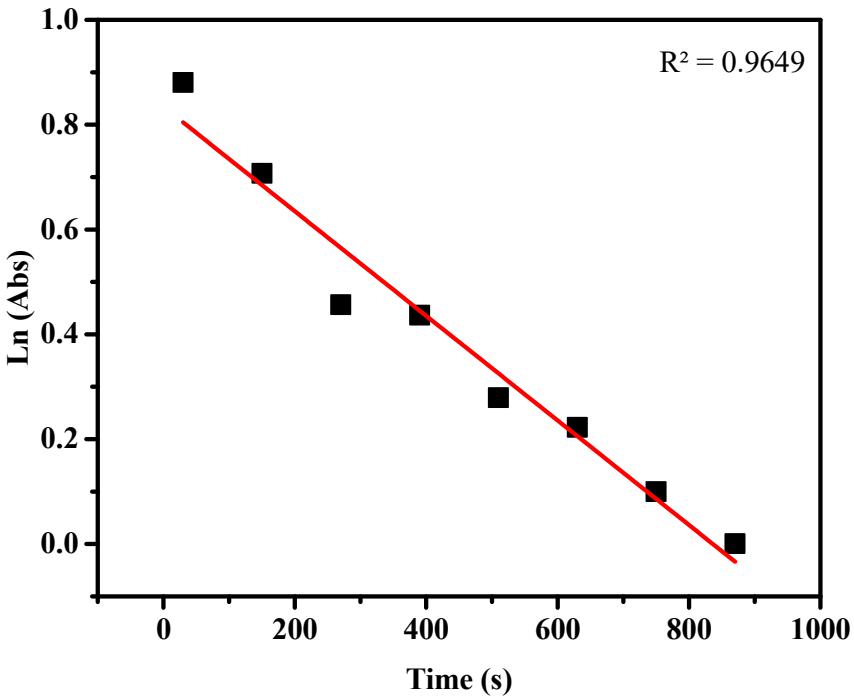

Figure 7- 11. The first-order behavior of the first 14 minutes of exposure

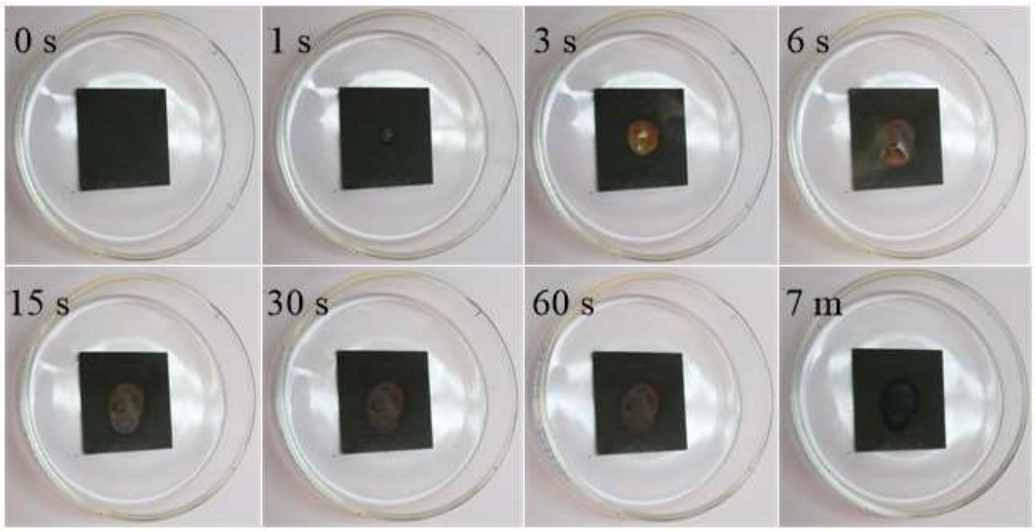

Figure 7- 12. Changing color during sensing of 35% H_2O_2 solution as a function of time using a TLC aluminum oxide sheet deposited with VOC_2O_4 solution

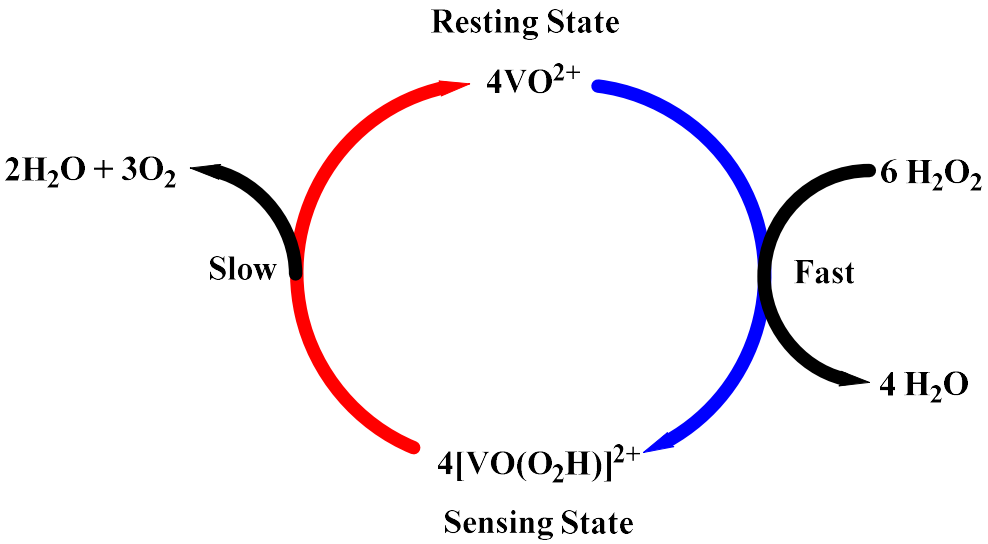

Figure 7- 13. Proposed mechanism of color regeneration of the colorimetric regent

Mixed metal solution of aluminum-, yttrium-, and lanthanum-vanadium nanoparticulates solutions were also tested for hydrogen peroxide detection. The strips with nanoparticulates solutions change their original dark blue and green colors to orange reddish color after the hydrogen peroxide (35 %) exposure as shown in Figure 14. The color changes were not able or hardly detected in case of using lower concentration of hydrogen peroxide 1 % and 10 %, respectively. To enhance their performance, the nanoparticulates of mixed metal were supported on aluminum oxide thin layer sheet and exposed to different concentrations of hydrogen peroxide. In aluminum vanadyl particulate solution supported on aluminum oxide TLC slide (Figure 15), the yellow color took 40 seconds to appears in case of 1 % hydrogen peroxide while it took 5 second in case of 35 % hydrogen peroxide. In supported lanthanum vanadyl particulate (Figure 16), the color change was not detectable for 1 %, and the yellow color start to appears after 8 seconds and settle after 3 minutes, while with less than a second the orange color observed in case of 35 % hydrogen peroxide. The exposure of hydrogen peroxide using the supported yttrium vanadyl particulates synthesized from the bulk- and nano-yttrium oxide are shown in Figure 17 and Figure 18, respectively. In case of bulk material within 6 seconds the orange color detected with exposure of

35 %. Sensing hydrogen peroxide using this material also could be done with the 1 % concentration as illustrated. In contrast, the nano materials could not be or more precisely hardly able to detect either 1 % or 10 % hydrogen peroxide. In fact, fading color was detected after 15 minutes using 10 % hydrogen peroxide which the same in case of 35 % but within 10 seconds and by adding another 20 µl to the same slide the color turned to orange-reddish in 10 seconds and turn to green after 20 minutes. The sensing reaction was aggressive releasing gasses.

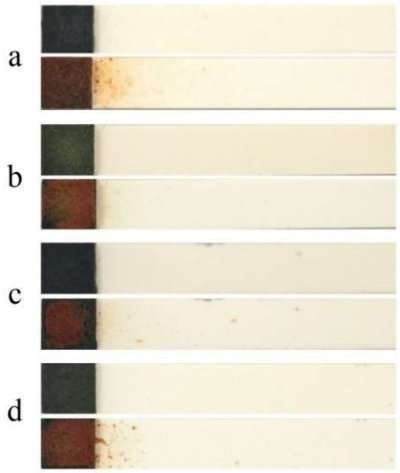

Figure 7- 14. Strips with aluminum-(a), lanthanum (b), from using bulk yttrium oxide for the yttrium- (c), and from using nano-yttrium oxide for the yttrium-(d) vanadyl nanoparticulates, for each as manufactured (top); after the exposure to 20 µl of 35% hydrogen peroxide (bottom)

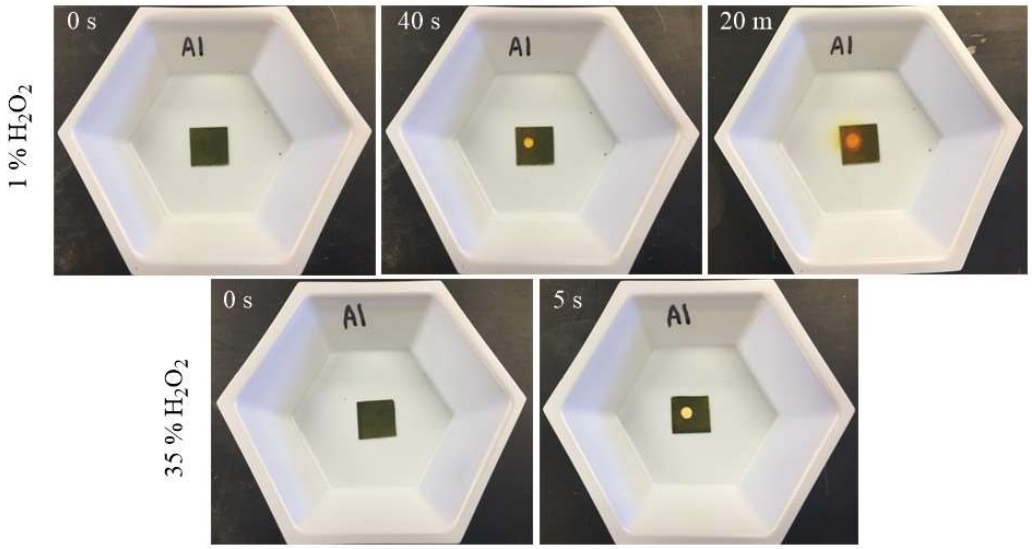

Figure 7- 15.Changing color during sensing of 1 % and 35% H_2O_2 solution as a function of time using a TLC aluminum oxide sheet deposited with aluminum vanadyl particulate solution

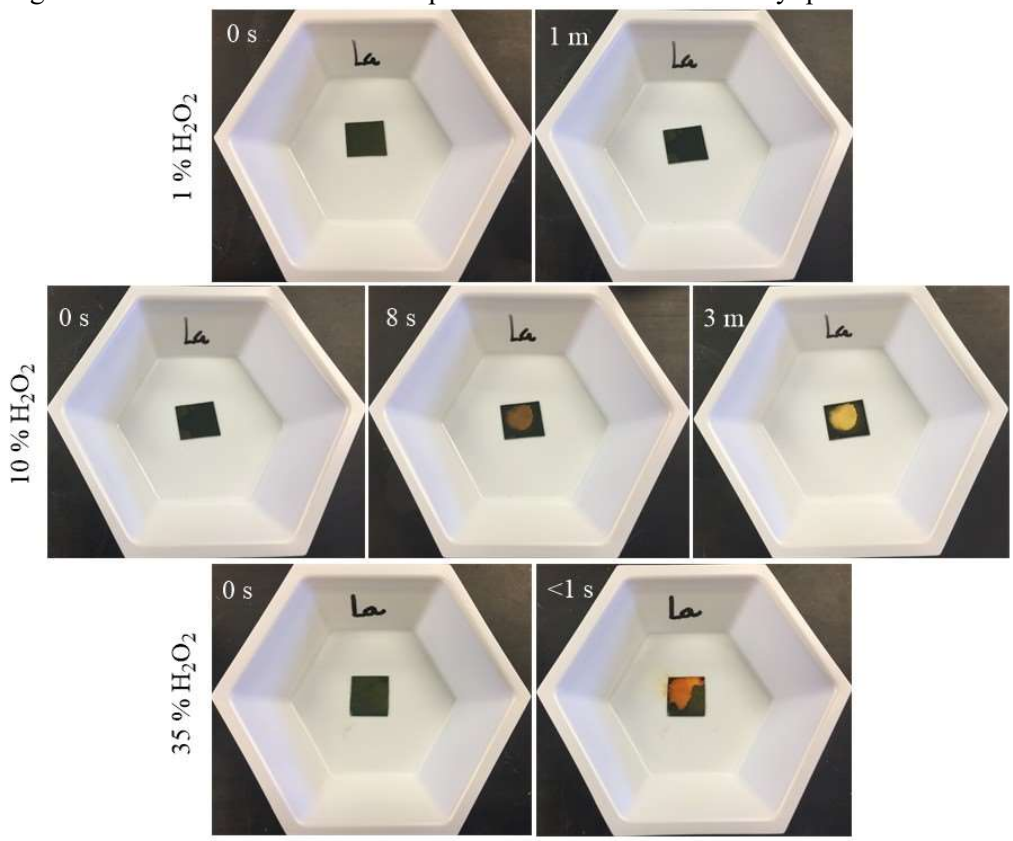

Figure 7- 16. Changing color during sensing of 1 %, 10 %, and 35% H_2O_2 solution as a function of time using a TLC aluminum oxide sheet deposited with lanthanum vanadyl particulate solution

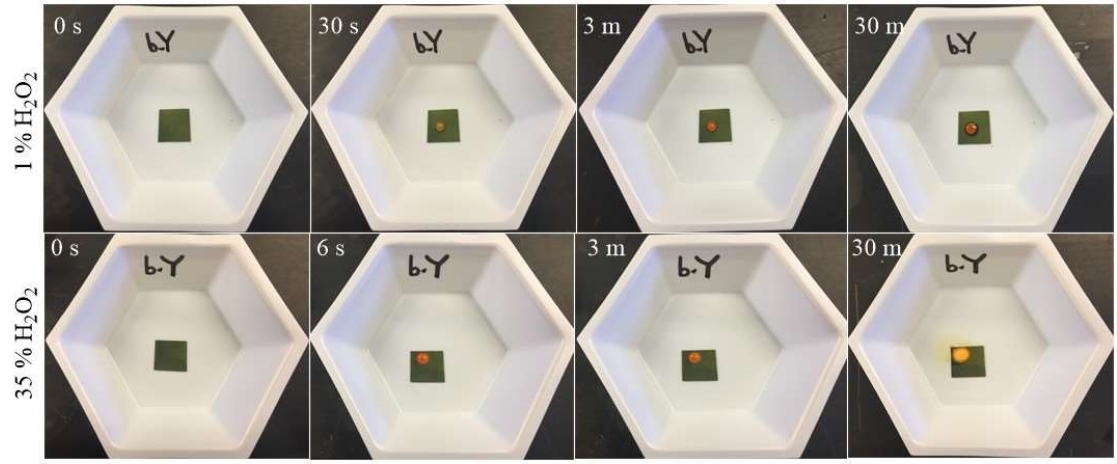

Figure 7- 17. Changing color during sensing of 1 % and 35% H_2O_2 solution as a function of time using a TLC aluminum oxide sheet deposited with yttrium vanadyl particulate solution (synthesized from bulk-yttrium oxide)

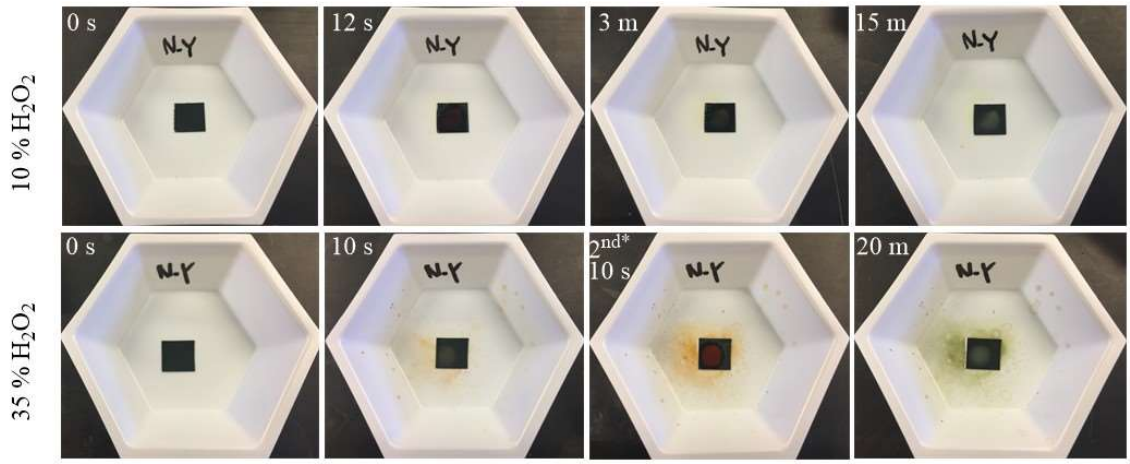

Figure 7- 18. Changing color during sensing 20 µl of 10 % and 35% H_2O_2 solution as a function of time using a TLC aluminum oxide sheet deposited with yttrium vanadyl particulate solution (synthesized from nano-yttrium oxide), * another 20 µl was added to the same slide

Vanadyl pyruvate was also supported onto aluminum oxide TLC slide forming a dark green- blush color and then tested for hydrogen peroxide detection. The color change with a second after the exposure and the orange-reddish color intensity become more intense with time associated with gaseous release (Figure 19). This suggest that the hydrogen peroxide oxidize and assist in decomposition of vanadyl pyruvate as illustrated:

$$VO(pyuravte)_2 + H_2O_2 \longrightarrow V_2O_5 + \text{volatile small molecules}$$

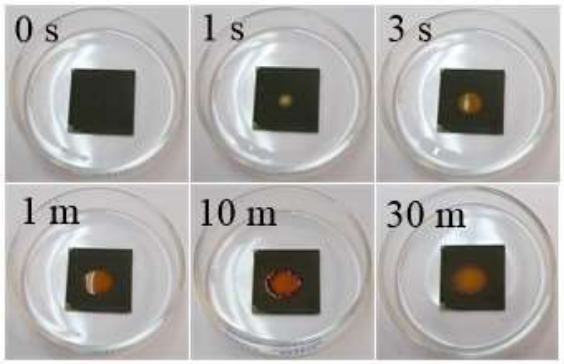

Figure 7- 19. Changing color during sensing of 35% H_2O_2 solution as a function of time using a TLC aluminum oxide sheet deposited with vanadyl pyruvate solution

3.2.Sensors based thin film

UV/VIS spectrum for colloidal solution (Figure 20) shows three bands for vanadyl ion, with d^1 electron configuration corresponding to transition from $^2T_2$ ground state to ^2E excited state. Dynamic light scattering (DLS) analysis for the solutions of colloidal particles distributed around 220 nm as shown in Figure 21.

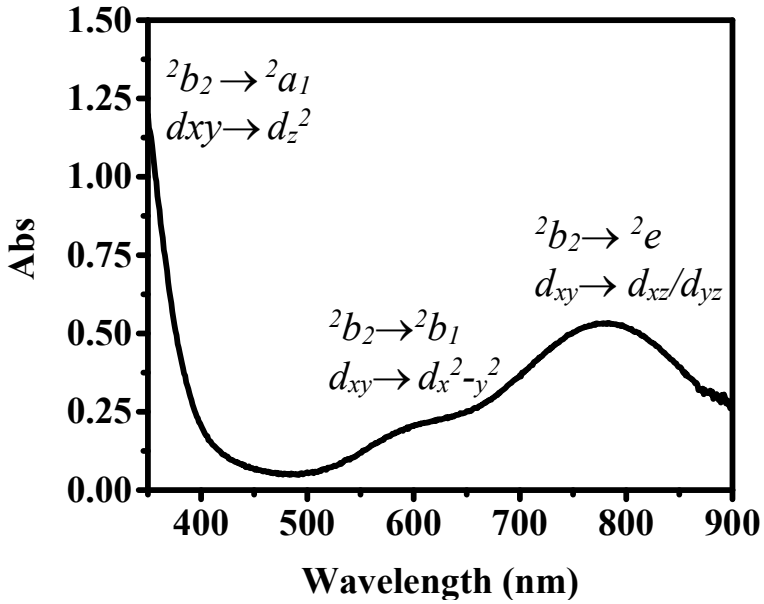

Figure 7- 20. UV/VIS spectrum for nanoparticulate VO_2 solution

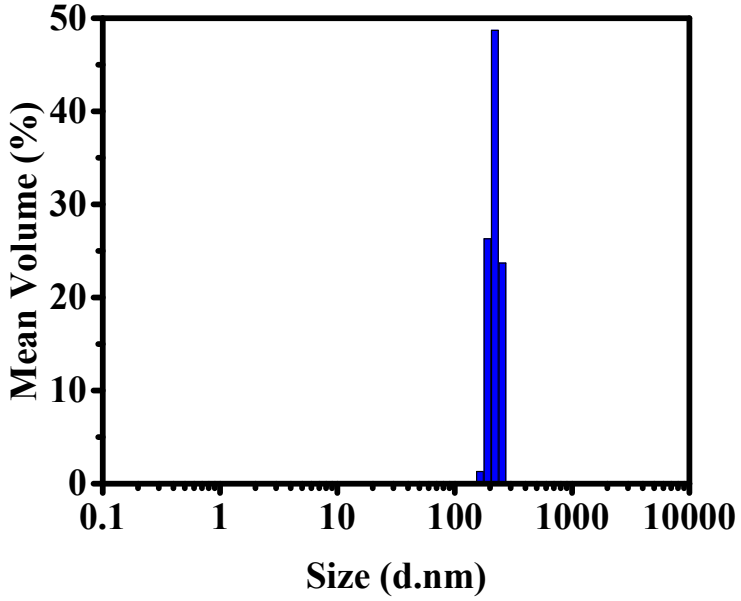

Figure 7- 21. DLS analysis for nanoparticulate VO_2 solution

The FTIR spectrum for the resulting thin film (Figure 22) shows vibrational frequency bands at the 978 sharp and strong and the 921 weak which are characteristic for vanadyl (V=O) starching vibration in mixed valence vanadium (IV,V) compounds. [255] The weak broad diffraction peaks of the resulting products (Figure 23) can be indexed to monoclinic $V_{10}O_{24}\cdot 12H_2O$. [46, 255] The

water content results in the large d_{004} spacing of 9.61 Å and overall peaks broadened are due to nanocrystallinity since the average crystallites size determined using Scherrer equation was 5.89 ± 0.11. TGA analysis for the dried vanadyl thin film showed that the thermal decomposition of the product occurred in two steps attributed to decomposition of water content (Figure 24). The slight weight gain at higher temperature is due to oxidation of V^{4+} to V^{5+}. The conductivity measurements through electrochemical impedance spectroscopy show that the obtained film is electrically conductive through two mechanisms that represented as semi-circles as Nyquist plot represent (Figure 25). These two semi-circles are not fully resolved as Figure 26 shows. The un resolved process at higher frequency according to Bode plot (Figure 27) was attributed to electron conduction with estimated resistance found to be 425 Ω, while at lower frequency the conduction related to ionic mobility with measured resistance of 10.7 kiloΩ. Similar to the higher resistance process seen by Impedance spectroscopy the resistance of the film found to be 19 kiloΩ based on four point probe measurements. The film was tested for sensing hydrogen peroxide. Same responses were observed at different concentrations of peroxide by a rapid change in colors. It was hard to capture the color change by camera because the rapid self- color regeneration. Furthermore, the used film change its texture after multiple exposures. Moreover, since long stability (one year) of this film along to the color regeneration involve oxidation of V(4+) in the resting state to V(5+) in the sensing state and vice versa, this film have the potential to be use in the development of electronic device for monitoring and detection of hydrogen peroxide.

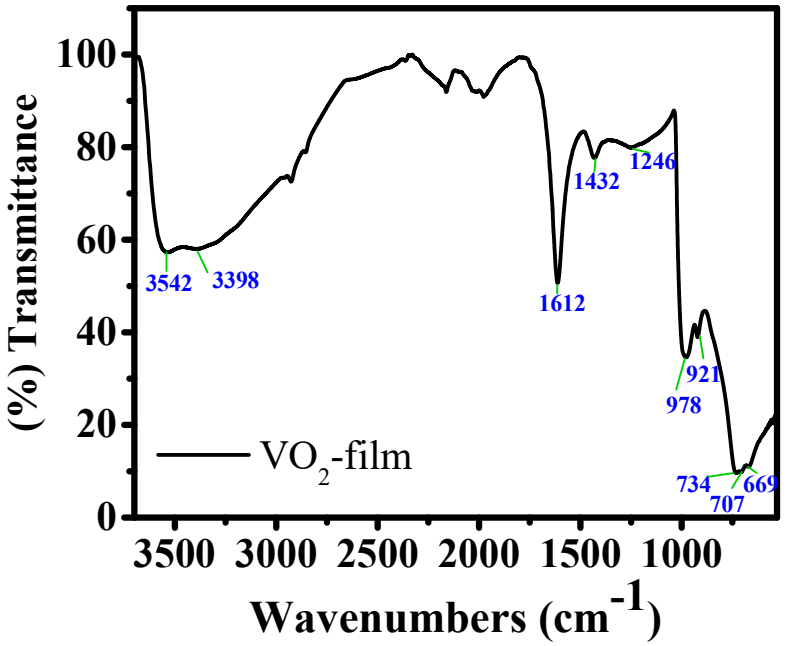

Figure 7- 22. The FTIR spectrum for thin film

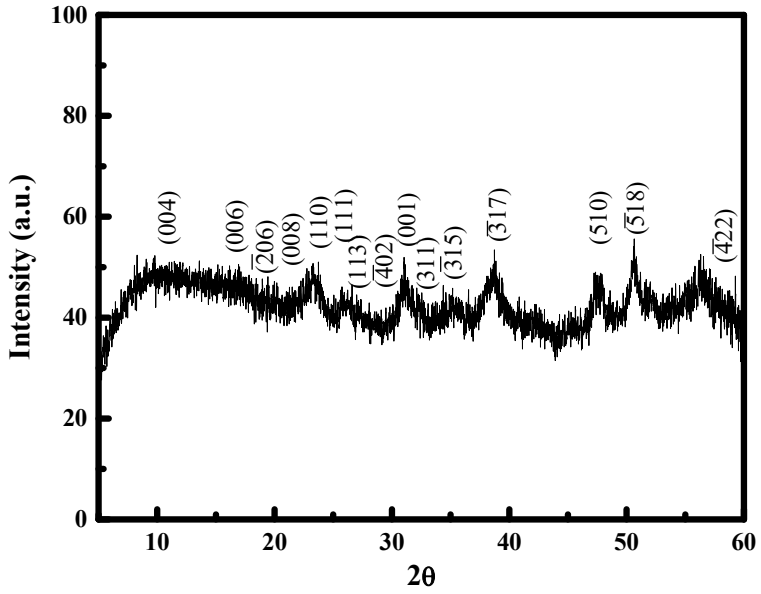

Figure 7- 23. The XRD pattern for thin film

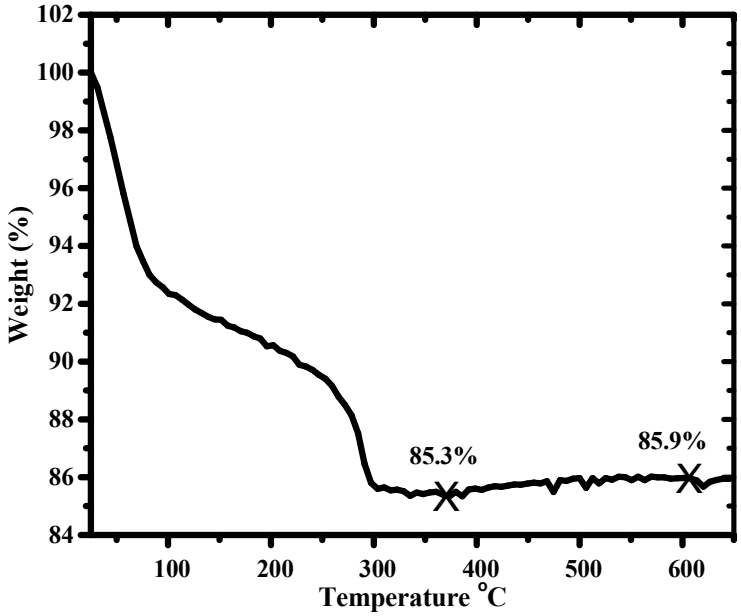

Figure 7- 24. TGA curve for thin film

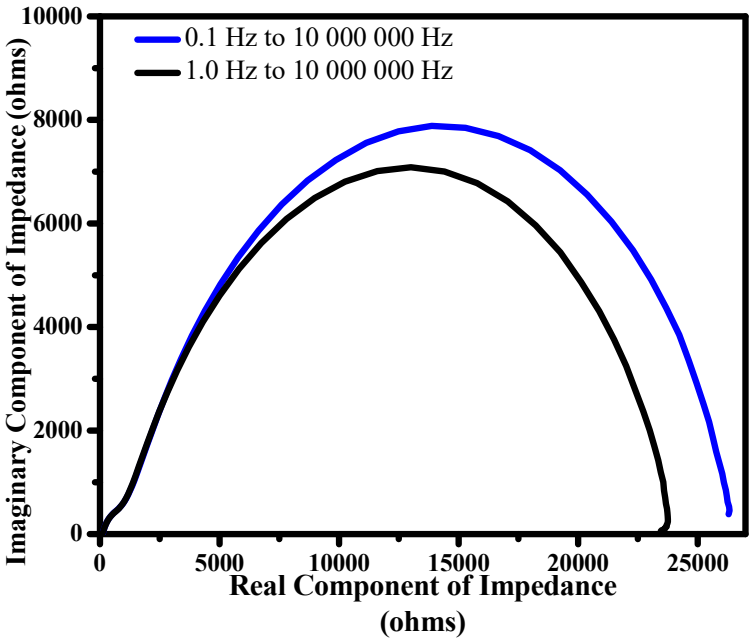

Figure 7- 25. Nyquist plot for vanadium oxide film

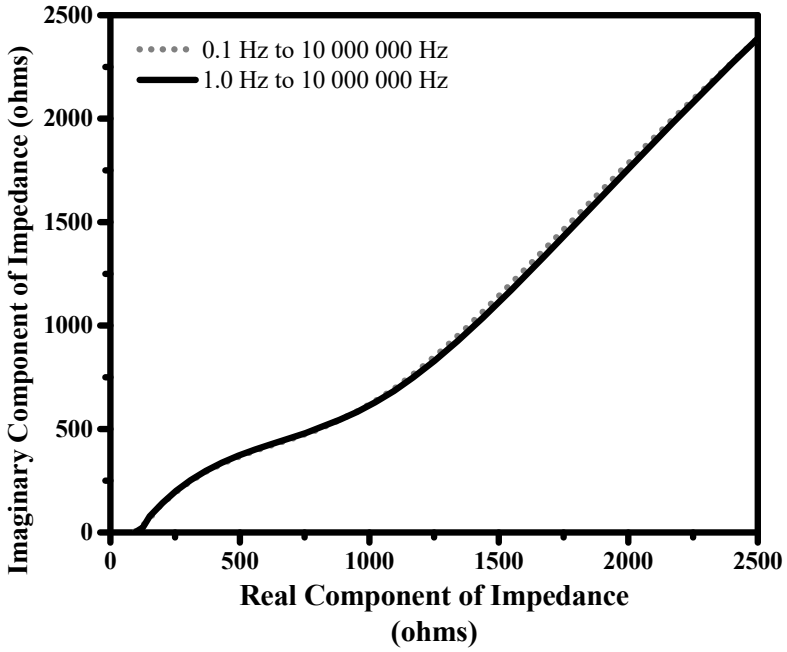

Figure 7- 26. Expanded Nyquist plot for vanadium oxide film

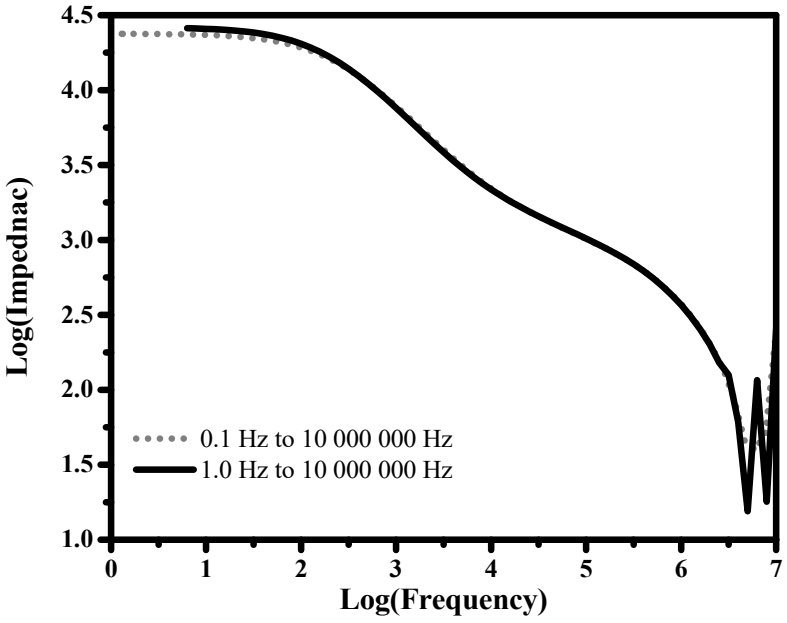

Figure 7- 27. Bode plot for vanadium oxide film

4. Conclusion:

Colorimetric reagents have been successfully developed and tested for sensing hydrogen peroxide. The developed reagents showed the ability to response rabidly for hydrogen peroxide. Their reposes were obviously observed through dramatic color change. Vanadium bronzes based colorimetric reagent was first investigated, they were made through reduction of colloidal vanadium pentoxide with different amount of sodium dithionite. The problem with them is the lacking of stabilities where the nanometric particles precipitate with time. Therefore, the materials were placed on to TLC aluminum oxide slides. The responses of the slides to hydrogen peroxide was rapid and gave a distinct color change from green to yellow. Unfortunately, these slides were sensitive to air as well.

The second reagent based colorimetric reagent was developed using a vanadyl oxalate solution synthesis through reduction of vanadium pentoxide with oxalic acid. This solution was used as-prepared and submerged onto strip and they responded rapidly to hydrogen peroxide solution resulting in a distinct color change from blue to reddish orange. Through the investigation it was notice that the blue color of vanadyl solution regenerate itself after the exposure. The color regeneration during the exposure was kinetically measured with a UV-visible spectrometer. Observation of this phenomena show potential sensing application through utilizing of the developed materials in electrochromic devices for monitoring and detecting hydrogen peroxide, several organic peroxides, and to oxidizers in general. TLC Aluminum oxide slides impregnated with vanadyl solutions were made and found to be useful to detect hydrogen peroxide as well. Supporting these reagents onto aluminum oxide surface significantly enhance the sensing sensitivity toward the peroxide offering the ability to manufacture a system that has the ability to display dramatic color changes when exposed to hydrogen peroxide vapors or other oxidizers.

Thin film of vanadyl oxide made successfully from colloidal suspension of vanadium material through reduction of peroxovanadic acid by oxalic acid. The conductivity measurements

show that this film is conductive and can be used as a peroxide sensor. The color of this films regenerate rapidly which make it hard to photo capture its respond to hydrogen peroxide. In addition, the film change texture after several exposures. This film was stable for long period showing potential for use as electronic sensing devise demand further investigation to enhance it durability and performance.

REFERENCES

1. Dickens, P.G. and M.S. Whittingham, *Tungsten bronzes and related compounds.* Quart. Rev. (London), 1968. **22**(1): p. 30-44.
2. Seabold, J.A. and K.-S. Choi, *Efficient and Stable Photo-Oxidation of Water by a Bismuth Vanadate Photoanode Coupled with an Iron Oxyhydroxide Oxygen Evolution Catalyst.* Journal of the American Chemical Society, 2012. **134**(4): p. 2186-2192.
3. Saegebarth, K.A., *Mechanism of the Tungstic Acid Catalyzed Hydroxylation of Olefins.* The Journal of Organic Chemistry, 1959. **24**(9): p. 1212-1214.
4. Wasmi, B.A., A.A. Al-Amiery, A.A.H. Kadhum, and A.B. Mohamad, *Novel Approach: Tungsten Oxide Nanoparticle as a Catalyst for Malonic Acid Ester Synthesis via Ozonolysis.* Journal of Nanomaterials, 2014. **2014**: p. 7.
5. Tanaka, T., S. Takenaka, T. Funabiki, and S. Yoshida, *Selective Photooxidation of Propane to Propanone over Alkali-ion-modified Silica-supported Vanadium Oxides.* Chemistry Letters, 1994. **23**(9): p. 1585-1588.
6. Tanaka, T., T. Ito, S. Takenaka, T. Funabiki, and S. Yoshida, *Photocatalytic oxidation of alkane at a steady rate over alkali-ion-modified vanadium oxide supported on silica.* Catalysis Today, 2000. **61**(1–4): p. 109-115.
7. Mugdan, M. and D.P. Young, *Catalytic hydroxylation of unsaturated compounds.* J. Chem. Soc., 1949: p. 2988-3000.
8. Li, B., Y. Xu, G. Rong, M. Jing, and Y. Xie, *Vanadium pentoxide nanobelts and nanorolls: from controllable synthesis to investigation of their electrochemical properties and photocatalytic activities.* Nanotechnology, 2006. **17**(10): p. 2560-6.
9. Jalan, V.M., *Method for making a supported vanadium oxide catalyst*. 1982, Google Patents.
10. Farzaneh, F., E. Zamanifar, and C.D. Williams, *V-MCM-41 as selective catalyst for epoxidation of olefins and trans-2-hexene-1-ol.* Journal of Molecular Catalysis A: Chemical, 2004. **218**(2): p. 203-209.
11. Bond, G.C. and S.F. Tahir, *Vanadium oxide monolayer catalysts Preparation, characterization and catalytic activity.* Applied Catalysis, 1991. **71**(1): p. 1-31.
12. Bergsteinsson, I., *Catalytic hydroxylation of olefinic double bonds*. 1945, Shell Development Co. .
13. Asmamaw, T., *Cyclotrimerization of nitriles with alpha-heteroatoms catalyzed by using tungsten and molybdenum bronzes*. 2011, Oklahoma State University: Ann Arbor. p. 56.
14. Bakhteeva, Y.A., N.V. Podval'naya, and V.L. Volkov, *Gas-sensing properties of nanostructured M x V2O5 (M = Na, K, Rb, Cs) oxides.* Inorganic Materials, 2010. **46**(10): p. 1112-1114.

15. Braman, R.S., T.J. Shelley, and W.A. McClenny, *Tungstic acid for preconcentration and determination of gaseous and particulate ammonia and nitric acid in ambient air.* Analytical Chemistry, 1982. **54**(3): p. 358-364.
16. Nagata, S., A. Inouye, S. Yamamoto, B. Tsuchiya, K. Takano, K. Toh, and T. Shikama, *Hydrogen incorporation and gasochromic coloration of tungsten oxide films.* Journal of Alloys and Compounds, 2007. **446–447**(0): p. 558-561.
17. Sigsworth, S.W. and A.W. Castleman, *Reaction of Group V and VI transition metal oxide and oxyhydroxide anions with oxygen, water, and hydrogen chloride.* Journal of the American Chemical Society, 1992. **114**(26): p. 10471-10477.
18. Privman, M. and T. Hepel, *Electrochemistry of vanadium electrodes Part 1. Cyclic voltammetry in aqueous solutions.* Journal of Electroanalytical Chemistry, 1995. **382**(1–2): p. 137-144.
19. Privman, M. and T. Hepel, *Electrochemistry of vanadium electrodes Part 2. Anodic and cathodic polarization over a wide range of pH and temperature.* Journal of Electroanalytical Chemistry, 1995. **382**(1–2): p. 145-152.
20. Ban, C., *Synthesis and characterization of nano-scale vanadium oxides, vanadium phosphates as cathodes for lithium batteries*. 2008, State University of New York at Binghamton: Ann Arbor. p. 194.
21. Chernova, N.A., M. Roppolo, A.C. Dillon, and M.S. Whittingham, *Layered vanadium and molybdenum oxides: batteries and electrochromics.* Journal of Materials Chemistry, 2009. **19**(17): p. 2526-2552.
22. Gao, S., Z. Chen, M. Wei, K. Wei, and H. Zhou, *Single crystal nanobelts of V3O7·H2O: A lithium intercalation host with a large capacity.* Electrochimica Acta, 2009. **54**(3): p. 1115-1118.
23. Legagneur, V., A. Le Gal La Salle, A. Verbaere, Y. Piffard, and D. Guyomard, *Lithium insertion/deinsertion properties of new layered vanadium oxides obtained by oxidation of the precursor H2V3O8.* Electrochimica Acta, 2002. **47**(7): p. 1153-1161.
24. Mho, S.-I., C.V.S. Reddy, Y. Kim, I.-H. Yeo, and S.-M. Park, *Hydrothermal synthesis of H2V3O8 nanobelts from V2O5 xerogels for lithium battery applications.* J. Korean Phys. Soc., 2009. **54**(6): p. 2420-2424.
25. Millet, M., J. Farcy, J.P. Pereira-Ramos, E.M. Sabbar, M.E. De Roy, and J.P. Besse, *A new hydrated sodium vanadium bronze as Li insertion compound.* Solid State Ionics, 1998. **112**(3–4): p. 319-327.
26. Pan, A., H.B. Wu, L. Yu, and X.W. Lou, *Template-Free Synthesis of VO2 Hollow Microspheres with Various Interiors and Their Conversion into V2O5 for Lithium-Ion Batteries.* Angewandte Chemie International Edition, 2013. **52**(8): p. 2226-2230.
27. Xu, Y., L. Zheng, and Y. Xie, *From synthetic montroseite VOOH to topochemical paramontroseite VO2 and their applications in aqueous lithium ion batteries.* Dalton Transactions, 2010. **39**(44): p. 10729-10738.
28. Bechinger, C., S. Ferrere, A. Zaban, J. Sprague, and B.A. Gregg, *Photoelectrochromic windows and displays.* Nature, 1996. **383**(6601): p. 608-610.
29. Granqvist, C.G., *Electrochromic tungsten oxide films: Review of progress 1993–1998.* Solar Energy Materials and Solar Cells, 2000. **60**(3): p. 201-262.

30. He, T. and J. Yao, *Photochromic materials based on tungsten oxide.* Journal of Materials Chemistry, 2007. **17**(43): p. 4547-4557.
31. He, Z., Q. Liu, H. Hou, F. Gao, B. Tang, and W. Yang, *Tailored Electrospinning of WO3 Nanobelts as Efficient Ultraviolet Photodetectors with Photo-Dark Current Ratios up to 1000.* ACS Applied Materials & Interfaces, 2015. **7**(20): p. 10878-10885.
32. Sanchez, C., F. Babonneau, R. Morineau, J. Livage, and J. Bullot, *Semiconducting properties of V2O5 gels.* Philosophical Magazine Part B, 1983. **47**(3): p. 279-290.
33. Xue, Y., X. Zhang, J. Zhang, J. Wu, Y. Sun, Y. Tian, and Y. Xie, *Sodium vanadium oxide Na2V6O16[middle dot]3H2O nanobelts and nanorings: A new room-temperature ferromagnetic semiconductor.* Journal of Materials Chemistry, 2012. **22**(6): p. 2560-2565.
34. Popuri, S.R., M. Miclau, A. Artemenko, C. Labrugere, A. Villesuzanne, and M. Pollet, *Rapid Hydrothermal Synthesis of VO2 (B) and Its Conversion to Thermochromic VO2 (M1).* Inorganic Chemistry, 2013. **52**(9): p. 4780-4785.
35. Wu, C., J. Dai, X. Zhang, J. Yang, and Y. Xie, *Synthetic Haggite V4O6(OH)4 Nanobelts: Oxyhydroxide as a New Catalog of Smart Electrical Switch Materials.* Journal of the American Chemical Society, 2009. **131**(21): p. 7218-7219.
36. Zavalij, P.Y. and M.S. Whittingham, *Structural chemistry of vanadium oxides with open frameworks.* Acta Crystallogr B, 1999. **55**(Pt 5): p. 627-663.
37. Kharisov, B.I., O.V. Kharissova, and M. Jose-Yacaman, *Nanostructures with Animal-like Shapes.* Industrial & Engineering Chemistry Research, 2010. **49**(18): p. 8289-8309.
38. Livage, J., *Hydrothermal Synthesis of Nanostructured Vanadium Oxides.* Materials, 2010. **3**(8): p. 4175-4195.
39. Khairy, M., D. Tinet, and H. van Damme, *The synthesis of pillared vanadium oxide.* Journal of the Chemical Society, Chemical Communications, 1990(12): p. 856-857.
40. Oka, Y., T. Yao, and N. Yamamoto, *Structure determination of H2V3O8 by powder X-ray diffraction.* Journal of Solid State Chemistry, 1990. **89**(2): p. 372-377.
41. Chang, K.-H. and C.-C. Hu, *H2V3O8 single-crystal nanobelts: Hydrothermal preparation and formation mechanism.* Acta Materialia, 2007. **55**(18): p. 6192-6197.
42. Nakayama, M., H. Komatsu, S. Ozuka, and K. Ogura, *Cathodic deposition of molybdenum and vanadium mixed oxyhydroxide films from V-substituted polymolybdophosphate.* Electrochimica Acta, 2005. **51**(2): p. 274-280.
43. Prado-Gonjal, J., B. Molero-Sánchez, D. Ávila-Brande, E. Morán, J.C. Pérez-Flores, A. Kuhn, and F. García-Alvarado, *The intercalation chemistry of H2V3O8 nanobelts synthesised by a green, fast and cost-effective procedure.* Journal of Power Sources, 2013. **232**(0): p. 173-180.
44. Muller, J. and J.C. Joubert, *Synthese en milieu hydrothermal et caractérisation de l'oxyhydroxyde de vanadium V3+OOH et d'une nouvelle variété allotropique du dioxyde VO2.* Journal of Solid State Chemistry, 1974. **11**(2): p. 79-87.
45. Djerdj, I., D. Sheptyakov, F. Gozzo, D. Arčon, R. Nesper, and M. Niederberger, *Oxygen Self-Doping in Hollandite-Type Vanadium Oxyhydroxide Nanorods.* Journal of the American Chemical Society, 2008. **130**(34): p. 11364-11375.

46. Li, G., K. Chao, C. Zhang, Q. Zhang, H. Peng, and K. Chen, *Synthesis of Urchin-like VO2 Nanostructures Composed of Radially Aligned Nanobelts and Their Disassembly.* Inorganic Chemistry, 2009. **48**(3): p. 1168-1172.
47. Sun, X., J. Wang, Y. Xing, Y. Zhao, X. Liu, B. Liu, and S. Hou, *Surfactant-assisted hydrothermal synthesis and electrochemical properties of nanoplate-assembled 3D flower-like Cu3V2O7(OH)2[middle dot]2H2O microstructures.* CrystEngComm, 2011. **13**(1): p. 367-370.
48. Zavalij, P.Y. and M.S. Whittingham, *Structural chemistry of vanadium oxides with open frameworks.* Acta Crystallographica Section B, 1999. **55**(5): p. 627-663.
49. Erik Lassner, W.-D.S., *Properties, Chemistry, Technology of the Element, Alloys, and Chemical Compounds*. 1999, New York: Springer Science & Business Media.
50. van der Vlies, A.J., G. Kishan, J.W. Niemantsverdriet, R. Prins, and T. Weber, *Basic Reaction Steps in the Sulfidation of Crystalline Tungsten Oxides.* The Journal of Physical Chemistry B, 2002. **106**(13): p. 3449-3457.
51. Bai, P., W. Xing, and Z. Yan, *Synthesis and characterization of mesostructured tungsten nitride by using tungstic acid as the precursor.* Journal of Porous Materials, 2006. **13**(2): p. 173-180.
52. Ravindra, C.L.a.N.M., *Vanadium Oxides for Energy and Security Applications*. Spectroscopic Techniques for Security, Forensic and Environmental Applications ed. S.B.R.J.P.S. Y. Dwivedi. 2014, Hauppauge, New York: Nova Science Publishers.
53. Wachs, I.E., *Catalysis science of supported vanadium oxide catalysts.* Dalton Transactions, 2013. **42**(33): p. 11762-11769.
54. Jackson, S.D. and J.S.J. Hargreaves, *Metal Oxide Catalysis*. 2008: Wiley.
55. Haber, J., M. Witko, and R. Tokarz, *Vanadium pentoxide I. Structures and properties.* Applied Catalysis A: General, 1997. **157**(1–2): p. 3-22.
56. Surnev, S., M.G. Ramsey, and F.P. Netzer, *Vanadium oxide surface studies.* Progress in Surface Science, 2003. **73**(4–8): p. 117-165.
57. Magee, J. and E. Richardson, *Some studies on vanadic acid.* Journal of Inorganic and Nuclear Chemistry, 1960. **15**(3–4): p. 272-278.
58. Gharbi, N., C. Sanchez, J. Livage, J. Lemerle, L. Nejem, and J. Lefebvre, *Mixed-valence poly(vanadic acid) gels.* Inorganic Chemistry, 1982. **21**(7): p. 2758-2765.
59. Uchida, N. and S. Kittaka, *Interlayer Water Molecules in Vanadium Pentoxide Hydrate, V2O5.cntdot.nH2O. 5. Dynamic Motion Analyzed by Impedance Measurements.* The Journal of Physical Chemistry, 1994. **98**(8): p. 2129-2133.
60. Wang, Y. and G. Cao, *Synthesis and Enhanced Intercalation Properties of Nanostructured Vanadium Oxides.* Chemistry of Materials, 2006. **18**(12): p. 2787-2804.
61. Konnert, J.A. and H.T. Evans Jr, *Crystal structure and crystal chemistry of melanovanadite, a natural vanadium bronze.* American Mineralogist, 1987. **72**(5-6): p. 637-644.
62. Cesbron, F. and H. Vachey, *Bariandite, a new vanadium (IV) and (V) oxide.* Bull. Soc. Fr. Mineral. Cristallogr., 1971. **94**(1): p. 49-54.

63. Sun, J.-P., G.-M. Wu, M.-X. Zhang, C.-J. Cui, H.-Y. Yang, Z.-H. Zhang, B. Zhou, and J. Shen, *Preparation and characterization of novel nanometer materials V10O24·12H2O.* Gaodeng Xuexiao Huaxue Xuebao, 2009. **30**(11): p. 2107-2111.
64. Wu, G., J. Sun, M. Zhang, J. Shen, B. Zhou, X. Ni, and Z. Zhang, *Preparation of V10O24·12H2O nanomaterial by sol-gel process*. 2009, Tongji University, Peop. Rep. China . p. 9pp.
65. Sun, H. and S. Shi, *Method for hydrothermal synthesis of V1O24·12H2O*. 2013, GCL Power New Material Yancheng Co., Ltd., Peop. Rep. China . p. 6pp.
66. Diederich, F.S., P. J.; Tykwinski, R. R., *Acetylene Chemistry*. 2005, Weinheim: Wiley-VCH.
67. Zhu, F., J. Zhou, H. Zhu, and H. Li, *Periodic mesoporous organogold(I)silica catalysts for hydration of alkyne to methyl ketone in water medium.* Cuihua Xuebao, 2012. **33**(6): p. 1061-1066.
68. Trentin, F., A.M. Chapman, A. Scarso, P. Sgarbossa, R.A. Michelin, G. Strukul, and D.F. Wass, *Platinum(II) Diphosphinamine Complexes for the Efficient Hydration of Alkynes in Micellar Media.* Adv. Synth. Catal., 2012. **354**(6): p. 1095-1104.
69. Rasolofonjatovo, E., B. Treguier, O. Provot, A. Hamze, E. Morvan, J.-D. Brion, and M. Alami, *Palladium-catalyzed coupling of N-tosylhydrazones with ortho substituted aryl halides: synthesis of 4-arylchromenes and related heterocycles.* Tetrahedron Lett., 2011. **52**(9): p. 1036-1040.
70. Pourzal, A.A. and P.H. Bonnet, *Boron trifluoride catalyzed, heavy metal-free hydration of alkynes.* Monatsh. Chem., 1983. **114**(6-7): p. 809-11.
71. Nishizawa, M., M. Skwarczynski, H. Imagawa, and T. Sugihara, *Mercuric triflate-tetramethylurea catalyzed hydration of terminal alkynes to give methyl ketones under mild conditions.* Chem. Lett., 2002(1): p. 12-13.
72. Nishizawa, M., H. Imagawa, and H. Yamamoto, *A new catalyst for organic synthesis: mercuric triflate.* Org. Biomol. Chem., 2010. **8**(3): p. 511-521.
73. Nishizawa, M. and H. Imagawa, *Mercuric triflate revisited: development of catalytic reactions.* Yuki Gosei Kagaku Kyokaishi, 2006. **64**(7): p. 744-751.
74. Mello, R., A. Alcalde-Aragones, and M.E. Gonzalez-Nunez, *Silica-supported HgSO4/H2SO4: a convenient reagent for the hydration of alkynes under mild conditions.* Tetrahedron Lett., 2010. **51**(32): p. 4281-4283.
75. Mazzone, G., N. Russo, and E. Sicilia, *Homogeneous gold catalysis: hydration of 1,2-diphenylacetylene with methanol in aqueous media. A theoretical viewpoint.* Organometallics, 2012. **31**(8): p. 3074-3080.
76. Lucey, D.W. and J.D. Atwood, *Insight into the Selective Room-Temperature Platinum(II) Catalytic Hydration of Alkynes in Water.* Organometallics, 2002. **21**(12): p. 2481-2490.
77. Leyva, A. and A. Corma, *Isolable Gold(I) Complexes Having One Low-Coordinating Ligand as Catalysts for the Selective Hydration of Substituted Alkynes at Room Temperature without Acidic Promoters.* J. Org. Chem., 2009. **74**(5): p. 2067-2074.

78. Kore, R., T.J.D. Kumar, and R. Srivastava, *Hydration of alkynes using Broensted acidic ionic liquids in the absence of nobel metal catalyst/H2SO4.* J. Mol. Catal. A: Chem., 2012. **360**: p. 61-70.
79. Jeong, J., D. Ray, and C.H. Oh, *Cationic gold-catalyzed regioselective hydration of 1-arylalkynes through carbonyl group participation.* Synlett, 2012. **23**(6): p. 897-902.
80. Jennings, P.W., J.W. Hartman, and W.C. Hiscox, *Alkyne hydration using Pt(II) catalysts.* Inorg. Chim. Acta, 1994. **222**(1-2): p. 317-22.
81. Janout, V. and S.L. Regen, *Phenylmercuric hydroxide. A highly selective reagent for the hydration of nonconjugated terminal alkynes.* J. Org. Chem., 1982. **47**(17): p. 3331-3.
82. Israelsohn, O., K.P.C. Vollhardt, and J. Blum, *Further studies on hydration of alkynes by the PtCl4-CO catalyst.* J. Mol. Catal. A: Chem., 2002. **184**(1-2): p. 1-10.
83. Hiscox, W.C., *Mechanisms of platinum(II) and palladium(II) catalyzed organic transformations: hydration of alkynes and the Cope rearrangement*. 1993. p. 283 pp.
84. Hashmi, A.S.K., T. Hengst, C. Lothschuetz, and F. Rominger, *New and Easily Accessible Nitrogen Acyclic Gold(I) Carbenes: Structure and Application in the Gold-Catalyzed Phenol Synthesis as well as the Hydration of Alkynes.* Adv. Synth. Catal., 2010. **352**(8): p. 1315-1337.
85. Czegeni, C.E., G. Papp, A. Katho, and F. Joo, *Water-soluble gold(I)-NHC complexes of sulfonated IMes and SIMes and their catalytic activity in hydration of alkynes.* J. Mol. Catal. A: Chem., 2011. **340**(1-2): p. 1-8.
86. Corominas, A. and A.M. Montana, *Methodological optimization of catalytic hydration of alkynes with mercury(II) p-toluenesulfonamidate under neutral conditions.* Curr. Catal., 2013. **2**(1): p. 35-47.
87. Hartman, J.W., W.C. Hiscox, and P.W. Jennings, *Catalytic hydration of alkynes with platinum(II) complexes.* J. Org. Chem., 1993. **58**(26): p. 7613-14.
88. Chevallier, F. and B. Breit, *Self-assembled bidentate ligands for Ru-catalyzed anti-Markovnikov hydration of terminal alkynes.* Angew. Chem., Int. Ed., 2006. **45**(10): p. 1599-1602.
89. Blum, J., H. Huminer, and H. Alper, *Alkyne hydration promoted by rhodium(III) chloride and quaternary ammonium salts.* J. Mol. Catal., 1992. **75**(2): p. 153-60.
90. Alvarez, P., M. Bassetti, J. Gimeno, and G. Mancini, *Hydration of terminal alkynes to aldehydes in aqueous micellar solutions by ruthenium(II) catalysis; first anti-Markovnikov addition of water to propargylic alcohols.* Tetrahedron Lett., 2001. **42**(48): p. 8467-8470.
91. Baidossi, W., M. Lahav, and J. Blum, *Hydration of Alkynes by a PtCl4-CO Catalyst.* J. Org. Chem., 1997. **62**(3): p. 669-672.
92. Ranu, B.C., A. Sarkar, M. Saha, and R. Chakraborty, *Silica gel supported zinc borohydride. A novel reagent for hydration of unactivated alkenes and alkynes.* Tetrahedron, 1994. **50**(22): p. 6579-84.
93. Suzuki, T., M. Tokunaga, and Y. Wakatsuki, *Ruthenium complex-catalyzed anti-Markovnikov hydration of terminal alkynes.* Org. Lett., 2001. **3**(5): p. 735-737.

94. Tokunaga, M., T. Suzuki, N. Koga, T. Fukushima, A. Horiuchi, and Y. Wakatsuki, *Ruthenium-Catalyzed Hydration of 1-Alkynes to Give Aldehydes: Insight into anti-Markovnikov Regiochemistry.* J. Am. Chem. Soc., 2001. **123**(48): p. 11917-11924.
95. Kribber, T.C., *Ruthenium-catalyzed hydration of terminal alkynes and their use in synthetic strategies*. 2009. p. No pp.
96. Gao, Q., S. Li, Y. Pan, Y. Xu, and H. Wang, *The indium-catalysed hydration of alkynes using substoichiometric amounts of PTSA as additive.* Tetrahedron, 2013. **69**(19): p. 3775-3781.
97. Campelo, J.M., R. Chakraborty, and J.M. Marinas, *AlPO4 supported zinc borohydride as a novel reagent for the hydration of aromatic alkenes and alkynes.* Synth. Commun., 1996. **26**(9): p. 1639-50.
98. Boeck, F., T. Kribber, L. Xiao, and L. Hintermann, *Mixed Phosphane η5-CpRuCl(PR3)2 Complexes as Ambifunctional Catalysts for Anti-Markovnikov Hydration of Terminal Alkynes.* J. Am. Chem. Soc., 2011. **133**(21): p. 8138-8141.
99. Finiels, A., P. Geneste, F. Marichez, and P. Moreau, *Hydration reaction of alkynes catalyzed by zeolites.* Catal. Lett., 1989. **2**(3): p. 181-4.
100. Finiels, A., P. Geneste, M. Lasperas, F. Marichez, and P. Moreau, *Triple bond hydration using zeolites as catalysts.* Stud. Surf. Sci. Catal., 1991. **59**(Heterog. Catal. Fine Chem. 2): p. 565-71.
101. Meier, I.K. and J.A. Marsella, *Hydration of acetylenic compounds without using mercury.* J. Mol. Catal., 1993. **78**(1): p. 31-42.
102. Wu, X.-F., D. Bezier, and C. Darcel, *Development of the first iron chloride-catalyzed hydration of terminal alkynes.* Adv. Synth. Catal., 2009. **351**(3): p. 367-370.
103. Cabrero-Antonino, J.R., A. Leyva-Perez, and A. Corma, *Regioselective Hydration of Alkynes by Iron(III) Lewis/Bronsted Catalysis.* Chem. - Eur. J., 2012. **18**(35): p. 11107-11114, S11107/1-S11107/35.
104. Tachinami, T., T. Nishimura, R. Ushimaru, R. Noyori, and H. Naka, *Hydration of Terminal Alkynes Catalyzed by Water-Soluble Cobalt Porphyrin Complexes.* J. Am. Chem. Soc., 2013. **135**(1): p. 50-53.
105. Venkateswara Rao, K.T., P.S. Sai Prasad, and N. Lingaiah, *Solvent-free hydration of alkynes over a heterogeneous silver exchanged silicotungstic acid catalyst.* Green Chem., 2012. **14**(5): p. 1507-1514.
106. Cabrero-Antonino, J.R., A. Leyva-Pérez, and A. Corma, *Regioselective Hydration of Alkynes by Iron(III) Lewis/Brønsted Catalysis.* Chemistry – A European Journal, 2012. **18**(35): p. 11107-11114.
107. Kline, C.H. and V. Kollonitsch, *CATALYTIC ACTIVITY OF TUNGSTEN. II.* Industrial & Engineering Chemistry, 1965. **57**(9): p. 53-60.
108. Kline, C.H. and V. Kollonitsch, *CATALYTIC ACTIVITY OF TUNGSTEN-I.* Industrial & Engineering Chemistry, 1965. **57**(7): p. 53-60.
109. Kob, N., R.S. Drago, and V. Young, *Preparation, Characterization, and Acidity of a Silica Gel/Tungsten Oxide Solid Acid.* Inorganic Chemistry, 1997. **36**(22): p. 5127-5131.
110. Morey, M.S., J.D. Bryan, S. Schwarz, and G.D. Stucky, *Pore Surface Functionalization of MCM-48 Mesoporous Silica with Tungsten and Molybdenum*

Metal Centers: Perspectives on Catalytic Peroxide Activation. Chemistry of Materials, 2000. **12**(11): p. 3435-3444.
111. Apblett Allen, W., B.P. Kiran, and K. Oden, *Reductive Dechlorination of Chloromethanes Using Tungsten and Molybdenum Hydrogen Bronzes or Sodium Hypophosphite*, in *Chlorinated Solvent and DNAPL Remediation*. 2002, American Chemical Society. p. 154-164.
112. Contescu, C., J. Jagiello, and J.A. Schwarz, *Chemistry of surface tungsten species on tungsten trioxide/alumina composite oxides under aqueous conditions.* The Journal of Physical Chemistry, 2002. **97**(39): p. 10152-10157.
113. Ngaosuwan, K., E. Lotero, K. Suwannakarn, J.G. Goodwin, and P. Praserthdam, *Hydrolysis of Triglycerides Using Solid Acid Catalysts.* Industrial & Engineering Chemistry Research, 2002. **48**(10): p. 4757-4767.
114. Varisli, D., T. Dogu, and G. Dogu, *Novel Mesoporous Nanocomposite WOx-Silicate Acidic Catalysts: Ethylene and Diethylether from Ethanol.* Industrial & Engineering Chemistry Research, 2002. **48**(21): p. 9394-9401.
115. Wang, A. and T. Zhang, *One-Pot Conversion of Cellulose to Ethylene Glycol with Multifunctional Tungsten-Based Catalysts.* Accounts of Chemical Research, 2013. **46**(7): p. 1377-1386.
116. Bollapragada, P.K.S., *Chemical transformations using tungsten and molybdenum hydrogen bronzes*. 2003, Oklahoma State University: Ann Arbor. p. 118-118 p.
117. Khan, K.R., *Preparation and nitrobenzene reaction kinetics of microcrystalline tungsten bronze thin films with or without transition metal (silver, titanium, chromium, manganese, iron, cobalt, nickel and copper) coatings*. 2006, Oklahoma State University: Ann Arbor. p. 66-66 p.
118. Ma, J., J. Zhang, S. Wang, T. Wang, J. Lian, X. Duan, and W. Zheng, *Topochemical Preparation of WO3 Nanoplates through Precursor H2WO4 and Their Gas-Sensing Performances.* The Journal of Physical Chemistry C, 2011. **115**(37): p. 18157-18163.
119. Balázsi, C., M. Farkas-Jahnke, I. Kotsis, L. Petrás, and J. Pfeifer, *The observation of cubic tungsten trioxide at high-temperature dehydration of tungstic acid hydrate.* Solid State Ionics, 2001. **141–142**: p. 411-416.
120. Deepa, M., N. Sharma, P. Varshney, S.P. Varma, and S.A. Agnihotry, *FTIR investigations of solid precursor materials for sol-gel deposition of WO3 based electrochromic films.* Journal of Materials Science, 2000. **35**(21): p. 5313-5318.
121. Sawamoto, M. and T. Higashimura, *Cationic oligomerization of unsaturated dimers of styrene and p-methylstyrene.* Macromolecules, 1981. **14**(3): p. 467-471.
122. Venkatesan, C. and A.P. Singh, *Condensation of acetophenone to α,β-unsaturated ketone (dypnone) over solid acid catalysts.* Journal of Molecular Catalysis A: Chemical, 2002. **181**(1–2): p. 179-187.
123. Colquhoun, H.M., J. Holton, D.J. Thompson, and M.V. Twigg, *New Pathways for Organic Synthesis: Practical Applications of Transition Metals*. 2012: Springer US.
124. Hubert, A.J. and H. Reimlinger, *The Isomerization of Olefins Part II. Thermal and Catalytic lsomerization of Olefins using Acids, Metals, Metal Complexes, or Boron Compounds as Catalysts.* Synthesis, 1970. **1970**(08): p. 405-430.

125. Noyce, D.S., D.R. Hartter, and F.B. Miles, *The kinetics and mechanism of the acid-catalyzed isomerization of cis-stilbene.* Journal of the American Chemical Society, 1968. **90**(17): p. 4633-4637.
126. Deng, K., Q.-Y. Huai, Z.-L. Shen, H.-J. Li, C. Liu, and Y.-C. Wu, *Rearrangement of Dypnones to 1,3,5-Triarylbenzenes.* Organic Letters, 2015. **17**(6): p. 1473-1476.
127. Carey, F.A., *Advanced Organic Chemistry: Part B: Reactions and Synthesis*. 2013: Springer US.
128. Zakharova, G.S. and V.L. Volkov, *Intercalation compounds based on vanadium(V) oxide xerogel.* Russian Chemical Reviews, 2003. **72**(4): p. 311-325.
129. Oka, Y., N. Yamamoto, and T. Yao, *Ion-exchange properties of hydrated vanadium oxide with a layered structure of alkali-metal ions.* Solid State Ionics, 1992. **57**(1–2): p. 103-107.
130. Sarina, S., A. Bo, D. Liu, H. Liu, D. Yang, C. Zhou, N. Maes, S. Komarneni, and H. Zhu, *Separate or Simultaneous Removal of Radioactive Cations and Anions from Water by Layered Sodium Vanadate-Based Sorbents.* Chemistry of Materials, 2014. **26**(16): p. 4788-4795.
131. Barber, K.A., Allen W.; Al-Fadul, Sulaiman; Piquette, Alan; Chehbouni, Mohamed, *Nanotechnology for uranium separations and immobilization.* Ceram. Trans., 2010. **222**: p. 177-187.
132. Kiran, B.P.A., Allen W., *Process for selective removal and concentration of actinides and heavy metals from water.* Ceram. Trans., 2004. **155**: p. 371-380.
133. Barber, K.N., C.K. Perkins, and A.W. Apblett, *Reduction of chromate by molybdenum hydrogen bronze.* Canadian Journal of Chemistry, 2015. **94**(4): p. 401-405.
134. Apblett, A.W. and N.F. Materer, *Nanometric ink for detection of explosives*. 2011, Oklahoma State University, USA . p. 13pp.
135. Apblett, A.W.K., B. P.; Malka, Srilatha; Materer, Nicholas F.; Piquette, Alan, *Nanotechnology for neutralization of terrorist explosives.* Ceram. Trans., 2006. **172**: p. 29-35.
136. Barber, K.N., *Novel environmental and explosives detection applications for molybdenum oxides*. 2009, Oklahoma State University: Ann Arbor. p. 204.
137. Kadossov, E.B., A.R. Soufiani, A.W. Apblett, and N.F. Materer, *Density-functional studies of hydrogen peroxide adsorption and dissociation on MoO3(100) and H0.33MoO3(100) surfaces.* RSC Advances, 2015. **5**(118): p. 97755-97763.
138. Chippindale, A.M., P.G. Dickens, and A.V. Powell, *Synthesis, characterization, and inelastic neutron scattering study of hydrogen insertion compounds of VO2(rutile).* Journal of Solid State Chemistry, 1991. **93**(2): p. 526-533.
139. Hirata, T. and K. Yagisawa, *Infrared spectra of platinum-impregnated V2O5 powders on hydrogen insertion.* Journal of Alloys and Compounds, 1992. **185**(1): p. 177-182.
140. Livage, J., *Vanadium pentoxide gels.* Chemistry of Materials, 1991. **3**(4): p. 578-593.
141. Bondarenka, V., Z. Martunas, S. Kaciulis, and L. Pandolfi, *Sol–gel synthesis and XPS characterization of sodium–vanadium oxide bronze thin films.* Journal of Electron Spectroscopy and Related Phenomena, 2003. **131–132**(0): p. 99-103.

142. Aldebert, P., N. Baffier, N. Gharbi, and J. Livage, *Layered structure of vanadium pentoxide gels.* Materials Research Bulletin, 1981. **16**(6): p. 669-676.
143. Oka, Y., T. Yao, and N. Yamamoto, *Hydrothermal Synthesis of Alkali-Containing Hydrated Vanadium Oxides with Layered Structures.* Journal of the Ceramic Society of Japan, 1990. **98**(1144): p. 1365-1367.
144. Bermejo, E., R. Carballo, A. Castiñeiras, and A.B. Lago, *Coordination of α-hydroxycarboxylic acids with first-row transition ions.* Coordination Chemistry Reviews, 2013. **257**(19–20): p. 2639-2651.
145. Hlaibi, M., S. Chapelle, M. Benaissa, and J.-F. Verchere, *Structures and Stabilities of Tungstate Complexes of .alpha.-Hydroxy Acids. 183W NMR Study of the Influence of Ligand Substitution.* Inorganic Chemistry, 1995. **34**(17): p. 4434-4440.
146. Moneeb, A.M., A.M. Alabdulrahman, A.A. Bagabas, C.K. Perkins, and A.W. Apblett, *Bimetallic single-source precursor for the synthesis of pure nanocrystalline room temperature-stabilized β-NiMoO4.* Ceramics International, 2016. **42**(1, Part B): p. 1366-1372.
147. Perkins, C.K., K.N. Barber, and A.W. Apblett, *Direct conversion of a nanometric suspension of molybdenum trioxide into nanometric lead molybdate.* CrystEngComm, 2014. **16**(14): p. 2869-2873.
148. Brauer, G., *Handbook of Preparative Inorganic Chemistry*. 2012: Elsevier Science.
149. James, T., A. Apblett, and N.F. Materer, *Rapid Quantification of Sodium Dithionite by Ion Chromatography.* Industrial & Engineering Chemistry Research, 2012. **51**(22): p. 7742-7746.
150. Brauer, G., *SECTION 23 - Vanadium, Niobium, Tantalum*, in *Handbook of Preparative Inorganic Chemistry (Second Edition)*, G. Brauer, Editor. 1965, Academic Press. p. 1252-1333.
151. Fo Tsang, C., J. Kim, and A. Manthiram, *Synthesis of reduced vanadium oxides in aqueous solutions.* Journal of Materials Chemistry, 1998. **8**(2): p. 425-428.
152. Tinet, D., H. Estrade-Szwarckopf, and J.J. Fripiat, *HYDROGEN VANADIUM PENTOXIDE BRONZE, HxV2O5 A2 - VEZIROĞLU, T. NEJAT*, in *Metal–Hydrogen Systems*. 1982, Pergamon. p. 459-466.
153. Dickens, P.G., A.M. Chippindale, S.J. Hibble, and P. Lancaster, *Hydrogen insertion compounds of V6O13 and V2O5.* Materials Research Bulletin, 1984. **19**(3): p. 319-324.
154. Chippindale, A.M. and P.G. Dickens, *The thermochemistry of the hydrogen vanadium bronzes HxV2O5.* Solid State Ionics, 1987. **23**(3): p. 183-188.
155. Zuckerman, J.J. and A.P. Hagen, *Inorganic Reactions and Methods, The Formation of Bonds to Hydrogen*. 2009: Wiley.
156. Taylor, M.J.C. and J.F. van Staden, *Spectrophotometric determination of vanadium(IV) and vanadium(V) in each other's presence. Review.* Analyst, 1994. **119**(6): p. 1263-1276.
157. Rinker, R.G., S. Lynn, D.M. Mason, and W.H. Corcoran, *Kinetics and Mechanism of Thermal Decomposition of Sodium Dithionite in Aqueous Solution.* Industrial & Engineering Chemistry Fundamentals, 1965. **4**(3): p. 282-288.

158. Subba Reddy, C.V., S.-i. Mho, R.R. Kalluru, and Q.L. Williams, *Hydrothermal synthesis of hydrated vanadium oxide nanobelts using poly (ethylene oxide) as a template.* Journal of Power Sources, 2008. **179**(2): p. 854-857.
159. Ballhausen, C.J. and H.B. Gray, *The Electronic Structure of the Vanadyl Ion.* Inorganic Chemistry, 1962. **1**(1): p. 111-122.
160. Furman, S.C. and C.S. Garner, *Absorption Spectra of Vanadium(III) and Vanadium(IV) Ions in Complexing and Non-complexing Media.* Journal of the American Chemical Society, 1950. **72**(4): p. 1785-1789.
161. Crans, D.C., J.J. Smee, E. Gaidamauskas, and L. Yang, *The Chemistry and Biochemistry of Vanadium and the Biological Activities Exerted by Vanadium Compounds.* Chemical Reviews, 2004. **104**(2): p. 849-902.
162. Kittaka, S., N. Uchida, H. Miyahara, and Y. Yokota, *Crystal structure of vanadium pentaoxide hydrate 1. Electron diffraction study of the a-b structure.* Materials Research Bulletin, 1991. **26**(5): p. 391-398.
163. Natalio, F., R. Andre, A.F. Hartog, B. Stoll, K.P. Jochum, R. Wever, and W. Tremel, *Vanadium pentoxide nanoparticles mimic vanadium haloperoxidases and thwart biofilm formation.* Nat Nano, 2012. **7**(8): p. 530-535.
164. Nielsen, U.G., A. Boisen, M. Brorson, C.J.H. Jacobsen, H.J. Jakobsen, and J. Skibsted, *Aluminum Orthovanadate (AlVO4): Synthesis and Characterization by 27Al and 51V MAS and MQMAS NMR Spectroscopy.* Inorganic Chemistry, 2002. **41**(24): p. 6432-6439.
165. Pavasupree, S., Y. Suzuki, A. Kitiyanan, S. Pivsa-Art, and S. Yoshikawa, *Synthesis and characterization of vanadium oxides nanorods.* Journal of Solid State Chemistry, 2005. **178**(6): p. 2152-2158.
166. Yao, T., Y. Oka, and N. Yamamoto, *Layered structures of vanadium pentoxide gels.* Materials Research Bulletin, 1992. **27**(6): p. 669-675.
167. Chang, K.-H. and C.-C. Hu, *H2V3O8 single-crystal nanobelts: Hydrothermal preparation and formation mechanism.* Acta Mater., 2007. **55**(18): p. 6192-6197.
168. Blangenois, N., M. Florea, P. Grange, R.P. Silvy, S.P. Chenakin, J.M. Bastin, N. Kruse, B.P. Barbero, and L. Cadús, *Influence of the co-precipitation pH on the physico-chemical and catalytic properties of vanadium aluminum oxide catalyst.* Applied Catalysis A: General, 2004. **263**(2): p. 163-170.
169. Chenakin, S.P., R. Prada Silvy, and N. Kruse, *Effect of X-rays on the Surface Chemical State of Al2O3, V2O5, and Aluminovanadate Oxide.* The Journal of Physical Chemistry B, 2005. **109**(30): p. 14611-14618.
170. Chenakin, S.P., R.P. Silvy, and N. Kruse, *XPS–SIMS Surface Characterization of Aluminovanadate Oxide Catalyst Precursors Co-Precipitated at Different pH: Effect of Calcination.* Topics in Catalysis, 2012. **55**(11-13): p. 731-746.
171. Pan, A., J.-G. Zhang, Z. Nie, G. Cao, B.W. Arey, G. Li, S.-q. Liang, and J. Liu, *Facile synthesized nanorod structured vanadium pentoxide for high-rate lithium batteries.* Journal of Materials Chemistry, 2010. **20**(41): p. 9193-9199.
172. Abeysinghe, D., M.D. Smith, J. Yeon, G. Morrison, and H.-C. zur Loye, *Observation of Multiple Crystal-to-Crystal Transitions in a New Reduced Vanadium Oxalate Hybrid Material, Ba3[(VO)2(C2O4)5(H2O)6]·(H2O)3,*

Prepared via a Mild, Two-Step Hydrothermal Method. Crystal Growth & Design, 2014. **14**(9): p. 4749-4758.
173. Sathyanarayana, D.N. and C.C. Patel, *Studies on oxovanadium (IV) oxalate hydrates.* Journal of Inorganic and Nuclear Chemistry, 1965. **27**(2): p. 297-302.
174. Costisor, O., M. Brezeanu, Y. Journaux, K. Mereiter, P. Weinberger, and W. Linert, *A Novel Salt Formed by Mixed-Valence Vanadium(IV, V) [(VO)2O(bpy)2(C2O4)2] Anions and Ferromagnetic [Cu2(bpy)4(C2O4)] Cations: Structure, Spectroscopic Characterization and Magnetic Properties.* European Journal of Inorganic Chemistry, 2001. **2001**(8): p. 2061-2966.
175. Kalinnikov, V.T., V.V. Zelentsov, and M.N. Volkov, *Infrared absorption spectra of the vanadyl salts of some α, ω-dicarboxylic acids.* Journal of Structural Chemistry, 1967. **8**(1): p. 50-54.
176. Tarama, K., S. Yoshida, S. Ishida, and H. Kakioka, *Spectroscopic Studies of Catalysis by Vanadium Pentoxide.* Bulletin of the Chemical Society of Japan, 1968. **41**(12): p. 2840-2845.
177. Wu, M., X. Zhang, S. Gao, X. Cheng, Z. Rong, Y. Xu, H. Zhao, and L. Huo, *Construction of monodisperse vanadium pentoxide hollow spheres via a facile route and triethylamine sensing property.* CrystEngComm, 2013. **15**(46): p. 10123-10131.
178. Peys, N., Y. Ling, D. Dewulf, S. Gielis, C. De Dobbelaere, D. Cuypers, P. Adriaensens, S. Van Doorslaer, S. De Gendt, A. Hardy, and M.K. Van Bael, *V6O13 films by control of the oxidation state from aqueous precursor to crystalline phase.* Dalton Trans, 2013. **42**(4): p. 959-68.
179. Barriga, C., W. Jones, P. Malet, V. Rives, and M.A. Ulibarri, *Synthesis and Characterization of Polyoxovanadate-Pillared Zn−Al Layered Double Hydroxides: An X-ray Absorption and Diffraction Study.* Inorganic Chemistry, 1998. **37**(8): p. 1812-1820.
180. Baldovino-Medrano, V.G., B. Farin, and E.M. Gaigneaux, *Establishing the Role of Graphite as a Shaping Agent of Vanadium–Aluminum Mixed (Hydr)oxides and Their Physicochemical Properties and Catalytic Functionalities.* ACS Catalysis, 2012. **2**(3): p. 322-336.
181. Martínez-Huerta, M.V., X. Gao, H. Tian, I.E. Wachs, J.L.G. Fierro, and M.A. Bañares, *Oxidative dehydrogenation of ethane to ethylene over alumina-supported vanadium oxide catalysts: Relationship between molecular structures and chemical reactivity.* Catalysis Today, 2006. **118**(3–4): p. 279-287.
182. Rossetti, I., G.F. Mancini, P. Ghigna, M. Scavini, M. Piumetti, B. Bonelli, F. Cavani, and A. Comite, *Spectroscopic Enlightening of the Local Structure Of VOX Active Sites in Catalysts for the Odh of Propane.* The Journal of Physical Chemistry C, 2012. **116**(42): p. 22386-22398.
183. Fang, Z.M., Q. Hong, Z.H. Zhou, S.J. Dai, W.Z. Weng, and H.L. Wan, *Oxidative dehydrogenation of propane over a series of low-temperature rare earth orthovanadate catalysts prepared by the nitrate method.* Catalysis Letters, 1999. **61**(1): p. 39-44.
184. Martínez-Huerta, M.V., J.M. Coronado, M. Fernández-García, A. Iglesias-Juez, G. Deo, J.L.G. Fierro, and M.A. Bañares, *Nature of the vanadia–ceria interface in*

V5+/CeO2 catalysts and its relevance for the solid-state reaction toward CeVO4 and catalytic properties. Journal of Catalysis, 2004. **225**(1): p. 240-248.
185. Tsipis, E.V., M.V. Patrakeev, V.V. Kharton, N.P. Vyshatko, and J.R. Frade, *Ionic and p-type electronic transport in zircon-type Ce1 - xAxVO4 +/- [small delta] (A = Ca, Sr).* Journal of Materials Chemistry, 2002. **12**(12): p. 3738-3745.
186. Terada, Y., K. Shimamura, V.V. Kochurikhin, L.V. Barashov, M.A. Ivanov, and T. Fukuda, *Growth and optical properties of ErVO4 and LuVO4 single crystals.* Journal of Crystal Growth, 1996. **167**(1): p. 369-372.
187. Picardi, G., F. Varsano, F. Decker, U. Opara-Krasovec, A. Surca, and B. Orel, *Electrochemical characterization of optically passive CeVO4 counterelectrodes.* Electrochimica Acta, 1999. **44**(18): p. 3157-3164.
188. Liu, J., Q. Yao, and Y. Li, *Effects of downconversion luminescent film in dye-sensitized solar cells.* Applied Physics Letters, 2006. **88**(17): p. 173119.
189. Huignard, A., T. Gacoin, and J.-P. Boilot, *Synthesis and Luminescence Properties of Colloidal YVO4:Eu Phosphors.* Chemistry of Materials, 2000. **12**(4): p. 1090-1094.
190. Gaur, K. and H.B. Lal, *Unusual magnetic behaviour of heavy rare earth vanadates at higher temperature.* Journal of Materials Science Letters, 1983. **2**(12): p. 744-746.
191. Xu, Z., X. Kang, C. Li, Z. Hou, C. Zhang, D. Yang, G. Li, and J. Lin, *Ln3+ (Ln = Eu, Dy, Sm, and Er) Ion-Doped YVO4 Nano/Microcrystals with Multiform Morphologies: Hydrothermal Synthesis, Growing Mechanism, and Luminescent Properties.* Inorganic Chemistry, 2010. **49**(14): p. 6706-6715.
192. Feng, W., L.-D. Sun, Y.-W. Zhang, and C.-H. Yan, *Synthesis and assembly of rare earth nanostructures directed by the principle of coordination chemistry in solution-based process.* Coordination Chemistry Reviews, 2010. **254**(9–10): p. 1038-1053.
193. Yu, M., J. Lin, Z. Wang, J. Fu, S. Wang, H.J. Zhang, and Y.C. Han, *Fabrication, Patterning, and Optical Properties of Nanocrystalline YVO4:A (A = Eu3+, Dy3+, Sm3+, Er3+) Phosphor Films via Sol−Gel Soft Lithography.* Chemistry of Materials, 2002. **14**(5): p. 2224-2231.
194. Yan, Z.-G. and C.-H. Yan, *Controlled synthesis of rare earth nanostructures.* Journal of Materials Chemistry, 2008. **18**(42): p. 5046-5059.
195. Zhang, H., X. Fu, S. Niu, G. Sun, and Q. Xin, *Low temperature synthesis of nanocrystalline YVO4:Eu via polyacrylamide gel method.* Journal of Solid State Chemistry, 2004. **177**(8): p. 2649-2654.
196. Rives, V., *From Solid-State Chemistry to Soft Chemistry Routes*, in *Perovskites and Related Mixed Oxides*. 2016, Wiley-VCH Verlag GmbH & Co. KGaA. p. 1-24.
197. Chang-Wei, L., Q. Hai-Bo, F. Chu-De, X. Tong-Geng, Y. Xue-Hua, C. Yun-Xian, and G. Jing-kun, *Investigation on the mechanism of n-butanol interaction with zirconia powder.* Thermochimica Acta, 1994. **246**(1): p. 99-105.
198. Sudrajat, H., S. Babel, H. Sakai, and S. Takizawa, *Rapid enhanced photocatalytic degradation of dyes using novel N-doped ZrO2.* Journal of Environmental Management, 2016. **165**: p. 224-234.

199. Kouva, S., K. Honkala, L. Lefferts, and J. Kanervo, *Review: monoclinic zirconia, its surface sites and their interaction with carbon monoxide.* Catalysis Science & Technology, 2015. **5**(7): p. 3473-3490.
200. Kantcheva, M., *Spectroscopic characterization of vanadium(V) oxo species deposited on zirconia.* Physical Chemistry Chemical Physics, 2000. **2**(13): p. 3043-3048.
201. Sohn, J.R., S.G. Cho, Y.I. Pae, and S. Hayashi, *Characterization of Vanadium Oxide–Zirconia Catalyst.* Journal of Catalysis, 1996. **159**(1): p. 170-177.
202. Sohn, J.-R., K.-C. Seo, and Y.-I. Pae, *Characterization of Vanadium Oxide Supported on Zirconia and Modified with MoO 3.* Bulletin of the Korean Chemical Society, 2003. **24**(3): p. 311-317.
203. Lin, C., C. Zhang, and J. Lin, *Phase Transformation and Photoluminescence Properties of Nanocrystalline ZrO2 Powders Prepared via the Pechini-type Sol−Gel Process.* The Journal of Physical Chemistry C, 2007. **111**(8): p. 3300-3307.
204. Calatayud, J.M., P. Pardo, and J. Alarcon, *V-containing ZrO2 inorganic yellow nano-pigments.* RSC Advances, 2015. **5**(72): p. 58669-58678.
205. Khodakov, A., J. Yang, S. Su, E. Iglesia, and A.T. Bell, *Structure and properties of vanadium oxide-zirconia catalysts for propane oxidative dehydrogenation.* Journal of Catalysis, 1998. **177**(2): p. 343-351.
206. Li, X., Q. Li, Z. Xia, L. Wang, W. Yan, J. Wang, and R.I. Boughton, *Growth and Characterization of Single-Crystal Y2O3:Eu Nanobelts Prepared with a Simple Technique.* Crystal Growth & Design, 2006. **6**(10): p. 2193-2196.
207. Atabaev, T.S., O.S. Jin, J.H. Lee, D.-W. Han, H.H.T. Vu, Y.-H. Hwang, and H.-K. Kim, *Facile synthesis of bifunctional silica-coated core-shell Y2O3:Eu3+,Co2+ composite particles for biomedical applications.* RSC Advances, 2012. **2**(25): p. 9495-9501.
208. Atabaev, T.S., H.-H. Thi Vu, Y.-D. Kim, J.-H. Lee, H.-K. Kim, and Y.-H. Hwang, *Synthesis and luminescence properties of Ho3+ doped Y2O3 submicron particles.* Journal of Physics and Chemistry of Solids, 2012. **73**(2): p. 176-181.
209. Fleming, P., R.A. Farrell, J.D. Holmes, and M.A. Morris, *The Rapid Formation of La(OH)3 from La2O3 Powders on Exposureto Water Vapor.* Journal of the American Ceramic Society, 2010. **93**(4): p. 1187-1194.
210. Nakamoto, K., *Infrared and Raman spectra of inorganic and coordination compounds*. 1986: Wiley.
211. Bashir, J. and M.N. Khan, *X-ray powder diffraction analysis of crystal structure of lanthanum orthovanadate.* Materials Letters, 2006. **60**(4): p. 470-473.
212. Ma, J., Q. Wu, and Y. Ding, *Selective synthesis of monoclinic and tetragonal phase LaVO4 nanorods via oxides-hydrothermal route.* Journal of Nanoparticle Research, 2008. **10**(5): p. 775-786.
213. Sigel, A. and H. Sigel, *Metal Ions in Biological Systems: Volume 31: Vanadium and its Role for Life*. 1995: Taylor & Francis.
214. Volkert, W.A. and T.J. Hoffman, *Therapeutic radiopharmaceuticals.* Chemical reviews, 1999. **99**(9): p. 2269-2292.

215. Apblett, A.W., G.D. Georgieva, and J.T. Mague, *Synthesis and Spectroscopic and Thermal Decomposition Studies of Alkali Metal Salts of 2-Oximidopropionate.* Inorganic Chemistry, 1997. **36**(12): p. 2656-2661.
216. Bagabas, A.A., *Low temperature precursors for metal oxide catalysts*. 2005, Oklahoma State University: Ann Arbor. p. 319-319 p.
217. El-Tabl, A.S., M. Mohamed Abd El-Waheed, M.A. Wahba, and N. Abd El-Halim Abou El-Fadl, *Synthesis, Characterization, and Anticancer Activity of New Metal Complexes Derived from 2-Hydroxy-3-(hydroxyimino)-4-oxopentan-2-ylidene)benzohydrazide.* Bioinorganic Chemistry and Applications, 2015. **2015**: p. 126023.
218. Lampeka Rostislav, D., D. Uzakbergenova Zamira, and V. Skopenko Victor, *Spectroscopic and X-Ray Investigation of Cobalt(III) Complexes with 2-Oximinocarboxylic Acids*, in *Zeitschrift für Naturforschung B*. 1993. p. 409.
219. Malek, K., H. Kozłowski, and L.M. Proniewicz, *Interaction of Na(I), Ni(II) and Cu(II) with 2-cyano-2-(hydroxyimino)acetic acid: Spectroscopic and theoretical studies.* Polyhedron, 2005. **24**(10): p. 1175-1184.
220. Cato, M.A., *New Developments in Organometallic Chemistry Research*. 2006: Nova Science Publishers.
221. Apblett, A.W., J. Lei, and G.D. Georgeva, *Molecular design of carboxylic precursors for zirconia.* Mater. Res. Soc. Symp. Proc., 1992. **271**(Better Ceramics through Chemistry V): p. 77-82.
222. Apblett, A.W. and G.D. Georgieva, *Low temperature precursors for titanium oxide.* Phosphorus, Sulfur Silicon Relat. Elem., 1994. **93-94**(1-4): p. 479-80.
223. Hexem, J.G., M.H. Frey, and S.J. Opella, *Influence of nitrogen-14 on carbon-13 NMR spectra of solids.* Journal of the American Chemical Society, 1981. **103**(1): p. 224-226.
224. Opella, S.J., *Solid-state NMR and Membrane Proteins.* Journal of magnetic resonance (San Diego, Calif. : 1997), 2015. **253**: p. 129-137.
225. Rakovský, E., Ľ. Žúrková, and J. Marek, *Synthesis, Crystal Structure, and IR Spectroscopic Characterization of 1,6-Hexanediammonium Dihydrogendecavanadate.* Monatshefte für Chemie / Chemical Monthly, 2002. **133**(3): p. 277-283.
226. Siddiqi, Z.A., Anjuli, P.K. Sharma, M. Shahid, M. Khalid, A. Siddique, and S. Kumar, *Novel decavanadate cluster complexes [H2V10O28][LH]4·nH2O (L = Imidazole, n = 2 or 2-methylimidazole, n = 0): Preparation, characterization and genotoxic studies.* Journal of Molecular Structure, 2012. **1029**: p. 86-91.
227. Evans Jr, H.T., *The molecular structure of the isopoly complex ion, decavanadate (V10O286-).* Inorganic Chemistry, 1966. **5**(6): p. 967-977.
228. Rehder, D., *Bioinorganic Vanadium Chemistry*. 2008: Wiley.
229. Selbin, J., L.H. Holmes, and S.P. McGlynn, *Electronic structure, spectra and magnetic properties of oxycations—IV ligation effects on the infra-red spectrum of the vanadyl ion.* Journal of Inorganic and Nuclear Chemistry, 1963. **25**(11): p. 1359-1369.

230. Scheurell, K. and E. Kemnitz, *Amorphous aluminium fluoride as new matrix for vanadium-containing catalysts.* Journal of Materials Chemistry, 2005. **15**(45): p. 4845-4853.
231. Jones, C.W., *Applications of Hydrogen Peroxide and Derivatives*. 1999: Royal Society of Chemistry.
232. Armitage, J.B. and H.W. Strauss, *SAFETY CONSIDERATIONS IN INDUSTRIAL USE OF ORGANIC PEROXIDES.* Industrial & Engineering Chemistry, 1964. **56**(12): p. 28-32.
233. Mageli, O.L. and J.R. Kolczynski, *ORGANIC PEROXIDES.* Industrial & Engineering Chemistry, 1966. **58**(3): p. 25-32.
234. OSHA; Labor, U.S.D.o., Ed. 1910.
235. *Institute for Economics and Peace. Global Terrorism Index report; Global Terrorism Index November 2015*.
236. Robert J. Bunker, C.F., *Body Cavity Bombers: The New Martyrs: A Terrorism Research Center Book*. 2013: iUniverse.
237. Olley, D.A., E.J. Wren, G. Vamvounis, M.J. Fernee, X. Wang, P.L. Burn, P. Meredith, and P.E. Shaw, *Explosive Sensing with Fluorescent Dendrimers: The Role of Collisional Quenching.* Chemistry of Materials, 2011. **23**(3): p. 789-794.
238. Diehl, K.L. and E.V. Anslyn, *Array sensing using optical methods for detection of chemical and biological hazards.* Chemical Society Reviews, 2013. **42**(22): p. 8596-8611.
239. Lichtenstein, A., E. Havivi, R. Shacham, E. Hahamy, R. Leibovich, A. Pevzner, V. Krivitsky, G. Davivi, I. Presman, R. Elnathan, Y. Engel, E. Flaxer, and F. Patolsky, *Supersensitive fingerprinting of explosives by chemically modified nanosensors arrays.* Nat Commun, 2014. **5**.
240. Dubnikova, F., R. Kosloff, Y. Zeiri, and Z. Karpas, *Novel approach to the detection of triacetone triperoxide (TATP), its structure and its complexes with ions.* J. Phys. Chem. A, 2002. **106**: p. 4951–4956.
241. Schulte-Ladbeck, R., P. Kolla, and U.T. Karst, *Trace Analysis of Peroxide-Based Explosives.* Analytical Chemistry, 2003. **75**(4): p. 731-735.
242. Apblett, A.W., B.P. Kiran, S. Malka, N.F. Materer, and A. Piquette, *Nanotechnology for neutralization of terrorist explosives.* Ceramic Transactions, 2006. **172**(Ceramic Nanomaterials and Nanotechnologies IV): p. 29-35.
243. Wilson, P.F., B.J. Prince, and M.J. McEwan, *Application of Selected-Ion Flow Tube Mass Spectrometry to the Real-Time Detection of Triacetone Triperoxide.* Analytical Chemistry, 2006. **78**(2): p. 575-579.
244. Xu, M., B.R. Bunes, and L. Zang, *Paper-Based Vapor Detection of Hydrogen Peroxide: Colorimetric Sensing with Tunable Interface.* ACS Applied Materials & Interfaces, 2011. **3**(3): p. 642-647.
245. Royer, J.E., E.D. Kappe, C. Zhang, D.T. Martin, W.C. Trogler, and A.C. Kummel, *Organic Thin-Film Transistors for Selective Hydrogen Peroxide and Organic Peroxide Vapor Detection.* The Journal of Physical Chemistry C, 2012. **116**(46): p. 24566-24572.

246. James, T.H., C. Cannon, D. Scott, Z. AlOthman, A. Apblett, and N.F. Materer, *Titania–Hydroxypropyl Cellulose Thin Films for the Detection of Peroxide Vapors.* ACS Applied Materials & Interfaces, 2014. **6**(13): p. 10205-10212.
247. Marks, P., B. Radaram, M. Levine, and I.A. Levitsky, *Highly efficient detection of hydrogen peroxide in solution and in the vapor phase via fluorescence quenching.* Chemical Communications, 2015. **51**(32): p. 7061-7064.
248. Apblett, A.W. and N.F. Materer, *Nanometric ink for detection of explosives*. 2011, Google Patents.
249. Schwarzmann, E. and R. Birkenberg, *Hydrogen analogs of tungsten bronzes.* Zeitschrift fuer Naturforschung, Teil B: Anorganische Chemie, Organische Chemie, Biochemie, Biophysik, Biologie, 1971. **26**(10): p. 1069-70.
250. Tinet, D. and J.J. Fripiat, *Hydrogen bronzes formation process, structure and physical properties.* Solid State Protonic Conduct. 1 Fuel Cells Sens., Dan.-Fr. Workshop \"Solid State Mater. Low Medium Temp. Fuel Cells Monit., Spec. Emphasis Proton Conduct.\", 1982: p. 259-68.
251. Fripiat, J.J., *Hydrogen bronzes: a review of some of their physical and catalytic properties.* NATO ASI Series, Series C: Mathematical and Physical Sciences, 1983. **105**(Surf. Prop. Catal. Non-Met.): p. 477-91.
252. Sotani, N., K. Eda, and M. Kunitomo, *Hydrogen insertion compounds of molybdenum trioxide (hydrogen molybdenum bronze, HxMoO3).* Trends in Inorganic Chemistry, 1990. **1**(1): p. 23-39.
253. Barber, K.N., *Novel environmental and explosives detection applications for molybdenum oxides*. 2009, Oklahoma State University: Ann Arbor. p. 203.
254. Zhang, Q., S. Fu, H. Li, and Y. Liu, *A Novel Method for the Determination of Hydrogen Peroxide in Bleaching Effluents by Spectroscopy*. 2013. Vol. 8. 2013.
255. Grigorieva, A.V., S.M. Badalyan, E.A. Goodilin, M.N. Rumyantseva, A.M. Gaskov, A. Birkner, and Y.D. Tretyakov, *Synthesis, Structure, and Sensor Properties of Vanadium Pentoxide Nanorods.* European Journal of Inorganic Chemistry, 2010. **2010**(33): p. 5247-5253.

VITA

ASMA ABDULLAH ALOTHMAN
Candidate for the Degree of
Doctor of Philosophy

Thesis: THE SYNTHESIS AND APPLICATIONS OF TUNGSTEN AND VANADIUM OXIDES/OXYHYDROXIDES IN BOTH BULK AND NANOPATICULATE FORMS
Major Field: CHEMISTRY

Education: Completed the requirements for the Doctor of Philosophy in Inorganic Chemistry at Oklahoma State University, Stillwater, Oklahoma in December, 2016. Completed the requirements for the Master of Science in Inorganic Chemistry at King Saud University, Riyadh, Kingdom of Saudi Arabia in July, 2008. Completed the requirements for the Bachelor of Science in Chemistry at King Saud University, Riyadh, Kingdom of Saudi Arabia in July, 2003.

Experience: Employed by King Saud University, Riyadh, Kingdom of Saudi Arabia as a teaching assistant from 2010 - 2014. Employed by King Saud University, Riyadh, Kingdom of Saudi Arabia as a Lecturer from 2014 - present. Worked as a graduate research assistant in the department of chemistry, Oklahoma State University, Stillwater, Oklahoma, USA, with scholarship from King Saud University from 2011 -2016.

Selected Abstracts:

- Alothman, A. and A. Apblett. Synthesis and characterization of vanadium oxide thin solid films produced from colloidal suspensions of bronze substrates. in 252th American Chemical Society (ACS) National Meeting & exposition 2016. Philadelphia, PA, USA: American Chemical Society.
- Alothman, A., N. Materer, Z. Alothman, and A. Apblett. Investigation of vanadium-based bronze materials for the detection of peroxide based explosives. in 251th American Chemical Society (ACS) National Meeting & exposition. 2016. San Diego, CA, USA: American Chemical Society.
- Alothman, A.A. and A.W. Apblett. Low-temperature precursors for vanadium oxide nanomaterials for catalytic application. in 250th American Chemical Society (ACS) National Meeting & exposition. 2015. Boston, MA, USA: American Chemical Society.
- Alothman, A.A. and A.W. Apblett. Synthesis, characterization, and application of mixed metal vanadium oxyhydroxides. in 249th American Chemical Society (ACS) National Meeting & exposition. 2015. Denver, CO, USA: American Chemical Society.
- Al Othman, A. and A. Apblett. Tungstic acid catalyzed cyclotrimerization of alkynes. in 248th American Chemical Society (ACS) National Meeting & exposition. 2014. San Francisco, CA, USA: American Chemical Society.
- Alothman, A. and A. Apblett. Preparation of aluminum vanadate and vanadic acid materials using vanadyl oxalate. in 247th American Chemical Society (ACS) National Meeting & exposition. 2014. Dallas, Texas, USA: American Chemical Society.
- Alothman, A. and A. Apblett. Chemical transformations of alkene and alkyne using tungstic acid as a catalyst: Kinetics and reactions mechanisms. in 246th American Chemical Society (ACS) National Meeting & exposition. 2013. Indianapolis, NI, USA: American Chemical Society.

Professional Memberships: American Chemical Society, and its Inorganic Chemistry Division, and Oklahoma Local Section, Saudi Chemical Society, Phi Kappa Phi Society